9.C.2.4.2.3 Experiment E11.5

Experiment E11.5 is performed with a large break LOCA at the lowest possible position (room R1405) with subsequent small-break releases (see Fig. 9.C.2-92). An overview of experimental results is presented by L. Wolf, K. Mun, 1996.

The containment pressure during the large break heatup phase is shown in Figure 9.C.2-93. At the end of the initial steam blowdown (50 seconds), the pressure reaches the peak of 2.56 bars (see Figure 9.C.2-93), then continuously decreases due to the condensation at the cold surfaces. Note that the external dome cooling is not applied during this experiment.

The 15-hour (900 minute) containment pressure history is presented in Figure 9.C.2-94. The gas release and steam injection following the initial blowdown slows the depressurization (see Figure 9.C.2-94). Over the time intervals 155-219 minutes, 245-545 minutes, and 695-820 minutes, the pressure slowly increases inside the containment due to the additional gas and steam releases. During the sump heating phase, the pressure first decreases and then increases. The increase in pressure coincides with the moment when the sump reaches saturated conditions and starts to evaporate. After reaching a second peak value of 1.6 bar at the end of the steam release into the subcompartment R1405, containment pressure decreases to atmospheric pressure. The containment depressurizes through the vent lines at the 0 m and 10 m elevations.

Temperatures along the main stairway during the heatup phase are presented in Figure 9.C.2-95. The combination of steam and gas releases during the heatup phase results in thermal stratification. This is shown by a 25 °C temperature differential over the height of the containment after 80 minutes and a 12 °C differential from top to bottom of the dome - see Figure 9.C.2-95.

Figure 9.C.2-96 presents the temperatures in both major flow paths (main and spiral staircases) at the same three axial positions. The temperature differences are relatively constant through time at each elevation, although smaller at the high elevations. Circulation is sufficient to keep the temperature difference between the two chimneys small (e.g., ΔT is approximately 5 °C at the +16.5 elevation), for the various steam, dry heat, and sump boiling releases that occur in the lower portion of the containment.

The temperature distributions for the entire containment are presented in Figures 9.C.2-97 and 9.C.2-98 over time intervals 2.0 to 75.0 minutes and 123 to 345 minutes, respectively. After the initial rise, the temperatures decrease quickly during the first 25 minutes (Figure 9.C.2-97). The decrease then continues at a slower rate (see Figure 9.C.2-98). The temperatures stratify in the main staircase, while in the spiral staircase they are almost uniform. Temperature differences between the top of the containment and the release level are approximately 10 °C in the main staircase and 5 °C in the spiral staircase. The temperature difference below

the main stair case, between the level of the release and the bottom of the containment (between CT5301 and CT3802) is around 15°C.

The temperature decreases slowly in the upper region of the dome. The effects of the global circulation on the upper region of the dome are noticeable after the end of the steam release. This is evident from a comparison of the H_2/He concentrations during the gas mixture release (Figure 9.C.2-98). After the release, the temperature in the containment is relatively uniform, except for below the releases (see temperature distribution on the main stairway side).

During the sump heatup phase (but before the start of the boiling, 570 - 655 minutes), a convection circulation loop affects the region up to 15 m. This region has a uniform temperature gradient, while the region above is stagnant. After sump evaporation begins, the convection circulation loop affects the entire volume and homogenizes the temperatures.

The steam and gas concentrations over time correspond to the temperature distributions. Note that there are no large local changes in gas concentrations in the regions (radially) away from the two staircases, see Figures 9.C.2-99 and 9.C.2-100.

The flow patterns in the compartments may be inferred by comparing the velocities in the two staircases (see Figures 9.C.2-101, 9.C.2-102, and 9.C.2-103). Upward flow is recorded in both stairways at the early stage of the blowdown (first 30 seconds, see Figure 9.C.2-101). The upward flow in the spiral staircase is the result of the unplanned vent connection with the release point. A pressure wave destroyed the separating wall during the blowdown. This indicates that the break compartment pressurization forced flow out of all the openings in the break compartment.

After 80 seconds (end of blowdown is at 50 seconds), upward and downward flows are recorded in the main and spiral staircases, respectively (see velocities in Figure 9.C.2-101). During the steam releases ST1, ST2, ST3, ST4, and ST5 (see Figures 9.C.2-103 and 9.C.2-104), upward flows are recorded in both staircases. During the gas mixture release phases GT1, GT2, and GT3, the flow is downwards in the spiral staircase (see Figure 9.C.2-103).

During the sump heatup phase the flow is upwards in the main staircase and downwards in the spiral staircase (see Figure 9.C.2-104). The weak circulation loop reaches the 15 m level before the start of sump boiling. After the start of sump boiling, the circulation loop extends over the total containment height and the flow velocities are higher (see Figure 9.C.2-104 for 655 - 695 minutes).

Various global circulation flow patterns are established during the E11.5 experiment as a result of the various steam and gas release phases, as well as the sump heatup and boiling phases. The temperatures, steam, and gas concentrations follow similar distributions. Global circulation effects contribute to reduced gradients in the vertical direction of temperature and concentration fields.

Application to AP600 and AP1000

The release position in experiment E11.5 is the closest to the possible AP600 and AP1000 LOCA cases. However, in the HDR, chimney and heat storage effects (heat sink and source effects) along the two main flow paths cause dominant global circulation flow patterns below the operating deck. After the blowdown, the plume rises from the break compartment and entrains laterally, yielding global circulation.

In the passive containment, upward flow patterns are formed in the core of containment (depending on the break location). Downward flow is present near the vertical walls due to the relatively high cooling rates of the steel shell. The overall effects are shallower vertical density gradients in the above-deck region compared with E11.5 test. The shallow gradients are the result of the additional wall layer entrainment that is not present in HDR.

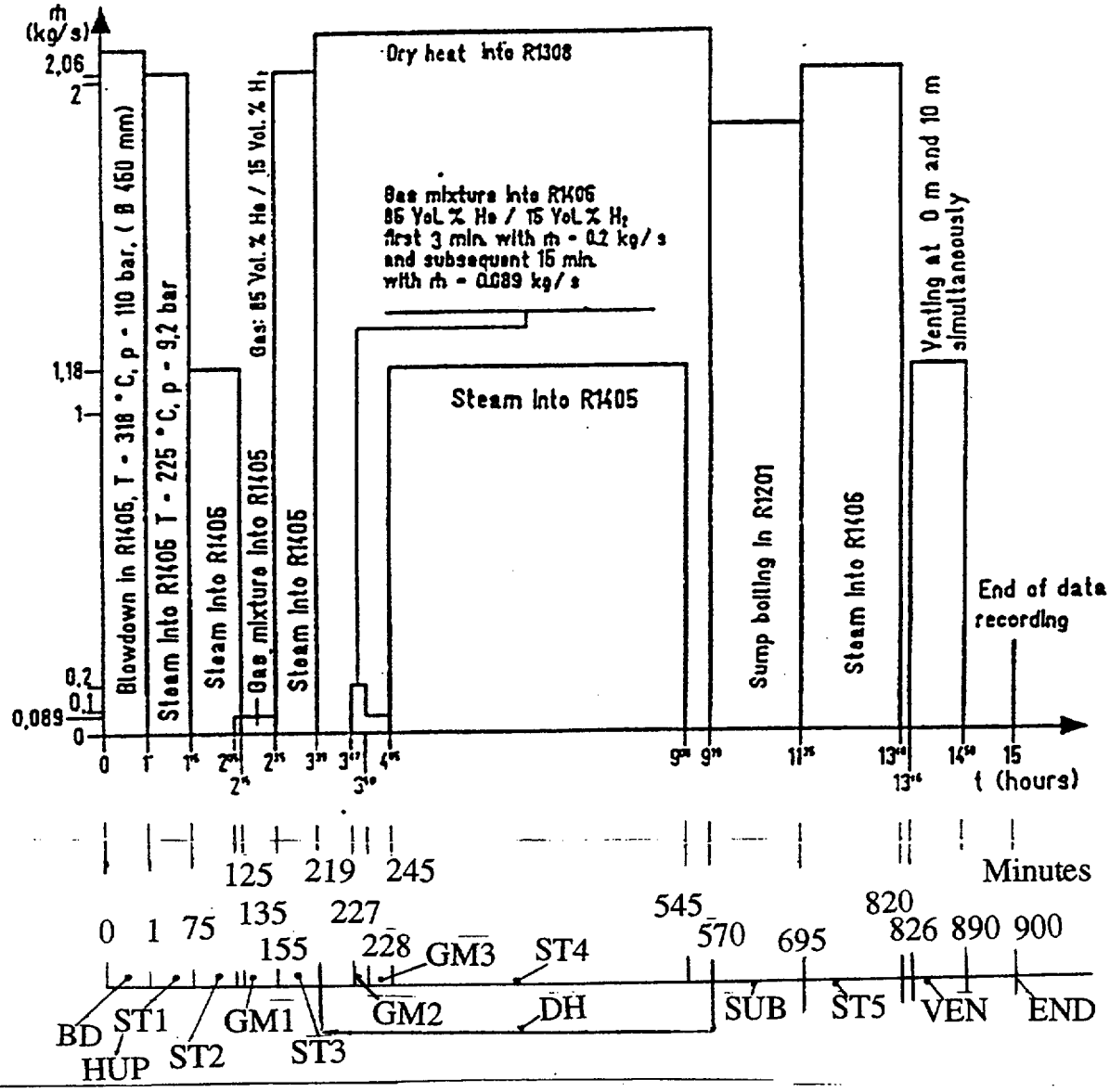

Figure 9.C.2-92a HDR-E11.5 Sequence of Experimental Test Procedures

(reprinted from: L. Wolf, K. Mun, "Overview of experimental results for long-term, Large-scale natural circulations in LWR-containments after large LOCAs, Vol. II: Assessment of HDR Experiments V21.1, V43, T31.5 and E11.5", University of Maryland at College Park, for DOE - Project HDR Hydrogen Mixing Evaluation for Containment Safety Evaluations Natural Global Circulation, Order Number: DE-AP07-96ID10765", April 1996)

Event	Time minutes	Event Description
BD	0-1	Blowdown in R1.405
HUP ST1	1-75	Steam supply with m = 2.06 kg/s
ST2	75-135	Reduced external steam with m = 1.18 kg/s in R1.405
GM1	125-155	H_2/He gas mixture release into R1.405 with 0.089 kg/s
ST3	155-219	Steam release into R1.405 with 2.06 kg/s
DH	219-570	Dry heat addition into R1.308
GM2	227-228	H_2/He gas mixture release into R1.405 with 0.2 kg/s
GM3	228-245	H_2/He gas mixture release into R1.405 with 0.089 kg/s
ST4	245-545	Start of steam release into R1.405 with m = 1.18 kg/s
SUB	570-695	Sump boiling
ST5	695-820	Steam release into R1.405 with m = 2.06 kg/s
VEN	826-890	Containment venting
END	900	End of data acquisition

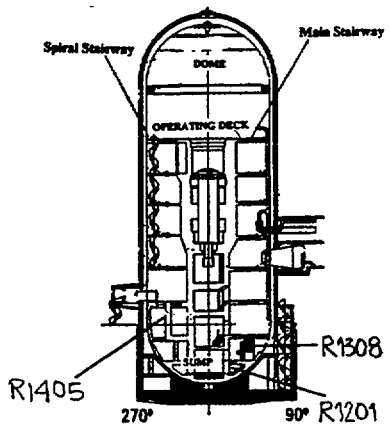

Figure 9.C.2-92b HDR-E11.5 Sequence of Experimental Test Procedures

(reprinted from: L. Wolf, K. Mun, "Overview of experimental results for long-term, Large-scale natural circulations in LWR-containments after large LOCAs, Vol. II: Assessment of HDR Experiments V21.1, V43, T31.5 and E11.5", University of Maryland at College Park, for DOE - Project HDR Hydrogen Mixing Evaluation for Containment Safety Evaluations Natural Global Circulation, Order Number: DE-AP07-96ID10765", April 1996)

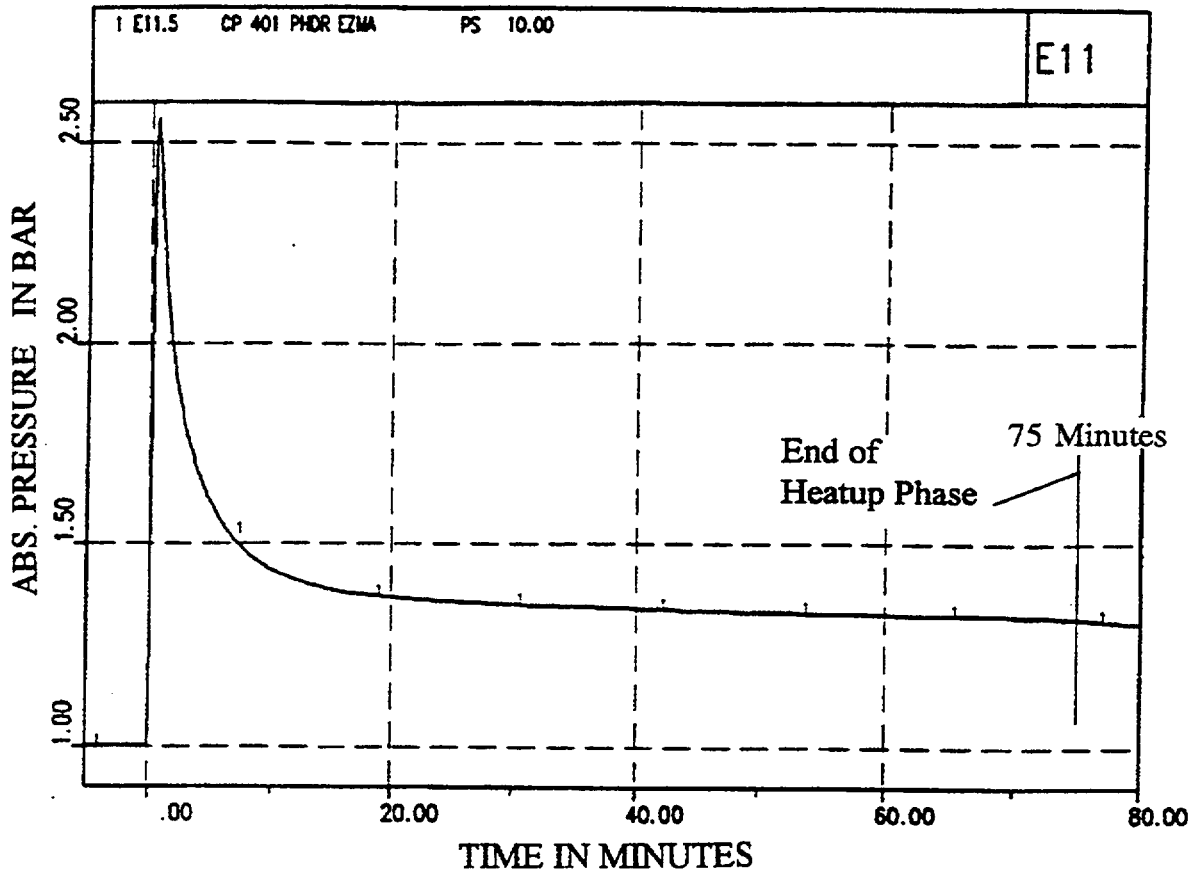

Figure 9.C.2-93 HDR-E11.5 Containment pressure

(reprinted from: L. Wolf, K. Mun, "Overview of experimental results for long-term, Large-scale natural circulations in LWR-containments after large LOCAs, Vol. II: Assessment of HDR Experiments V21.1, V43, T31.5 and E11.5", University of Maryland at College Park, for DOE - Project HDR Hydrogen Mixing Evaluation for Containment Safety Evaluations Natural Global Circulation, Order Number: DE-AP07-96ID10765", April 1996)

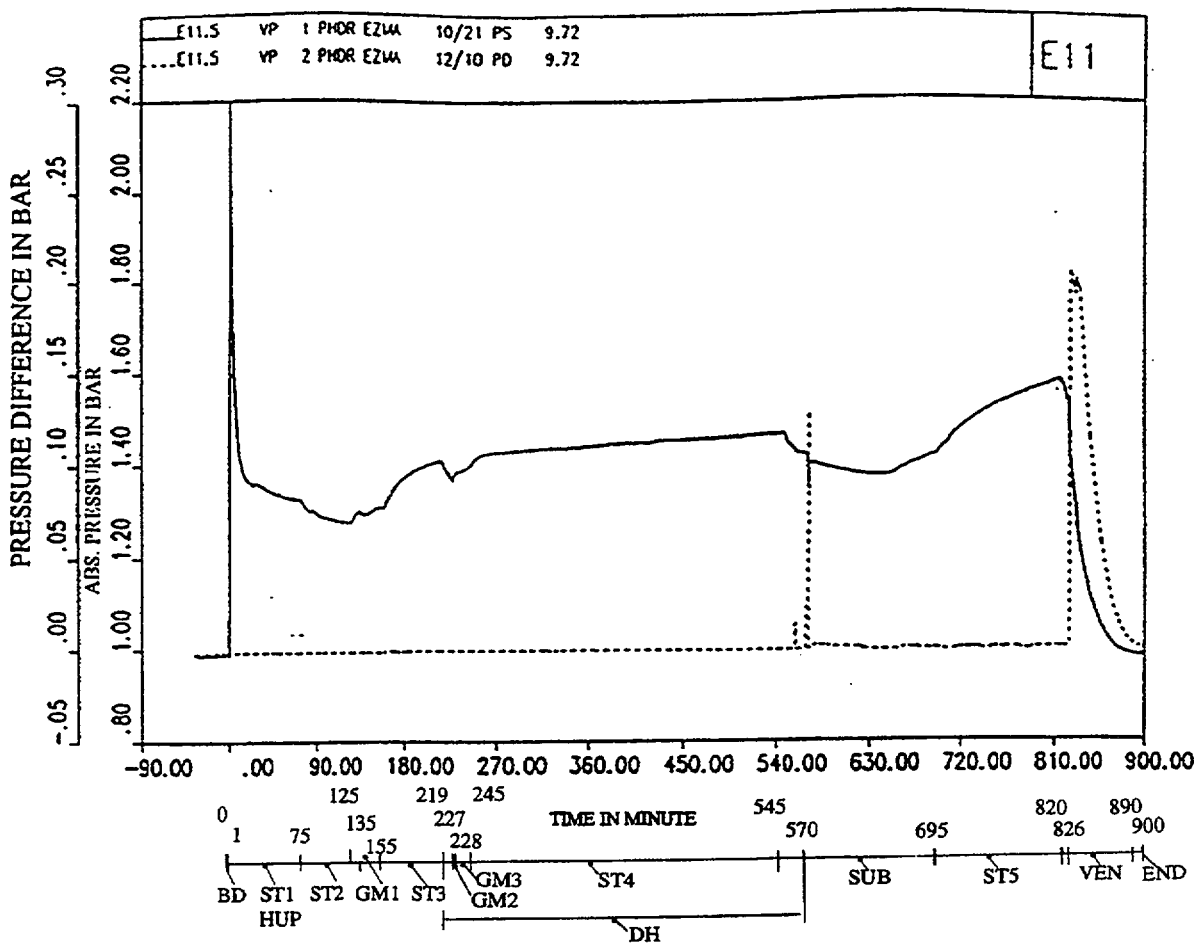

Figure 9.C.2-94 HDR-E11.5 Containment pressure history

(reprinted from: L. Wolf, K. Mun, "Overview of experimental results for long-term, Large-scale natural circulations in LWR-containments after large LOCAs, Vol. II: Assessment of HDR Experiments V21.1, V43, T31.5 and E11.5", University of Maryland at College Park, for DOE - Project HDR Hydrogen Mixing Evaluation for Containment Safety Evaluations Natural Global Circulation, Order Number: DE-AP07-96ID10765", April 1996)

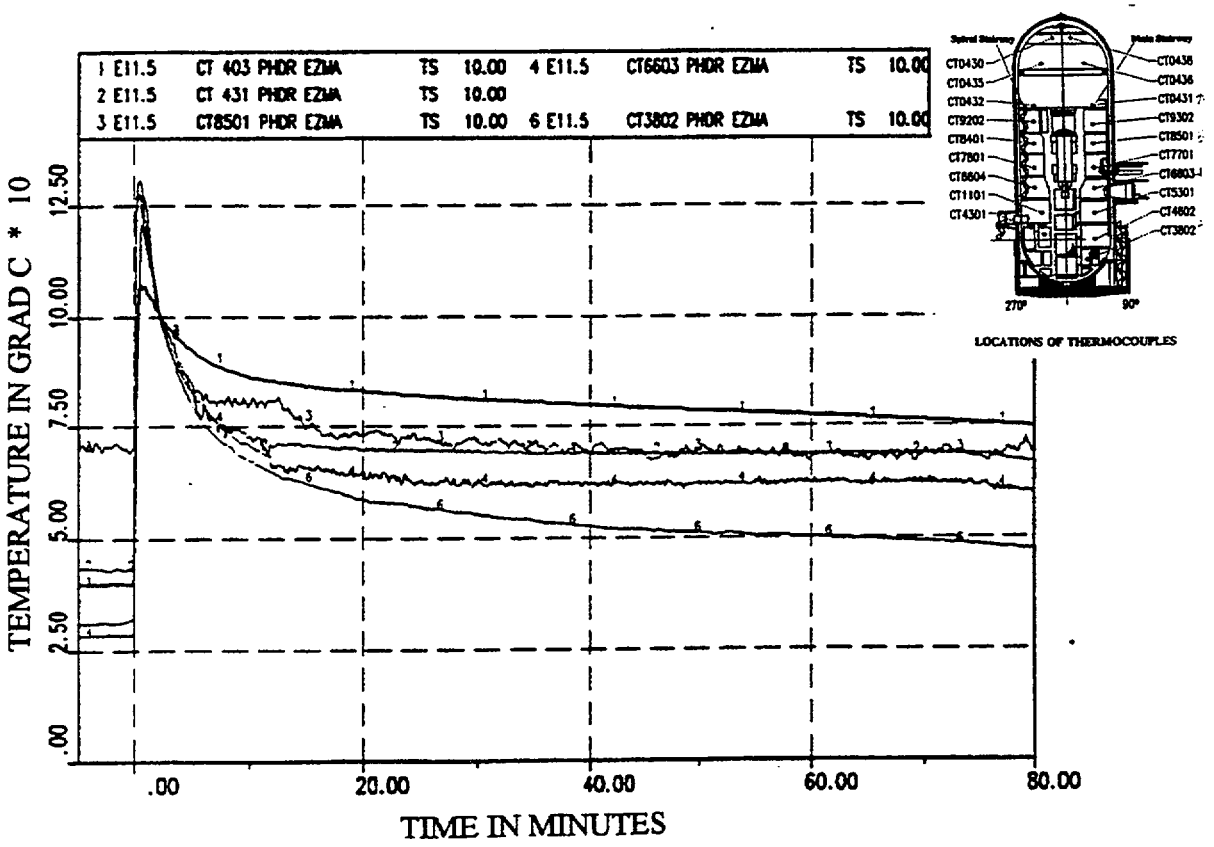

Figure 9.C.2-95 HDR-E11.5 Containment temperatures along main stairway during containment heatup phase

(reprinted from: L. Wolf, K. Mun, "Overview of experimental results for long-term, Large-scale natural circulations in LWR-containments after large LOCAs, Vol. II: Assessment of HDR Experiments V21.1, V43, T31.5 and E11.5", University of Maryland at College Park, for DOE - Project HDR Hydrogen Mixing Evaluation for Containment Safety Evaluations Natural Global Circulation, Order Number: DE-AP07-96ID10765", April 1996)

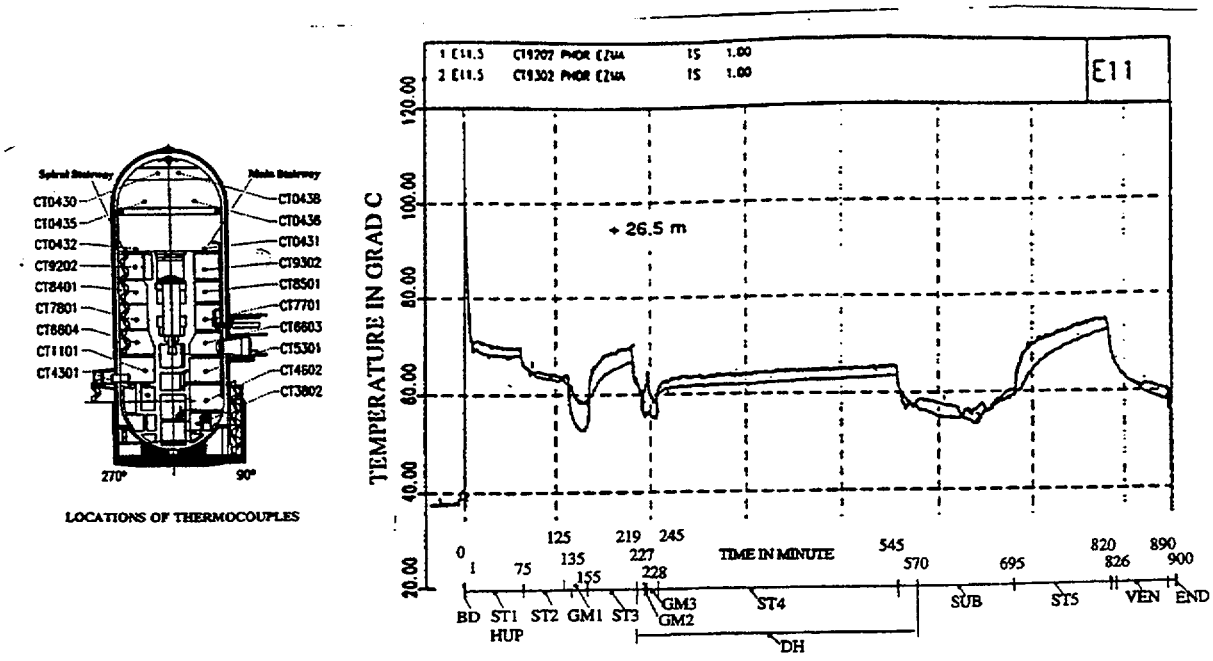

Figure 9.C.2-96a **HDR-E11.5 Temperatures in both major flow paths at the same axial positions for three heights in the containment**

(reprinted from: L. Wolf, K. Mun, "Overview of experimental results for long-term, Large-scale natural circulations in LWR-containments after large LOCAs, Vol. II: Assessment of HDR Experiments V21.1, V43, T31.5 and E11.5", University of Maryland at College Park, for DOE - Project HDR Hydrogen Mixing Evaluation for Containment Safety Evaluations Natural Global Circulation, Order Number: DE-AP07-96ID10765", April 1996)

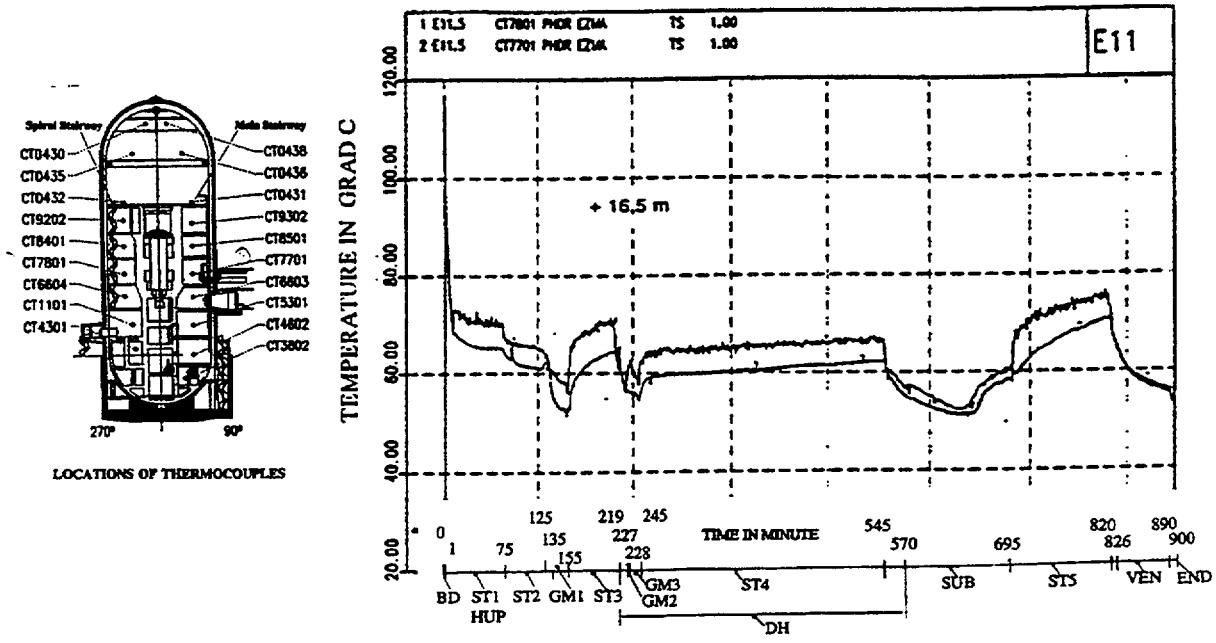

Figure 9.C.2-96b HDR-E11.5 Temperatures in both major flow paths at the same axial positions for three heights in the containment

(reprinted from: L. Wolf, K. Mun, "Overview of experimental results for long-term, Large-scale natural circulations in LWR-containments after large LOCAs, Vol. II: Assessment of HDR Experiments V21.1, V43, T31.5 and E11.5", University of Maryland at College Park, for DOE - Project HDR Hydrogen Mixing Evaluation for Containment Safety Evaluations Natural Global Circulation, Order Number: DE-AP07-96ID10765", April 1996)

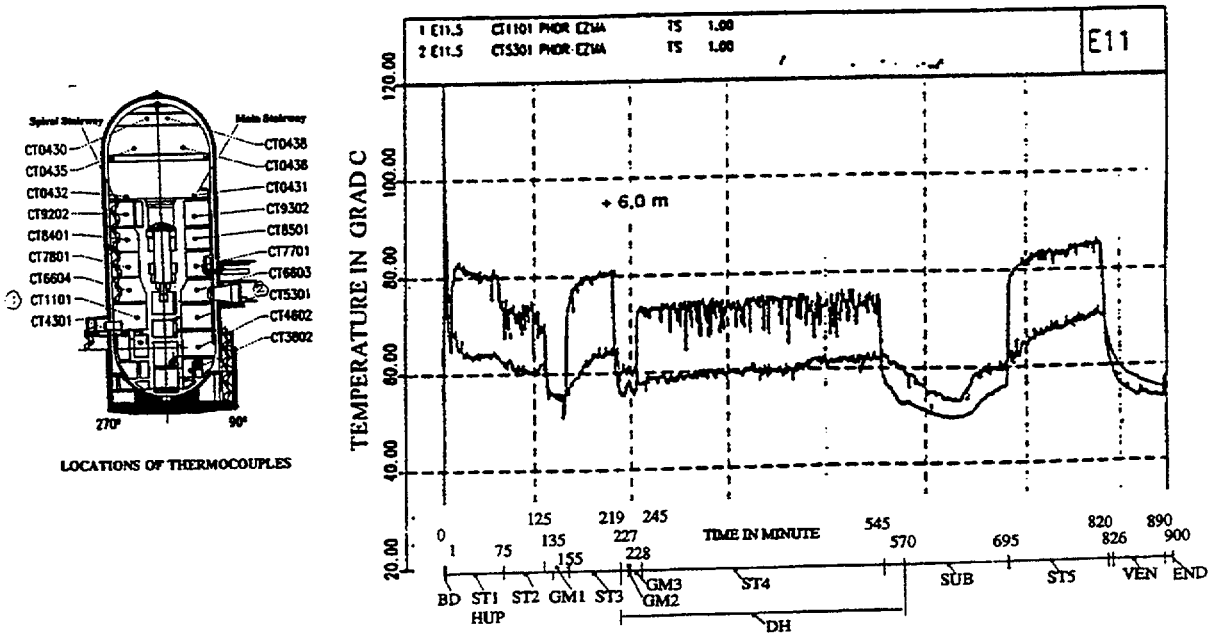

Figure 9.C.2-96c HDR-E11.5 Temperatures in both major flow paths at the same axial positions for three heights in the containment

(reprinted from: L. Wolf, K. Mun, "Overview of experimental results for long-term, Large-scale natural circulations in LWR-containments after large LOCAs, Vol. II: Assessment of HDR Experiments V21.1, V43, T31.5 and E11.5", University of Maryland at College Park, for DOE - Project HDR Hydrogen Mixing Evaluation for Containment Safety Evaluations Natural Global Circulation, Order Number: DE-AP07-96ID10765", April 1996)

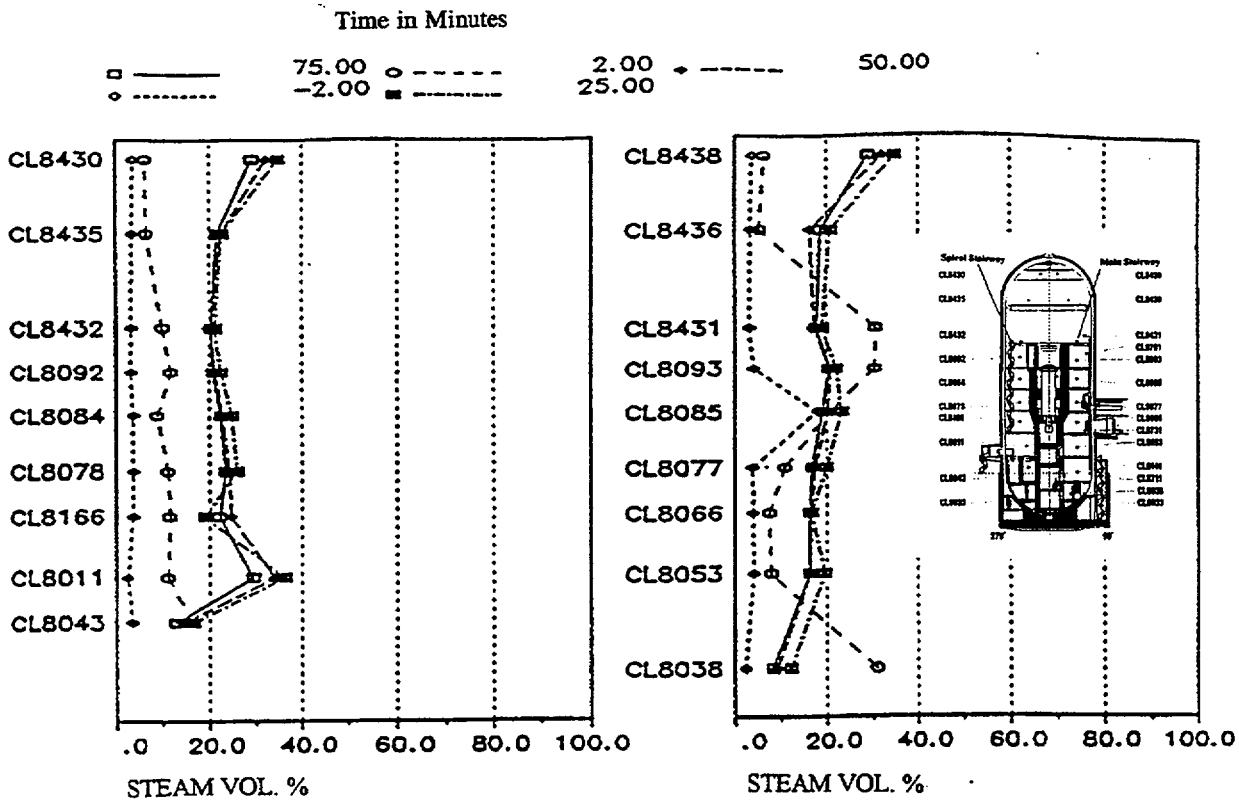

Figure 9.C.2-97a **HDR-E11.5 Axial steam concentration profiles in spiral (left) and main (right) stairways for different instants in time for large break LOCA release in lower containment region**

(reprinted from: L. Wolf, K. Mun, "Overview of experimental results for long-term, Large-scale natural circulations in LWR-containments after large LOCAs, Vol. II: Assessment of HDR Experiments V21.1, V43, T31.5 and E11.5", University of Maryland at College Park, for DOE - Project HDR Hydrogen Mixing Evaluation for Containment Safety Evaluations Natural Global Circulation, Order Number: DE-AP07-96ID10765", April 1996)

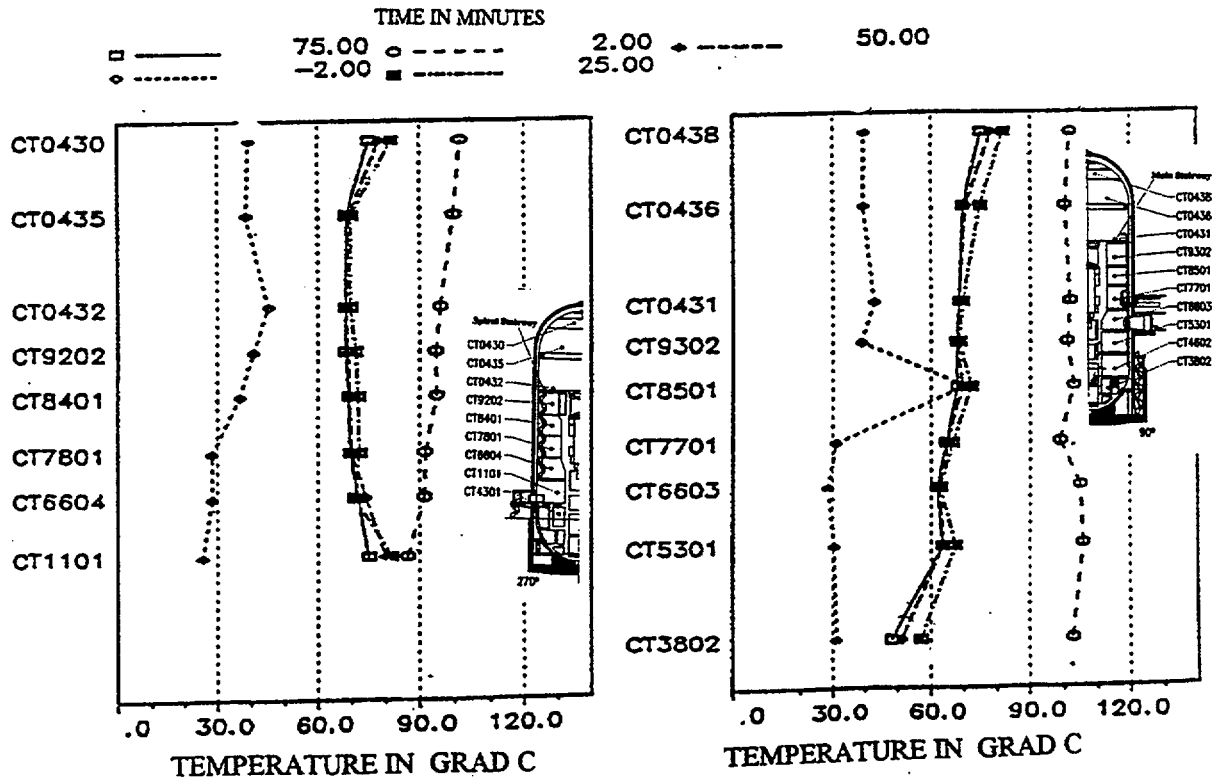

Figure 9.C.2-97b **HDR-E11.5 Axial temperature profiles in spiral (left) and main (right) stairways for different instants in time for large break LOCA release in lower containment region**

(reprinted from: L. Wolf, K. Mun, "Overview of experimental results for long-term, Large-scale natural circulations in LWR-containments after large LOCAs, Vol. II: Assessment of HDR Experiments V21.1, V43, T31.5 and E11.5", University of Maryland at College Park, for DOE - Project HDR Hydrogen Mixing Evaluation for Containment Safety Evaluations Natural Global Circulation, Order Number: DE-AP07-96ID10765", April 1996)

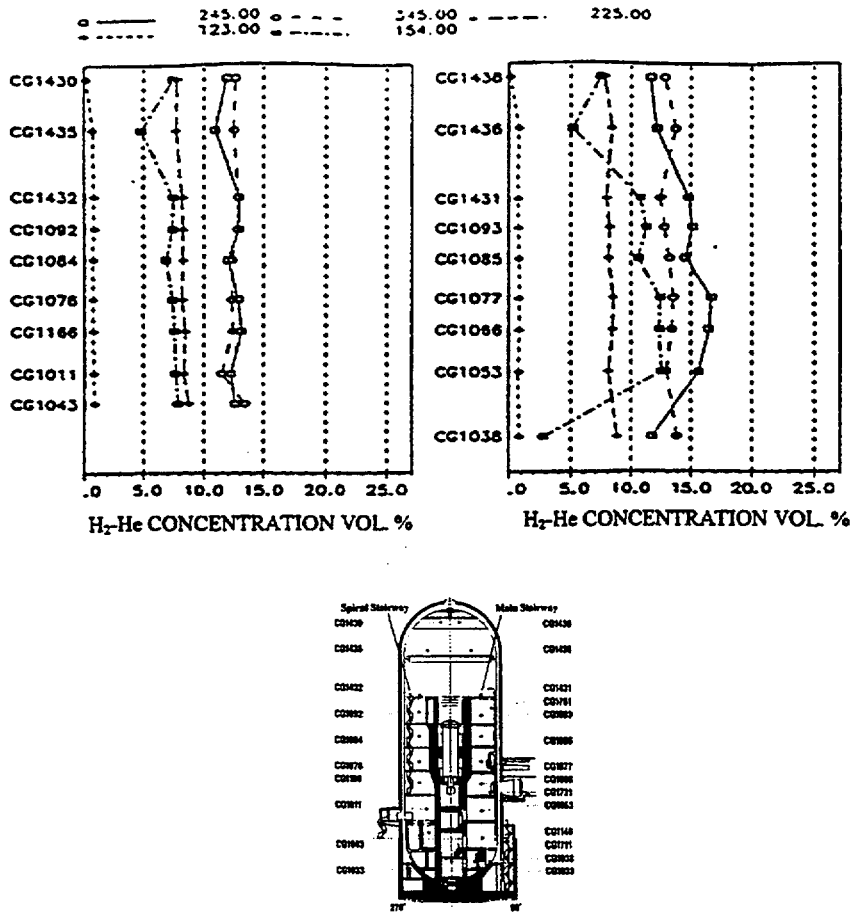

Figure 9.C.2-98a HDR-E11.5 Axial H_2-He gas mixture concentration profiles along spiral (left) and main (right) stairways during gas release phase (total mass 291 kg)

(reprinted from: L. Wolf, K. Mun, "Overview of experimental results for long-term, Large-scale natural circulations in LWR-containments after large LOCAs, Vol. II: Assessment of HDR Experiments V21.1, V43, T31.5 and E11.5", University of Maryland at College Park, for DOE - Project HDR Hydrogen Mixing Evaluation for Containment Safety Evaluations Natural Global Circulation, Order Number: DE-AP07-96ID10765", April 1996)

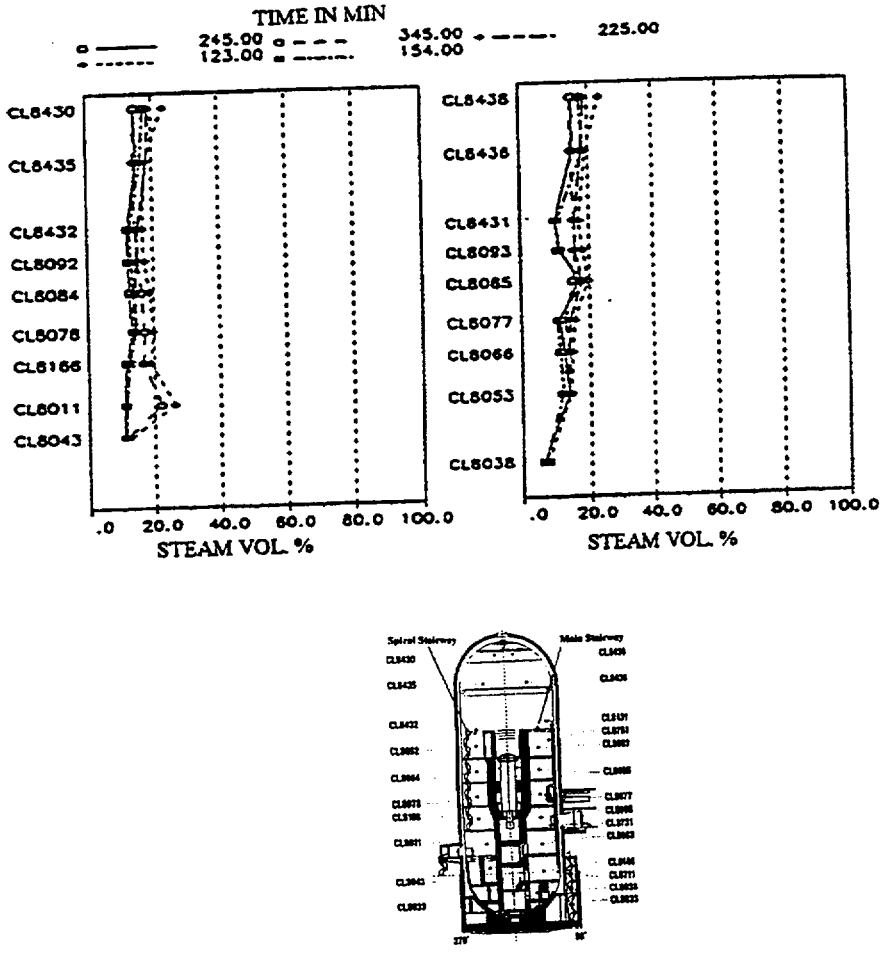

Figure 9.C.2-98b **HDR-E11.5 Axial steam concentration profiles along spiral (left) and main (right) stairways during gas release phase (total mass 291 kg)**

(reprinted from: L. Wolf, K. Mun, "Overview of experimental results for long-term, Large-scale natural circulations in LWR-containments after large LOCAs, Vol. II: Assessment of HDR Experiments V21.1, V43, T31.5 and E11.5", University of Maryland at College Park, for DOE - Project HDR Hydrogen Mixing Evaluation for Containment Safety Evaluations Natural Global Circulation, Order Number: DE-AP07-96ID10765", April 1996)

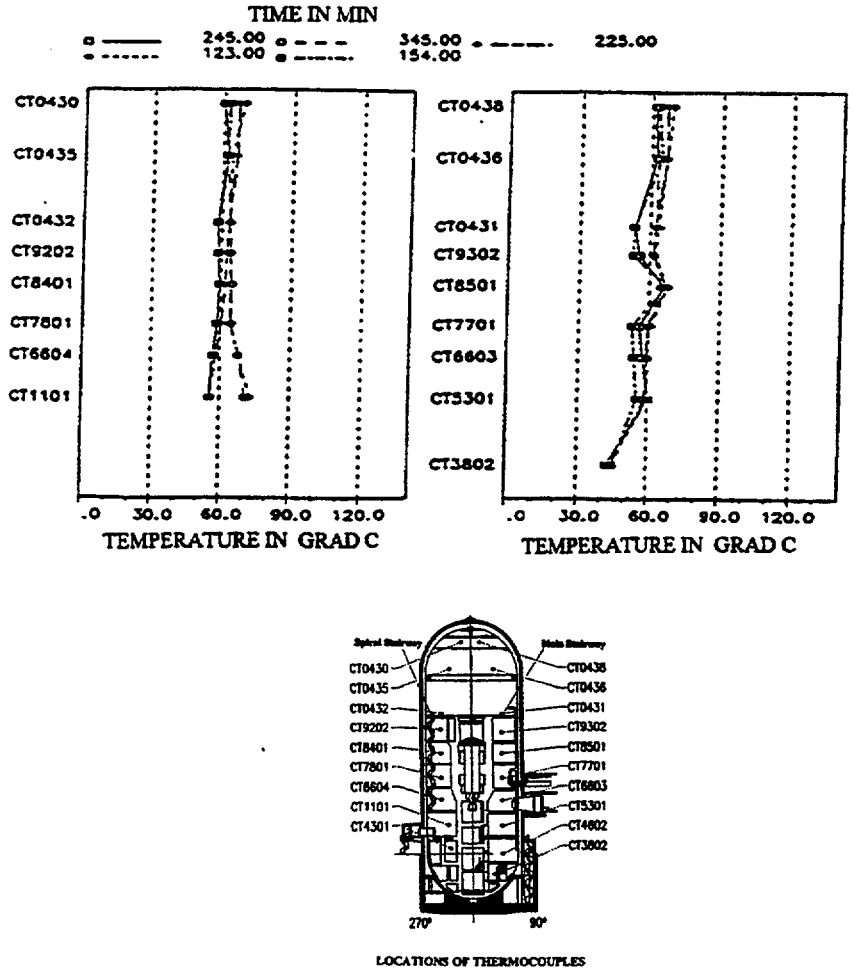

Figure 9.C.2-98c **HDR-E11.5 Axial temperature profiles along spiral (left) and main (right) stairways during gas release phase (total mass 291 kg)**

(reprinted from: L. Wolf, K. Mun, "Overview of experimental results for long-term, Large-scale natural circulations in LWR-containments after large LOCAs, Vol. II: Assessment of HDR Experiments V21.1, V43, T31.5 and E11.5", University of Maryland at College Park, for DOE - Project HDR Hydrogen Mixing Evaluation for Containment Safety Evaluations Natural Global Circulation, Order Number: DE-AP07-96ID10765", April 1996)

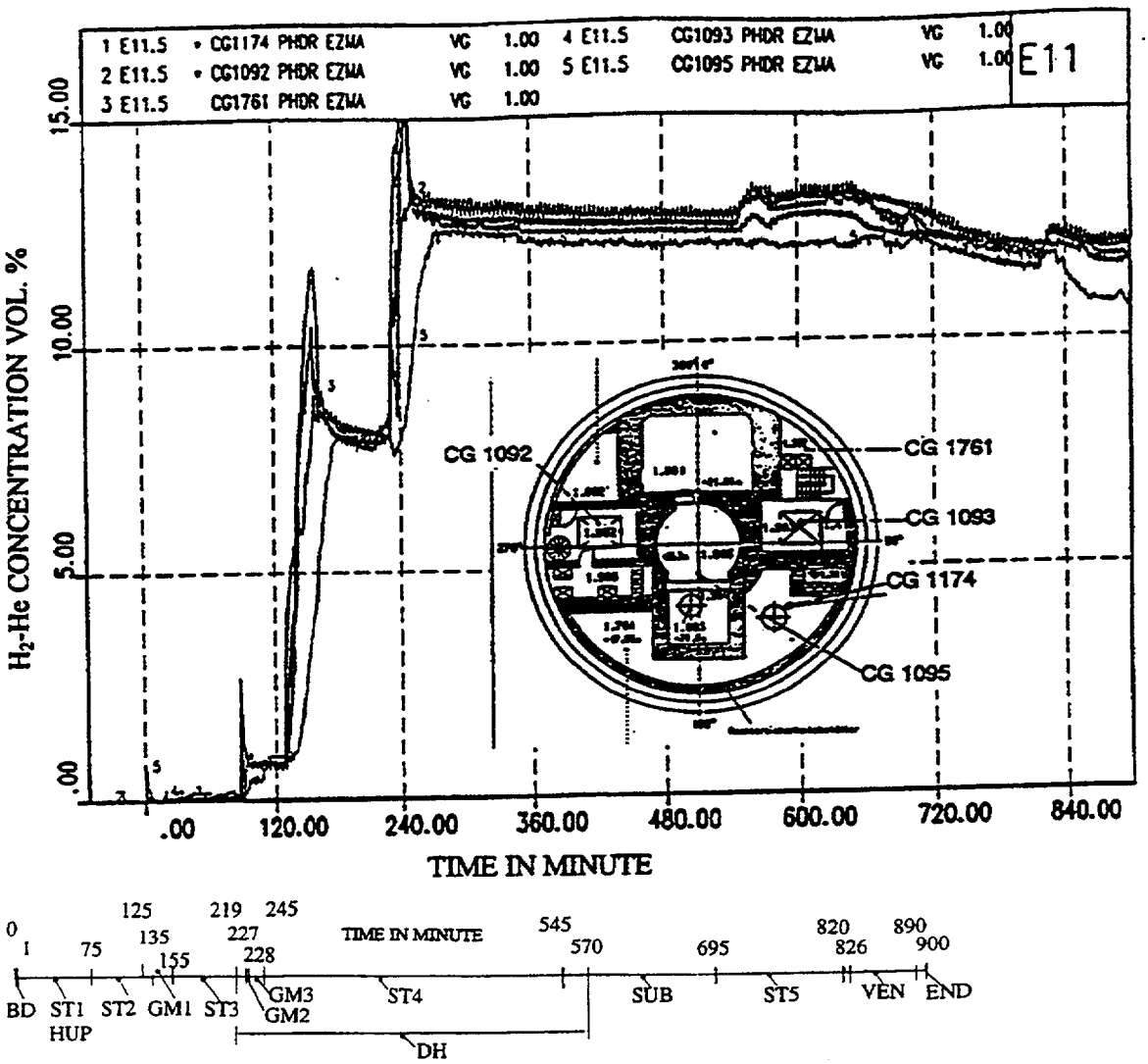

Figure 9.C.2-99a **HDR-E11.5 Gas concentrations in the major flow paths and in regions and subcompartments away from the stairways (H=22m up to 27 m)**

(reprinted from: L. Wolf, K. Mun, "Overview of experimental results for long-term, Large-scale natural circulations in LWR-containments after large LOCAs, Vol. II: Assessment of HDR Experiments V21.1, V43, T31.5 and E11.5", University of Maryland at College Park, for DOE - Project HDR Hydrogen Mixing Evaluation for Containment Safety Evaluations Natural Global Circulation, Order Number: DE-AP07-96ID10765", April 1996)

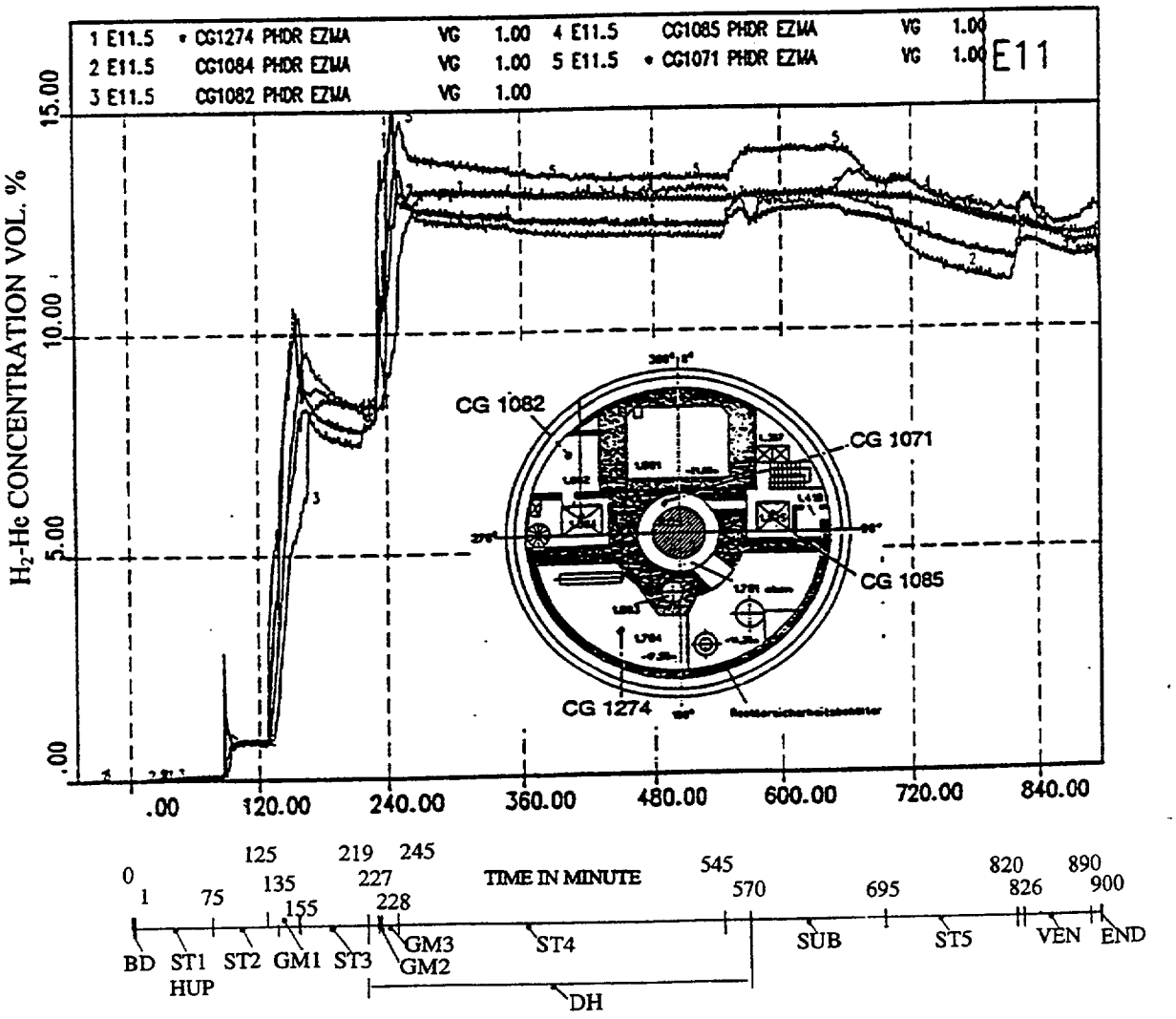

Figure 9.C.2-99b **HDR-E11.5 Gas concentrations in the major flow paths and in regions and subcompartments away from the stairways (H=22m up to 27 m)**

(reprinted from: L. Wolf, K. Mun, "Overview of experimental results for long-term, Large-scale natural circulations in LWR-containments after large LOCAs, Vol. II: Assessment of HDR Experiments V21.1, V43, T31.5 and E11.5", University of Maryland at College Park, for DOE - Project HDR Hydrogen Mixing Evaluation for Containment Safety Evaluations Natural Global Circulation, Order Number: DE-AP07-96ID10765", April 1996)

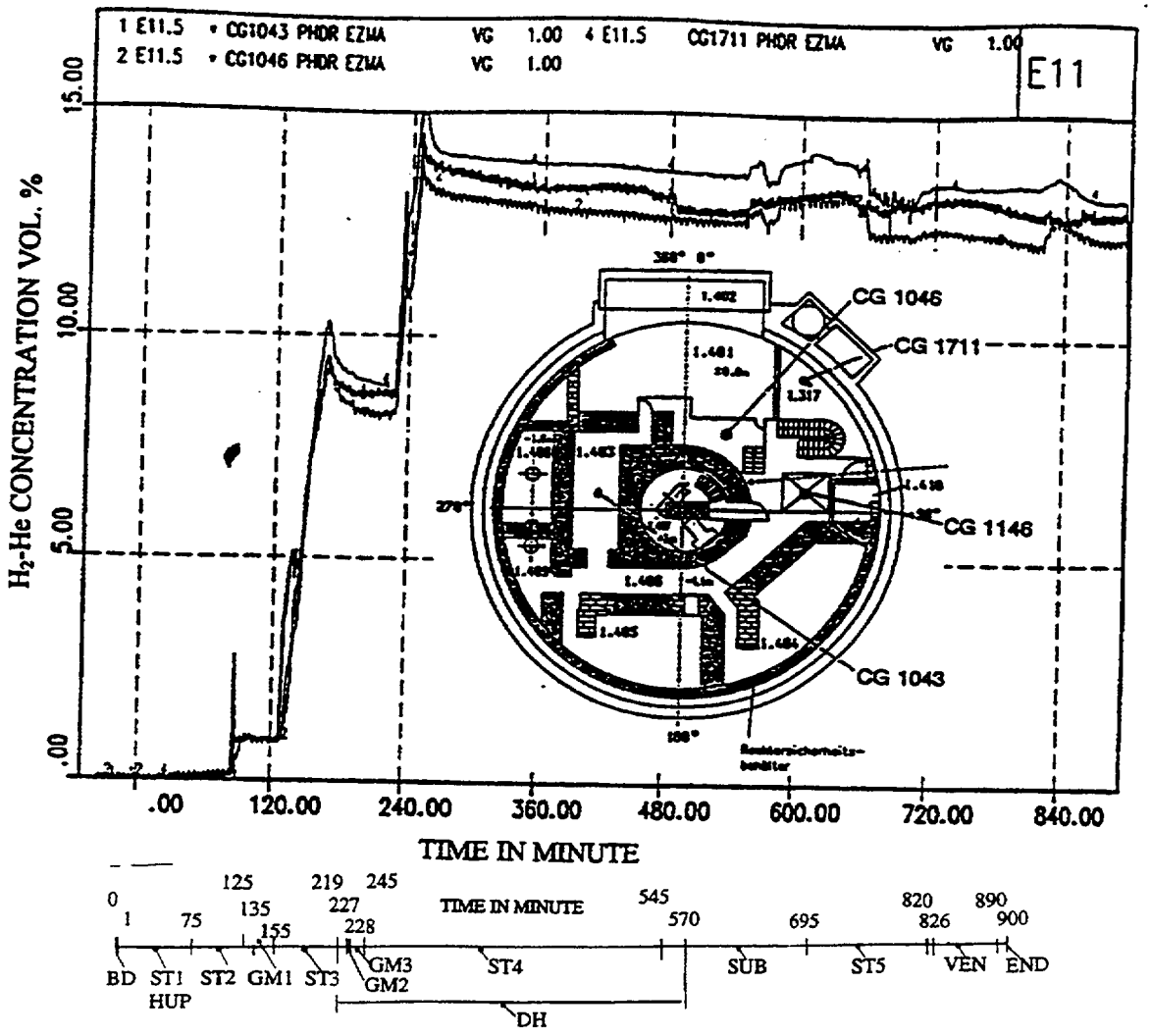

Figure 9.C.2-100a **HDR-E11.5 Gas concentrations in the major flow paths and in regions and subcompartments away from the stairways (H=-4.5m up to +2.0 m)**

(reprinted from: L. Wolf, K. Mun, "Overview of experimental results for long-term, Large-scale natural circulations in LWR-containments after large LOCAs, Vol. II: Assessment of HDR Experiments V21.1, V43, T31.5 and E11.5", University of Maryland at College Park, for DOE - Project HDR Hydrogen Mixing Evaluation for Containment Safety Evaluations Natural Global Circulation, Order Number: DE-AP07-96ID10765", April 1996)

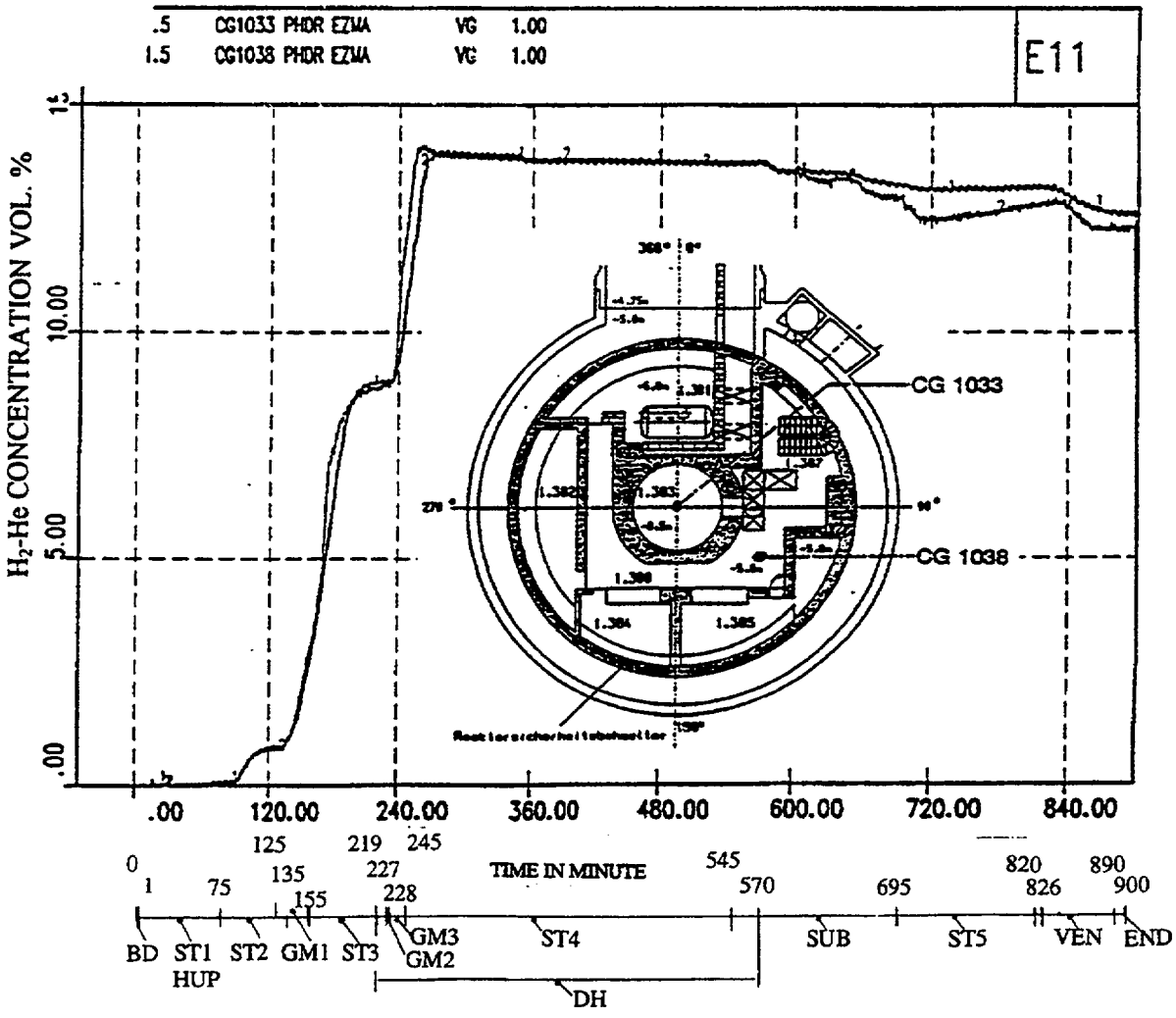

Figure 9.C.2-100b HDR-E11.5 Gas concentrations in the major flow paths and in regions and subcompartments away from the stairways (H=-4.5m up to +2.0 m)

(reprinted from: L. Wolf, K. Mun, "Overview of experimental results for long-term, Large-scale natural circulations in LWR-containments after large LOCAs, Vol. II: Assessment of HDR Experiments V21.1, V43, T31.5 and E11.5", University of Maryland at College Park, for DOE - Project HDR Hydrogen Mixing Evaluation for Containment Safety Evaluations Natural Global Circulation, Order Number: DE-AP07-96ID10765", April 1996)

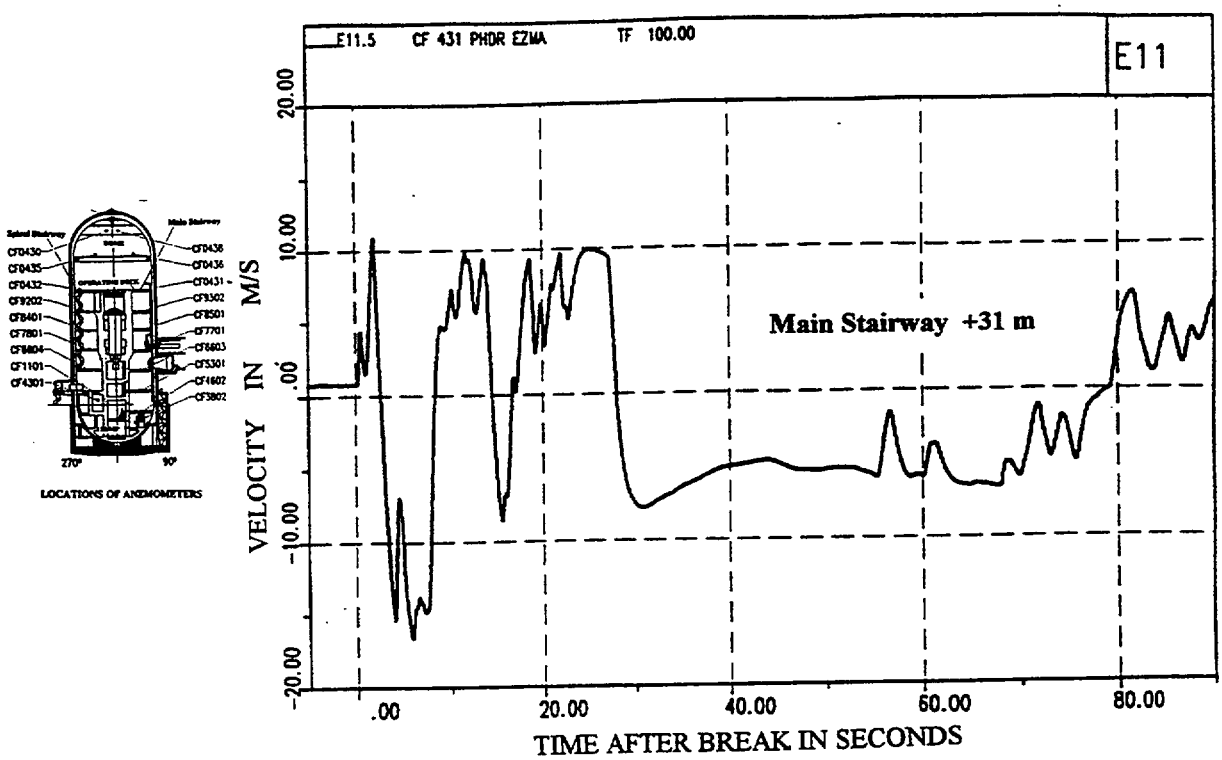

Figure 9.C.2-101a HDR-E11.5 Velocities in the main stairway during blowdown

(reprinted from: L. Wolf, K. Mun, "Overview of experimental results for long-term, Large-scale natural circulations in LWR-containments after large LOCAs, Vol. II: Assessment of HDR Experiments V21.1, V43, T31.5 and E11.5", University of Maryland at College Park, for DOE - Project HDR Hydrogen Mixing Evaluation for Containment Safety Evaluations Natural Global Circulation, Order Number: DE-AP07-96ID10765", April 1996)

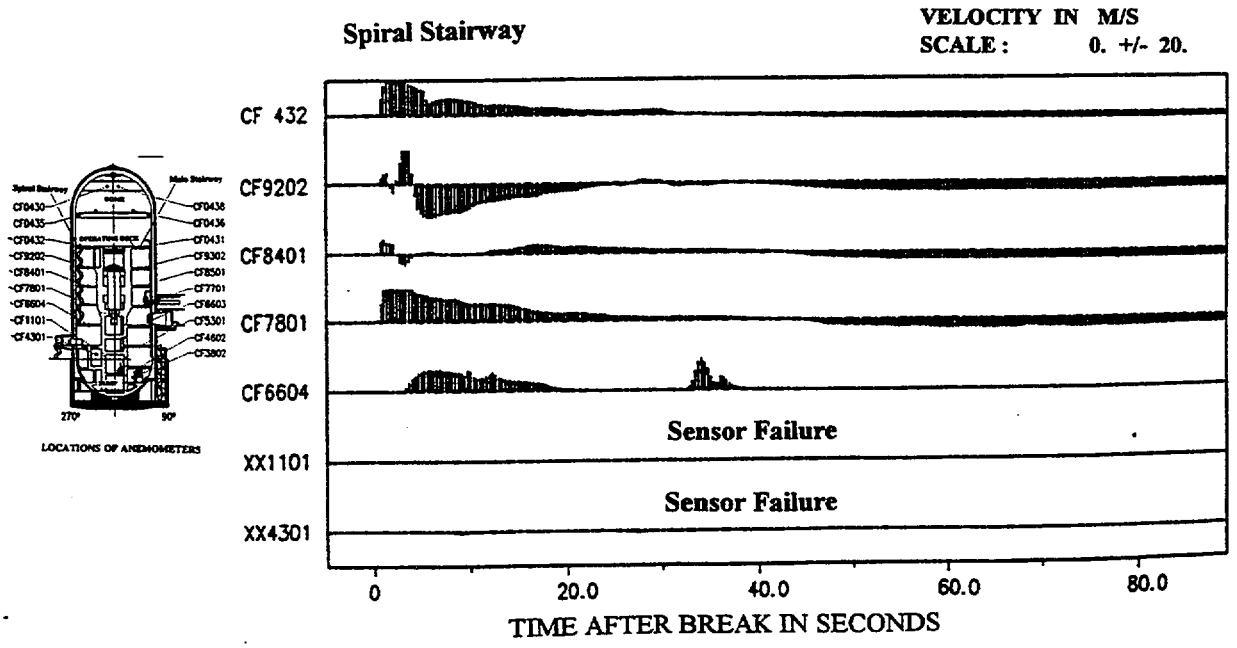

Figure 9.C.2-101b HDR-E11.5 Velocities in the spiral stairway during blowdown

(reprinted from: L. Wolf, K. Mun, "Overview of experimental results for long-term, Large-scale natural circulations in LWR-containments after large LOCAs, Vol. II: Assessment of HDR Experiments V21.1, V43, T31.5 and E11.5", University of Maryland at College Park, for DOE - Project HDR Hydrogen Mixing Evaluation for Containment Safety Evaluations Natural Global Circulation, Order Number: DE-AP07-96ID10765", April 1996)

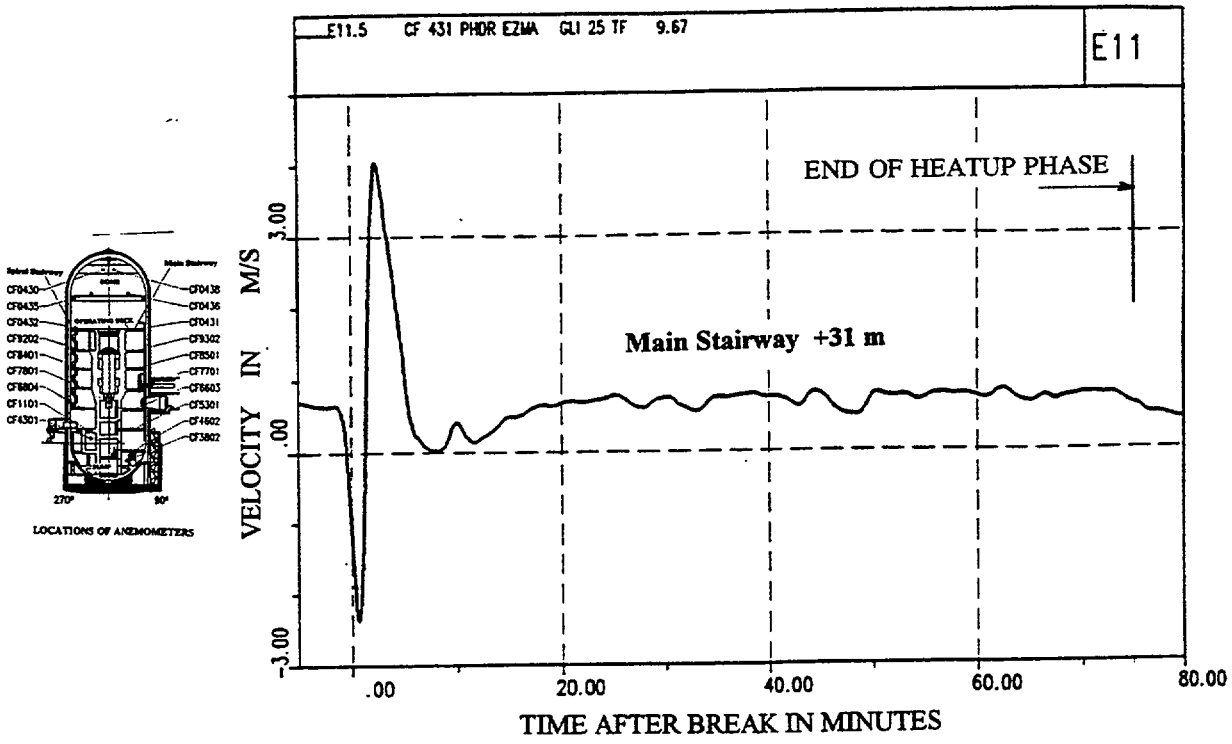

Figure 9.C.2-102a HDR-E11.5 Velocities in the main stairway during containment heatup phase

(reprinted from: L. Wolf, K. Mun, "Overview of experimental results for long-term, Large-scale natural circulations in LWR-containments after large LOCAs, Vol. II: Assessment of HDR Experiments V21.1, V43, T31.5 and E11.5", University of Maryland at College Park, for DOE - Project HDR Hydrogen Mixing Evaluation for Containment Safety Evaluations Natural Global Circulation, Order Number: DE-AP07-96ID10765", April 1996)

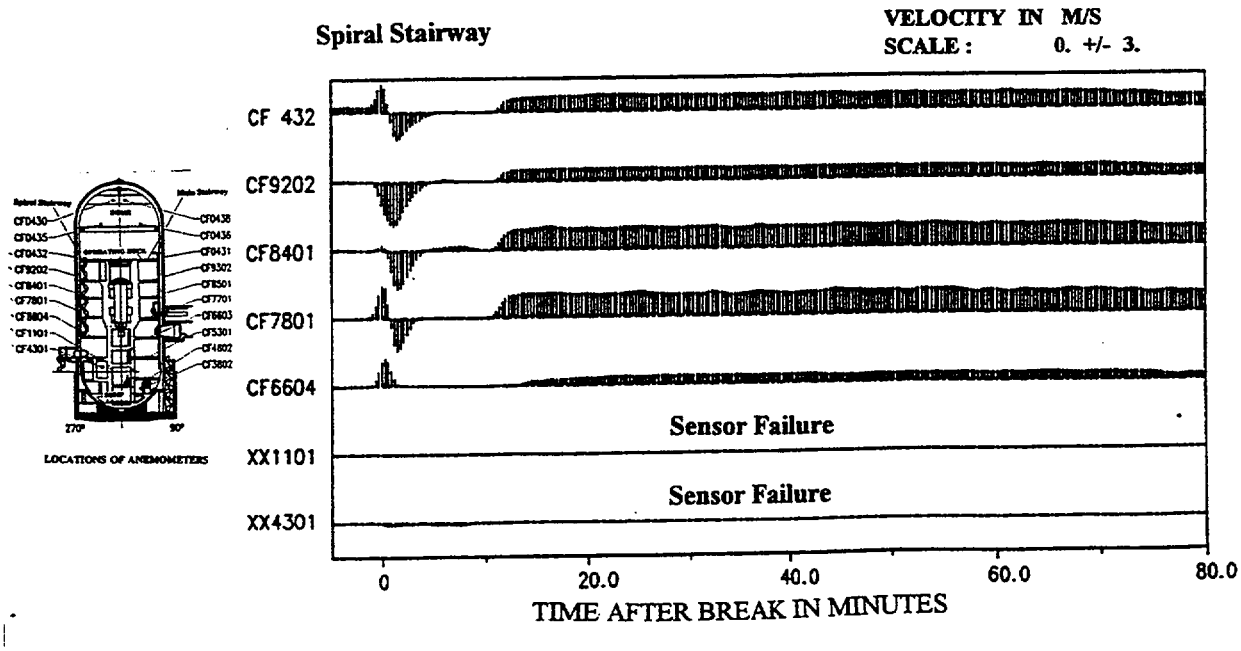

Figure 9.C.2-102b HDR-E11.5 Velocities in the spiral stairway during containment heatup phase

(reprinted from: L. Wolf, K. Mun, "Overview of experimental results for long-term, Large-scale natural circulations in LWR-containments after large LOCAs, Vol. II: Assessment of HDR Experiments V21.1, V43, T31.5 and E11.5", University of Maryland at College Park, for DOE - Project HDR Hydrogen Mixing Evaluation for Containment Safety Evaluations Natural Global Circulation, Order Number: DE-AP07-96ID10765", April 1996)

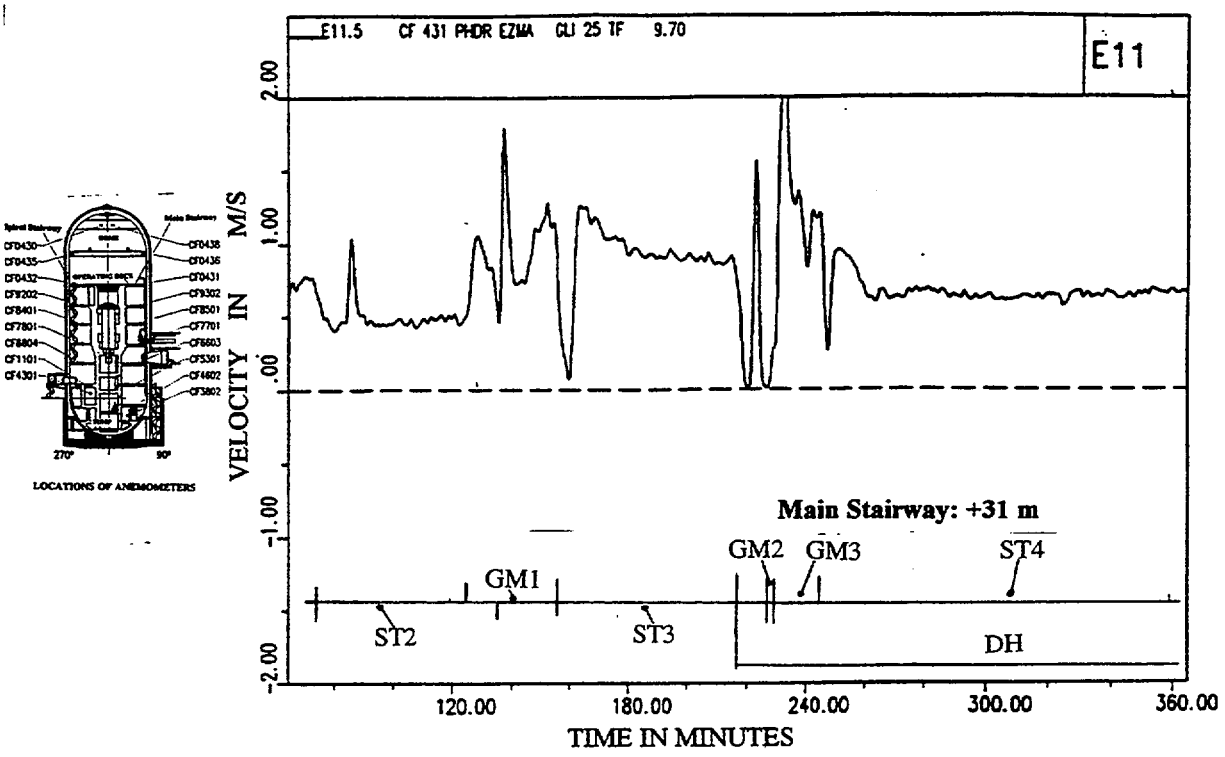

Figure 9.C.2-103a **HDR-E11.5 Velocities in the main stairway during H_2-He gas mixture release phase**

(reprinted from: L. Wolf, K. Mun, "Overview of experimental results for long-term, Large-scale natural circulations in LWR-containments after large LOCAs, Vol. II: Assessment of HDR Experiments V21.1, V43, T31.5 and E11.5", University of Maryland at College Park, for DOE - Project HDR Hydrogen Mixing Evaluation for Containment Safety Evaluations Natural Global Circulation, Order Number: DE-AP07-96ID10765", April 1996)

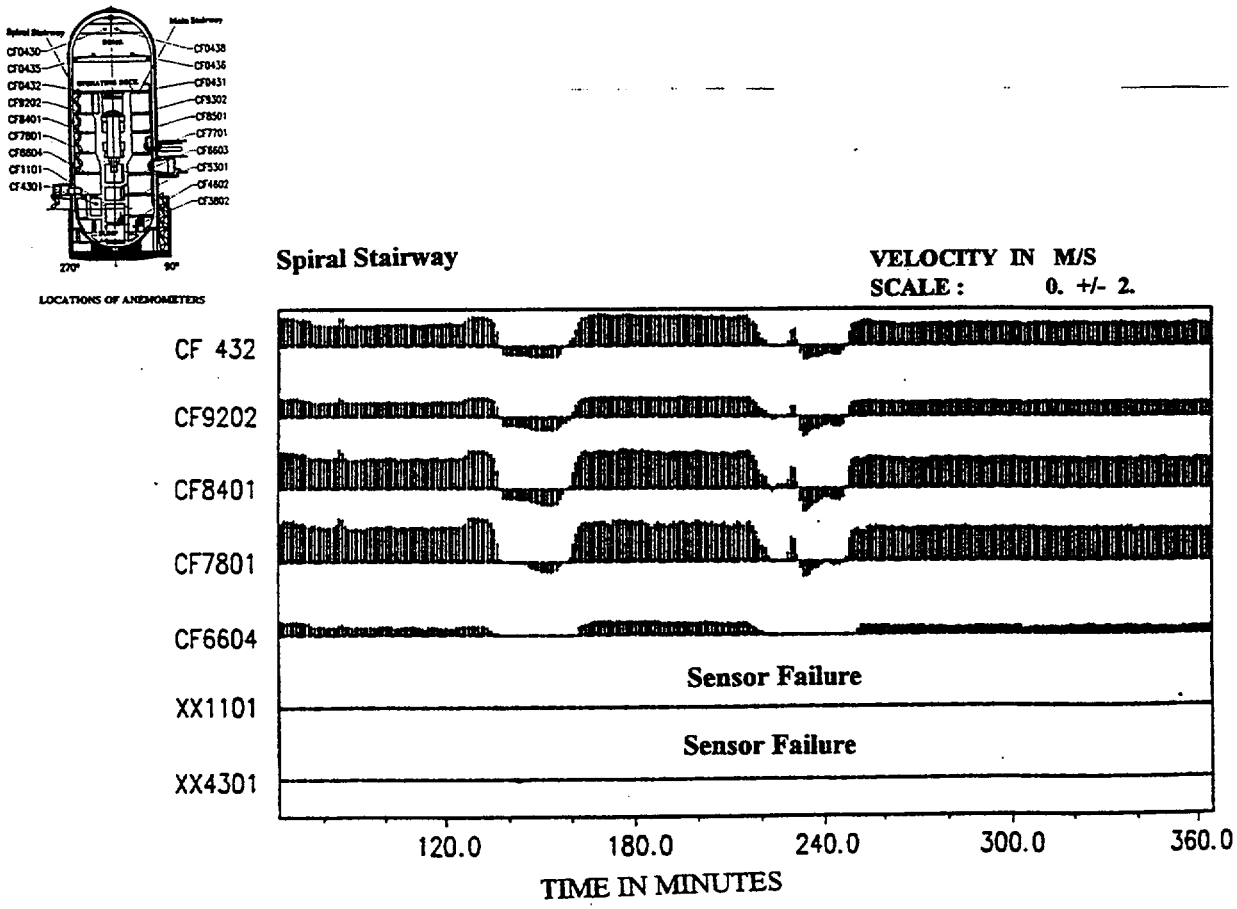

Figure 9.C.2-103b HDR-E11.5 Velocities in the spiral stairway during H_2-He gas mixture release phase

(reprinted from: L. Wolf, K. Mun, "Overview of experimental results for long-term, Large-scale natural circulations in LWR-containments after large LOCAs, Vol. II: Assessment of HDR Experiments V21.1, V43, T31.5 and E11.5", University of Maryland at College Park, for DOE - Project HDR Hydrogen Mixing Evaluation for Containment Safety Evaluations Natural Global Circulation, Order Number: DE-AP07-96ID10765", April 1996)

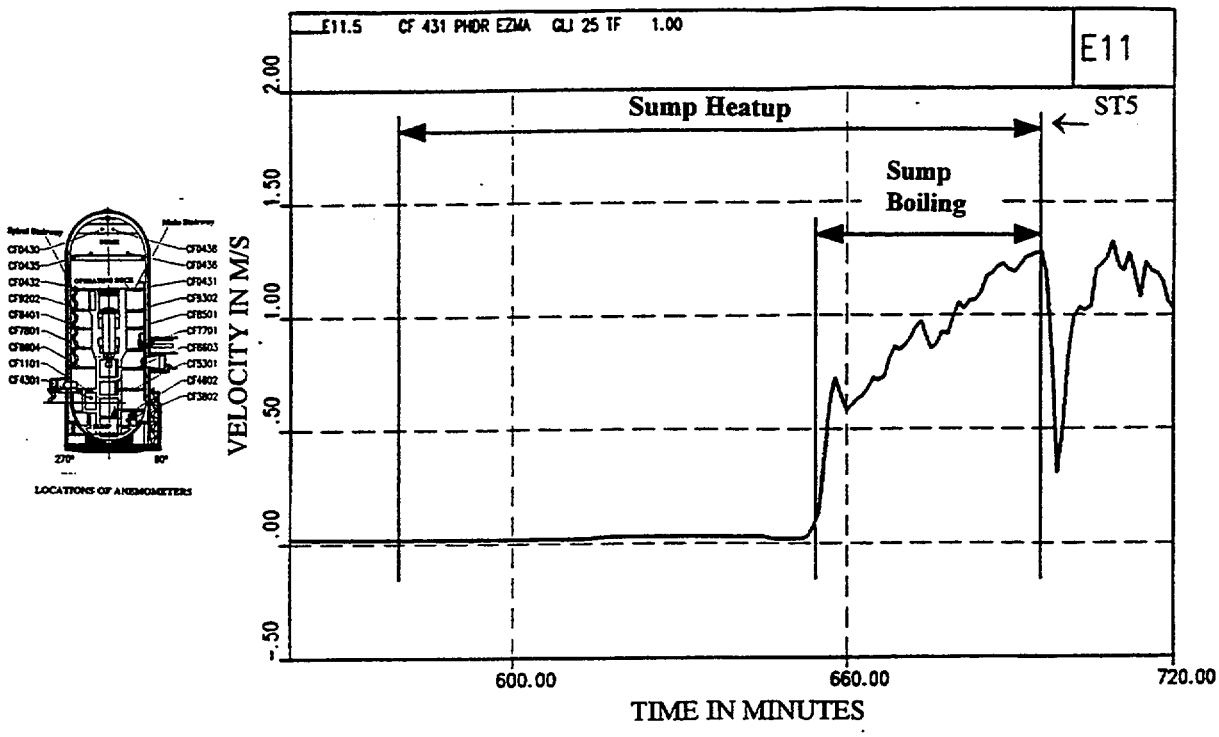

Figure 9.C.2-104a **HDR-E11.5 Velocities in the main stairway during sump heatup and boiling phase**

(reprinted from: L. Wolf, K. Mun, "Overview of experimental results for long-term, Large-scale natural circulations in LWR-containments after large LOCAs, Vol. II: Assessment of HDR Experiments V21.1, V43, T31.5 and E11.5", University of Maryland at College Park, for DOE - Project HDR Hydrogen Mixing Evaluation for Containment Safety Evaluations Natural Global Circulation, Order Number: DE-AP07-96ID10765", April 1996)

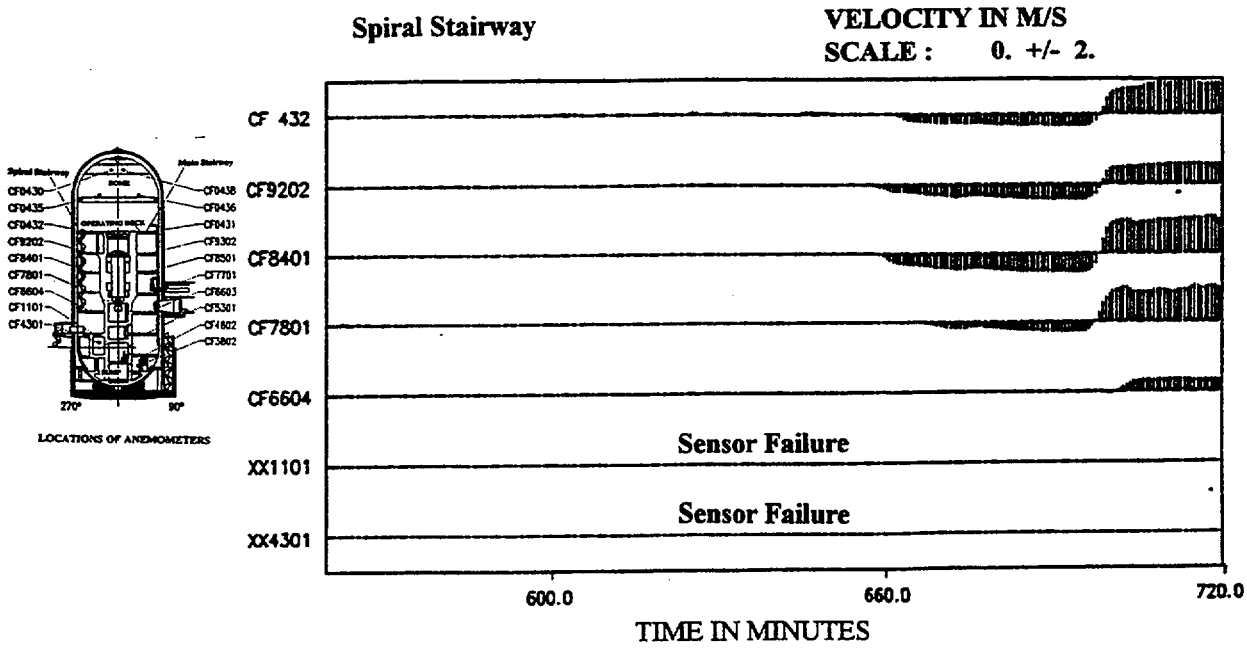

Figure 9.C.2-104b HDR-E11.5 Velocities in the spiral stairway during sump heatup and boiling phase

(reprinted from: L. Wolf, K. Mun, "Overview of experimental results for long-term, Large-scale natural circulations in LWR-containments after large LOCAs, Vol. II: Assessment of HDR Experiments V21.1, V43, T31.5 and E11.5", University of Maryland at College Park, for DOE - Project HDR Hydrogen Mixing Evaluation for Containment Safety Evaluations Natural Global Circulation, Order Number: DE-AP07-96ID10765", April 1996)

9.C.2.4.3 References

1. T. Cron, D. Schrammel, (1993)
"Investigations on Hydrogen Distribution in a Reactor Containment, Quick Look Report, Test Group E11, Experiments E11.0-6"
(In German), PHDR Technical Report PHDR 111-92, 1993

2. H. Holzbauer, L. Wolf, (1994)
"GOTHIC verification on behalf of HDR-Hydrogen mixing experiments"
International Conference on New Trends in Nuclear System Thermohydraulics, Volume II, pp. 331-340., Pisa, Italy, May 30th - June 2nd, 1994

3. T. Kanzleiter, L. Valencia, (1984)
"Blowdown-Experiments in a Reactor Containment, Quick Look Report, Test Group CONW and COND, Experiments V21.1, V21.3, V45"
(In German), Technical PHDR Report No. 49/84, Nuclear Center Karlsruhe, Germany, May, 1984

4. L. Valencia, (1987)
"Design Report, Blowdown and Hydrogen Distribution Experiments, HDR-Test Group CON, Experiments T31.4-5"
(In German), PHDR-Working Report No. 3.516/87, Nov. 1987

5. H. H. Wenzel, R. Grimm, L. L'hr, (1987)
"Test Report, Blowdown and Hydrogen Distribution Experiments, HDR-Test Group CON, Experiments T31.5"
(In German), PHDR-Working Report No. 3.520/88, Dec. 1987

6. L. Wolf, L. Valencia, (1988)
"Results of the Preliminary Hydrogen Distribution Experiment at HDR and Future Experiments for Phase III"
16th Water Reactor Safety Information Meeting, Gaithersburg, MD, USA, Oct. 24-27, 1988.

7. L. Wolf, L. Valencia, (1989)
"Experimental Results of the Preliminary HDR-Hydrogen Distribution Test T31.5" 4th Intl. Topical Mtg. on Nuclear Reactor Thermal-Hydraulics, Karlsruhe, Oct. 10-13, 1989, vol. 2, pp. 967-973.

8. L. Wolf, H. Holzbauer, T. Cron, (1994)
"Detailed Assessment of the HDR-Hydrogen mixing experiments E11"

International Conference on New Trends in Nuclear System Thermohydraulics, Volume II, pp. 91-103., Pisa, Italy, May 30th - June 2nd, 1994

9. L. Wolf, K. Mun, J. Floyd, (1995)
"HDR hydrogen mixing evaluation for containment safety evaluations, Final Report, DOE-Project Order No.: DE-AP07-95ID81401, Dept. of Materials and Nuclear Engineering, University of Maryland, College Park, MD, Sept. 1995

10. L. Wolf, K. Mun, (1996)
"Overview of experimental results for long-term, large-scale natural circulations in LWR-containments after large LOCAS - Vol. II: Assessment of HDR Experiments V21.1, V43, T31.5 and E11.5"
DOE - Project, HDR Hydrogen Mixing Evaluation for Containment Safety Evaluations Natural Global Circulation, Order Number: DE - AP07 - 96ID10765
University of Maryland at College Park, April 1996

11. L. Wolf, M. Gavrilas, K. Mun, (1996)
"Overview of experimental results for long-term, large-scale natural circulations in LWR-containments after large LOCAS"
Final Report for DOE - Project, Order Number: DE - AP07 - 96ID10765
University of Maryland at College Park, July 1996

9.C.2.5 CONCLUSION

Eleven of the twenty experiments presented have a low release position $H_r/H_t < 0.2$. These experiments may be compared to the AP600 and AP1000.

They include the seven BMC experiments with a low release position (F2 set, Phase 2, 3 and 4, Test 2 - Phase I, Test 20 - Phase II and RX4), the NUPEC experiment M-4-3, and the three HDR experiments (E11.3, E11.4 and E11.5). Most of these tests (except two - BMC Test 20 and NUPAC M-4-3) have global circulation through the dome which contributes towards homogenization of temperature and concentration fields.

The two experiments with the low release position where stratification is recorded are BMC Test 20 and NUPEC M-4-3. As already noted, the stratification occurs due to the special circumstances (boundary conditions). BMC Test 20 stratifies due to the initially stratified temperature field. Upper compartments are maintained at the higher temperature for several days. Global circulation starts first in the lower compartments, resulting in higher concentrations of the released gas mixture being recorded. Later, the circulation flow path penetrates the upper thermally-stratified layers and the vertical concentration gradients are smaller.

In the M-4-3 NUPEC test, the temperature stratification occurs after the end of the release, although injected gas mixture homogenized slowly. The thermally insulated shell of the NUPEC containment could be one cause for thermal stratification. The homogenization of the gas mixture concentration indicates that some circulation inside of the containment existed, probably due to the presence of the sump.

The external cooling of the AP600 and AP1000, as well as the hot concrete structures positioned in the lower portion of the containment, will produce global circulation.

Seven experiments have high release positions ($H_r/H_t > 0.5$), two BMC (Test 4 and Test 12), all three CVTR experiments, and two HDR experiments (E11.2 and T31.5). Thermal stratification is present in six of the seven tests, with the exception of BMC Test 12. BMC Test 12 includes only hydrogen injection.

Due to the uniform initial temperature field (boundary conditions) and circulation patterns formed by hydrogen injection, the concentration field was uniform in BMC Test 12. In the second and third CVTR experiments, the application of the internal sprays decreases the pressure and vertical temperature gradients.

In HDR experiments E11.2 and T31.5, the temperature and concentration fields stratify at the beginning of the experiments. Later, the global circulation decreases the vertical gradients.

In experiment E11.2, additional steam release in the lower compartment and the application of external sprays generates global circulation and decreases vertical gradients.

A review of the tests indicates that global circulation and atmosphere homogenization will occur if:

1) The position of the steam or hydrogen release ($H_r/H_t < 0.2$) is low
2) External sprays are applied
3) Internal sprays are active
4) Openings between compartments are large
5) The temperature field is not initially stratified
6) Heat sources, such as hot concrete walls or a sump, are at the low positions
7) Compartments are connected (not dead-ended)

In the case of AP600 and AP1000 passive containment designs, all conditions except 3) and partially 7) are satisfied.

9.C.3 APPLICATION OF LUMPED-PARAMETER CODES FOR MODELING LARGE CONTAINMENT FACILITIES

Results of codes using the lumped parameter approach are summarized in this chapter. The ability of the lumped parameter codes to model large facilities is assessed and guidelines to improve predictions are presented.

Tests from several facilities included in an international database are used to compare and validate the results of the lumped parameter containment analysis computer codes. Among the test facilities in the database are BMC, NUPEC, and HDR. Results from these experiments have been described in sections 9.C.2.1, 9.C.2.2, and 9.C.2.4, respectively.

9.C.3.1 VALIDATION OF THE LUMPED PARAMETER CONTAINMENT ANALYSIS COMPUTER CODES BASED ON BMC EXPERIMENTAL RESULTS

The BMC F2 tests are used to validate various containment codes (Fisher et al., 1991 and Fisher et al., 1993). BMC tests 2, 4, 6, 12, and 20 are used to compare various lumped parameter and distributed-parameter GOTHIC models (L. Wolf, H. Holzbauer, M. Schall, 1994).

9.C.3.1.1 F2 Experiments - Natural Convection Phenomena Inside the Multi-Compartment Containment

A comparison of the experimental results of the F2 experiments with the results of various codes is presented by L. Wolf, M. Gavrilas, K. Mun, 1996. The comparison is based on thermal-hydraulic benchmark exercises by Fisher et al., 1991 for Phase 1 and by Fisher et al., 1993 for Phases 2, 3, and 4. Many different codes including FUMO, JERICHO, FIPLOC, WAVCO, CONTAIN, MELCOR, and COBRA/FATHOMS are compared. The comparisons demonstrate the state of containment code development with respect to multi-compartment thermal-hydraulics.

Figures 1.17 through 1.37 (in Wolf et al., 1996) illustrate both the experimental data and the results of various containment analysis codes for F2-Experiment Heatup Phase (Phase I) over a long period of time (48 hours). Single-node models are specified for this exercise. This results in three mean sources of deviations between measurement and code results:

1) **Single-node models are not able to model stratification** (due to the penetration of the steam front) inside the dead-end compartments.

2) **One-node lumped parameter models cannot model the stratification front passing through horizontal vents.** One-node models provide artificially perfect mixing between the connected compartments, while in reality only a portion of the vents are available for circulation.

3) **Sump liquid level and sump temperature are not predicted well due to the instanta**neous transport of high temperature condensate into sump and stratification phenomena inside the sump. (Note that the temperature of the condensate is too high.)

The influence of all three discrepancies between the experimental and numerical results can be decreased by applying a series of nodes in a vertical direction or subdivision, as in the GOTHIC distributed parameter model.

Figures 1.50 through 1.55 (in Wolf et al., 1996) compare the experimental data for the F2-Experiment Phase II with the results of various codes. All compartments except the external annulus have almost homogeneous temperatures due to the presence of the natural circulation. A comparison of the measured and predicted velocities through the vents is in agreement for the majority of the codes, which supports the conclusion (L. Wolf, M. Gavrilas, K. Mun, 1996) that containment codes based on lumped parameter models can predict fully-developed natural circulation flows.

However, **some codes produced results that are not correct. It was established that the incorrect codes missed or oversimplified the buoyancy terms** (see K. Fischer et al., 1993).

9.C.3.1.2 Influence of Initial Temperature Distribution, Location of Hydrogen Injection, Duration of Injection, and Size of Vent Openings on Hydrogen Distribution (BMC Tests 2, 4, 6, 12, and 20)

A comparison of the multi-dimensional and lumped parameter GOTHIC containment analyses and the BMC experimental data is presented in Wolf et al., 1994b. Tests 2, 4, and 6, described in Section 9.C.2.1.2, are performed with only the central compartments R1, R2, and R3. Only two-dimensional GOTHIC results are presented.

Three different models are used to compare the results with multi-compartment experiments 12 and 20. Test 12, which uses a uniform initial temperature distribution, results in homogenized hydrogen concentrations in the entire containment. The lumped parameter model simulates hydrogen concentration histories in the various compartments (see Figure 9 in Wolf et al., 1994b, see also Figure 9.C.2-20 in this appendix). **To account for recirculation flows, the applied lumped parameter model uses double-junctions in the horizontal direction.**

Test 20 has a stratified initial temperature distribution, which results in a higher hydrogen distribution in the lower rooms. The conventional lumped parameter model, with one junction connection between two subvolumes, results in a hydrogen concentration profile (in R1 and R2 rooms) that is opposite to that measured (see Figure 9 in L. Wolf, H. Holzbauer, M. Schall, 1994b). Also, the experimental results indicate a stratified hydrogen concentration during the first three hours, while the computed generated hydrogen distribution is more uniform. **The calculation performed with double-junction lumped parameter modeling (second model) does not improve results. This model also results in a high degree of hydrogen homogenization inside the containment.**

The third type of model uses a two-dimensional model (distributed parameter model) for all containment rooms except room R2 and uses double-junctions for horizontal connections. The results are presented in Figure 11 in L. Wolf, H. Holzbauer, M. Schall, 1994b and Figure 9.C.2-21 of this appendix. Improvement between experimental and computed results is obvious (except in the source room R6). A finer nodalization of the source compartment R6 could further improve the results, because the processes in this compartment affect the hydrogen distribution phenomena in all other portions of the containment. Therefore, a more complete momentum formulation, such as that in GOTHIC distributed parameters, is needed to accurately model H_2 distributions.

9.C.3.2 VALIDATION OF THE LUMPED PARAMETER CONTAINMENT ANALYSIS COMPUTER CODES BASED ON NUPEC EXPERIMENTAL RESULTS

9.C.3.2.1 M-7-1 Test

A comparison of the M-7-1 test results with the various computer codes results is presented in report NEA/CSNI/R(94)29. The WGOTHIC (Westinghouse modified GOTHIC) code results are also included (see pages 125, 130, 135, blind test calculation results - pages 246-253, open test calculations - pages 322-327, preheating calculation - 374-378). However, the M-7-1 test is not directly applicable to the passive containment design, because internal sprays are active during the test.

9.C.3.2.2 M-4-1 Test

The experimental results of NUPEC M-4-3 test (T. Hirose, 1993) are used to validate various lumped parameter codes and to check the input geometry and boundary conditions, before applying them to blind and open comparisons with the NUPEC M-7-1 database. WGOTHIC is also compared with NUPEC M-4-3 experimental data. A comparison of the WGOTHIC results with the M-4-3 test, which is performed without internal sprays, is presented by R. P. Ofstun, J. Woodcock, D. L. Paulsen, 1994. The location of the break is at a low position in the first level of the containment. A mixture of steam and helium is injected at a constant flow rate during the first 30 minutes and experimental data is recorded for 2 hours.

A comparison of the experimentally and numerically obtained pressure of the dome is illustrated in Figure 9.C.3-1. Figures 9.C.3-2 through 9.C.3-5 present comparisons of the temperatures and helium concentrations inside the compartments 8, 15, dome, and 7. These compartments are affected by the global circulation loop. Lumped parameter modeling methods developed for NUPEC M-4-3 are summarized in Section 9.2.4. Good agreement exists between the numerical and experimental results for the multiple, connected, lumped parameter compartments in the circulating regions.

However, a paper by R.P. Ofstun, J. Woodcock, D. L. Paulsen, 1994 shows a discrepancy between the measured and calculated (lumped parameter model) helium concentrations in dead-end compartments. Calculated values for in-core chase node and two pressurizer nodes (which are all dead-end compartments) are presented and compared with M-4-3 test data (see Figures 3-8, in R.P. Ofstun, J. Woodcock, D. L. Paulsen, 1994). The discrepancy shows that the lumped parameter model has difficulty predicting circulation effects within dead-end compartments.

It is postulated that asymmetric temperatures on the vertical walls of the dead-ended compartments induce a natural circulation within the compartment that is not modeled in the lumped parameter model. To improve the results for dead-end compartments, a WGOTHIC distributed parameter model is applied to the dead-

ended compartments and interfaced to the lumped parameter model (see Figures 9 - 14 in R. P. Ofstun, J. Woodcock, D. L. Paulsen, 1994).

The lumped parameter model predicts pressure, temperature and helium concentrations inside the compartments affected by the global circulation loop. However, a distributed parameter model is necessary to improve predictions inside the dead-end compartments.

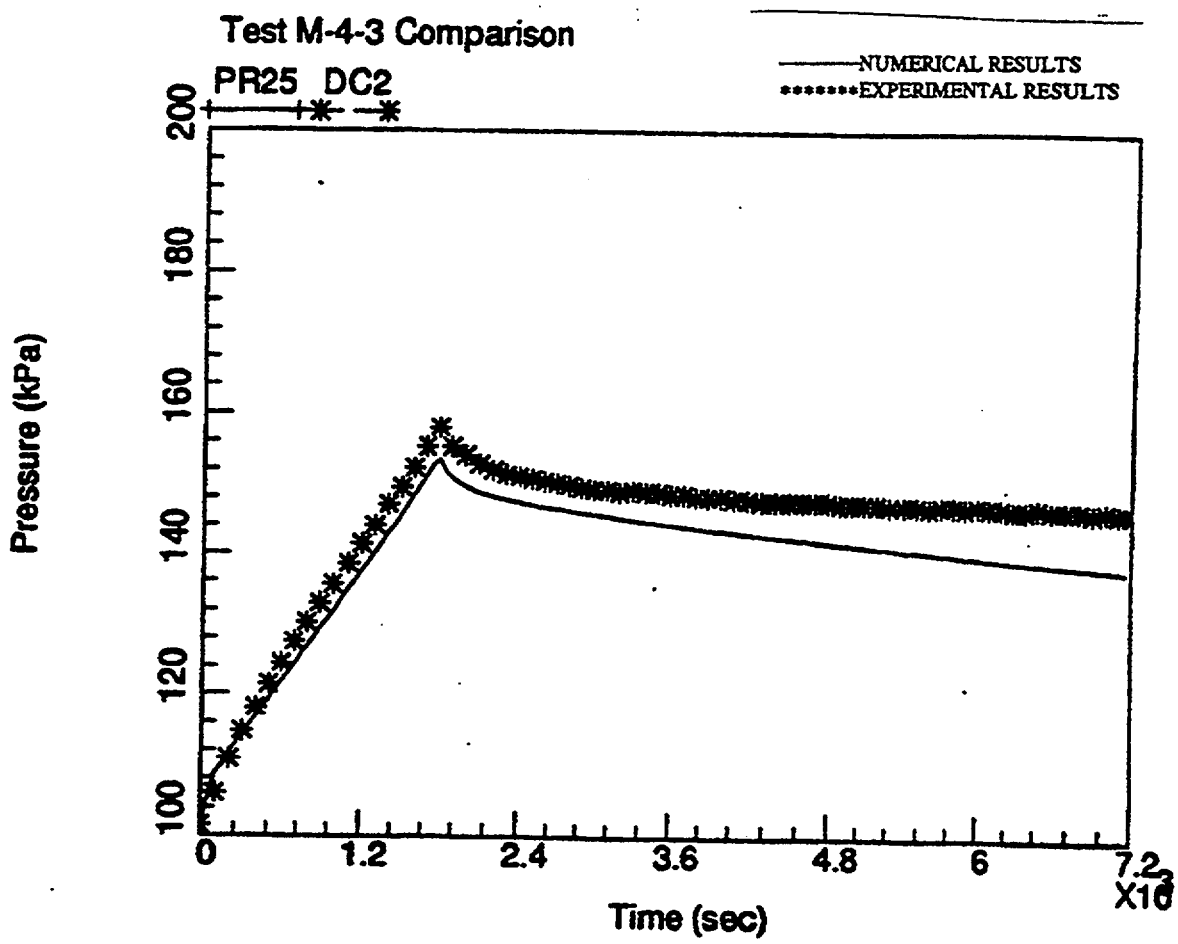

Figure 9.C.3-1 Dome pressure history

(Numerical results are produced in the framework of: R.P. Ofstun, J. Woodcock, D.L. Paulsen, "Westinghouse-GOTHIC modeling of NUPEC's hydrogen mixing and distribution test M-4-3", The Third International Conference on Containment Design and Operation, Volume 1, Toronto, Canada, October 19 - 21, 1994)

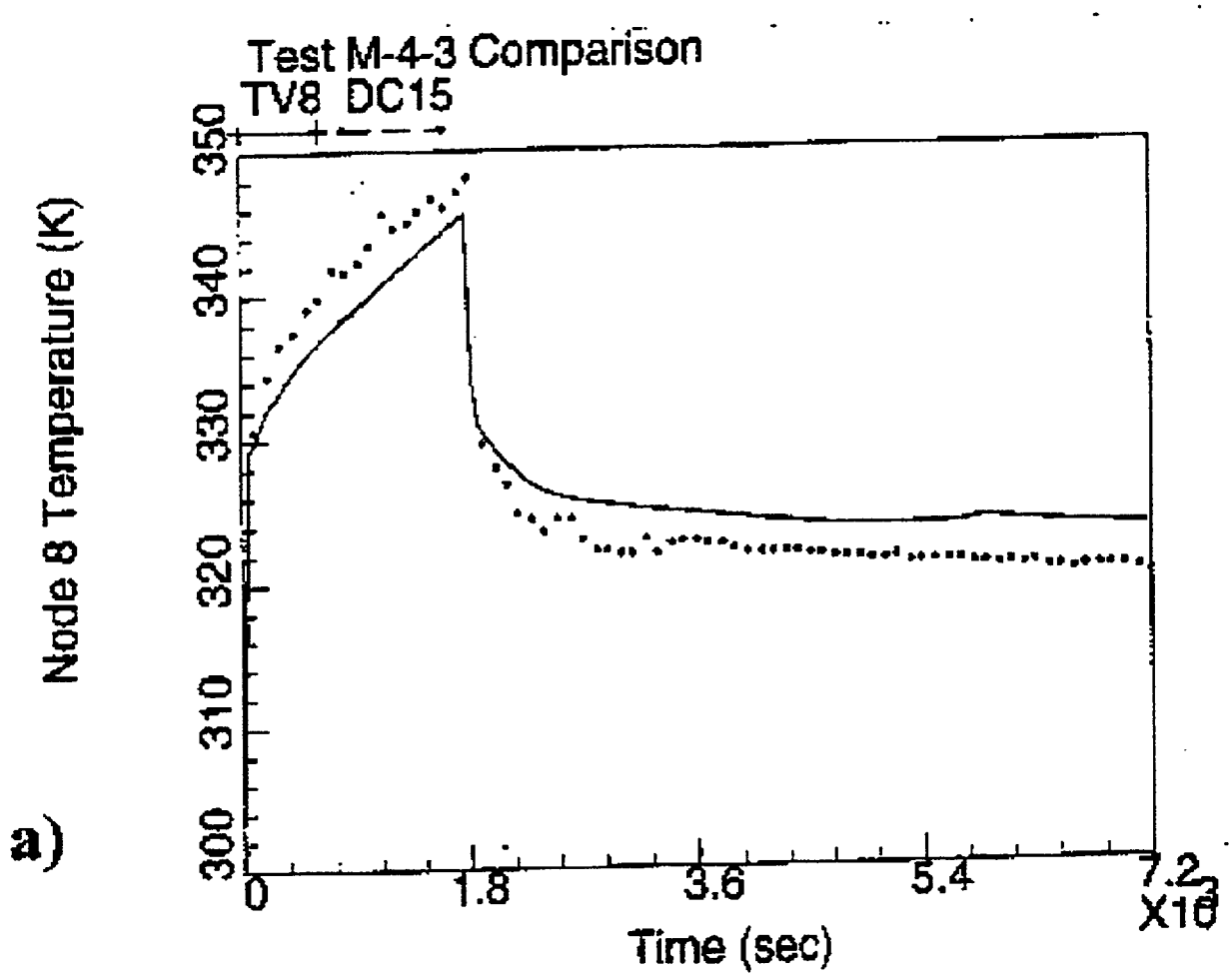

Figure 9.C.3-2a Temperature history inside node 8

(Numerical results are produced in the framework of: R.P. Ofstun, J. Woodcock, D.L. Paulsen, "Westinghouse-GOTHIC modeling of NUPEC's hydrogen mixing and distribution test M-4-3", The Third International Conference on Containment Design and Operation, Volume 1, Toronto, Canada, October 19 - 21, 1994)

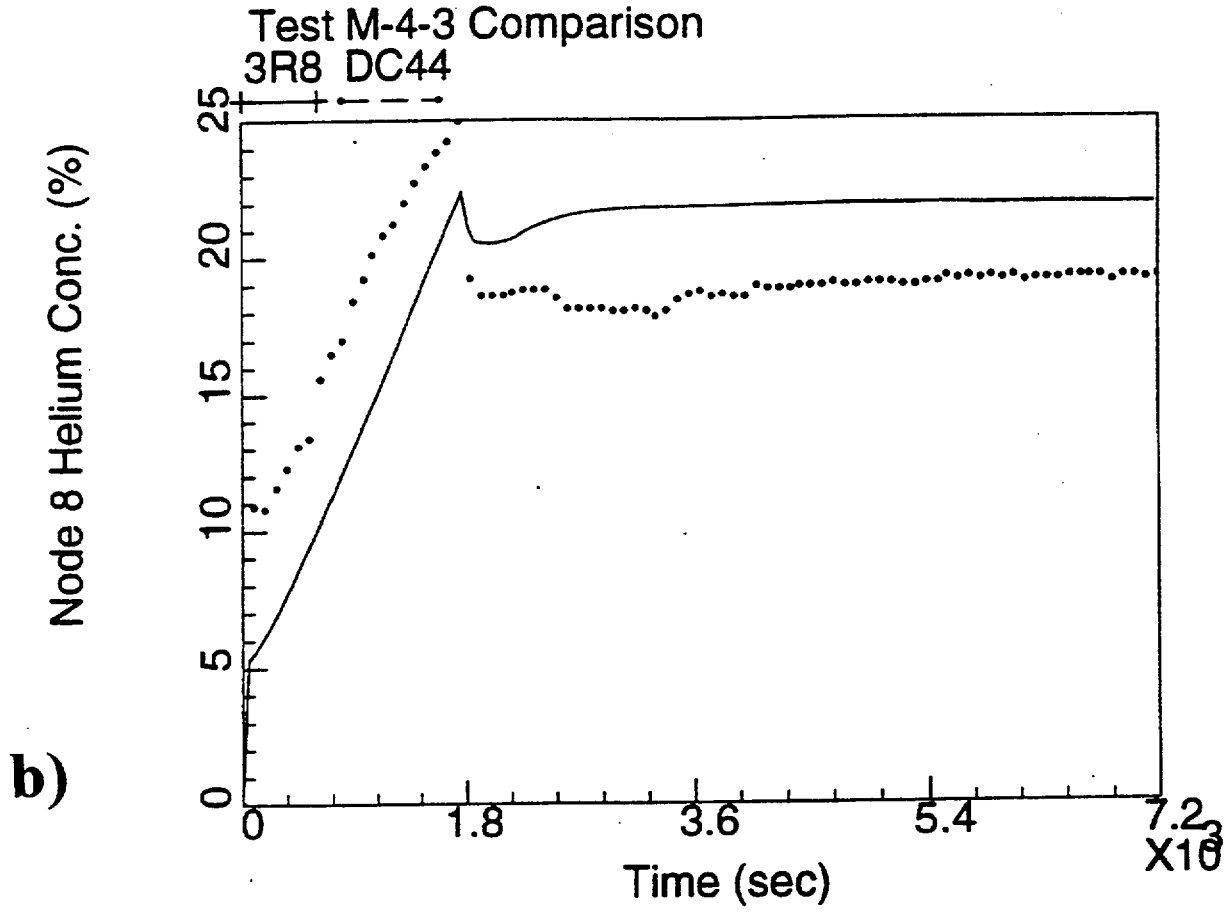

Figure 9.C.3-2b Helium concentration history inside node 8

(Numerical results are produced in the framework of: R.P. Ofstun, J. Woodcock, D.L. Paulsen, "Westinghouse-GOTHIC modeling of NUPEC's hydrogen mixing and distribution test M-4-3", The Third International Conference on Containment Design and Operation, Volume 1, Toronto, Canada, October 19 - 21, 1994)

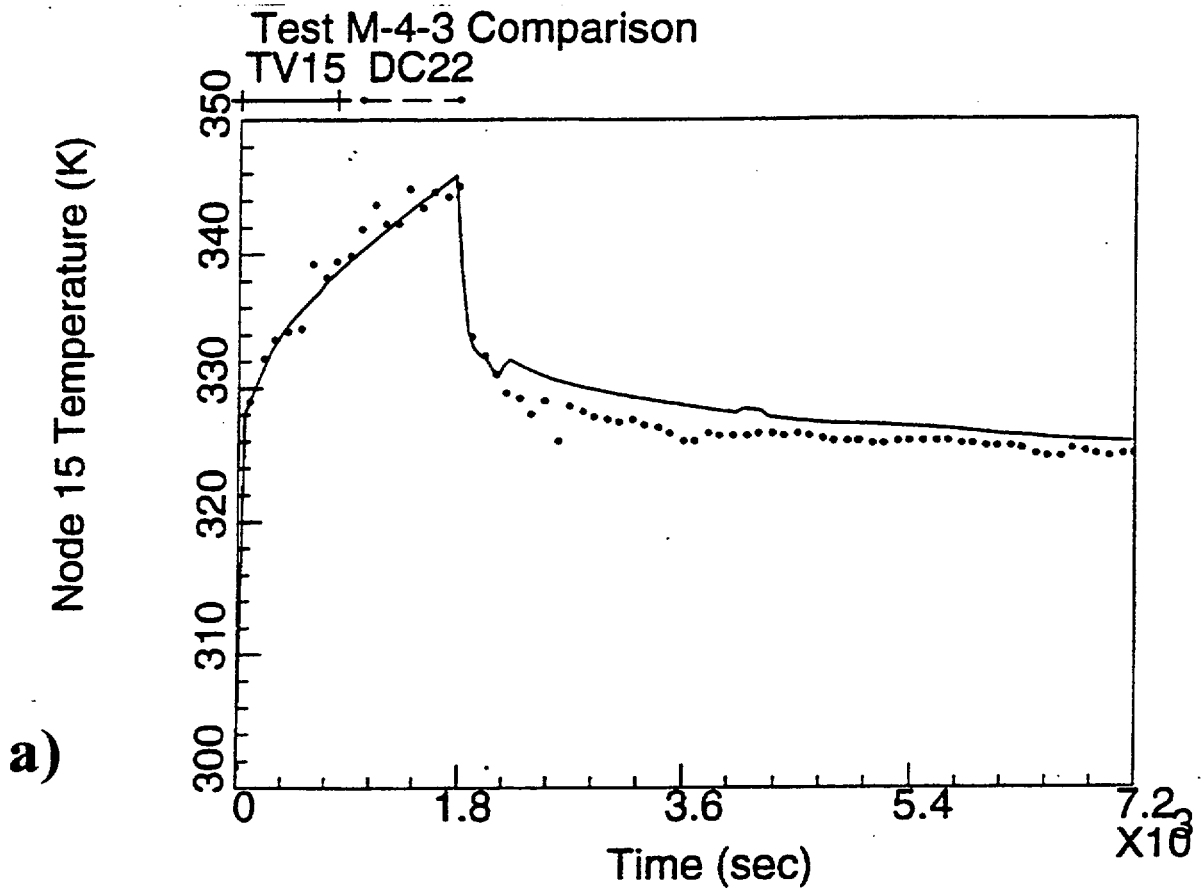

Figure 9.C.3-3a Temperature history inside node 15

(Numerical results are produced in the framework of: R.P. Ofstun, J. Woodcock, D.L. Paulsen, "Westinghouse-GOTHIC modeling of NUPEC's hydrogen mixing and distribution test M-4-3", The Third International Conference on Containment Design and Operation, Volume 1, Toronto, Canada, October 19 - 21, 1994)

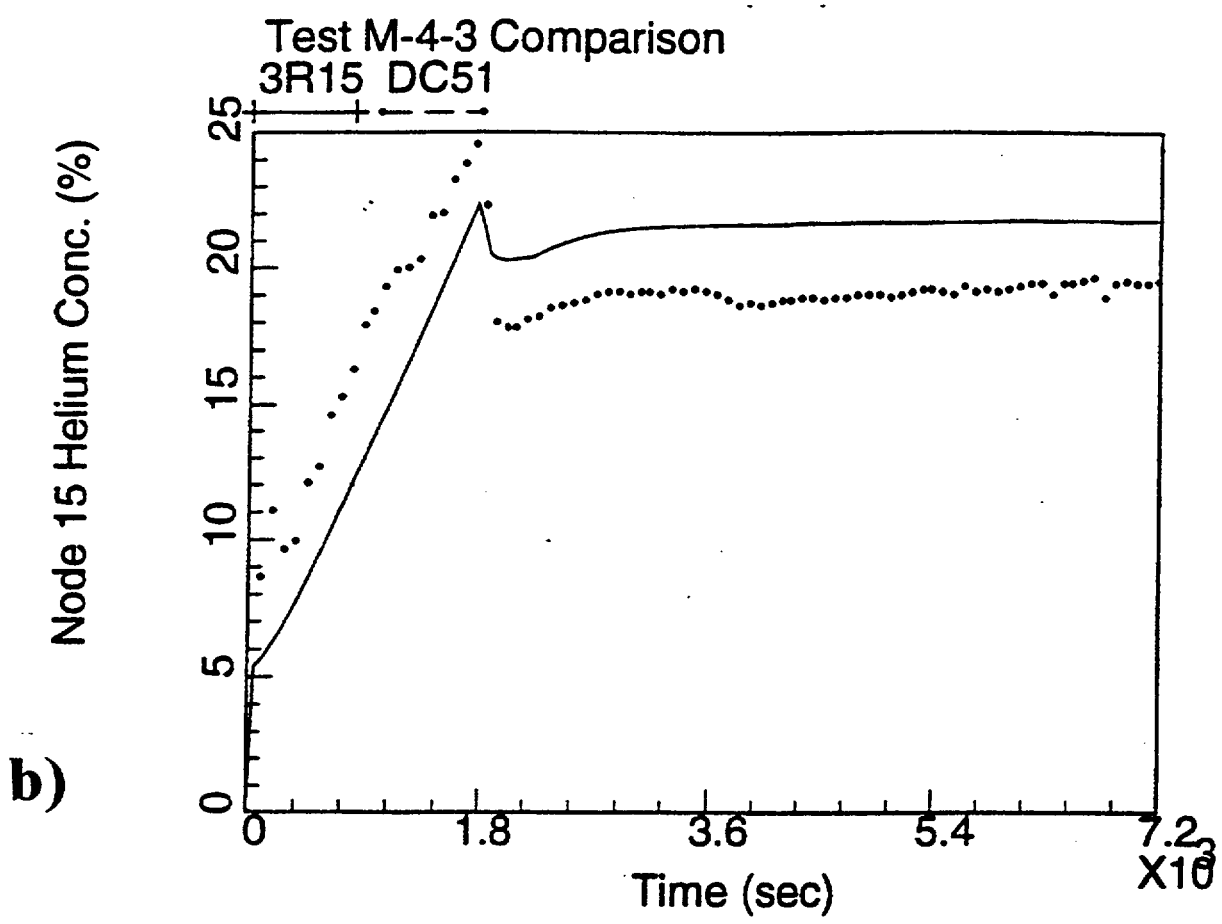

Figure 9.C.3-3b Helium concentration history inside node 15

(Numerical results are produced in the framework of: R.P. Ofstun, J. Woodcock, D.L. Paulsen, "Westinghouse-GOTHIC modeling of NUPEC's hydrogen mixing and distribution test M-4-3", The Third International Conference on Containment Design and Operation, Volume 1, Toronto, Canada, October 19 - 21, 1994)

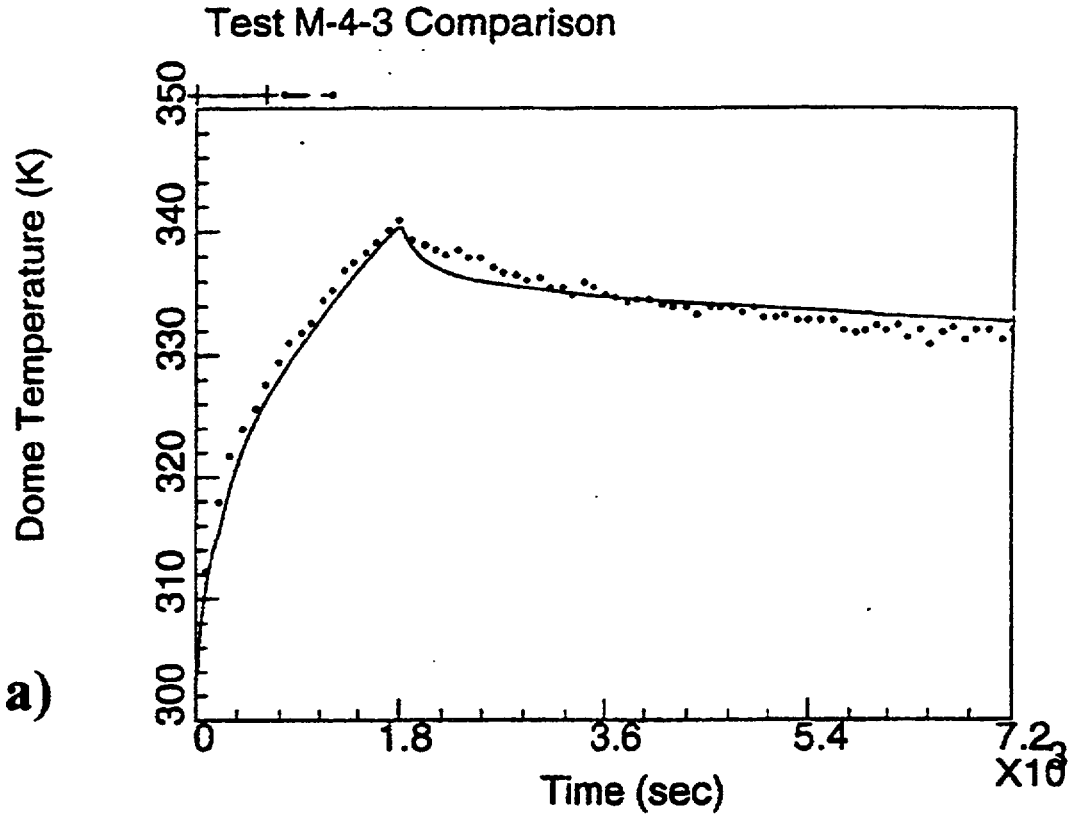

Figure 9.C.3-4a Temperature history inside dome

(Numerical results are produced in the framework of: R.P. Ofstun, J. Woodcock, D.L. Paulsen, "Westinghouse-GOTHIC modeling of NUPEC's hydrogen mixing and distribution test M-4-3", The Third International Conference on Containment Design and Operation, Volume 1, Toronto, Canada, October 19 - 21, 1994)

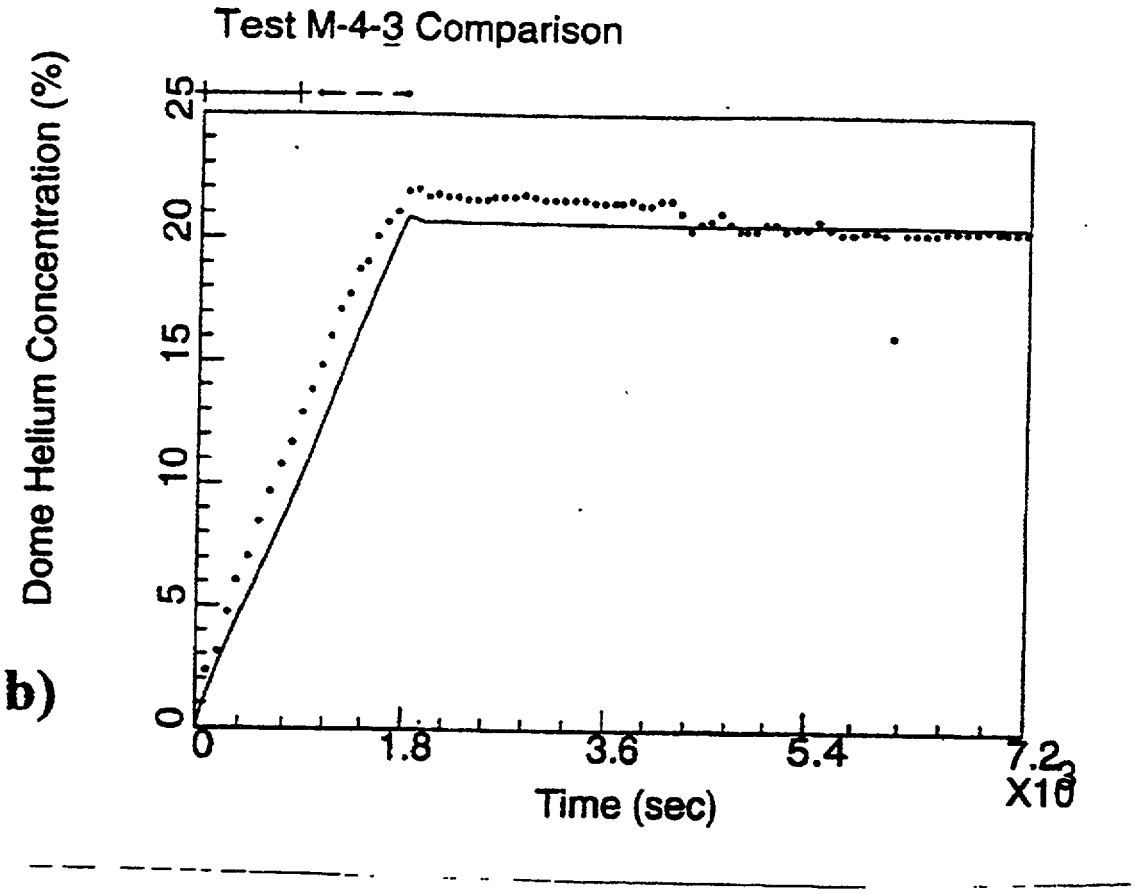

Figure 9.C.3-4b Helium concentration history inside dome

(Numerical results are produced in the framework of: R.P. Ofstun, J. Woodcock, D.L. Paulsen, "Westinghouse-GOTHIC modeling of NUPEC's hydrogen mixing and distribution test M-4-3", The Third International Conference on Containment Design and Operation, Volume 1, Toronto, Canada, October 19 - 21, 1994)

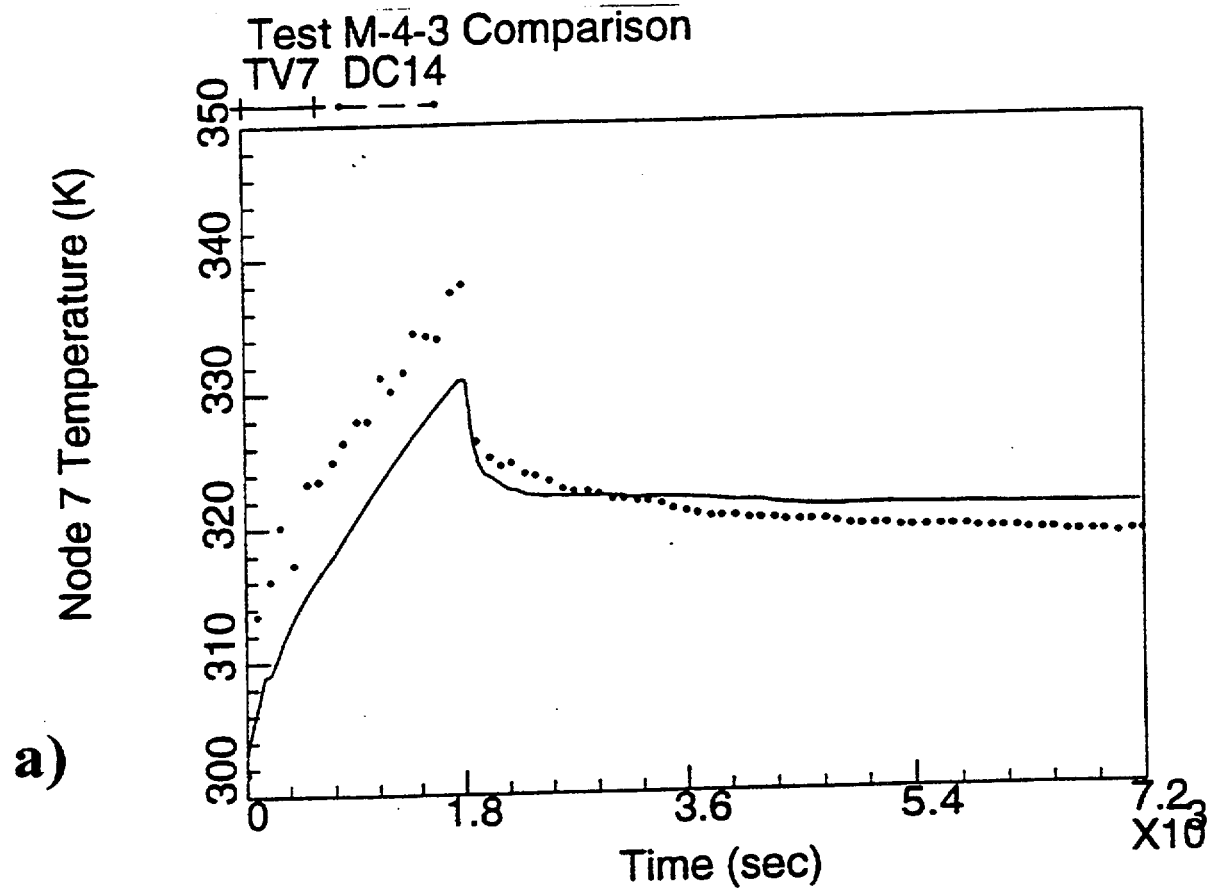

Figure 9.C.3-5a Temperature history inside node 7

(Numerical results are produced in the framework of: R.P. Ofstun, J. Woodcock, D.L. Paulsen, "Westinghouse-GOTHIC modeling of NUPEC's hydrogen mixing and distribution test M-4-3", The Third International Conference on Containment Design and Operation, Volume 1, Toronto, Canada, October 19 - 21, 1994)

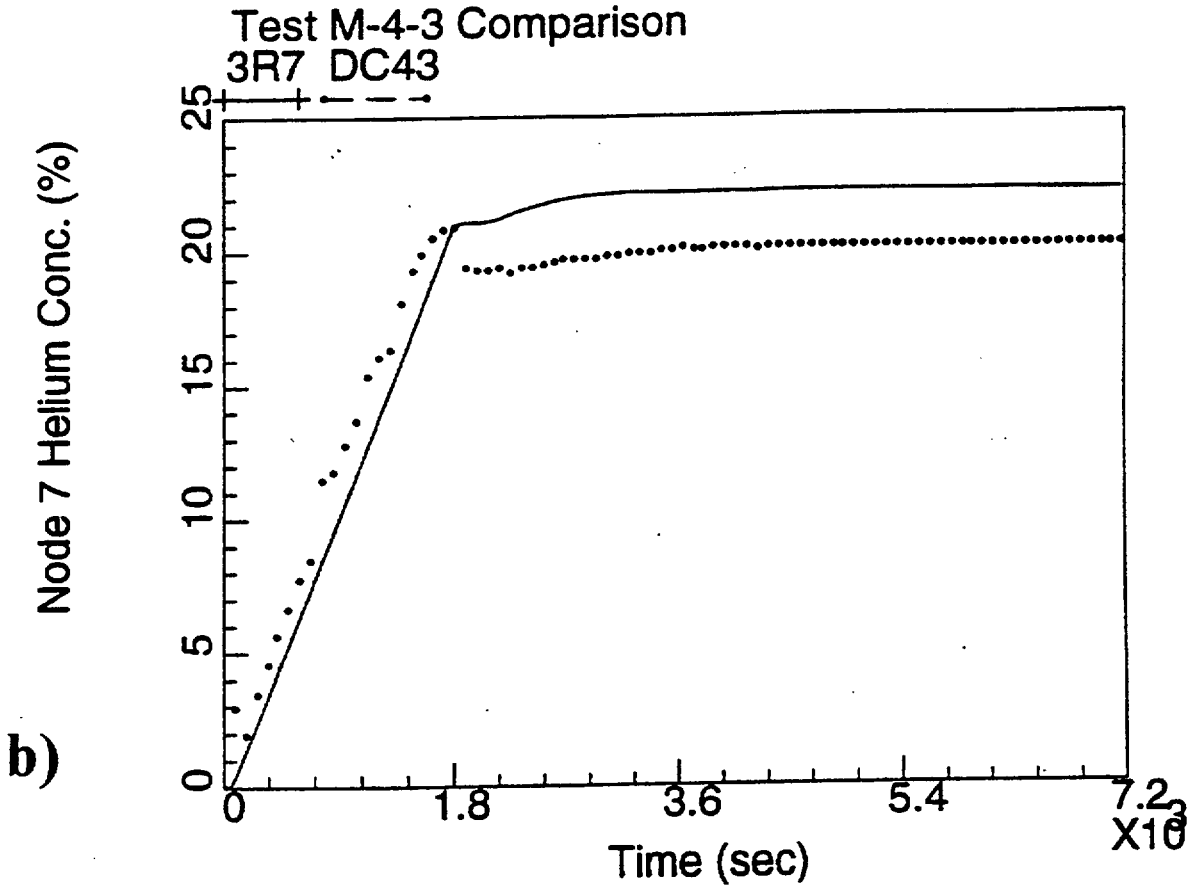

Figure 9.C.3-5b Helium concentration history inside node 7

(Numerical results are produced in the framework of: R.P. Ofstun, J. Woodcock, D.L. Paulsen, "Westinghouse-GOTHIC modeling of NUPEC's hydrogen mixing and distribution test M-4-3", The Third International Conference on Containment Design and Operation, Volume 1, Toronto, Canada, October 19 - 21, 1994)

9.C.3.3 VALIDATION OF THE LUMPED-PARAMETER CONTAINMENT ANALYSIS COMPUTER CODES BASED ON HDR EXPERIMENTAL RESULTS

Comparisons of the results of best-estimate open post-test predictions of various containment analysis computer codes (as RALOC, WAVCO, CONTAIN, MELCOR, and GOTHIC) for E11.2 and E11.4 HDR experiments presented by L. Wolf, H. Holzbauer and T. Cron, 1994a. Detailed comparisons and verifications of the blind and open GOTHIC results for the E11.2 and E11.4 HDR experiments are presented by H. Holzbauer and L. Wolf, 1994. More details about E11.2 and E11.4, and comparisons with the experimental results of large blowdown tests T31.5, V21.1, and E11.5, are presented in the report by K. Fischer, M. Schall, L. Wolf, 1995.

Following is a summary of observations from the comparison of the experiments with codes:

1) **Scenarios with homogeneous containment atmosphere (like E11.4 and E11.5) can be simulated successfully with lumped parameter models.**

   The results of the E11.4 computation agree with the corrected experimental input data (open test - see Figures 17-21 in H. Holzbauer and L. Wolf, 1994) .

   The same conclusion is valid for accidents initiated by a large-break LOCA in the lower positions of containments, accompanied by subsequent steam and gas releases (as in E11.5). Good agreement has been achieved by the GOTHIC lumped-parameter model using a modest number of nodes (see Figures 10.9 - 10.22 in K. Fischer, M. Schall, L. Wolf, 1995). A comparison of the experimentally and numerically obtained pressure histories is presented in Figure 9.C.3-6. The calculated pressure history is slightly higher than the experimental results. Figure 9.C.3-7 presents a comparison for sump temperature. Note that the sump temperature sensor is exposed to the containment atmosphere for the first 8 hours. It is then submerged by higher sump water level. **The history of sump boiling is well simulated.** Comparisons of temperatures in main and spiral stairways at 6 m level are presented in Figures 9.C.3-8 and 9.C.3-9, respectively. Gas mixture concentration comparisons for the same staircase elevation are presented in Figures 9.C.3-10 and 9.C.3-11. The measured velocity in spiral stairway at 15 m elevation is presented in Figure 9.C.3-12. **Since the order of magnitude of the computed velocities matches the data, it can be concluded that trends in the direction of the flow are predicted well; however, predicted velocities differ by as much as factor of two.**

2) **The lumped parameter method is not capable of predicting the hydrogen distribution in a stratified containment atmosphere (as in E11.2 test with high-positioned release).**

The pressure history is well predicted after applying the correct steam inflow experimental data and accounting for energy sink of the sensors cooling system. Comparisons between the experimental data and the "optimized" post-test prediction for containment pressure are presented in Figure 9.C.3-13. GOTHIC lumped parameter results overpredict pressure by 0.25 bar (11%).

Temperatures, steam, and gas concentrations are underestimated and overestimated above and below the break location, respectively, (see Figures 7 and 8 in H. Holzbauer and L. Wolf, 1994). **Therefore, for a high-positioned release, the steam and gas transport to the lower parts of the containment are overpredicted.**

Artificial limitation of convective flows (by reduction of flow path areas) in all modeled flow paths improves the prediction of temperatures and gas concentrations in the lower containment regions (Figures. 13, 15, and 16 in H. Holzbauer and L. Wolf, 1994), but overestimates the containment pressure and temperatures in the upper containment (see results of parametric calculations NA15 and NA16, Figures 11 and 12 in H. Holzbauer and L. Wolf, 1994).

3) **Application of distributed parameter models may improve prediction of a stratified containment atmosphere** (as in E11.2 test).

A study of the influence of the number of nodes applied for a simple volume proportional to the HDR E11.2 facility volume using a distributed parameter model is presented by J.S. Narula and J. Woodcock, 1994. The authors conclude that in situations requiring detailed flow distribution in non-homogenous environments, a fine mesh may be required to obtain realistic results. A coarse mesh (small number of nodes) may reduce the accuracy of the results, despite a highly accurate containment model in all other aspects, including momentum representation.

A detailed study of the influence of the nodalization, and a comparison of the lumped parameter results with distributed parameter model results for E11.2 case are presented by K.K. Mun, 1996. This report also includes a comparison of the pressure, temperature, steam and hydrogen concentrations histories (see Figures 67 - 91 in K.K. Mun, 1996). The author concludes that, in general, the modeling approach of merging the distributed and lumped parameter models improves the prediction. However, to improve the prediction further, a proper distributed parameter nodalization for the lower break compartment and dome, together with the correct connections for the associated flow paths, are required.

All specified observations 1, 2, and 3 for GOTHIC applications are in agreement with comparisons of the results of other well-known codes (see L. Wolf, H. Holzbauer and T. Cron, 1994a).

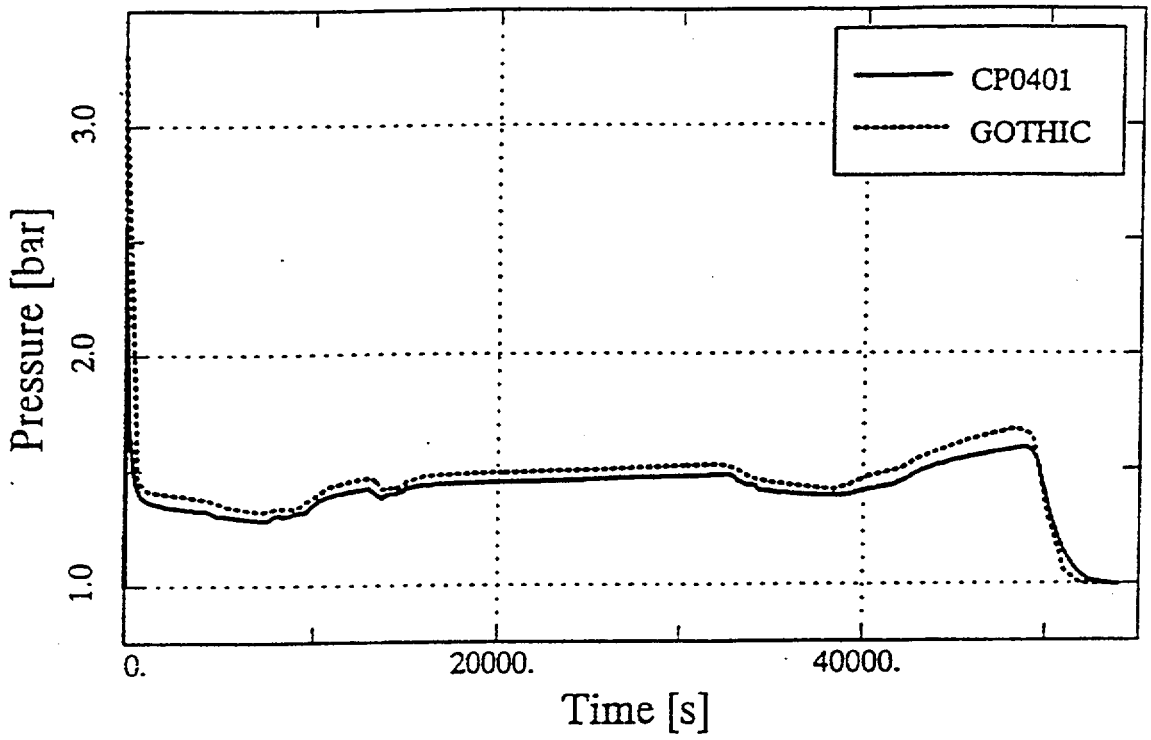

Figure 9.C.3-6 HDR-E11.5: Comparison between measured long-term containment pressure and GOTHIC open post-test prediction

"Reproduced with permission from a report funded by the EPRI GOTHIC Advisory Group: K. Fischer, M. Schall, L. Wolf, " Simulations of GOTHIC Large Scale Containment Experiments", Battelle Ingenieurtechnik GmbH, Eschborn, Fachbericht BF - V - 68317 - 01, October 1995)

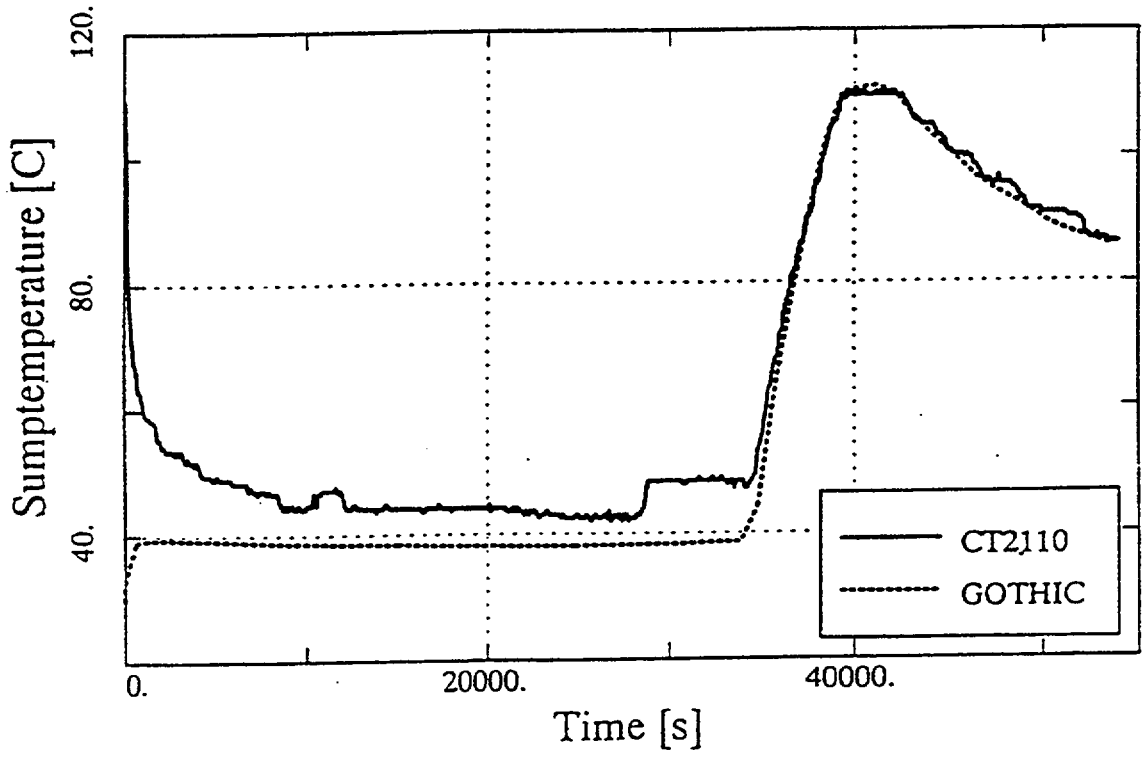

Figure 9.C.3-7 HDR-E11.5: Comparison between measured sump temperature and GOTHIC open post-test prediction

"Reproduced with permission from a report funded by the EPRI GOTHIC Advisory Group: K. Fischer, M. Schall, L. Wolf, " Simulations of GOTHIC Large Scale Containment Experiments", Battelle Ingenieurtechnik GmbH, Eschborn, Fachbericht BF - V - 68317 - 01, October 1995)

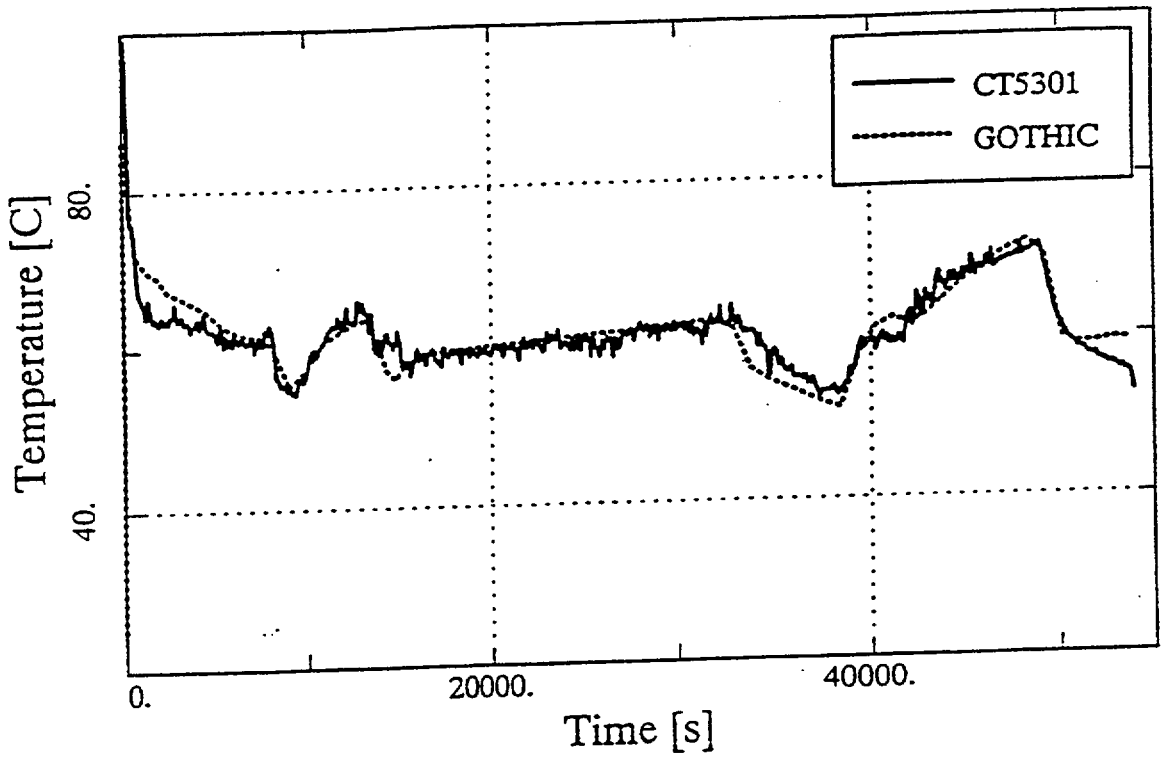

Figure 9.C.3-8 HDR-E11.5: Comparison between measured temperature in main stairway (6m) and GOTHIC open post-test prediction

"Reproduced with permission from a report funded by the EPRI GOTHIC Advisory Group: K. Fischer, M. Schall, L. Wolf, " Simulations of GOTHIC Large Scale Containment Experiments", Battelle Ingenieurtechnik GmbH, Eschborn, Fachbericht BF - V - 68317 - 01, October 1995)

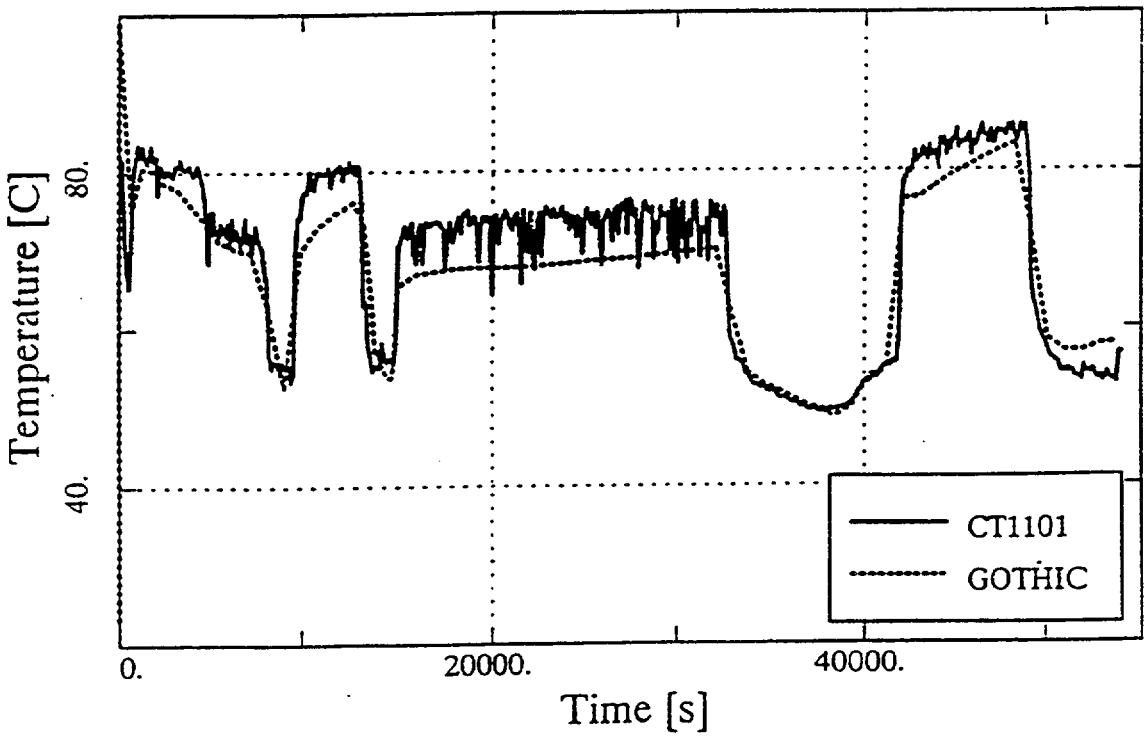

Figure 9.C.3-9 **HDR-E11.5: Comparison between measured temperature in spiral stairway (6m) and GOTHIC open post-test prediction**

"Reproduced with permission from a report funded by the EPRI GOTHIC Advisory Group: K. Fischer, M. Schall, L. Wolf, " Simulations of GOTHIC Large Scale Containment Experiments", Battelle Ingenieurtechnik GmbH, Eschborn, Fachbericht BF - V - 68317 - 01, October 1995)

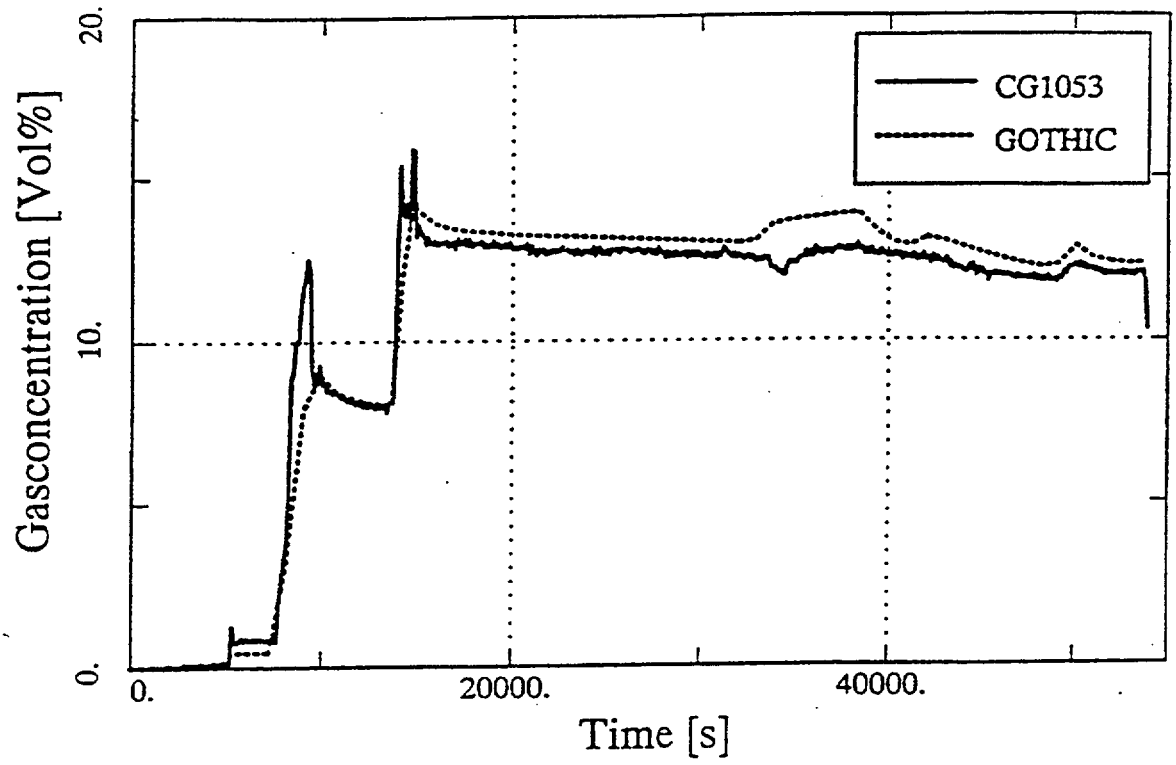

Figure 9.C.3-10 **HDR-E11.5: Comparison between measured gas mixture concentration in main stairway (6m) and GOTHIC open post-test prediction**

"Reproduced with permission from a report funded by the EPRI GOTHIC Advisory Group: K. Fischer, M. Schall, L. Wolf, " Simulations of GOTHIC Large Scale Containment Experiments", Battelle Ingenieurtechnik GmbH, Eschborn, Fachbericht BF - V - 68317 - 01, October 1995)

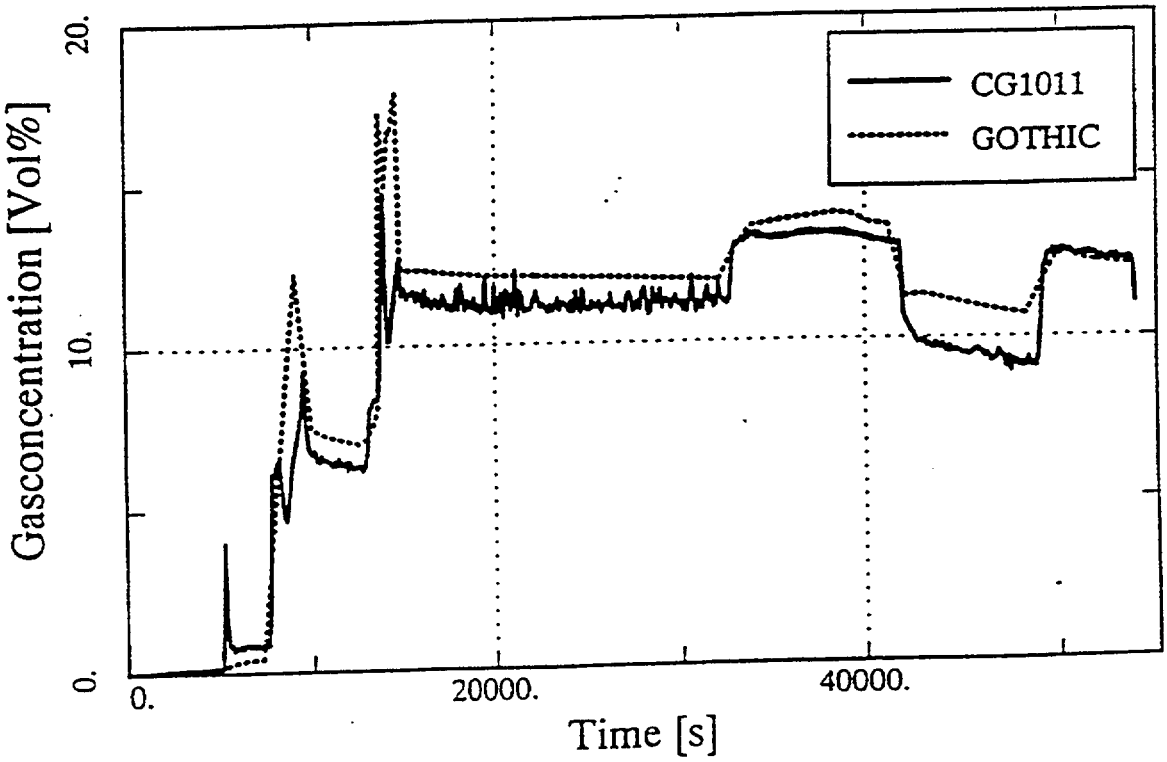

Figure 9.C.3-11 **HDR-E11.5: Comparison between measured gas mixture concentration in spiral stairway (6m) and GOTHIC open post-test prediction**

"Reproduced with permission from a report funded by the EPRI GOTHIC Advisory Group: K. Fischer, M. Schall, L. Wolf, " Simulations of GOTHIC Large Scale Containment Experiments", Battelle Ingenieurtechnik GmbH, Eschborn, Fachbericht BF - V - 68317 - 01, October 1995)

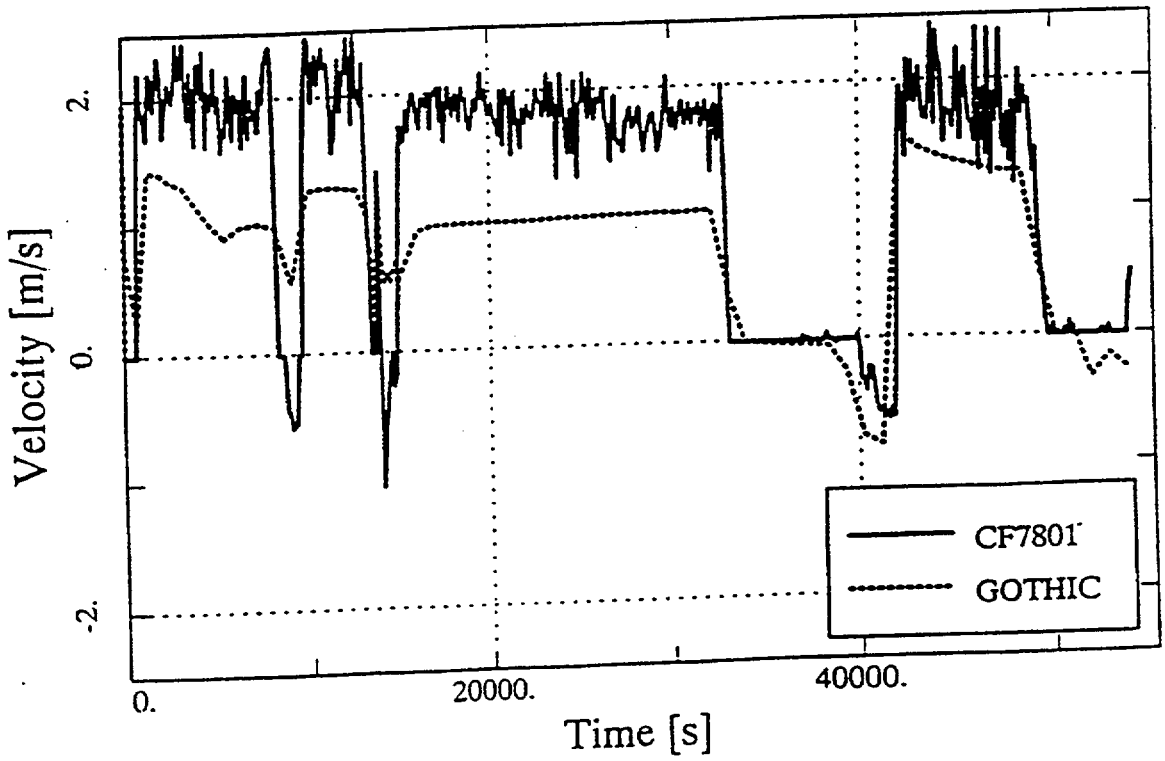

Figure 9.C.3-12 **HDR-E11.5: Comparison between measured velocity in spiral stairway (15m) and GOTHIC open post-test prediction**

"Reproduced with permission from a report funded by the EPRI GOTHIC Advisory Group: K. Fischer, M. Schall, L. Wolf, " Simulations of GOTHIC Large Scale Containment Experiments", Battelle Ingenieurtechnik GmbH, Eschborn, Fachbericht BF - V - 68317 - 01, October 1995)

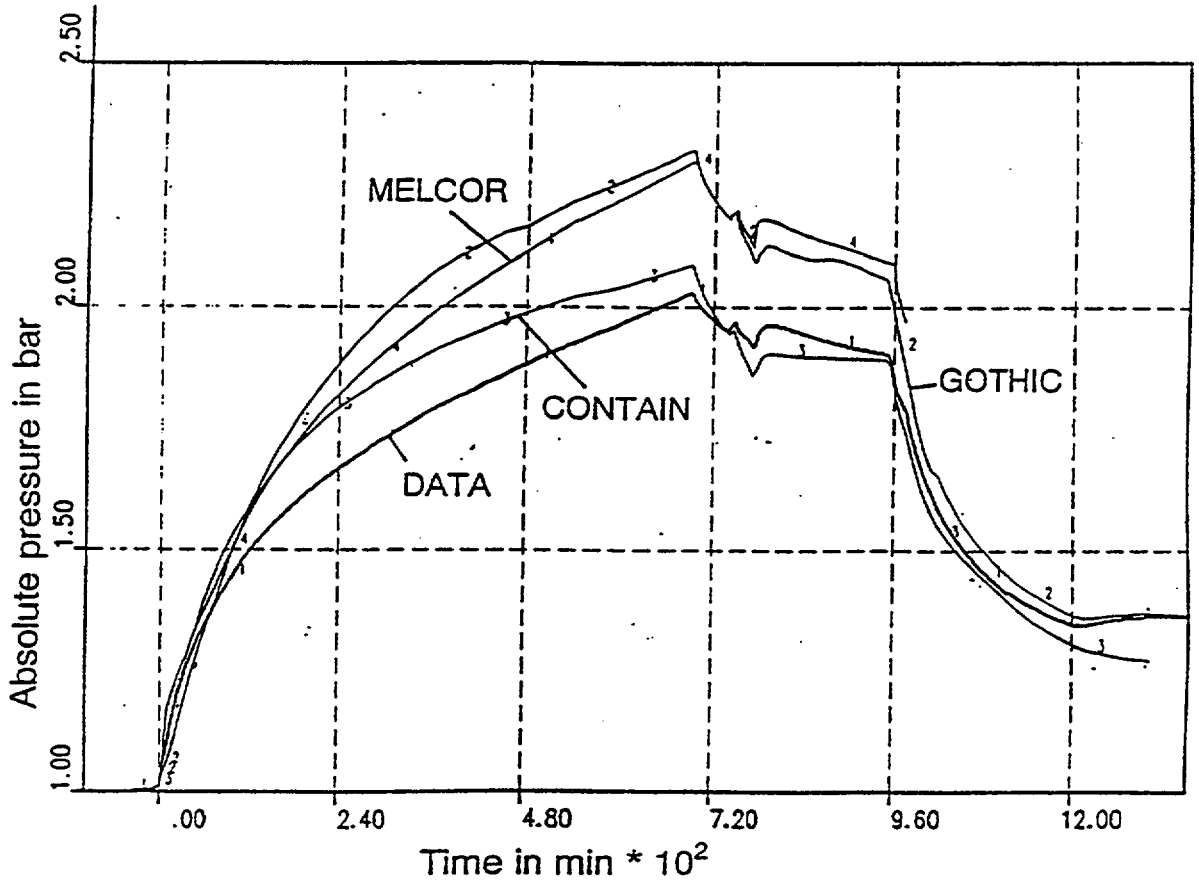

Figure 9.C.3-13 HDR-E11.2: Comparison between measured long-term containment pressure and various "optimized" open post-test predictions

(Reproduced with permission from a report funded by the EPRI GOTHIC Advisory Group: K. Fischer, M. Schall, L. Wolf, " Simulations of GOTHIC Large Scale Containment Experiments", Battelle Ingenieurtechnik GmbH, Eschborn, Fachbericht BF - V - 68317 - 01, October 1995)

9.C.3.4 CONCLUSIONS

Lumped parameter models can predict pressure, and in some cases temperature, steam, and hydrogen concentrations inside the containment. Good predictions exist for the situations where the global circulation loop, which contributes towards the homogenization of atmosphere, is present inside the containment (see comparison with BMC F2 experiments and BMC test 12 experiments, NUPEC M-4-3 tests and HDR E11.4 and E11.5 tests). Additional improvements are possible if double-junctions between compartments in the horizontal direction are applied (allowing simulation of recirculation flows).

Single-node, lumped parameter models are not able to model stratification inside dead-end compartments due to the steam front penetration. They also do not include cases where the stratification front passes through horizontal vents, nor do they simulate sump liquid level, temperature, and stratification inside the sump. (See the BMC F2 experiments and the NUPEC M-4-3 results for dead-end compartments (R. Ofstun et al., 1994). The remedy can be an increase in the number of the nodes in the vertical direction or the application of distributed parameter model for dead-ended compartments (R. Ofstun et al., 1994).

For a stratified initial temperature distribution (BMC test 20) and a stratified containment atmosphere (HDR E11.2 test), the lumped parameter models do not predict the correct hydrogen distribution (they overmix the atmosphere). The artificial limitation of the size of the flow path areas in the HDR E11.2 test improved the prediction of temperatures and gas concentrations in the lower containment regions, but overestimated the containment pressure and temperatures in the upper levels.

Application of distributed parameter models may improve prediction capability. See BMC test 20 (L. Wolf, H. Holzbauer, M. Schall, 1994b; HDR E11.2 test - J. S. Narula and J. Woodcock, 1994; and K. K. Mun, 1996). All three publications conclude that proper distributed parameter nodalization for break and dome compartments is required to improve results. However, the increase of the number of nodes in all important regions of containment increases required memory and computing time beyond current practical limits.

The next step towards better space resolution and modeling would be the application of commercial CFD (Computational Fluid Dynamics) codes with built-in capabilities for multi-phase flows simulation, and multi-block, unstructured, or embedded grid options. Considering that three-dimensional transient multi-phase flow simulation would be required, only codes prepared for parallel multi-processor machines would produce results in a reasonable time. In addition, there are limitations related to noding convergence (see Gavrilas et al., 1997). Finally, an appropriate set of constitutive models (see Royl et al., 1997), such as condensation and sump evaporation, are not presently available in many CFD codes.

For the AP600 and AP1000 with a low break release position and an established global circulation pattern that improves homogenization (see conclusion of the review of international experimental data base), a careful application of lumped parameter models could produce results which would be in agreement with test data.

In summary, biases that should be addressed when applying lumped parameter codes are:

1. Single-node models are not able to model stratification, or the passing of a stratification front through horizontal vents.

2. Sump liquid level and sump temperature are not predicted well.

3. Some codes produced results that are not correct due to missing or oversimplified buoyancy terms.

4. To account for recirculation flows, the applied lumped parameter model uses double junctions in the horizontal direction. (This does not help in the case of an elevated release and resulting stratified containment.)

5. For releases low in containment, typical for the AP600 and AP1000 DECLG LOCA, the lumped parameter model predicts pressure, temperature, and helium concentrations inside the compartments that are affected by the global circulation loop. Improvements are needed to account for postulated circulation effects inside dead-ended compartments.

6. Scenarios with homogeneous containment atmosphere (HDR E11.4 and E11.5) are simulated successfully with lumped parameter models. (Such conditions typically result from breaks located below 20 percent of the containment height.)

7. Circulation effects due to sump boiling (releases generated at the bottom of containment) are well simulated.

8. The order of magnitude of computed velocities matches the experimental data. Trends in the direction of the flow are predicted well; however, predicted velocities differ by as much as a factor of two.

9. The lumped parameter method is not capable of predicting the hydrogen distribution in a stratified containment atmosphere, as in HDR E11.2 with high-positioned release. In a break scenario with a buoyant plume (released at about 50 percent of containment height), the steam and gas transport to the lower parts of the containment are over-predicted. (When convective flows are artificially

limited by decreasing flow areas, predicted concentrations in the lower regions improve, but the containment pressure and temperatures in upper compartments are overestimated.)

9.C.3.5 REFERENCES

1. Fischer, K., T., Schall, M., Wolf, L., 1991, "CEC Thermal-Hydraulic Benchmark Exercise on FIPLOC Verification Experiment F2 in BMC-Long-Term Heatup Phase - Results for Phase I," Final Report, EUR 13588 EN, 1991

2. Fischer, K., T., Schall, M., Wolf, L., 1993, "CEC Thermal-Hydraulic Benchmark Exercise on FIPLOC Verification Experiment F2 in BMC, Experiment F2 in BMC, Experimental Phases - Results for Phase 2, 3, and 4, Results of Comparisons," Final Report, EUR 14454 EN, 1993

3. K. Fischer, M. Schall, L. Wolf, 1995, "Simulations of GOTHIC Large-Scale Containment Experiments," Battelle Ingenieurtechnik GmbH, Eschborn Fachbericht BF - V - 68317 - 01, October 1995

4. M. Gavrilas, B. T. Mattingly, M.J. Driscoll, 1997, "WGOTHIC Noding and Parametric Studies of a Passively-Cooled Small Rating PWR Containment," Proceedings of the International Topical Meeting on Advanced Reactors Safety, Volume I, Orlando, Florida, June 1-5, 1997, pp. 549 - 560.

5. H. Holzbauer, L. Wolf, 1994, "GOTHIC Verification on Behalf of HDR-Hydrogen Mixing Experiments," International Conference on New Trends in Nuclear System Thermohydraulics, Volume II, pp. 331-340., Pisa, Italy, May 30th - June 2nd, 1994

6. T. Hirose, 1993, Letter, floppy disk which contains the M-4-3 test data, an attached document, and a video-cassette, NUPEC Nuclear Power Engineering Corporation, ISP35-035, 30 April, 1993

7. K. K. Mun, 1996, "Modeling of HDR Experiment E11.2 with the Distributed Parameter Feature of the GOTHIC - Code," M.S. Scholar's Paper, University of Maryland at College Park, September 1996

8. J. S. Narula, J. Woodcock, 1994, "Westinghouse - GOTHIC Distributed Parameter Modeling of HDR Test E11.2," The Third International Conference on Containment Design and Operation, Volume 1, Toronto, Canada, October 19 - 21, 1994

9. NEA/CSNI/R(94)29: Final Comparison Report on ISP-35: NUPEC Hydrogen Mixing and Distribution Test (Test M-7-1), Committee on the Safety of Nuclear Installations OECD Nuclear Energy Agency, December 1994

10. R. P. Ofstun, J. Woodcock, D. L. Paulsen, 1994, "Westinghouse - GOTHIC Modeling of HDR NUPEC'S Hydrogen Mixing and Distribution Test M-4-3," The Third International Conference on Containment Design and Operation, Volume 1, Toronto, Canada, October 19 - 21, 1994

11. P. Royl, Breitung, J.R. Travis, H. Wilkening, L. Seyffarth, 1977, "Simulation of Hydrogen Transport with Mitigation Using the 3D Field Code Gasflow," Proceedings of the International Topical Meeting on Advanced Reactors Safety, Volume I, Orlando, Florida, June 1-5, 1997, pp. 578 - 588.

12. L. Wolf, H. Holzbauer, T. Cron, 1994a, "Detailed Assessment of the HDR-Hydrogen Mixing Experiments E11," International Conference on New Trends in Nuclear System Thermohydraulics, Volume II, pp. 91-103., Pisa, Italy, May 30th - June 2nd, 1994

13. L. Wolf, H. Holzbauer, M. Schall, 1994b, "Comparisons Between Multi-dimensional and Lumped Parameter GOTHIC Containment Analyses with Data", International Conference on New Trends in Nuclear System Thermohydraulics, Volume II, pp. 321-330., Pisa, Italy, May 30th - June 2nd, 1994

14. L. Wolf, M. Gavrilas, K. Mun, 1996, "Overview of Experimental Results for Long-Term Large-Scale Natural Circulations in LWR-containments after Large LOCAS," DOE - Project, Order Number: DE - AP07 - 96ID10765, University of Maryland at College Park, July 1996

Appendix 9.D

Basis for Assuming Homogeneous Bulk Conditions for AP600 and AP1000Containment Pressure Design Basis Analysis

TABLE OF CONTENTS

LIST OF TABLES

LIST OF FIGURES

9.D.1 INTRODUCTION

During the blowdown phase of a DECLG LOCA, forced jet momentum from the break source provides vigorous mixing of steam and air inside containment. The jet momentum helps establish homogeneous conditions within a few seconds (Reference 9.D-12, Section 10.2.1.5). Consequently, treating the containment as homogeneous or well-mixed during the blowdown phase is appropriate.

After the blowdown phase, however, the physical processes are different. The forced jet momentum quickly decreases and actually ceases for a brief period during the refill phase before the break source reestablishes itself as a buoyant plume. Although the forced jet momentum ceases during the refill phase of a DECLG LOCA, wall boundary layers are quickly established, on the order of seconds (see Reference 9.D-12, Section 4.8) and according to work by Hartley, quasi-isotropic turbulence resulting from the jet momentum continues mixing enclosed volumes for some time after the source jet ceases. The turbulent wall boundary layers provide entrainment of the bulk region inside containment and hence contribute to mixing of the containment atmosphere as well.

This appendix addresses the buoyant plume, wall boundary layers, and enclosure test data as they relate to mixing inside containment during the post-blowdown time period during a DECLG LOCA.

9.D.2 APPROACH

Thermal and concentration gradients in the horizontal direction, including the boundary layer next to the shell, are addressed using results of 1) theoretical, or first principles, calculations 2) LST temperature/concentration data, and 3) separate effects enclosure test data. The wall boundary layer steam concentration profile is examined using turbulent boundary layer models. Entrainment and boundary layer profile calculations are used to estimate the magnitude of the steam concentration in the wall layer and rising plume as compared to the bulk average steam concentration at a given elevation. Test data, where available, are used to support the conclusions.

Horizontal gradients in AP600 and AP1000 during the post-blowdown LOCA periods are addressed for the base case scenario which assumes that the source mass rises from the east steam generator compartment as a buoyant plume, having lost its momentum as it passes around the equipment and structure in the compartment.

The potential magnitude of horizontal gradients are examined in three radial regions: (1) the turbulent buoyant plume (2) the bulk region between the plume and boundary layer and (3) the turbulent boundary layer. The three radial regions are depicted in Figure 9.D-1. This three-region approach is similar to that

suggested by Peterson (Reference 9.D-1). In the region-wise discussions, area fractions are developed and processes which affect horizontal temperature and concentration gradients within each region are described. The test bases for the discussions include the LST, as well as smaller scale separate effects natural convection enclosure tests. The general interaction between the regions via entrainment is then used to summarize how the integral system performs.

9.D.3 REGION 1 HORIZONTAL GRADIENTS ADDRESSED THROUGH TURBULENT BUOYANT PLUME ANALYTICAL MODEL

Referring to Figure 9.D-1, Region 1 is comprised of the rising plume and its entrained flow. In Region 1, the concentration profile within a turbulent buoyant plume is characterized by an exponential (i.e., $e^{-57(r/z)^2}$) profile at any given elevation, with the steam concentration at the boundary of the plume equal to that of the bulk (Region 2). Such a profile is summarized by Blevins (Reference 9.D-2). The turbulent buoyant plume analytical model, based upon Reference 9.D-2, shows that the plume centerline steam concentration at the exit of the plume is within 10 percent (0.04/(1-0.6) = 0.10) (see Section 9.D-7) of the bulk (Region 2), assuming uniform temperature and concentration in Region 2. With the assumption that the buoyant plume develops freely to the dome region, the plume occupies about 10 percent of the cross-sectional area at the top of containment. An axisymmetric round plume with a divergent angle of 7.5 degrees from the exit of the steam generator compartment is assumed. The calculated plume equivalent diameter at the top of containment is 38 feet based on the net exit area of the trapezoidal steam generator compartment opening, the containment radius of 65 feet, and plume height of 121 feet. It is recognized that negatively buoyant plumes may descend from the dome region and limit the free development height of the positively buoyant plume. However, since this phenomenon results in an additional mixing mechanism (i.e., counter-current plume mixing of positively and negatively buoyant plumes), it is conservatively neglected in the simple analytical plume model.

9.D.4 REGION 2 HORIZONTAL GRADIENTS ADDRESSED THROUGH LST TEMPERATURE DATA AND SEPARATE EFFECTS ENCLOSURE TEST DATA

The horizontal gradients in Region 2 can be assessed based on indications from LST temperature data and separate effects enclosure test data and by examining the postulated condition of a non-uniform horizontal gradient.

The LST has been examined for evidence of horizontal gradients outside the wall boundary layer. Time-averaged thermocouple rake data for LST tests in the LOCA configuration at two different steam flows (220.1 at 0.5 lbm/sec; 217.1 at 1.0 lbm/sec) show a near-zero horizontal temperature gradient except above the steam plume and over the distance within one inch of the wall (see Figures 9.D-6 and 9.D-7). Since the

convective processes operating in the bulk gas region mix temperature differences and gas species at about the same rate, the observation that there is no horizontal temperature gradient also shows that there is no horizontal gas concentration gradient, and therefore, no density gradient. The data show that all of the measurable temperature drop in the vessel wall boundary layer occurs between the wall and the thermocouple located one inch away from the wall. This is consistent with boundary layer calculations which indicate that the majority (60 percent) of the gradient occurs within the first 0.25 inch of the 7-inch boundary layer at the LST operating deck level.

LST thermocouple rake data at successive, incremental data collection times, shows evidence of buoyancy forces eliminating horizontal gradients. Data from the thermocouple rake was taken every 90 seconds during the LST matrix tests. The data at some point in time may show that the temperature at a measurement location may deviate less than ten degrees Fahrenheit from the horizontal average. Data at the next time interval indicate that horizontal gradients are not maintained for more than the 90-second data acquisition interval. This is evidence that a perturbation which creates a nonhomogeneous density at a given elevation also creates a local relative density driving force which tends to level out the horizontal density gradient. This is to be expected since gravity will neutralize any gradients that attempt to form, tending to result in a time-averaged flat profile.

Separate effects enclosure test data show that as the Rayleigh number, Ra, increases from 3.5×10^4 to 1×10^6, the circulation mechanism fully transitions to turbulent, and the horizontal gradient becomes primarily concentrated in the thin wall boundary layer (Section 9.C.1.1.2.1, see for example Figure 9.C.1-5). These tests show that at $Ra > 10^6$, the horizontal gradient in the bulk region is nearly zero in two-dimensional enclosures. Data from three-dimensional enclosures suggest that the transition to turbulence may occur at $Ra < 10^6$, due to vortices which affect mixing inside the enclosure by communicating between the front and back walls through the middle of the enclosure. The Rayleigh number between the plume centerline and the cooled wall for both AP600 and AP1000 is 4.2×10^{12} based on a relatively low value of 9°F temperature difference. Therefore, both the AP600 and AP1000 are fully turbulent and would be expected to show little or no horizontal gradient in Region 2.

Negatively buoyant falling plumes have been shown to occur with upper horizontal surfaces cooler than the enclosure and to result in an additional mixing mechanism (Figures 9.C.1-15 and 9.C.1-16) which would further homogenize the containment gases. The presence of plumes of cooler gases descending from the underside of the dome, suggested by the large vertical Grashof number on the order of 2×10^{13}, based on a relatively low temperature difference of 9°F (Section 9.C.1.3.1), are conservatively ignored.

Separate effects enclosure test data span up to Ra equal to 10^9. Numerical studies by Markatos and Pericleous predict that the heat transfer behavior is constant (Nusselt number linearly increases with length) at increasing Ra over many decades up through Ra of 10^{16} (Figure 9.C.1-6), suggesting that increased heat

transfer is primarily a result of thinning of the boundary layer. The implication is that the Nusselt number varies monotonically over that range, and thus no unexpected performance is introduced at higher Ra values.

In a bulk region such as Region 2 in the AP600 or AP1000, while one may not rule out some minor transient horizontal temperature or concentration gradients, a horizontal gradient outside the relatively small volumes occupied by the plume and falling wall layer is difficult to sustain at high Ra number. That is, any postulated deviation from horizontal uniformity would tend to be readily flattened by buoyant forces. Therefore, horizontal gradients may be assumed to occur solely within the plume and wall layer.

9.D.5 REGION 3 HORIZONTAL GRADIENTS ADDRESSED THROUGH TURBULENT BOUNDARY LAYER ANALYTICAL MODEL

Region 3 consists of the negatively buoyant turbulent wall boundary layer. Equations for the velocity, temperature, and air concentration boundary layer profiles are presented in Section 9.D.9. The profiles are based on turbulent boundary layer 1/7 power laws, as used by Eckert and Jackson. More recent work in the area of turbulent boundary layer profiles has led to the refinement of the boundary layer into three or more layers, such as the viscous sublayer, logarithmic-law layer, and outer layer, to attempt to increase accuracy. Such multi-layer models may indeed increase the accuracy; but results show the 1/7 power profile to be reasonable to use for simple calculations.

The results of the boundary layer calculation for the LOCA post-blowdown atmosphere are compared to calculations for the LST in the LOCA configuration, that is, having a diffuser below the steam generator compartment. The LST includes the effects of both temperature and concentration as driving forces for natural convection. Conclusions regarding the thin part of the boundary layer near the wall, over which most of the gradient occurs are consistent with observations of the internal thermocouple rake data from LST.

The normalized steam concentration profile versus normalized distance through the boundary layer is plotted in Figure 9.D-2a. The parameter, C, represents local boundary layer steam concentration, and the subscripted values represent: s for surface, and b for bulk. The normalized value, η, is x/δ, where x is distance from the wall and δ is the boundary layer thickness. From Figure 9.D-2a, it can be seen that the average steam concentration in the boundary layer is only 12.5 percent lower than the steam concentration in the bulk.

The maximum boundary layer thickness has been calculated from the Eckert and Jackson style model to be less than 31 inches at the operating deck level in AP600 (assuming that a turbulent boundary layer exists for the full AP600 containment height). From the calculated profile, it is found that 60 percent of the change from bulk to wall conditions occurs over the first 2½ percent of the boundary layer, or over less than the first

inch in AP600. Furthermore, these boundary layer calculations conservatively overpredict wall layer thickness due to neglecting the effects of suction at the boundary (velocity normal toward the wall due to condensation). The boundary layer occupies less than 9 percent of the AP600 cross-sectional area at the operating deck elevation, based on the boundary layer thickness calculations and the AP600 containment radius of 65 feet. The region of significant concentration difference occupies less than 0.5 percent of the AP600 and AP1000 cross-sectional area.

9.D.6 COMPOSITE REGION DISCUSSION

Referring to Figure 9.D-1, Region 1 is comprised of the rising plume and its entrained flow; Region 2 is the bulk region of low velocity and nearly zero horizontal temperature/concentration gradient; and Region 3 is the falling turbulent wall boundary layer and its entrained flow.

Region 1 occupies about 10 percent of the cross-section at the top, and Region 3 occupies about 9 percent of the cross-section at the bottom, the maximum cross-section for each. Thus, it is reasonable to neglect momentum-related interaction between the rising plume and the falling wall layer in simple first principles calculations. Since the plume occupies about 10 percent of the cross-sectional area at the top, and even less at lower elevations, as a first approximation the effects of the enclosure walls and dome on plume entrainment over the plume height is neglected. Similarly, with the even smaller area occupied by the falling wall layer, the effects of the enclosure are neglected when calculating wall boundary layer entrainment rates.

At a given instant in time, the rising plume of Region 1 is supplied to the above-deck volume from the top of the steam generator cavity. Plume entrainment calculations (Section 9.D.8) show that 5 to 14 times the source flow is entrained from Region 2 over the height of a buoyant plume above the operating deck in AP600. Therefore, the plume average steam concentration would be expected to be near that of the bulk by the time it discharges to the top of Region 2. As discussed previously, entrainment is shown to result in a centerline plume steam concentration at the top that is within 10 percent of the bulk average steam concentration.

The flow leaving Region 1 spreads horizontally and feeds Region 2 at the top. Since higher order mixing mechanisms have been neglected, by continuity, the vertical flow velocity at the top of Region 2 is a low velocity net downward flow with a steam concentration reduced by condensation and heat transfer on the dome to a value lower than the steam concentration discharged from Region 1.

In Region 3, condensation develops a liquid film over the full height of the containment shell and a negatively buoyant gas boundary layer that grows with distance down the shell. Noting that at quasi-steady conditions, the volumetric condensation rate on the wall is just equal to the source flow rate, Q_o, wall

boundary layer entrainment calculations (Section 9.D.8) show that the volume of steam condensed on the shell is only 1/6 to 1/13 of the volumetric flow rate of gas entrained into the falling wall layer. Such large entrainment rates relative to the condensation rate suggest that the average steam concentration exiting Region 3 would be near the bulk steam concentration of Region 2. These results are consistent with wall boundary layer profile calculations, discussed previously, which show that the average steam concentration through the boundary layer is only 12.5 percent below the steam concentration in the bulk.

Because global, or large-scale, circulation through the operating deck reduces stratification in the above-deck region (Section 9.C.1.4.2.4), global circulation through the operating deck is conservatively neglected for this discussion. By continuity, the flow exiting the bottom of Region 3 spreads out over the operating deck area, rising in Region 2 with a low net upward velocity and with the same steam concentration as the exit flow of Region 3. Because the top of Region 2 is fed by the plume and the bottom of Region 2 is fed by the wall layer, Region 2 will have a higher steam concentration at the top than at the bottom (neglecting negatively buoyant plumes in the dome region).

In this simplified model, as one moves from the top down in Region 2, entrainment into both the plume and the wall layer on either side of Region 2 steadily reduces the downward flow; similarly the upward flow from the bottom is reduced as one moves upward from the operating deck. There is, therefore, a neutral plane in Region 2 where the vertical velocity approaches zero.

A simplified representation summarizing horizontal gradients through the three regions, consistent with the above discussion, is shown in Figure 9.D-2b.

9.D.7 TURBULENT BUOYANT PLUME ANALYTICAL MODEL - SPECIES CONCENTRATION

This section addresses the assumptions, methodology, equations, and results for the turbulent buoyant plume analytical model - species concentration.

9.D.7.1 TIME PERIOD OF APPLICATION

The turbulent buoyant plume analytical model is applicable in the post-refill phase (when break flow into containment is re-established) and beyond, as shown in Figure 9.D-3.

9.D.7.2 NOMENCLATURE (SEE FIGURE 9.D-4)

u	=	velocity in plume
C	=	concentration of air in plume
T	=	temperature in plume
u_∞	=	bulk velocity
C_∞	=	bulk air concentration
T_∞	=	bulk temperature
C_{cl}	=	plume centerline air concentration

Subscripts:

∞	=	bulk
o	=	source
CL	=	centerline

9.D.7.3 MAJOR ASSUMPTIONS

1. Plume is turbulent and buoyant (i.e., density inside plume is less than the bulk region, Region 2).

2. Plume is not confined by wall surfaces or descending negatively buoyant plumes. It freely develops until it reaches dome region. It is recognized that descending negatively buoyant plumes may be generated in the dome region, and may limit the development height of the positively buoyant plume generated at the outlet of the steam generator compartment. However, the interaction of the positively and negatively buoyant plumes further enhances mixing, and therefore, this potential phenomenon is neglected in this simple analytical model.

3. Bulk conditions are uniform (i.e., homogeneous reservoir)

4. Plume is axisymmetric/round

9.D.7.4 SOLUTION

The analytical solution to the turbulent, buoyant plume model with the above assumptions is already known, and the results are summarized in Table 9.D-1 (Reference 9.D-5, Table 9-7 - Turbulent Plumes in Constant Density Reservoirs).

9.D.7.5 APPLICATION OF TURBULENT BUOYANT PLUME RESULTS TO LST/AP600

Applying the plume centerline species concentration analytical solution, an expression for plume centerline air concentration, C_{CL} is obtained. (Note that C replaces T, and z replaces x from Table 9-7 of Reference 9.D-5)

$$C_{CL} = C_\infty - 11(Q_o \Delta C_o)\, B^{-1/3}\, z^{-5/3}$$

$$B = gQ_o\left(\frac{\rho_\infty\ \rho_{stm}}{\rho_\infty}\right) = \text{BuoyancyFlux}$$

where:

ΔC	=	Difference in concentration of air in plume and ambient
Q_0	=	Volumetric flow rate of source

Applying the above expression to LST Test 213.1B and AP600 at the same total pressure (i.e., 29.8 psia) and air concentration (i.e., 0.60), the air concentration values near the top of containment can be obtained:

For LST Test 213.1B:

$p_\infty = 29.8$ psia, $p_{air} = 17.9$ psia, $p_{stm} = 11.9$ psia, $T_\infty = 218°F$, $z = 13.2$ ft

$C_\infty = p_{air}/p_\infty = 0.60$, $\rho_{stm} = 0.03$ lbm/ft^3, $\rho_{air} = 0.073$ lbm/ft^3, $\rho_{stm,0} = 0.067$ lbm/ft^3

$$Q_o = \frac{\dot{m}_o}{\rho_{stm,0}} = \frac{0.54\ \text{lbm/sec}}{0.067\ \text{lbm/ft}^3} = 8\ \text{ft}^3/\text{sec}$$

$B = 32.2 \times 8 \times 0.35 = 90.2$

$$\frac{\rho_\infty - \rho_{stm,0}}{\rho_\infty} = 0.35$$

where:

$$\rho_\infty = \rho_{air} + \rho_{stm}$$

$\Delta C_o = C_\infty - 0 = 0.60$

$\Delta C = C_\infty \times 11 \times 8 \times (90.2)^{-1/3} \times (13.2)^{-5/3} = 0.16$

For AP600: (assuming the same bulk air concentration as LST 213.1)

$p_\infty = 29.8$ psia, $p_{air} = 17.9$ psia, $p_{stm} = 11.9$ psia, $T_\infty = 202°F$, $z = 110$ ft

$C_\infty = p_{air}/p_\infty = 0.60$, $\rho_{stm,0} = 0.0723$ lbm/ft^3

$$Q_o = \frac{\dot{m}_o}{\rho_{stm,0}} = \frac{15.4 \text{ lbm/sec}}{0.0723 \text{ lbm/ft}^3} = 213 \text{ ft}^3/\text{sec}$$

$B = 32.2 \times 211 \times 0.305 = 2072$

$$\frac{\rho_\infty - \rho_{stm,0}}{\rho_\infty} = 0.305$$

$\Delta C = 0.60 \times 11 \times 213 \times (2072)^{-1/3} \times (110)^{-5/3} = 0.04$

Air Concentration, C_{CL} at the Top Centerline of Buoyant Plume								
	Pressure (atm)	$\frac{\rho_\infty - \rho_{stm,0}}{\rho_\infty}$	**Q_o (ft^3/sec)**	**C_∞**	**z (ft)**	**B (ft^4/sec^3)**	**ΔC**	**C_{CL}**
LST	2	0.35	8	0.60	13.2	90.2	0.16	0.44
AP600	2	0.305	213	0.60	110	2072	0.04	0.56

9.D.7.6 TURBULENT BUOYANT PLUME CONCLUSIONS

1. AP600 turbulent buoyant plume should provide better dilution of steam compared to LST due to the increased height above the source in AP600, and the $z^{-5/3}$ dependence for mixing/entrainment.

2. Based on the assumption of a well-mixed Region 2, the centerline concentration in the plume is close to ambient conditions for both AP600 and LST near the top of containment. Due to turbulent mixing, the average concentration in the plume should be even closer to the Region 2 bulk conditions.

9.D.8 ENTRAINMENT INTO THE BREAK PLUME AND WALL LAYER, AND THE EFFECT ON MASS TRANSFER RATE

The purpose of this calculation is to determine the volumetric entrainment rate into the break plume and into the negatively buoyant wall layer in AP600 containment during a large LOCA. The plume and buoyant wall layer entrainment models recommended by Peterson for mixing in large stratified volumes are used. The entrainment rates are used to calculate the dilution of the plume and buoyant layer to get the steam/air concentrations at the top (dome) and bottom (deck elevation) of containment. With the steam/air concentrations, the effect on the mass transfer rate in the dome region and at the operating deck level is determined.

9.D.8.1 TIME PERIOD OF APPLICATION

The entrainment models for the buoyant plume are applicable in the post-refill period and beyond and models for the wall boundary layers are applicable to the post blowdown period and beyond, as shown in Figure 9.D-3.

9.D.8.2 KEY ASSUMPTIONS

- Bulk fluid (Region 2) is at a constant density

9.D.8.3 ENTRAINMENT INTO A BUOYANT PLUME

The volumetric flow rate entrained is:

$$Q_{ent} = 0.15 B^{1/3} Z^{5/3}$$

where:
- Z = 108 ft, the height of the plume (conservatively low value of height from steam generator cavity outlet to dome)
- B = $g\, Q_o(\rho_{amb} - \rho_o)/\rho_{amb}$, the buoyancy
- Q_o = the break steam volumetric flow rate
- ρ_o = the break steam density (assumed to be the saturation density at the total pressure)
- ρ_{amb} = density of the ambient gas, the same density as the entrained gas, ρ_{ent}

It is convenient to define the plume entrainment ratio:

$$r_p \equiv Q_{ent}/Q_o = 0.15\, g^{1/3} (\Delta\rho/\rho)^{1/3} Z^{5/3} Q_o^{-2/3}$$

For entrainment into the plume, conservation of mass $\dot{m}_{out} = \dot{m}_{ent} + \dot{m}_o$ with $\dot{m} = Q\rho$, gives $Q_{out}\rho_{out} = Q_{ent}\rho_{ent} + Q_o\rho_o$. Conservation of mass for each species produces the relationships $Q_{out}\rho_{s,out} = Q_{ent}\rho_{s,ent} + Q_o\rho_{s,o}$ and $Q_{out}\rho_{a,out} = Q_{ent}\rho_{a,ent}$, where the s and a subscripts indicate the partial densities of the steam and air. With partial density and pressure $\rho_i = P_i/R_iT$, so mass conservation for each species becomes $Q_{out}P_{s,out}/T_{out} = Q_{ent}P_{s,ent}/T_{ent} + Q_oP_{s,o}/T_o$ and $Q_{out}P_{a,out}/T_{out} = Q_{ent}P_{a,ent}/T_{ent}$. Since the absolute temperature does not differ significantly throughout the system, the species equations can be approximated as $Q_{out}P_{s,out} = Q_{ent}P_{s,ent} + Q_oP_{s,o}$ and $Q_{out}P_{a,out} = Q_{ent}P_{a,ent}$. Note that the entrained flow is several times larger than the source flow, so the effect of the higher source temperature is not very significant. These latter equations permit the calculation of the steam and air concentration at the outlet of the plume.

Conservation of mass on a molar basis $\dot{n}_{out} = \dot{n}_{ent} + \dot{n}_o$. With $\dot{n} = \hat{\rho}uA$, $\hat{\rho} = P/RT$, and $Q = uA$, conservation of moles can be written $P_{out}Q_{out}/RT_{out} = P_{ent}Q_{ent}/RT_{ent} + P_oQ_o/RT_o$. Since the total pressure, P is the same for each, and the absolute temperature T only differs by a small amount, conservation of mass on a molar basis can be approximated as $Q_{out} = Q_{ent} + Q_o$.

With conservation of mass in terms of steam partial pressure, $P_{s,out} = (Q_{ent}P_{s,ent} + Q_oP_{s,o})/Q_{out}$, and $Q_{out} = Q_{ent} + Q_o$, the outlet steam partial pressure is $P_{s,out} = (Q_{ent}P_{s,ent} + Q_oP_{s,o})/(Q_{ent} + Q_o)$. Written in terms of the plume entrainment ratio r_p, $P_{s,out} = (r_pP_{s,ent} + P_{s,o})/(r_p + 1)$.

where:

$\dot{m}$	=	mass flow rate
$\dot{n}$	=	molar flow rate
$\hat{\rho}$	=	molar density
Q	=	volumetric flow rate
ρ	=	mass density
R	=	gas constant
T	=	absolute temperature

Subscripts:

a	=	air
s	=	steam
ent	=	entrained
out	=	outlet

o	=	source
stm	=	steam
bl	=	boundary layer

Values for densities and break flow rates at different times using values representative of post-refill and peak pressure are as follows:

		90 sec	1200 sec	units
ρ_{amb}	=	0.13584	0.16325	lbm/ft^3
ρ_o	=	0.10487	0.13373	lbm/ft^3
$P_{s,o}$	=	46	60	psia
$P_{s,ent}$	=	26.94	40.30	psia
$(\rho_{amb}- \rho_o)/\rho_{amb}$	=	0.2280	0.1808	
$\dot{m}_{g,brk,o}$	=	200	45	lbm/sec
$Q_0 = \dot{m}_{g,brk,o}/\rho_o$	=	1907	336.5	ft^3/sec
$B = g\, Q_o(\rho_{amb} - \rho_o)/\rho_{amb}$	=	14,000	1959	ft^4/sec^3
$Q_{ent} = 0.15\, B^{1/3}\, Z^{5/3}$	=	8855	4597	ft^3/sec
r_p	=	4.64	13.66	
$P_{s,out} = (r_p P_{s,ent} + P_{s,o})/(r_p + 1)$	=	30.32	41.64	psia

Solving the equations for AP600 at 90 seconds and at the time of peak pressure (1200 sec.) results in the following:

Steam Partial Pressure at Top of AP600 Plume from Entrainment Relations

Time sec	$\Delta\rho/\rho$	Q_o ft^3/sec	Q_{ent} ft^3/sec	r_p	$P_{stm,top}$ psia
90	0.2280	1,907	8,855	4.6	30.3
1200	0.1808	336.5	4,597	14	41.6

9.D.8.4 ENTRAINMENT INTO A NEGATIVELY BUOYANT WALL LAYER

The volumetric flow rate entrained is:

$$Q_{ent} = \frac{0.0979 \nu Gr_z^{2/5} p_{wall}}{(1 + 0.494 Pr^{2/3})^{2/5} Pr^{8/15}}$$

where:

Z	=	121 ft, the height of the wall (deck to dome)
Gr_z	=	$g(\rho_{amb}-\rho_w)Z^3/(\rho_{amb}\nu^2)$, the Grashof number
Pr	=	the Prandtl number of the boundary layer
δ	=	boundary layer thickness
ν	=	μ/ρ, the boundary layer kinematic viscosity based on the average of bulk and surface values of dynamic viscosity and density
p_{wall}	=	the wall perimeter (πD) = 408.4 ft
ρ_w	=	the total gas density adjacent to the liquid film surface
ρ_{amb}	=	the density of the ambient gas, the same density as the entrained gas, ρ_{ent}
V	=	volume

It is convenient to define the boundary layer entrainment ratio in terms of the entrained and condensed volumetric flow rates:

$$r_{bl} \equiv Q_{ent}/Q_{cond}$$

For entrainment into the boundary layer, the equations for conservation of mass $\dot{m}_{out} = \dot{m}_{ent} - \dot{m}_{cond}$, and on a molar basis $\dot{n}_{out} = \dot{n}_{ent} - \dot{n}_{cond}$ can be developed as was done for the plume. The results are the important relationships for the steam partial pressure at the outlet of the wall layer:

for volumetric flow $Q_{out} = Q_{ent} - Q_{cond}$, the outlet steam partial pressure is $P_{s,out} = (Q_{ent}P_{s,ent} - Q_{cond}P_{s,cond})/(Q_{ent} - Q_{cond})$. In terms of the plume entrainment ratio r_p, $P_{s,out} = (r_pP_{s,ent} - P_{s,o})/(r_p - 1)$.

Values for densities and break flow rates at different times using representative values for post-refill (90 sec) and peak pressure (1200 sec) are as follows:

		90 sec	1200 sec	units
ρ_{amb}	=	0.13584	0.16325	lbm/ft^3
ρ_w	=	0.19020	0.20229	lbm/ft^3
ρ_{cond}	=	0.10487	0.13373	lbm/ft^3
$P_{s,cond}$	=	46	60	psia
$P_{s,ent}$	=	26.94	40.30	psia
Pr	=	0.81	0.83	
μ	=	1.23×10^{-5}	1.24×10^{-5}	lbm/sec-ft
ρ	=	0.16302	0.18277	lbm/ft^3
$\nu = \mu/\rho$	=	7.55×10^{-5}	6.78×10^{-5}	ft^2/sec
$(\rho_w - \rho_{amb})/\rho_{amb}$	=	0.4001	0.2391	
$Gr_z = g(\rho_w-\rho_{amb})Z^3/(\rho_{amb}\nu^2)$	=	4.00×10^{15}	2.97×10^{15}	
$1 + 0.494\ Pr^{2/3}$	=	1.4293	1.4363	

Q_{ent}	=	5098	4004	ft^3/sec
$\dot{m}_{cond} = \dot{m}_{g,brk,o}\ \pi_{m,es}$	=	85	40.5	lbm/sec
$Q_{cond} = \dot{m}_{cond}/\rho_{cond}$	=	810.5	302.8	ft^3/sec
$r_{bl} = Q_{ent}/Q_{cond}$	=	6.29	13.22	
$P_{s,out} = (r_{bl}P_{s,ent}-P_{s,cond})/(r_{bl}-1)$	=	23.34	38.69	psia

Summary Tables:

Time, sec	P_{total} psia	$P_{s,amb}$ psia	υ ft^2/sec	$\Delta\rho/\rho$	Gr_z	Pr	Q_{cond} ft^3/sec
90	46	26.9	$7.55x10^{-5}$	0.4004	$4.00x10^{15}$	0.81	810.5
1200	60	40.3	$6.78x10^{-5}$	0.2391	$2.98x10^{15}$	0.83	302.8

Time, sec	Q_{ent} ft^3/sec	r_{bl}	$P_{s,bot}$ psia	δ_{bl} ft	V_{bl} ft^3
90	5098	6.3	23.34	2.2	63,200
1200	4004	13.221	38.69	2.3	65,500

9.D.8.5 EFFECT OF ENTRAINMENT ON MASS TRANSFER RATE

The condensation heat flux for given total pressure, steam partial pressure, and bulk-to-surface temperature difference is determined and used to calculate the influence of the concentration differences.

Representative bulk-to-surface temperature differences are:

		90 sec	1200 sec
T_{bulk}	=	244.2	267.7 °F
T_{surf}	=	165.1	232.2 °F
$\Delta T = (T_{bulk} - T_{surf})$	=	79.1	45.5 °F

The refill time phase, from 30 to 90 sec., has no source, but does have a wall layer. Refill is represented by its end state that is assumed to have the same conditions as calculated at 90 sec, except that without a plume the steam partial pressure and heat flux at the top is the same as the ambient bulk conditions.

The steam partial pressure values at the top, middle, and bottom correspond to the steam partial pressure out of the plume, the bulk steam partial pressure, and the steam partial pressure out of the wall layer.

The average heat flux is a simple, unbiased average of the top, middle, and bottom values, that is $\bar{q} = \dot{q}_{top}/4 + \dot{q}_{amb}/2 + \dot{q}_{bot}/4$.

Summary of Mass Transfer Effects Due to Vertical Concentration Gradients									
Time sec	**P_{total} psia**	**ΔT °F**	**$P_{stm,top}$ psia**	**$P_{stm,amb}$ psia**	**$P_{stm,bot}$ psia**	**$\dot{q}_{top}$ B/sec-ft²**	**$\dot{q}_{amb}$ B/sec-ft²**	**$\dot{q}_{bot}$ B/sec-ft²**	**$\bar{q}$ Average B/sec-ft²**
refill	46	79	26.9	26.9	23.3	1.85	1.85	1.4	1.74
90	46	79	30.3	26.9	23.3	2.25	1.85	1.4	1.84
1200	60	43	41.6	40.3	38.7	1.5	1.4	1.3	1.4

The results in this table show that the upper estimates of vertical concentration differences in AP600 result in a 6 percent reduction on the net heat transfer to the shell during refill and less than 1 percent effect on net heat transfer during the 90 to 1200 sec time period.

9.D.8.6 BOUNDARY LAYER THICKNESS AND VOLUME

The thickness of the negatively buoyant wall layer can be calculated from the integral equations presented by Peterson (Reference 9.D-1).

$$\delta_{bl} = \frac{0.565(1+0.494\,Pr^{2/3})^{1/10} z}{Gr_z^{1/10} Pr^{8/15}}$$

The equation can also be integrated over its height, with the simplifying assumption that all properties are constant over the height, Z. This assumption is reasonable since the Prandtl number only changes a few percent over the range of conditions inside containment, and the only other parameters are contained in the term $\Delta\rho/(\rho v^2)$ which is estimated to change less than a factor of 2 over height, and when raised to the 1/10 power has only a 7 percent effect. Consequently, the product of the integral and the circumference gives a reasonable estimate of the boundary layer volume that can be used with the entrainment rate to estimate boundary layer transit times, or fill time.

The product of the circumference and the integral of the equation above is;

$$V_{bl} = \frac{0.565(1+0.494\,Pr^{2/3})^{1/10}(\nu^2/g)^{1/10}\pi D}{(\Delta\rho/\rho)^{1/10}Pr^{8/15}} \int_0^H z^{0.7}\,dz$$

$$= \frac{0.565\pi}{1.7} \frac{(1+0.494\,Pr^{2/3})^{1/10}(\nu^2/g)^{1/10}DH^{1.7}}{(\Delta\rho/\rho)^{1/10}Pr^{8/15}}$$

Evaluating this equation with the values from Section 9.D.8.3;

		90 sec	1200 sec	units
Pr	=	0.81	0.83	
ν	=	7.55×10^{-5}	6.78×10^{-5}	ft^2/sec
$(\rho_w - \rho_{amb})/\rho_{amb}$	=	0.4001	0.2391	
$1 + 0.494\ Pr^{2/3}$	=	1.4293	1.4363	
V (Equation 4)	=	63436	64553	ft^3

Summary Table:

AP600 Boundary Layer Volume and Fill Times			
Time, sec	V, ft^3	Q_{ent}, ft^3/sec	Boundary Layer Fill Time, sec V/Q_{ent}
90	63436	5098	12.4
1200	64553	4004	16.1

9.D.8.7 SUBLAYER PENETRATION TIME

A measure of the response time of the boundary layer temperature to a change in the environment is the sublayer penetration time. This represents the time it takes for steam to diffuse through the laminar sublayer, where most of the mass transfer resistance is located. The transient diffusion equation:

$$\frac{\partial \hat{\rho}}{\partial t} = D_v \frac{\partial^2 \hat{\rho}}{\partial y^2} \quad \text{becomes} \quad \frac{\delta_m^2}{D_v \tau} \frac{\partial \hat{\rho}^*}{\partial t^*} = \frac{\partial^2 \hat{\rho}^*}{\partial y^{*2}}$$

with the substitutions:

$$\hat{\rho} = \hat{\rho}_\infty \hat{\rho}^* \qquad y = \delta_m y^* \qquad t = \tau t^*$$

where:

$\hat{\rho}$	=	molar density
t	=	time
y	=	distance along the normal to the surface
δ_m	=	boundary layer thickness
D_v	=	air-steam gas diffusion coefficient
τ	=	time constant
∞	=	value at a large distance from surface
*	=	dimensionless variable

If the time constant is defined $\tau = \delta_m^2/D_v$, the coefficient on the left side of the dimensionless equation = 1, as required. The mass transfer sublayer thickness, δ_m, is related to the heat transfer sublayer thickness, δ_h, by $Nu/Sh = (Pr/Sc)^{1/3}$. The heat transfer sublayer thickness is $\delta_h = h/k$. Other assumed values are:

		90 sec.	1200 sec.	units
h	=	2.61	2.51	B/hr-ft^2-F
k	=	0.0164	0.0173	B/hr-ft-F
D_v	=	0.537	0.464	ft^2/hr
Pr	=	0.81	0.83	
Sc	=	0.51	0.51	
$\delta_h = h/k$	=	0.0063	0.0069	ft
$\delta_m = \delta_h(Pr/Sc)^{1/3}$	=	0.0073	0.0081	ft
$\tau = \delta_m^2/D_v$	=	0.357	0.509	sec

Consequently, the sublayer penetration time is on the order of 1 sec or less. This is very rapid in comparison to the structure time constants that are on the order of 100 sec, and the system pressurization time constant that is on the order of 1000 sec. Even the boundary layer fill time of 16 sec is short compared to both the structure and pressure time constants.

9.D.9 TURBULENT BOUNDARY LAYER ANALYTICAL MODEL

This section addresses the assumptions, methodology, equations, and results for the turbulent boundary layer analytical model. The analytical model is not intended to be an independent verification of LST, rather, it is used to estimate boundary layer thickness and temperature/concentration profiles for AP600 containment and LST. Measured thermal/concentration boundary conditions from LST tests 217.1 and 220.1 are applied in the analytical model since these represent realistic conditions to apply to the boundary layer model.

9.D.9.1 TIME PERIOD OF APPLICATION

The turbulent boundary layer analytical model (Figure 9.D-4) applies to the time period when quasi-steady conditions are established inside containment. The time period of applicability is shown in Figure 9.D-3.

9.D.9.2 KEY ASSUMPTIONS

- Surface is vertical flat plate
  - Containment shell radius of curvature is large so it can be treated locally as a flat plate.

- Velocity, temperature, concentration boundary layer profile is turbulent
  - This is appropriate since boundary layer is turbulent within a few feet of the top of the containment shell.

- Bulk (Region 2) fluid velocity $\cong 0$
  - This is true after blowdown period since the break source transitions from jet to buoyant plume and bulk containment area is large relative to plume/boundary layer.

- Condensate film is impermeable to noncondensible gases.
  - This is conservative since absorption by the film removes air from containment volume which enhances heat/mass transfer of steam.

- Condensate film is stationary relative to gas boundary layer.
  - This is appropriate since condensate film velocity is smaller than gas boundary layer velocity, and conservative because a moving film enhances heat transfer.

- Suction effect at wall is neglected.
  - This is conservative because suction thins the boundary layer.

- Thermal boundary layer thickness is the same as concentration boundary layer thickness.
  - This is appropriate since $Le^{1/3} = \left(\frac{Pr}{Sc}\right)^{1/3} \sim 1.0$.

- Saturation conditions exist at film surface.
  - This is appropriate since steam is condensing at the film surface.

- Bulk fluid (Region 2) temperature is uniform above the break source elevation.
  - Refer to LST test 217.1 and 220.1 temperature profiles in (Figures 9.D-6 and 9.D-7).

- Bulk fluid (Region 2) concentration is uniform above the break source elevation.

- Surface Temperature is approximately constant for purposes of applying the simple analytical model.

- Wall heat flux is modeled as forced convection using equations from Reference 9.D-6.

9.D.9.3 BOUNDARY LAYER PROFILES

The boundary layer profiles, used by Eckert and Jackson, are based on experimental data for turbulent boundary layers:

- Boundary Layer Velocity Profile (Reference 9.D-7, Equation 24)

$$u = U(1-\eta)^4\eta^{\frac{1}{7}} \text{ where } \eta=\frac{r}{\delta}$$

where:

u	=	local velocity in boundary layer
δ	=	boundary layer thickness
r	=	coordinate direction normal to condensing surface

- Boundary Layer Temperature Profile (Reference 9.D-7, Equation. 25)

$$T - T_\infty = (T_{surf} - T_\infty)\left(1-\eta^{\frac{1}{7}}\right)$$

where:

T = temperature

- Boundary Layer Air Concentration Profile

$$C - C_\infty = (C_{surf} - C_\infty)\left(1 - \eta^{\frac{1}{7}}\right)$$

where:

C = air concentration

- Boundary Layer Thickness (Reference 9.D-8, Equation. 10.121b)

$$\delta = Bz^n$$

where:

B, n are constants to be determined

- Maximum Velocity in Boundary Layer (Reference 9.D-8, Equation. 10.121a)

$$U = Az^m$$

A, m are constants to be determined

9.D.9.4 GOVERNING EQUATIONS

- Momentum Equation

$$\frac{d\left[\int_0^\delta u\ (T - T_\infty)dr\right]}{dz} = g\int_0^\delta \beta\ (T - T_\infty)\ dr - \frac{\tau_w}{\rho}$$

where:

τ_w = shear stress at condensing surface
β = volumetric thermal expansion coefficient
ρ = bulk density
g = local gravitation acceleration

- Energy Equation

$$\frac{d\left[\int_0^{\delta} u\,(T - T_\infty)dr\right]}{dz} = \frac{q''_w}{\rho C_p}$$

where:

C_p = specific heat at constant pressure
q''_w = wall heat flux

- Conservation of Mass Equation

Not used in this calculation since we are not calculating entrainment volumes/rates, but rather, temperature/concentration profiles.

- Boundary Conditions

Thermal and concentration boundary conditions are from LST tests are applied at the shell surface and in bulk (Region 2) locations because the boundary conditions are expected to be representative of AP600.

9.D.9.5 BOUNDARY LAYER MOMENTUM EQUATION DEVELOPMENT

Wall shear stress in the momentum equation is modeled using a correlation for forced turbulent convection. Eckert and Jackson argue the τ_w is similar to forced convection in the near surface region and can be represented as follows:

$$\frac{\tau_w}{\rho U^2} = 0.0225\left[\frac{U\delta}{\nu}\right]^{\frac{-1}{4}}$$

where:

ν = kinematic viscosity

$$\tau_w = 0.0225\rho U^2\left(\frac{\nu}{U\delta}\right)^{\frac{1}{4}}$$

where:

U = is a characteristic velocity interpreted by Eckert and Jackson as the maximum velocity in boundary layer.

The integral momentum equation then becomes:

$$\frac{d\left[\int_o^\delta u^2 dr\right]}{dz} = g\int_o^\delta \beta(T_\infty - T)dr - 0.0225U^2\left[\frac{\nu}{U\delta}\right]^{\frac{1}{4}}$$

Applying turbulent velocity and thermal boundary layer profiles, it can be shown that:

$$\int_0^\delta u^2\, dr = \delta\int_0^1 \left[U(1-\eta)^4\,\eta^{\frac{1}{7}}\right]^2 d\eta = 0.052315\delta U^2$$

and

$$\int_0^\delta (T_\infty - T)dr = \delta\int_0^1 (T_\infty - T_{surf})(1-\eta^{\frac{1}{7}})d\eta = \frac{\delta}{8}(T_\infty - T_{surf})$$

The boundary layer momentum equation becomes:

$$\frac{d}{dx}(0.052315U^2\delta) = g\beta(T_\infty - T_{surf})\frac{\delta}{8} - 0.0225U^2\left[\frac{\nu}{U\delta}\right]^{\frac{1}{4}}$$

Applying Reynolds Analogy for heat/momentum transfer:

$$\frac{h}{\rho C_p U} = \frac{f_z}{2} E_H$$ (Reference 9.D-7, Equation 5)

where:

f_z = local friction factor $= 0.045\left[\frac{\nu}{U\delta}\right]^{\frac{1}{4}}$ (Reference 9.D-7, Equation 32)

E_H = ratio of turbulent eddy diffusivity of heat to that of momentum

h = heat transfer coefficient

from Colburn Analogy:

$$E_H = Pr^{\frac{-2}{3}}$$ (Reference 9.D-7, Equation 6)

where:

Pr = Prandtl number

Therefore,

$$\frac{h}{\rho C_p U} = \frac{0.045}{2}\left[\frac{\nu}{U\delta}\right]^{\frac{1}{4}} Pr^{\frac{-2}{3}} = 0.0225\left[\frac{\nu}{U\delta}\right]^{\frac{1}{4}} Pr^{\frac{-2}{3}}$$

Now, since

$$q_w'' = \frac{q_w}{A_{surf}} = h(T_\infty - T_w)$$

heat flux can be modeled as follows:

$$\frac{q_w''}{\rho C_p} = 0.0225\left(T_\infty - T_{surf}\right) U\left[\frac{\nu}{U\delta}\right]^{\frac{1}{4}} Pr^{-\frac{2}{3}}$$

where:

A_{surf} = heat transfer surface area

Now,

$$\int_0^{\delta} u(T-T_\infty)dr = \delta\int_0^1 \left[U(1-\eta)^4\ \eta^{\frac{1}{7}}\right](T_\infty - T_{surf})\left(1 - \eta^{\frac{1}{7}}\right)d\eta = 0.036633(T_\infty - T_{surf})\delta U$$

The boundary layer energy equation becomes:

$$\frac{d}{dz}\left[0.03663(T_\infty - T_{surf})\delta U\right] = 0.0225Pr^{-\frac{2}{3}}(T_\infty - T_{surf})U\left[\frac{\nu}{U\delta}\right]^{\frac{1}{4}}$$

Substituting expressions for U and δ into boundary layer momentum and energy equations, differentiating the resulting equations, solve for exponents m and n by matching exponents. This procedure results in m=1/2 and n=7/10 which can also be found in Reference 9.D-8, page 335.

Therefore:

$U = Az^{\frac{1}{2}}$ and $\delta = Bz^{\frac{7}{10}}$

Substituting the expressions for U and δ into boundary layer equations and performing the differentiation, we obtain:

$$\left(\frac{17}{10}\right)\left[0.0252315A^2\right] = 0.125g\beta(T_\infty - T_{surf}) - 0.0225A^{\frac{7}{4}}B^{-\frac{5}{4}}\nu^{1/4}$$

and

$$\left(\frac{6}{5}\right)\left[0.03663A\right]Pr^{\frac{2}{3}} = 0.0225A^{\frac{3}{4}}B^{\frac{-5}{4}}\nu^{\frac{1}{4}}$$

Solving for constants A and B, an expression for boundary layer thickness can be obtained:

$$\delta = Bz^{\frac{7}{10}} = 0.565z(Gr_z)^{-\frac{1}{10}}(Pr)^{-\frac{8}{15}}\left[1 + 0.494Pr^{\frac{2}{3}}\right]^{-\frac{1}{10}}$$ (Reference 9.D-7, Equation 36)

The above equation agrees with that obtained in Reference 9.D-1, Equation 18.

From the expression for δ, the velocity, thermal and concentration boundary layer profiles can be calculated, where:

$$Gr_z = \frac{g\beta(T_\infty - T_{surf})z^3}{\nu^2}$$ (Reference 9.D-7, Equation 29)

9.D.9.6 BOUNDARY LAYER THICKNESS RESULTS

Rather than calculate Gr_z and δ for a mixture, the calculation is done using air or steam properties to examine the range of possible values.

AP600 Prediction (for thermodynamic properties based on LST test 217.1)

The following parametric values are associated with LST test 217.1 and are used to calculate boundary layer thicknesses below:

LOCATION	T_∞	T_{surf}	Pr (air)	v (air)
E	230°F	188°F	0.70	0.84×10^{-4} ft^2/sec

Based on AIR properties (Reference 9.D-10) and noting $\beta = 1/T$:

$$Gr_z = \frac{32.2\frac{ft}{sec^2}(230°F - 188°F)\left(\frac{1}{690°R}\right)(110ft)^3}{\left(0.84 \times 10^{-4}\frac{ft^2}{sec^2}\right)} = 3.7 \times 10^{14}$$

$$\delta = 0.565\ (110\ ft)\ [3.7 \times 10^{14}]^{-1/10}[0.7]^{-8/15}[1+0.494(0.7)^{2/3}]^{-1/10} = 30.5\ in.$$

Based on STEAM properties:

$$Gr_z = \frac{32.2(230 - 188)\left(\frac{1}{690}\right)(110)^3}{(0.84 \times 10^{-4})} = 3.7 \times 10^{14}$$

$$\delta = 0.565(110 \text{ ft})[3.4x10^{14}]^{-1/10}[1.1]^{-8/15}[1+0.494(1.1)^{2/3}]^{-1/10} = 23.9 \text{ in.}$$

LST Prediction (for thermodynamic properites based upon LST test 217.1)

Based on AIR properties:

$$Gr = \frac{32.2(230-188)\left(\frac{1}{690}\right)(13.2)^3}{(0.84 \times 10^{-4})} = 6.4 \times 10^{11}$$

at Point E in LST:

$$\delta = 0.565 \text{ [13.2 ft]} (6.4 \times 10^{11})^{-1/10} (0.70)^{-8/15} \left[1+0.494 (0.70)^{2/3}\right]^{-1/10} = 6.9 \text{ in.}$$

Based on STEAM properties (Pr = 1.10, $\nu = 0.87 \times 10^{-4}$ ft^2/sec):

$$Gr = \frac{32.2(230 - 188)\left(\frac{1}{690}\right)(13.2)^3}{(0.87 \times 10^{-4})^2} = 5.9 \times 10^{11}$$

at Point E in LST:

$$\delta = 0.565 \text{ [13.2 ft]} (5.9 \times 10^{11})^{-1/10} (1.1)^{-8/15} \left[1+0.494 (1.1)^{2/3}\right]^{-1/10} = 5.4 \text{ in.}$$

The following parametric values are associated with LST Test 220.1 and are used to calculate boundary layer thickness below:

LOCATION	T_∞	T_{surf}	Pr (air)	v (air)
E	200°F	155°F	0.70	1.0×10^{-4} ft²/sec

Based on AIR properties:

$$Gr = \frac{32.2(200-155)\left(\frac{1}{660}\right)(13.2)^3}{(1.0 \times 10^{-4})^2} = 5.0 \times 10^{11}$$

at Point E in LST:

$$\delta = 0.565\ [13.2\ ft]\ (5.0 \times 10^{11})^{-1/10}\ (0.70)^{-8/15}\left[1+0.494\ (0.70)^{2/3}\right]^{-1/10} = 7.1\ in.$$

9.D.9.7 CONCENTRATION PROFILE RESULTS

The concentration profile and integrated average in boundary layer are calculated from the turbulent analytical model for LST. The concentration at the surface is determined from inside surface temperature data and applying saturated conditions near the surface. See Figure 9.D-5 for relative measurement elevations. Radial positions are shown in Figures 9.D-6 and 9.D-7.

LST Test 220.1 P_{total} = 32 psia, $\dot{m}$ = 0.5 lbm/sec

Average LST Boundary Layer Air Concentration Based Upon Measured Bulk and Wall Conditions					
Location	T_{surf} (measured) (°F)	T_∞ (measured) (°F)	C_{surf} (calc)	C_∞ (measured)	$\overline{C}_{BL}$ (calc)
Dome	180	--	0.77	0.34	0.39
A	180	230	0.77	0.44	0.48
B	--	230	--	--	--
C	177	230	0.78	--	0.48
D	--	230	--	--	--
E	155	200	0.87	0.72	0.74

LST Test 217.1 P_{total} = 43 psia, $\dot{m}$ = 1.0 lbm/sec

Average LST Boundary Layer Air Concentration Based Upon Measured Bulk and Wall Conditions					
Location	T_{surf} (measured) (°F)	T_{∞} (measured) (°F)	C_{surf} (calc)	C_{∞} (measured)	$\overline{C}_{BL}$ (calc)
Dome	200	--	0.73	0.33	0.38
A	210	260	0.67	0.35	0.39
B	207	260	0.67	--	0.39
C	205	260	0.70	--	0.395
D	198	260	0.74	--	0.40
E	188	240	0.79	0.67	0.69

Notes:

1. C_{surf} is calculated from applying Dalton's law of partial pressures, assuming saturation conditions exist at the condensing surface, and using measured surface temperatures and total pressure from LST tests.

2. $\overline{C}_{BL}$, which represents the average air concentration in the boundary layer, is calculated from performing an integrated average which results in $\overline{C}_{BL} = (C_{surf} + 7C_{\infty})/8$.

3. Refer to inside wall temperature data (Table 4.8-1 for LST test 217.1 and Figure 4.11-6 for LST test 220.1) in Reference 9.D-11 for surface temperature data.

4. Bulk fluid temperatures shown in the above tables represent spatially-averaged values based upon attached LST time-averaged temperature profiles for LST tests 220.1 and 217.1 at quasi-steady conditions.

9.D.9.8 BOUNDARY LAYER CONCENTRATION PROFILE RESULTS - LST

1. Comparison of C_{∞} and $\overline{C}_{BL}$ shows that the difference in air concentration is small (within 15 percent) in the radial (horizontal) direction for LST. This along with temperature profile data indicate that LST is well-mixed in the radial direction throughout the above-deck region, outside of the relatively thin laminar sublayer.

2. The measured bulk fluid temperature in both horizontal and vertical directions shows little difference (i.e. a few degrees) between the dome region and region D as seen in Figures 9.D-6 and 9.D-7. There is however about 20°F difference in the bulk temperature between regions D and E, for LST test 217.1 and about 30°F difference for LST test 220.1. The data indicate some level of stratification between regions D and E, which is more pronounced in LST test 220.1. Since the LST does not have a flow connection from the simulated SG compartment, there is no global circulation. As a result, the stratification below the source elevation is not surprising.

3. Region E temperature/concentration is notably different than the regions above. This indicates an interface or gradient region exists between the higher temperature, steam-rich upper region (above the plane of the break) fed by the buoyant plume, and the lower temperature, air-rich region fed by the wall boundary layer.

4. Turbulent boundary layer mixing is significant such that boundary layer average properties are nearly at bulk conditions. It is expected that this will be the case for AP600.

9.D.9.9 BOUNDARY LAYER ANALYTICAL MODEL RESULTS - BOUNDARY LAYER THICKNESS

1. The maximum boundary layer thickness calculated from the analytical model for LST turbulent boundary layer ~ 7 inches. (LST 217.1 and 220.1)

2. The maximum total boundary layer thickness calculated from the analytical model for AP600 at similar thermodynamic conditions ~ 31 inches.

3. The calculated boundary layer thicknesses are conservative because suction effects due to steam condensation at the wall were not included. It is well known that suction reduces boundary layer thickness (refer to Schlicting, Boundary Layer Theory). Therefore, actual boundary layers should be thinner than calculated.

4. The boundary layer horizontal profile is rather "flat" due to mixing effects of turbulence. Consequently, most of the horizontal boundary layer gradient is contained in the much smaller region near the condensing surface.

9.D.10 INFLUENCE OF HORIZONTAL GRADIENTS ON MASS TRANSFER COEFFICIENTS

Since only free convection is assumed throughout the design basis containment transients, the velocities calculated in the lumped parameter model are not used in calculating mass transfer rates. Therefore, justification of the approach taken for mass transfer is based on steam concentration gradients.

The horizontal concentration gradients in the post-LOCA containment atmosphere are consistent with the lumped parameter noding and associated mass transfer coefficients used in the WGOTHIC Evaluation Model. The scale of significant concentration gradients near the wall are much less than the 2-foot thick calculation cell (node) used in the WGOTHIC Evaluation Model. Thus, the wall cell is large enough in the radial direction that cell properties can be used to represent the bulk condition for use with boundary layer heat and mass transfer correlations which are described in Reference 9.D-4.

9.D.11 CONCLUSION

The following conclusions apply to the containment atmosphere during the post blowdown period for a DECLG LOCA:

1. The turbulent buoyant plume (Region 1) entrains a significant volume from the bulk (Region 2) such that it is nearly at bulk thermal/concentration conditions in the dome region.

2. Based upon LST data and enclosure test data, the large bulk region (Region 2) is well-mixed horizontally and above the break source elevation, vertically as well.

3. The turbulent wall boundary layers entrain volume from the bulk region such that the average thermal/concentration in the boundary layer is nearly at bulk conditions.

9.D.12 REFERENCES

9.D-1 Peterson, P.F., "Scaling and Analysis of Mixing in Large Stratified Volumes," International Journal of Heat and Mass Transfer, Vol. 37, Suppl. 1, pp 97-106, 1994.

9.D-2 Blevins, "Jets, Plumes, Wakes, and Shear Layer," Applied Fluid Dynamics Handbook, 1984.

9.D-3 WCAP-14407, Rev. 2, "WGOTHIC Application to AP600,"April 1998.

9.D-4 WCAP-14326, Rev. 2, "Experimental Basis for the AP600 Containment Vessel Heat and Mass Transfer Correlations," April 1998.

9.D-5 Blevins, "Jets, Plumes, Wakes, and Shear Layers", Applied Fluid Dynamics Handbook, 1984, pp. 247-251.

9.D-6 Eckert and Jackson, "Analysis Turbulent Free Convection Boundary Layer on a Flat Plate," NACA Report 1015, 1951.

9.D-7 Corradini, "Turbulent Condensation on a Cold Wall in the Presence of a Non-Condensible Gas," Proceedings on Nuclear Reactor Thermal Hydraulics, Vol. 1, 1983.

9.D-8 Kakac and Yener, Convective Heat Transfer, 2nd edition, CRC Press, 1995.

9.D-9 Kays and Crawford, Convective Heat and Mass Transfer, 3rd Edition, McGraw-Hill.

9.D-10 Kreith, "Principles of Heat Transfer", 3rd Edition, Appendix.

9.D-11 WCAP-14135, "Final Data Report for PCS Large-Scale Tests, Phase 2 and Phase 3," Revision 1, April 1997.

9.D-12 WCAP-14845, "Scaling Analysis for AP600 Containment Pressure During Design Basis Accidents," Revision 3, March 1998.

Table 9.D-1 Analytical Solution to the Turbulent Buoyant Plume Model (Reference 9.D-5, Table 9-7)

Notation: b = half-width of the plume; i.e., transverse distance for the axial velocity to fall to one-half the centerline value; B = specific buoyancy flux, see Eqs. (9-50) and (9-54); Q = volume flow rate, per unit depth for plane plume; Q_0 = initial volume flow rate; r = radial distance from plume axis; ΔT = species concentration relative to reservoir level; ΔT_0 = initial relative species concentration; u = axial velocity; u_m = centerline axial velocity; v_e = transverse velocity of reservoir fluid into plume; x = axial distance from origin of the plume; y = transferse distance from center plane; ν = kinematic viscosity. (Refs. 9-1, 9-73.) The uncertainty in the coefficients is approximately ±10%.

Plume Characteristic[(a)]	Plane Plume	Axisymmetric (i.e., round) Plume
1. Centerline velocity, u_m	$1.7\ B^{1/3}$	$3.5\ B^{1/3}\ x^{-1/3}$
2. Width, b	$0.097\ x$	$0.11\ x$
3. Axial velocity profile[(b)], u/u_m	$e^{-74(y/x)^2}$	$e^{-57(r/x)^2}$
4. Volume flow rate, Q	$0.34\ B^{1/3}\ x$	$0.15\ B^{1/3}\ x^{5/3}$
5. Centerline species concentration, ΔT_m	$2.4\ (Q_o\Delta T_o)B^{-1/3}\ x^{-1}$	$11\ (Q_o\Delta T_o)B^{-1/3}\ x^{-5/3}$
6. Species concentration width, $b_{\Delta T}$	$0.13\ x$	$0.10\ x$
7. Species concentration profile[(b)], $\Delta T/\Delta T_m$	$e^{-41(y/x)^2}$	$e^{-69(r/x)^2}$
8. Entrainment velocity, v_e	$0.10\ u_m$	$0.041\ u_m$
9. Reynolds number, $u_m b/\nu$	$0.17\ \frac{B^{1/3}x}{\nu}$	$0.35\ \frac{B^{1/3}x^{2/3}}{\nu}$

(a) In fully developed region.

(b) These are consistent with the corresponding width.

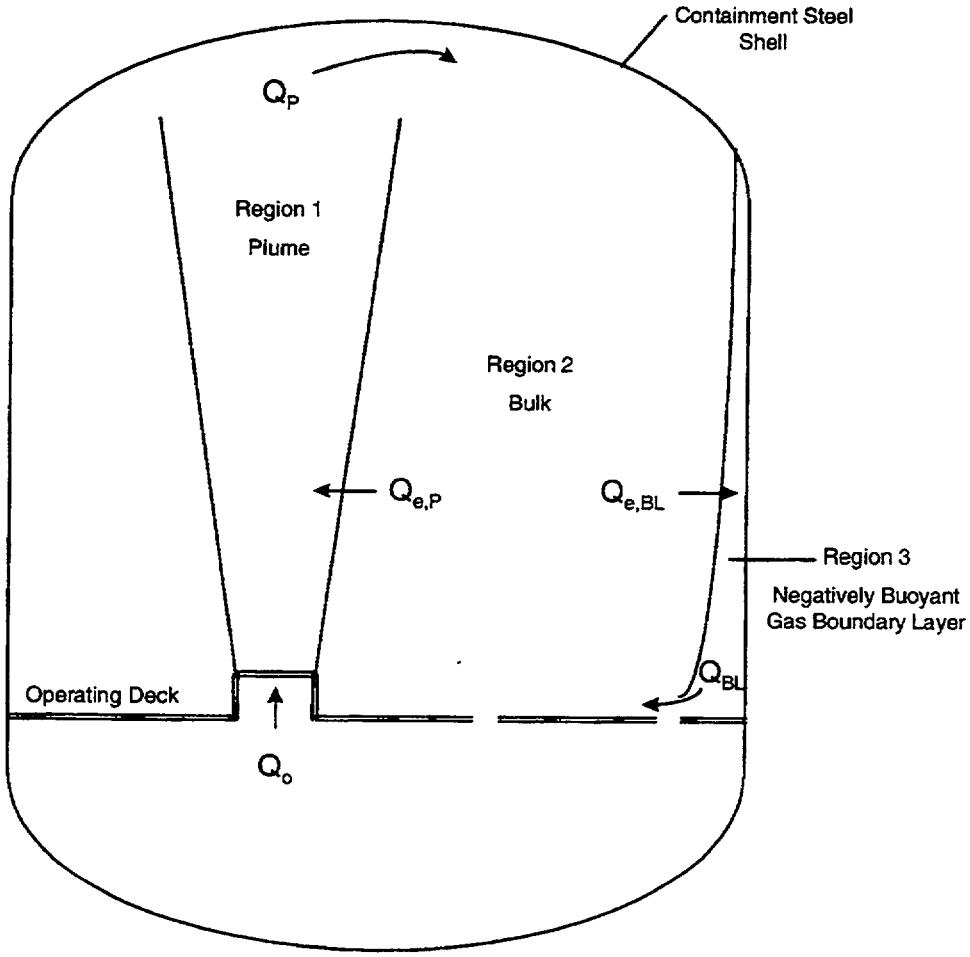

Q_o = Source plume volumetric flow at exit of steam generator compartment

$Q_{e,P}$ = Volumetric plume entrainment from Region 2

$Q_{e,BL}$ = Volumetric wall boundary layer entrainment from Region 2

Q_P = Volumetric plume flow feeding top of Region 2

Q_{BL} = Volumetric boundary layer flow feeding bottom of Region 2

Figure 9.D-1 Interactions Between Containment Regions During Post-Blowdown LOCA (Low Momentum)

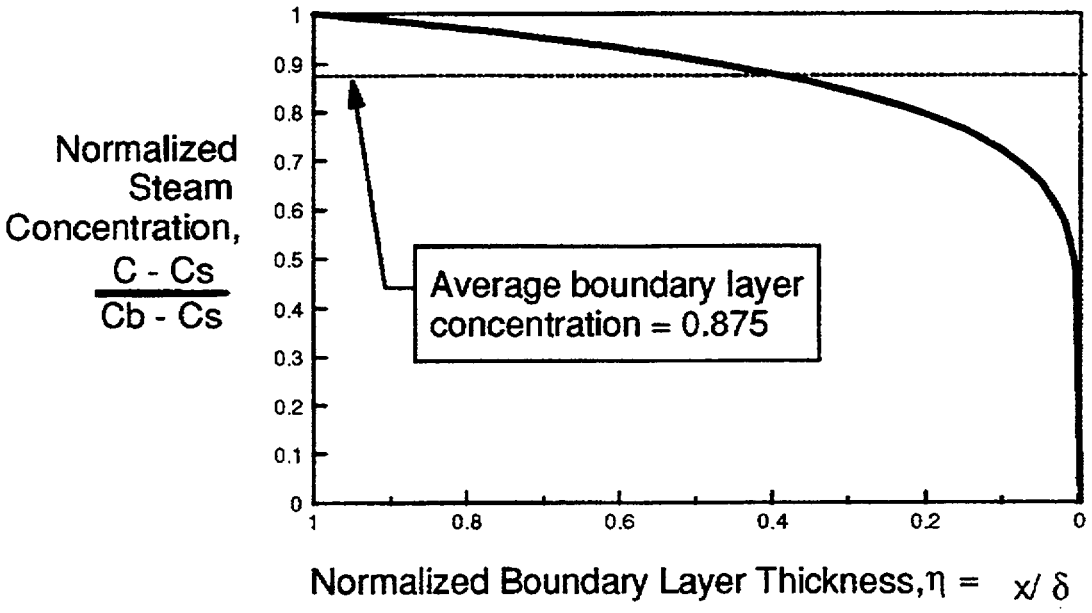

Figure 9.D-2a Detail of Steam Concentration Distribution in Boundary Layer

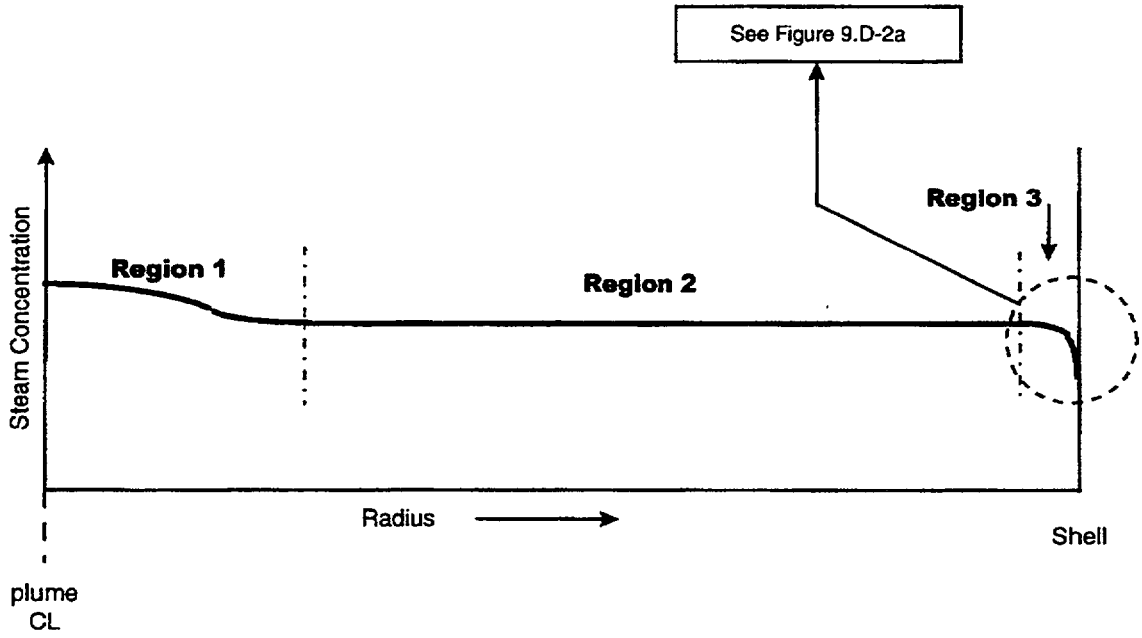

Figure 9.D-2b Qualitative Radial Concentration Profile from Plume Centerline to Shell at Mid Elevation

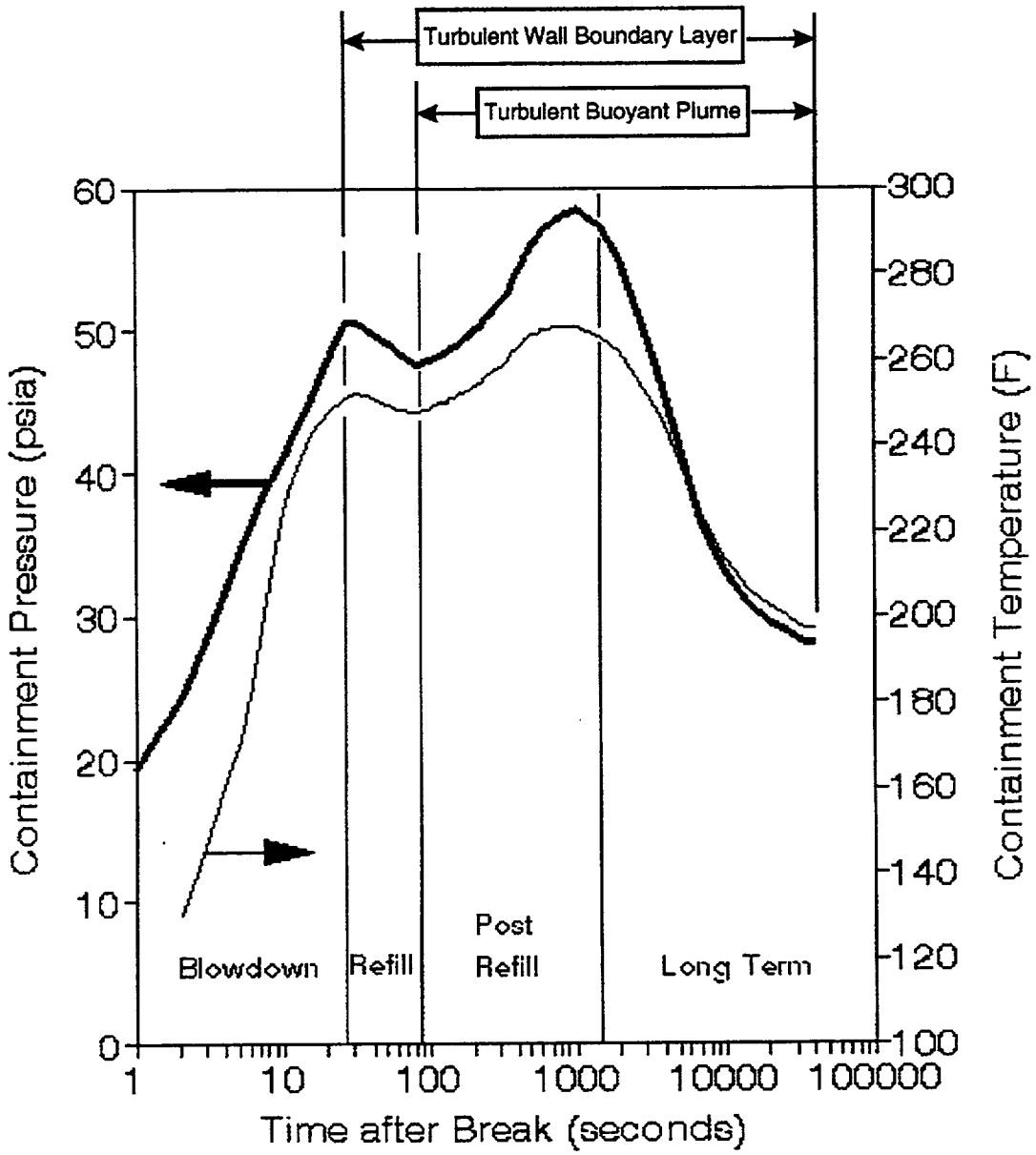

Figure 9.D-3 Period of Application of Analytical Models for Turbulent Wall Boundary Layer and Turbulent Bouyant Plume

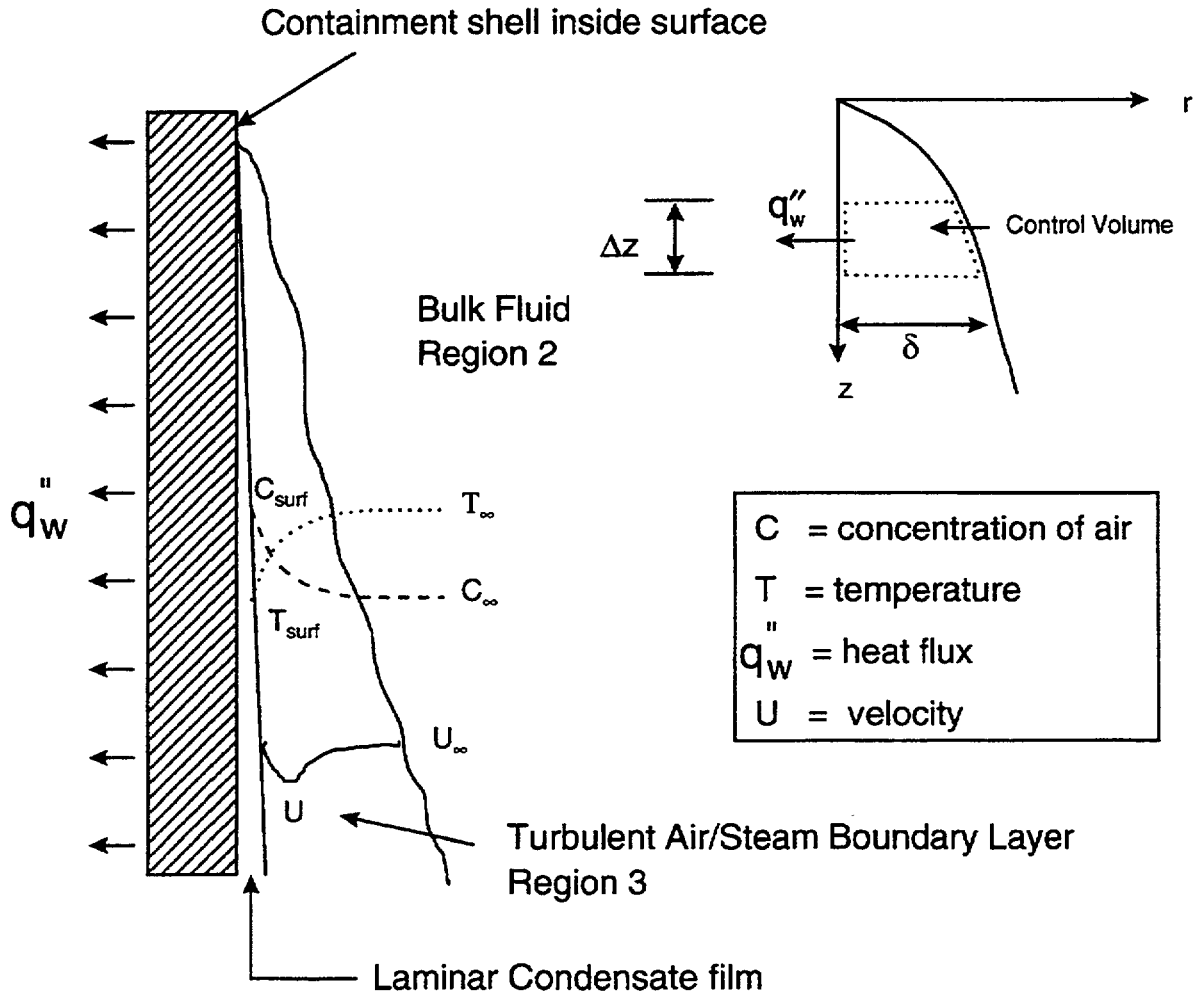

Figure 9.D-4 Turbulent Buoyant Plume Analytical Model

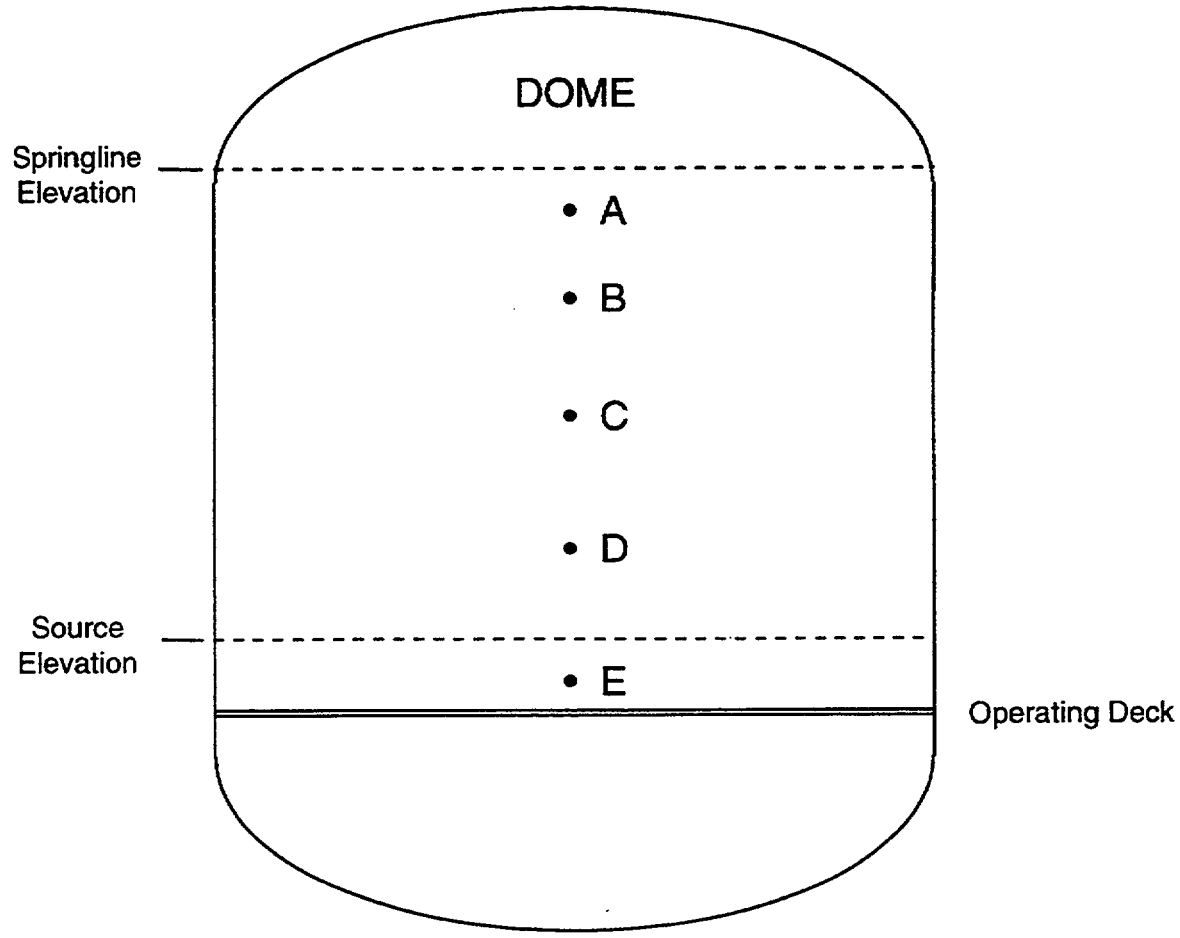

Figure 9.D-5 LST Measurement Locations

Figure 9.D-6 LST Temperature Profile - Test 220.1 @ Quasi-Steady Conditions

Figure 9.D-7 LST Temperature Profile - Test 217.1 @ Quasi-Steady Conditions

Section 10

Nominal Inputs and Correlations Sensitivities

TABLE OF CONTENTS

LIST OF TABLES

LIST OF FIGURES

10.1 INTRODUCTION

The input values for the WGOTHIC Evaluation Model have been biased to ensure a conservative prediction of containment pressure. A subset of these parameters has been selected to determine the impact of each parameter on the calculated pressure for the LOCA and MSLB transients, and to provide a quantification of the total conservatism in the Evaluation Model associated with these parameters. For these parameters, nominal values have been assumed.

Seven sensitivities were run for the LOCA transient to determine the additive sensitivity to each parameter. One sensitivity was run for the MSLB transient, which was a composite of six of the parameters investigated for the LOCA.

The results of these studies show that there is over 11.5 psi margin inherent in the AP600 Containment Evaluation Model for the LOCA peak pressure calculation due to the parameters studied. There is over 13 psi margin associated with the post-blowdown peak pressure, and for the final nominal case, the maximum pressure shifts to the blowdown phase. There is at least 4.9 psi margin in the MSLB calculation due to the parameters investigated. If nominal mass and energy releases were assumed for the MSLB case, even more margin would be shown.

10.2 SENSITIVITY STUDY RESULTS

An estimate of the amount of conservatism, quantified as the change in containment pressure and represented by some of the significant assumptions made for the Evaluation Model follows. These are not single-effect sensitivities. These results are cumulative, in that each additional modification is stacked upon those that immediately preceded it. These sensitivities provide insight into the effect of each parameter individually by comparison to the preceding case, as well as the total conservatism represented by these parameters.

The AP600 Containment Evaluation Model calculations for the LOCA and MSLB described in Section 4 were used as the basis for these studies, with the parameter changes described below, made in each succeeding case. Table 10-1 summarizes the basis for each case and the calculated pressure results for each case. Seven sensitivity cases were analyzed for the LOCA transient, as described below. Figure 10-1 shows a composite pressure curve for the LOCA cases. One MSLB sensitivity was run including all the parameters investigated for the LOCA, except for nominal mass and energy releases. Figure 10-2 shows the pressure results for the MSLB case.

Table 10-1 Nominal Inputs and Correlations Sensitivity Results

LOCA SENSITIVITIES

Case	Case Description	Blowdown Pressure (psig)	Post-Blowdown Peak Pressure (psig)	Pressure at 24 Hours (psig)
	AP600 Evaluation Model	34.4	43.9	18.9
1	Heat & Mass Transfer Multipliers on the Containment Shell	34.4	42.5	16.8
2	Nominal Initial and Ambient Conditions (plus case 1)	33.3	39.8	11.0
3	Nominal Clime Material Properties (plus Cases 1, 2)	33.3	39.0	10.4
4	Nominal Steel-to-Concrete Gap Thickness (plus Cases 1, 2, 3)	33.3	38.8	10.4
5	Nominal External Annulus Loss Coefficients (plus Cases 1, 2, 3, 4)	33.3	38.7	10.2
6	Condensation on Dead-Ended Compartment Heat Sinks Considered (plus Cases 1, 2, 3, 4, 5)	33.3	36.7	10.1
7	Nominal Mass and Energy Releases (plus Cases 1, 2, 3, 4, 5, 6)	32.4	30.6	9.2
	Total Conservatism Represented by Above Assumptions for LOCA Transient	**2.0**	**13.3**	**9.7**

MSLB SENSITIVITY

Case	Case Description	Peak Pressure (psig)
	Evaluation Model	44.8
8	Nominal Inputs and Correlations with Conservative Mass and Energy Releases and Stratification Bias	39.9
	Conservatism Shown	**4.9**

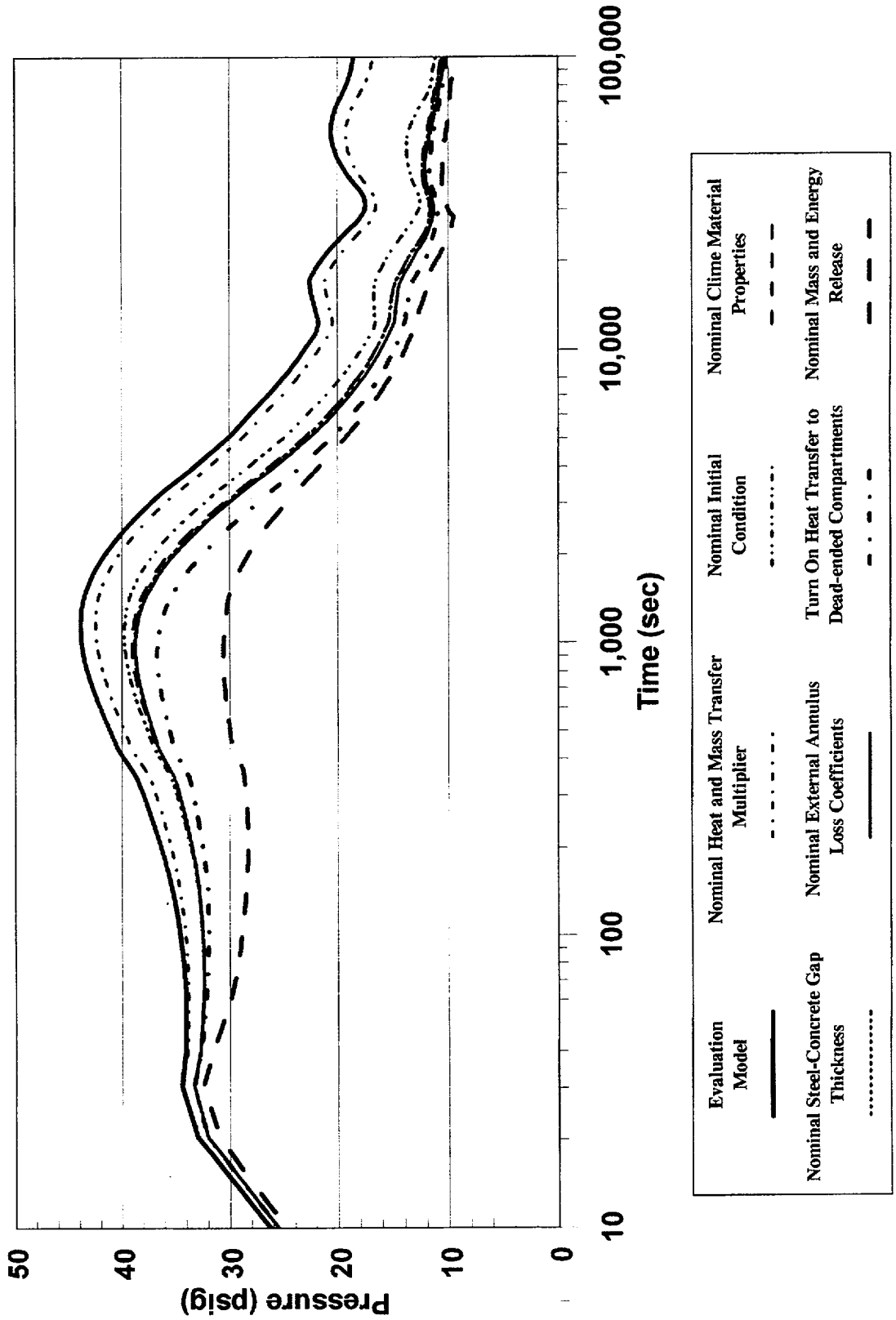

Figure 10-1 LOCA Sensitivities to Nominal Inputs and Correlations

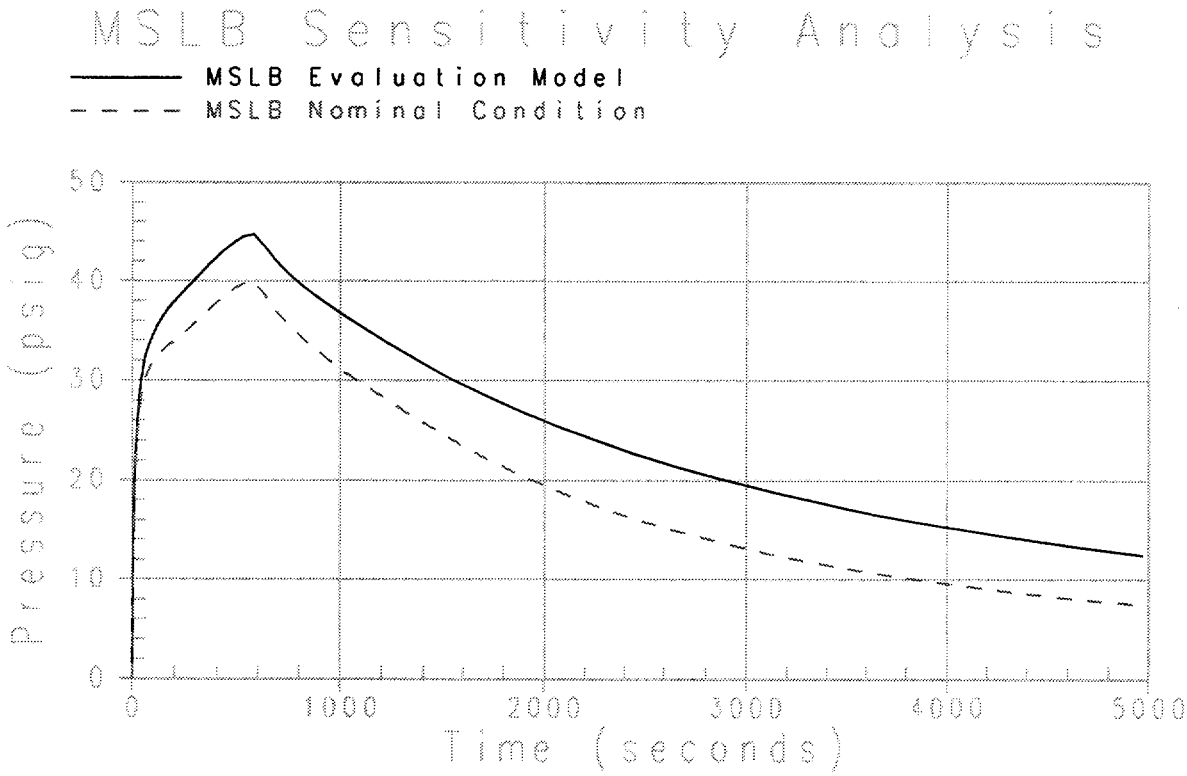

Figure 10-2 MSLB Sensitivity to Nominal Inputs and Correlations

10.2.1 Sensitivity Study Cases for LOCA

Case 1 considered nominal heat and mass transfer on the containment shell. Conservative multipliers have been applied to the heat and mass transfer coefficients calculated on the inside and outside surface of the containment shell in the Evaluation Model to ensure a conservative calculation. A multiplier of [ ]^{a,c} is assumed on the inner surface, where free convection only is considered, and a multiplier of [ ]^{a,c} is assumed on the outer surface, where mixed convection is considered. For this sensitivity, both multipliers were assumed to be 1.0, which represents a more nominal fit to the heat and mass transfer data with only a slight conservative bias remaining. (Ref. 10.1). The heat transfer regime assumptions were not changed.

The nominal heat and mass transfer modeling resulted in a 1.4 psi reduction in the post-blowdown peak pressure and a 2.1 psi reduction in the pressure at 24 hours. There was no significant impact on the peak blowdown pressure, since the heat removal from the shell has a small impact during this time period.

Case 2 considered the impact of nominal initial and ambient conditions. The parameters discussed in Section 5 were varied for this case, except they were set to a nominal set of conditions. The sensitivity case used initial conditions inside containment of 90°F, 14.7 psia, and 30 percent relative humidity as compared to 120°F, 15.7 psia, and 0 percent relative humidity in the Evaluation Model. The sensitivity case used ambient conditions of 70°F and 50 percent relative humidity compared to 115°F and 22 percent relative humidity in the Evaluation Model. The sensitivity case PCS water temperature was set to 70°F compared to 120°F in the Evaluation Model. The initial temperature assumptions for the conductors in the containment and annulus were consistent with their environment. The individual contribution of each of these parameters is discussed in Section 5.

As discussed in Section 5, the internal containment conditions and the PCS water temperature have the most impact on containment pressure. This sensitivity case showed a 1.1 psi reduction in containment pressure during blowdown, a 2.7 psi reduction in the post-blowdown phase, and a 5.8 psi reduction at 24 hours.

Case 3 added the assumption of nominal material properties (thermal conductivity and emissivity) in the clime modeling. In the Evaluation Model the emissivities were reduced by 10 percent to bound the range found in the literature for the materials used, and the conductivity of the carbo-zinc paint was reduced by a factor of four to conservatively account for the effects of oxidization. In this sensitivity case the 0.9 multiplier on the emissivities was removed and the conductivity of the carbo-zinc paint was set to its nominal value.

The nominal clime property modeling resulted in a 0.8 psi reduction in the peak post-blowdown pressure and a 0.6 psi reduction in the pressure at 24 hours. There was no significant impact on the peak blowdown pressure, since the heat removal from the shell has a small impact during this time period.

Case 4 modified the assumption of the gap between the steel liner and the concrete on the applicable internal heat sinks.

The steel surface plates are one-half inch thick and are connected to each other by vertical trusses at 30-inch centers. The steel surface plates are connected to the concrete by embedding these trusses and also by six-inch long welded studs. The surface plates are stainless steel for the IRWST and refueling canal boundaries and are carbon steel elsewhere. The shear studs on the stainless steel plates are spaced at 10 inches horizontally and 8 inches vertically. The shear studs on the carbon steel plates are spaced at 10 inches horizontally and 9.6 inches vertically. The welded studs plus trusses result in a direct steel conduction path across the interface between the surface plate and the concrete. The contribution of this steel with much higher thermal conductivity has been neglected in the WGOTHIC Evaluation Model

Concrete is placed into the structural modules and will initially bond to the surface plates. The wet concrete weight will load the steel plates and result in permanent outward deformation of the plates spanning between the trusses. Mechanical and thermal loading and shrinkage may break this bond due to relative motion. However, the welded studs will keep the surface plates in contact with the concrete at the stud locations and gaps between the studs would be very small. The Evaluation Model conservatively assumes a five mil gap for the steel-jacketed concrete heat sinks. A one mil gap was assumed for this sensitivity.

The results of this case show a 0.2 psi reduction in the post-blowdown peak pressure. The blowdown peak pressure was not affected significantly, since the heat capacity of the concrete has little impact on energy removal during this time. The pressure at 24 hours was not affected, since the heat sinks are effectively saturated at this time and the pressure is dictated by the balance between releases to the containment and heat removal via the PCS.

Case 5 included a modification to the pressure loss coefficient in the external annulus. The loss coefficient assumed in the Evaluation Model includes a 30 percent increase over the value derived from the test program. For this study, a loss coefficient 10 percent greater than measured was modeled.

The annulus loss coefficient has a small impact on the pressure, reducing the post-blowdown peak pressure by 0.1 psi and the pressure at 24 hours by 0.2 psi. There was no significant impact on the peak blowdown pressure since the heat removal via the PCS has a small impact during this time period.

Case 6 included the effects of heat sink utilization in the dead-ended compartments. As discussed in Section 9, condensation and convection on the heat sinks in the dead-ended compartments are not credited after blowdown to ensure a conservative treatment of their utilization. With only a small thermal asymmetry, convection would cause these heat sinks to continue to be exposed to steam after this time and would continue to provide a condensation surface. In this case, the structures were allowed to absorb energy based on conditions predicted by the WGOTHIC code. The WGOTHIC calculation limits the amount of steam entering these compartments, since circulation does not occur in lumped volumes, so the utilization of these

heat sinks is not expected to be grossly over-predicted. It is therefore acceptable to include the utilization of these heat sinks in these sensitivities.

The additional heat absorption capability of the heat sinks in the dead-ended compartment, with an initial temperature of 90°F, resulted in a 2.0 psi reduction in the post-blowdown peak pressure. There was no change in the blowdown peak pressure since the Evaluation Model already considers condensation on these surfaces during blowdown. The reduction in the pressure at 24 hours was only 0.1 psi, since the heat sinks are effectively saturated at this time in both cases.

Case 7 includes the use of nominal mass and energy release rates. The nominal mass and energy release rates are compared to those used in the AP600 Evaluation Model (described in Section 4) in Figure 10-3 and Figure 10-4, respectively. The following modifications were made in the mass and energy release calculation:

- Nominal full-power temperatures and pressure without uncertainty
- Nominal RCS volume with no uncertainties (thermal expansion was considered)
- Core licensed power without adding 2 percent for calorimetric error
- Nominal core stored energy without adding 15 percent
- 1979 ANS decay heat standard without uncertainty for an 800 day average burnup
- Steam generator energy was assumed to be released over a period of one hour for the broken loop and two hours for the intact loop rather than thirty minutes and one hour, respectively
- The refill period was modeled
- No heat generation due to zirc-water reaction
- Nominal initial accumulator, CMT, and IRWST fluid temperatures were used in the post-blowdown releases

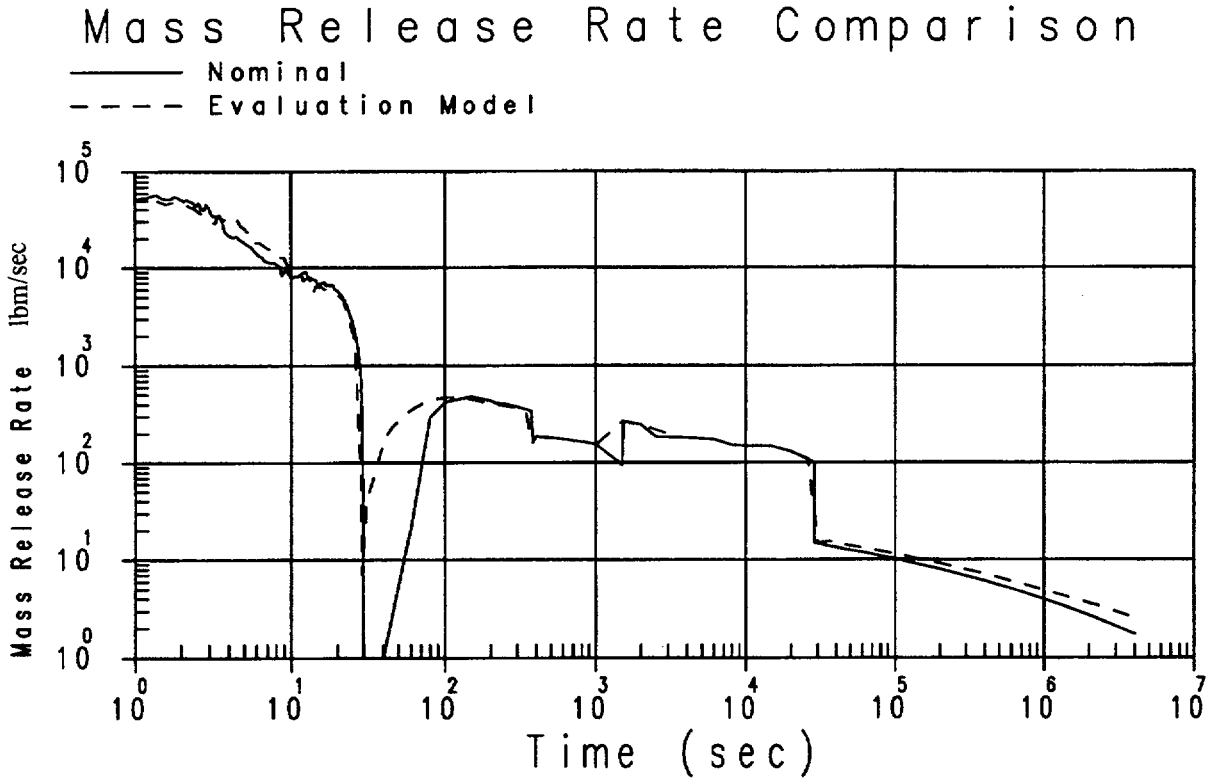

Figure 10-3 Comparison of Evaluation Model and Nominal Mass Release

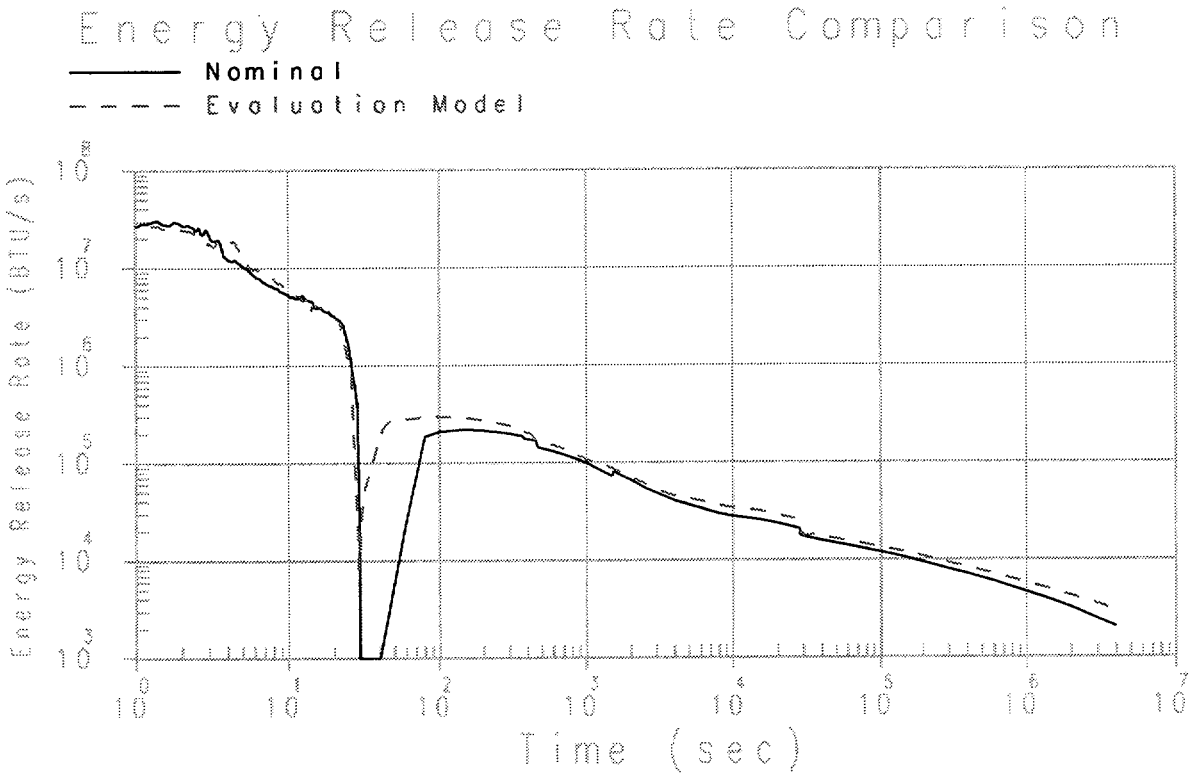

Figure 10-4 Comparison of Evaluation Model and Nominal Energy Release

This case demonstrates that the mass and energy input to the containment has the most impact on the resulting pressure and represents significant conservatism in the Evaluation Model. The blowdown peak pressure was reduced by 0.9 psi, the pressure during the post-blowdown period was reduced by 6.1 psi, and the pressure at 24 hours was reduced by 0.9 psi. The decrease in pressure is sufficient to shift the time of peak pressure for the entire transient from the post-blowdown phase to the blowdown phase. The large sensitivity during the post-blowdown phase is expected, since the mass and energy release models are deliberately biased to maximize the releases during this time in order to ensure that a conservative peak containment pressure is calculated.

10.2.2 Sensitivity Study Case for MSLB

A case was also run to provide quantification of the conservatism in some of the parameters for the MSLB transient. Case 8 included the nominal inputs and correlations embodied in cases 1 through 6 of the LOCA. Nominal mass and energy releases were not included in this calculation. The results of this case indicate that the conservative assumptions studied in the sensitivity case constitute 4.9 psi conservatism. Further reduction in containment pressure would result from the use of nominal mass and energy releases and a less conservative stratification bias. These results also do not credit the significant improvement to shell mass transfer, which would result from forced convection.

10.3 CONCLUSIONS

The results of the sensitivities in this section illustrate that the Containment Evaluation Model provides a conservative prediction of pressure. Some of the conservative nominal inputs and correlations in the Evaluation Model were removed to determine the impact on the calculated pressure for AP600 for the limiting LOCA and MSLB cases. These sensitivities are not intended to portray a best estimate calculation; other conservative features and modeling techniques have not been included that would further reduce the predicted pressure.

However, the conservatism represented by the parameters that were studied is significant. The LOCA cases investigated indicate a reduction of 2.0 psi during blowdown, 13.3 psi during the post-blowdown phase, and 9.7 psi at 24 hours. The summation of these cases switches the time of peak pressure from the post-blowdown period to the blowdown period. Comparison of the maximum pressures in the two cases shows 11.5 psi reduction in pressure. The MSLB case shows 4.9 psi margin due to nominal inputs included in this study. Incorporating other nominal conditions, such as mass and energy release rates and forced convection enhancements, would result in further pressure reduction.

10.4 REFERENCES

10.1 WCAP-14326, Revision 2, "Experimental Basis for the AP600 Containment Vessel Heat and Mass Transfer Correlations," April 1998.

Section 11

Timestep Sensitivity

TABLE OF CONTENTS

LIST OF TABLES

LIST OF FIGURES

11.1 INTRODUCTION

To establish WGOTHIC as an acceptable tool for use in the licensing process, it is necessary to perform a sensitivity to the timestep size selected by the code. The timestep size determines how far the transient is permitted to progress from calculational step to calculational step. The algorithm that is used to determine the maximum allowable timestep size should produce a timestep value that results in a stable, suitably accurate solution without prohibitive computer execution times.

In the WGOTHIC code, the algorithm that is used to determine the maximum allowable timestep size is based on two stability criteria: the amount of time it would take to completely replace the mass within a given volume (Courant limit), and one half of the natural period of oscillation for a gravity-driven system (gravitational limit). In addition, the algorithm also includes limits on timestep growth, checks on nonphysical results, and limits on the rates of change of primary variables. These limits are all discussed in Reference 11.1, Enclosure 2, Section 12.7.

11.2 METHODOLOGY

Subroutine timstp.f in the WGOTHIC solver program contains the timestep selection algorithm. This subroutine calculates the maximum allowable timestep size that can be used in the WGOTHIC transient calculations.

Subroutine timstp.f was modified to perform the timestep sensitivity study. The maximum allowable timestep size was reduced to study the effect of using a smaller timestep on the results of the WGOTHIC transient calculations. Use of timesteps that are smaller than the maximum allowable value maintains numerical stability.

Two new versions of subroutine timstp.f were created; in WGOTHIC_S version 4.1.1, the maximum allowable timestep size was halved, and in version 4.1.2, it was quartered. The timestep selection process was not impacted by these changes and there were no other differences between the three versions of WGOTHIC_S.

The AP600 containment evaluation model input deck described in Section 4 was used for the timestep sensitivity analyses. The loss-of-coolant-accident (LOCA) transient was chosen since it contains both rapid and extended pressurization and depressurization transients. The LOCA is a long transient that relies on the PCS for a substantial amount of energy transfer to the environment.

11.3 RESULTS

The LOCA transient containment response analysis was performed with each of the three code versions. Table 11-1 indicates the number of calculational steps taken, the peak predicted pressure, and the predicted pressure at 24 hours for each code version.

Table 11-1 Timestep Sensitivity Results

WGOTHIC_S Code Version	Number of Calculational Steps	Peak Pressure (psig)	Pressure at 24 Hours (psig)
Version 4.1 - 1.0*Δt	187380	43.85	18.86
Version 4.1.1 - 0.5*Δt	374414	43.76	18.88
Version 4.1.2 - 0.25*Δt	748680	43.72	18.85

The one-half timestep version of the code takes approximately twice the number of steps to complete the transient and the one-quarter-timestep version of the code takes about four times the number of steps to complete the transient. Since the timestep selection logic relies on the volume conditions at the end of each step, it is extremely difficult to get exactly twice or four times the number of steps. With the smaller timesteps, the changes in fluid conditions and other parameters used in the timestep selection process are smaller. The smaller changes permit larger timesteps to be allowed. As a result, slightly less than two times and four times the number of calculational steps are used in the modified versions of the code.

The reduced timestep versions predicted slightly lower peak pressures than the base version of the code. The predicted peak pressure for the quarter-timestep version was 0.04 psi lower than the one-half timestep version, and 0.13 psi lower than the full-timestep version. This indicates that the calculated peak pressure solution converges from above as the timestep is reduced.

In addition to the number of timesteps taken to complete the problem, the code output contains the number of times that a timestep was limited by some phenomenon. In all three cases, the timestep size was limited by either the phase change limit, the Courant limit, or the gravitational limit. Table 11-2 presents the number of times that the timestep was limited in each case.

Table 11-2 Timestep Limit Results

WGOTHIC_S Code Version	Courant Limit	Phase Change Limit	Gravitational Limit
Version 4.1 - 1.0 * Δt	4000	21	91612
Version 4.1.1 - 0.5 * Δt	8070	11	183305
Version 4.1.2 - 0.25 * Δt	16108	9	366639

During the pressurization phase of the LOCA transient, the timestep size was primarily limited by the Courant stability limit. This was not unexpected, since the volumetric break flow is so large during this phase. Since the circulation is primarily buoyancy-driven during the much longer depressurization phase, the time step size was primarily limited by the gravitational stability limit after the peak pressure was reached.

Note, the sum of the number of limiting timesteps in Table 11-2 does not add up to the total number of calculational timesteps given in Table 11-1 because, in some instances, the timestep size was not limited by any of the limits tracked in the output file. This could occur, for example, if the upper limit imposed by user input was less than the value calculated by the timestep selection algorithm.

The LOCA transient containment pressure predicted by each of the three code versions is shown in Figure 11-1. There is very little difference in the results. The transient results are further examined by comparing the differences in the predicted transient pressure from each of the three code versions. The percentage difference in the predicted transient pressure between the full-timestep version and the one-half-timestep version, and the percentage difference in the predicted transient pressure between the one-half timestep version and the one-quarter-timestep version is presented in Figure 11-2. The differences in the predicted transient pressure between successive versions of the code are very small (less than 1% over the entire 24-hour period).

11.4 SUMMARY

Two versions of WGOTHIC_S were created for this sensitivity study. The calculational timestep size was reduced to a value that was either one-half (Version 4.1.1) or one-quarter (Version 4.1.2) of the maximum allowable value calculated by the timestep selection algorithm.

A comparison of the predicted AP600 LOCA transient containment pressure response between the base version and the two versions created for the sensitivity study shows that there is very little difference in the results. Using smaller timesteps does not significantly affect the transient response. Therefore, the timestep selection algorithm produces a timestep value that results in a stable, suitably accurate solution.

Based on the timestep study results presented herein, it is concluded that the timestep selection logic for WGOTHIC_S is acceptable.

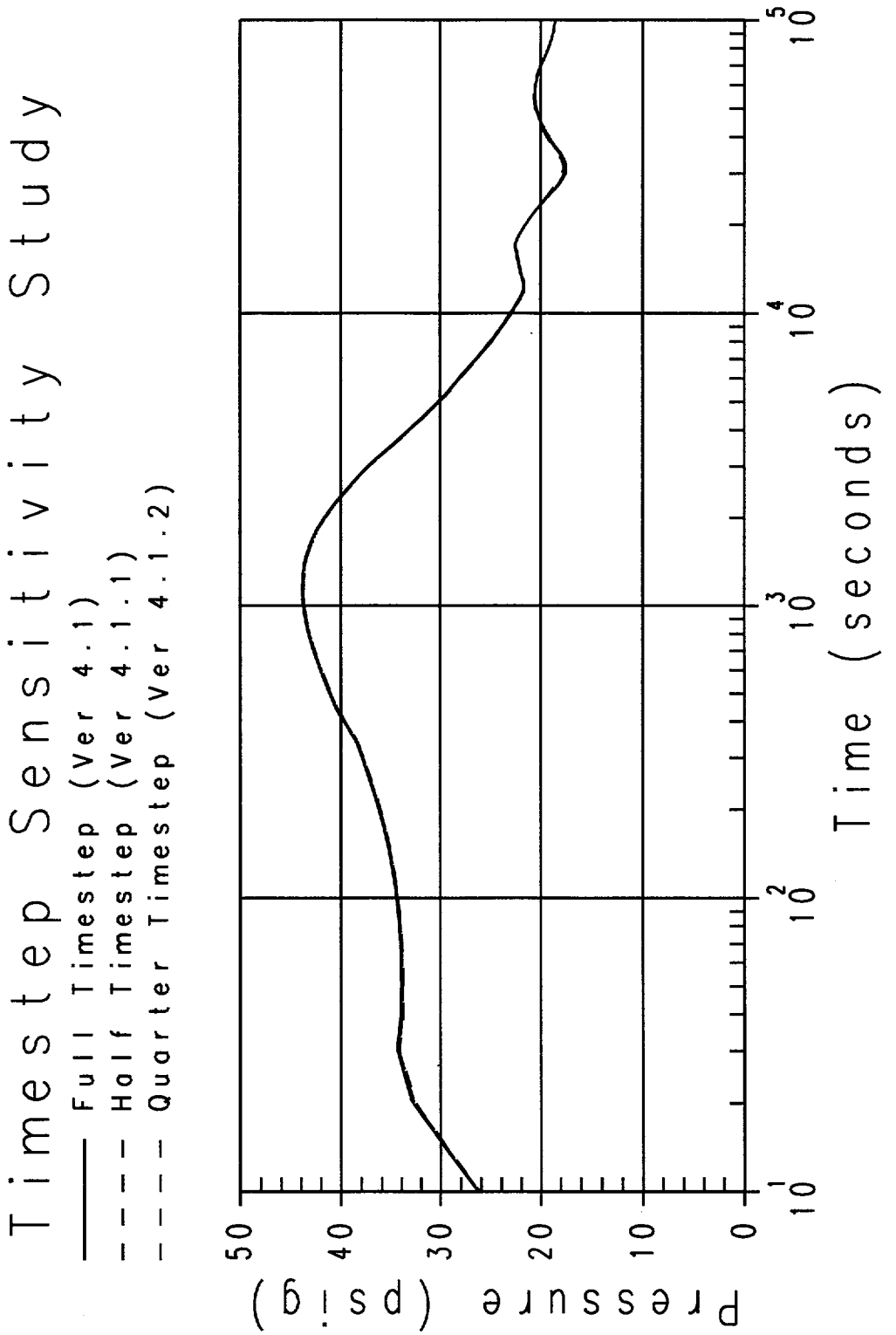

Figure 11-1 **AP600 Containment LOCA Transient Pressure Prediction with Full, One-Half, and One-Quarter Timesteps**

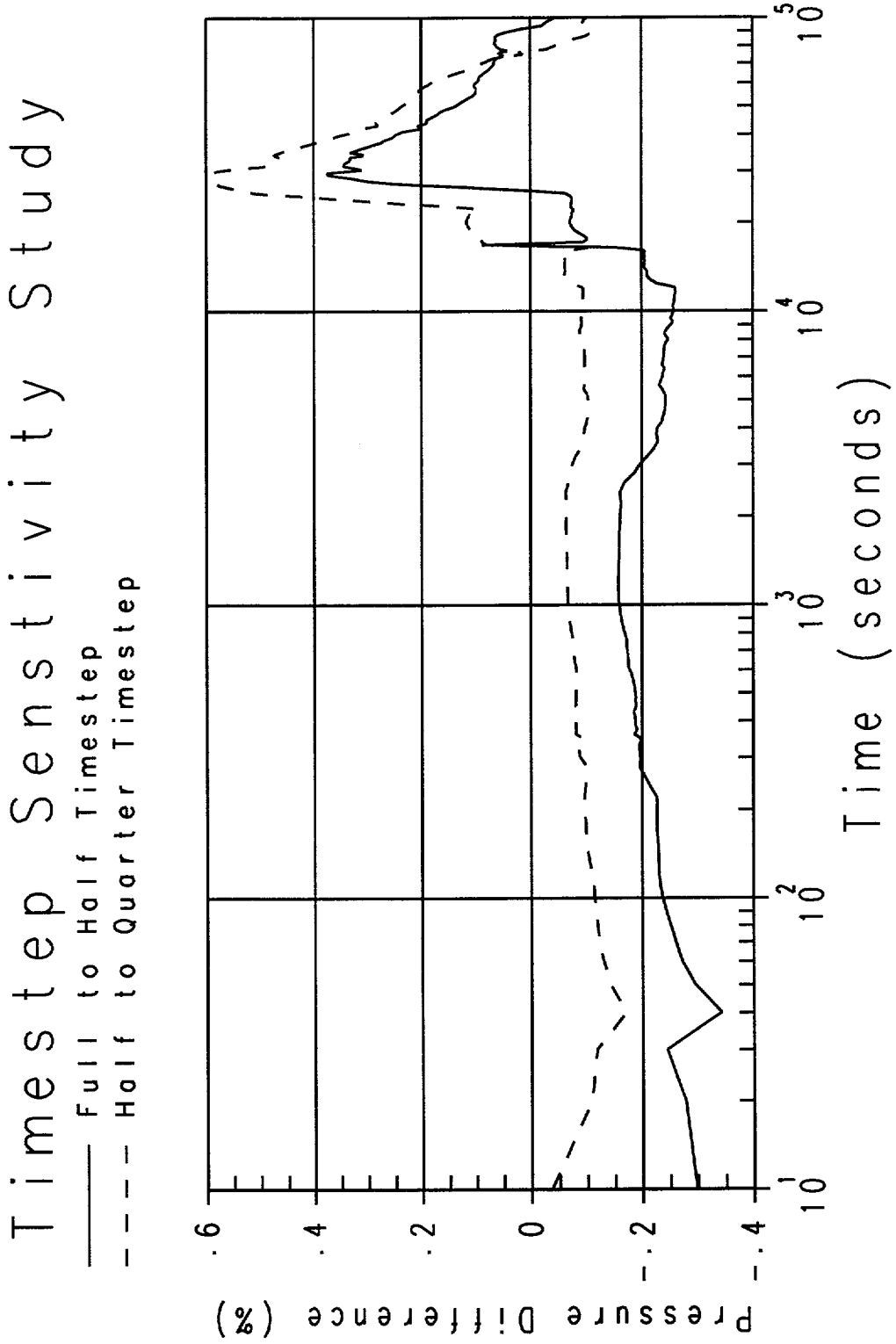

Figure 11-2 **AP600 Timestep Comparison, Percentage Difference in Predicted Pressures Between Successive Code Versions**

11.5 REFERENCES

11.1 Westinghouse Letter NTD-NRC-95-4563, B. A. McIntyre to Quay (NRC), "GOTHIC Version 4.0 Documentation," September 21, 1995.

Section 12

Sensitivity to Clime Noding

TABLE OF CONTENTS

LIST OF TABLES

LIST OF FIGURES

LIST OF FIGURES (Cont.)

12.1 INTRODUCTION

This section provides background associated with the WGOTHIC clime model, a statement of the issue associated with the application of the clime methodology, a description of the approach developed and taken to address the issue, a summary of the results of the analyses and the conclusions drawn from a review of those analyses.

12.1.1 Background

The GOTHIC code (Refs. 12.1 and 12.2) is a state-of-the-art program for modeling multi-phase flow for containment analysis. The code solves the integral form of the conservation equations for mass, momentum, and energy for multi-component, two-phase flow. The conservation equations are solved for three fields: continuous liquid, liquid drops, and a steam/gas phase. The three fields may be in thermal non-equilibrium within the same computational cell. Relative velocities are calculated for each field, as well as the effects of two-phase slip on pressure drop. Heat transfer between the phases, surfaces, and the fluid are also allowed.

As described in Section 3 of this report, the GOTHIC containment analysis code was modified by Westinghouse to include mechanistic convective heat and mass transfer correlations, a liquid film tracking model, a one-dimensional wall conduction model, and wall-to-wall radiant heat transfer to model heat removal by the PCS. The code with these modifications is called Westinghouse-GOTHIC, and is abbreviated as WGOTHIC.

A solution technique that includes wall-to-wall radiation at the conditions expected for the AP600 and AP1000 plant designs necessitates a close coupling of the participating walls. This coupling is accomplished by assigning boundaries that define the portions of the various walls that radiate to one another. Consistent with the basic formulation implemented for the GOTHIC code that considers conductors or heat sinks to be energy and mass sink or source terms, code modifications that include wall-to-wall radiant heat transfer can be thought of as the addition of a special type of conductor group. This special conductor type or group consists of a set of walls that radiate to each other and interface with GOTHIC fluid cells through mass and energy source terms. The term *clime*, meaning *region*, is used to differentiate and distinguish this special conductor type from those already existing in GOTHIC terminology.

A three-conductor clime is shown schematically in Figure 12-1. For the containment model, a clime is a horizontal slice of the containment structure consisting of the steel shell, the baffle, and the shield building and liquid films which may form on those solid surfaces, and representing the following transport processes:

- The heat and mass transfer source terms from the containment volume to the shell

- Liquid film mass and energy conservation and thermal resistance on shell, baffle, or shield building surfaces
- Conduction through the shell
- Heat and mass transfer source terms from the exterior shell to the riser air flow channel
- Radiation from the exterior shell to the interior baffle
- Heat and mass transfer source terms to the interior baffle from the riser air flow channel
- Conduction through the baffle
- Heat and mass transfer source terms from the exterior baffle to the downcomer air flow channel
- Radiant heat transfer from the exterior baffle to the interior surface of the shield building
- Heat transfer source terms to the interior surface of the shield building from the downcomer air flow channel
- Conduction through the wall of the shield building
- Both radiant and convective heat transfer from the exterior surface of the shield building to the environment

As shown schematically in Figure 12-1, the internal containment vessel volume, riser air flow channel volume, downcomer air flow channel volume, and environment volume are separate computational cells or fluid volumes in the GOTHIC model. The shell, baffle, and shield building walls are one-dimensional conductors representing solid wall structures between the computational cells. These conductors are further subdivided into regions of different materials with different numerical mesh sizes.

The climes are stacked vertically through the PCS to model the effects of changing properties both inside and outside the containment shell. Usually there are at least two stacks of climes a wet stack and a dry stack. The only difference between a wet and dry stack is that a time-dependent, water flow rate boundary condition is specified for each conductor surface of the top clime in a wet stack. Because condensation can occur on either wet or dry conductor surfaces, an initially dry stack of climes could contain some wet conductor surfaces and/or a partially wet conductor surface due to condensation. Likewise, an initially wet stack of climes could contain some dry conductor surfaces and/or a partially dry conductor surface due to evaporation.

The user must specify values for the area and circumferential perimeter for each conductor of each clime in both the wet and dry stacks. The input values for the area and circumferential perimeter for the clime conductors in the wet stacks are based on measurements of the water coverage from the full-scale water distribution tests. The water coverage input calculation method for the containment Evaluation Model is described in Section 7.

The WGOTHIC clime model calculates the temperature, flow rate, and thermal resistance of the water films on the various conductor surfaces of a clime. Liquid mass is conserved whenever the film reaches the bottom clime in a stack or a conductor surface dries out. The clime model takes the film flow rate from each conductor surface of the previous clime in the stack as input, then adds the local condensation rate, or subtracts the local evaporation rate to determine the output water flow rate on each of its corresponding conductor surfaces. Any liquid film remaining on the conductor surfaces of the last clime in a stack is added to the liquid field of the WGOTHIC cell in contact with the conductor surface, or an alternate drain cell specified by user input.

Dryout occurs when either the film flow rate is low enough or the heat flux is high enough to result in complete evaporation of the film before it can exit the conductor. The clime model calculates the evaporation heat and mass transfer and the location of the dryout elevation; the remainder of the conductor surface is treated as a dry surface.

The details of the clime equations and integration into the GOTHIC code are described in Sections 3.4 and 3.5.

12.1.2 Problem Statement

Simply stated, the objective of this effort is to demonstrate that the clime calculations are insensitive to increased numerical resolution relative to the noding pattern employed in the Evaluation Model.

12.1.3 Approach

The approach taken to address the problem statement given above is to:

- Perform sensitivity calculations using a simple two-channel annulus model with a constant temperature boundary condition. The simplified model is used to better isolate effects of clime noding. For this task, the number of climes in the model will vary from 4 to 16. Although not intended to simulate or scale to the AP600 or AP1000 plants, this two-channel annulus model will provide for thermo-fluid conditions similar to those expected in the annulus of the passive plant, i.e., evaporation into a buoyancy-driven air flow.

- Perform sensitivity calculations with an AP600 containment model for which the number of climes, stacks, and conductor layers are varied to confirm the results of the simpler models.

12.1.4 Selected Parameters

The following thermal-hydraulic parameters are used in evaluating the comparison of various model predictions:

- Containment pressures (for the AP600 model only)
- Temperatures – cooling air and liquid film
- Heat fluxes and/or heat rates from the shell

These parameters are primary indicators of the heat transfer process and were selected as a basis for evaluating the sensitivity of the calculated results to noding patterns.

12.1.5 Success Criteria

The noding pattern used for a model may affect the results of a calculation. For the purpose of this study, the following success criteria are used to evaluate the significance of change in calculated results with increasing detail in clime noding:

Success Criteria: The change between results calculated with two noding patterns is defined to be negligible; if:

1) The variation in results between two successive noding patterns is less than [ ]^{a,c} percent.

2) The variation in results from successively finer noding patterns is decreasing.

[

]^{a,c}

Thus, the criteria listed above establish that the variation between results obtained from different noding patterns must be small, and the variation must be converging as the noding pattern is increased.

12.2 MODEL DESCRIPTIONS

The sensitivity of the thermo-fluid calculations of the WGOTHIC clime methodology to the number of nodes associated with the flow channel was investigated using a two-channel annulus model. This section presents descriptions of the model and the boundary conditions used in this investigation. This simplified two-channel model is not intended to scale to the plant. It is a simplified model with fixed boundary conditions that allows study of changes caused by clime noding detail. The fixed boundary conditions allow direct comparison of clime heat removal predictions. A detailed comparison of the results calculated for this model to those calculated in the AP600 or AP1000 is not meaningful. However, the trends for the simple model, relative to the success criteria, are applicable to the passive plant design, as confirmed with the sensitivity calculations using an AP600 containment model as a basis (Section 12.3.2).

12.2.1 Simple Annulus Clime Model

Model Description

A simple two-channel model was developed to study the effects of increasing the number of climes over a wide range of film flow rates and film temperatures and is shown schematically in Figure 12-2. The modeled heated height was [ ]^{a,c} feet. This height was chosen to promote the calculation of velocities in the model representative of the lower bound of the range expected for AP600. The number of climes (and corresponding annulus cells) in the heated section of the model varied between 4 and 16. Figure 12-3 presents the noding structure for the 8 clime model. The noding pattern for the 4 and 16 clime models is similar to that of the 8 clime model, having one-half and double the number of axial cells, respectively.

The annulus clime model is connected to two stacks of lumped parameter cells, similar to the Evaluation Model. One stack represents the downcomer volume and the other represents the riser volume. The volumes of the riser and downcomer are [ ]^{a,c} cubic feet and [ ]^{a,c} cubic feet respectively. The downcomer volume was arbitrarily selected to be about twice the value of the riser volume. A set of equally spaced elevation planes crosses both the riser and downcomer to form the two stacks of lumped parameter cells. The volume, height, and vertical flow area of each cell in the riser stack and each cell in the downcomer stack is the same.

A natural draft flow of air from the downcomer through the riser develops as the riser channel is heated. Friction acts to retard the increase in air velocity. Except for the turning location and exit, the friction lengths for each flow path are equal to the cell height. The friction lengths at the riser entrance and exit are set to one half the cell height to conserve the total friction length and fL/D values between models. Loss coefficients of [ ]^{a,c} at the downcomer entrance and [ ]^{a,c} at the riser outlet are used to model the form losses representative of a contraction and an expansion, respectively.

For the 8 clime model shown in Figure 12-3, a thermal conductor located within the heat source (Volume 9), provides a [ ]^{a,c} constant temperature boundary condition for the model. A single stack of climes is used to thermally connect the heat source with the riser and downcomer volumes. There is one clime per cell in the riser. An additional clime at the bottom of the stack is used to model the runoff film flow. The last clime in the stack is connected to three dummy volumes. This modeling is used to allow the runoff from the last clime to collect in the drain volume (Volume 18) without affecting the heat removal in the active section of the annulus.

Each clime has two conductors; the first one represents a [ ]^{a,c} thick steel plate and the other represents an acrylic cover. The perimeter and heat transfer area is the same for each conductor on all climes.

To prevent the drain volume from overfilling, it is connected to a flow rate boundary condition. The boundary flow rate for the drain volume is controlled with trips based on the liquid level in the drain volume.

These features were also included in both the 4 and 16 clime models.

Boundary Conditions

Four cases were considered for this study. The independent variables for each case are listed in Table 12-1.

a,c

The film boundary conditions are selected to cover a range of temperatures and flow rates considered typical for the passive plant. For Case 4, the film mass flow rate is reduced to force the prediction of dryout about midway down the plate. Both the downcomer and riser are connected to a fixed pressure boundary set at [ ]^{a,c} psia.

12.2.2 AP600 Containment Model

A schematic of the AP600 containment model clime noding pattern is shown in Figure 12-24. The dashed lines represent divisions between the [ ]^{a,c} climes (and cells) in the annulus.

The AP600 clime noding sensitivity cases were performed using a preliminary Evaluation Model input deck. The differences between the AP600 containment model that was used for these sensitivity studies and the Evaluation Model, as described in Section 4, are irrelevant to the clime noding sensitivity study because each of the sensitivity cases used this same AP600 containment model as its basis. The major differences between the sensitivity model and the Evaluation Model, are summarized below:

- The mass and energy releases in the sensitivity model are lower during the peak pressure phase and higher during the long-term phase. The different phases of the LOCA containment pressurization transient are defined in Section 3.4.2.2 of Reference 12.3. [

  ]^{a,c}.

- The PCS flow rate input is higher in the sensitivity model for the first three hours, but lower for the remainder of time. [

  ]^{a,c}.

- The internal noding structure is different. [

  ]^{a,c}.

- The annulus initial conditions in the sensitivity model (15.7 psia, 120°F) are different from those in the Evaluation Model (14.7 psia, 115°F).

- [

  ]^{a,c}.

- The annulus loss coefficients are lower in the sensitivity model. [

]^{a,c}.

The base case AP600 containment model was modified for the clime noding sensitivity study to examine the following effects:

- Doubling the number of climes (or vertical segments) from [ ]^{a,c} to [ ]^{a,c} (see Figure 12-25)
- Doubling the number of stacks (or radial segments) from [ ]^{a,c} to [ ]^{a,c} (see Figure 12-26)
- Doubling the number of numerical mesh points through the thickness of the clime conductors (see Figure 12-27)

As with the simple annulus model noding study described in Section 12.2.1, the heat transfer parameters identified in Section 12.1.4 were used to evaluate the sensitivity of the calculations to changes in the noding pattern used for the calculations. In addition, plots comparing the annulus air pressure, density and velocity profiles are included for the vertical clime noding sensitivity comparison.

12.3 RESULTS

12.3.1 Simple Annulus Clime Model

The four test cases described in Table 12-1 of Section 12.2.1 were run using WGOTHIC Version 4.1. Transient calculations were performed until the time when little or no change in one or more governing parameters (pressure, film temperature, etc.) was predicted. Since constant boundary conditions were used, a steady-state solution was eventually reached for each case. All four cases were run out to 2000 seconds of transient time.

Plots of the predicted heat removal rate from the plate surface, shown in Figures 12-4 through 12-7, indicate that the four cases were close to steady-state conditions at the end of the 2000-second transient period. The difference between the heat rejection rates of the 4 and 8, and 8 and 16 clime models is shown in Figures 12-8 through 12-11. From these plots, it is noted that the predicted transient heat removal rate is quite insensitive to the level of clime noding detail; a change of less than 1 percent is observed for increasing the axial nodal pattern from 4 to 8 climes. The difference observed when the axial nodal pattern is increased from 8 climes to 16 is even less.

A comparison of the predicted heat removal rate from the plate surface at the end of the transient is shown in Table 12-2.

[a,c

For the first three tests (all dry or all wet), the steady-state heat removal rate increases slightly as the number of climes is doubled from 4 to 8. Doubling the number of climes from 8 to 16 increases the heat removal rate again, but by a much smaller amount. Therefore, for these cases, the predicted heat removal rate is converging from below.

For test case 4 (half wet), the steady-state heat removal rate decreases slightly as the number of climes is doubled from 4 to 8. Doubling the number of climes from 8 to 16 also decreases the heat removal rate, but by a smaller amount. Further comparisons show that the predicted heat removal rate decreases on the top [ ]^{a,c} feet, but increases on the bottom [ ]^{a,c} feet of the model surface as the number of climes is increased. The decrease on the top [ ]^{a,c} feet is larger than the increase on the bottom [ ]^{a,c} feet. Therefore, the total predicted heat removal decreases as the number of climes increases in case 4. At the low flow rate for this test, the increased resolution of the subcooled heat flux with more climes yields a slightly lower estimate of the predicted heat removal rate.

Figures 12-12 through 12-15 compare the calculated axial heat flux profiles, and Figures 12-16 through 12-19 compare the axial film temperature profiles at time t = 2000 seconds, where "film temperature" for the dry case represents the surface temperature. Note, the data from the 8 and 4 clime models is represented as 2 and 4 points respectively on the plots to match the 16 points from the 16 clime model.

For the wet tests, smoother axial heat flux and film temperature profiles are calculated as the number of climes increases. In the cold film tests (cases 2 and 4), the heat flux decreases and film temperature increases as the film flows from the first clime down. In the hot film test (case 3), the heat flux increases and the film temperature decreases as the film flows from the first clime down. The heat flux remains constant after the film reaches a temperature at which evaporation dominates. For the partially wet test (case 4), the heat flux

decreases rapidly and the film temperature increases to the dry surface temperature in the clime where dryout occurs.

The heat flux and surface temperature profiles are adequately represented with either 4, 8, or 16 climes for the dry test (case 1). The heat flux decreases linearly from the entrance (last clime) to the exit (first clime) of the channel while the surface temperature remains essentially constant.

Figures 12-20 through 12-23 compare the calculated axial air temperature profiles at time t = 2000 seconds. In all tests, the air temperature increases from the entrance (last clime) to the exit (first clime) of the heated channel.

12.3.2 AP600 Containment Model

The long-term mass and energy release input and PCS flow rate input were not finalized at the time the sensitivity cases were made, therefore, sensitivity results are presented up to the time the IRWST inventory was depleted (43500 seconds). This was a sufficient transient duration to determine if the AP600 containment model would be sensitive to doubling the number of climes, the number of stacks, or the conductor mesh points.

Clime Sensitivity Results

The number of climes and volumes in the annulus of the base AP600 containment model were doubled (while maintaining the same total volume and heat transfer area) and the case was run using WGOTHIC Version 4.1. Figure 12-28 shows a comparison of the transient pressure for the double clime case with the base case. There is essentially no difference between the two cases. Figures 12-29 and 12-30 present the axial wet heat flux profile for the [ ]^{a,c} and [ ]^{a,c} clime cases at transient time t=0, 30, 1500, and 43500 seconds. The profiles are similar, but the wet heat flux profile for the [ ]^{a,c} clime case has better resolution of the subcooled region at the top of the dome at 1500 seconds and of the dryout elevation at 43500 seconds.

Figures 12-31 and 13-32 present the axial dry heat flux profile for the [ ]^{a,c} and [ ]^{a,c} clime cases at transient time t=0, 30, 1500, and 43500 seconds. The profiles are similar.

Figures 12-33 and 12-34 present the axial external film temperature profile for the [ ]^{a,c} and [ ]^{a,c} clime cases at transient time t=0, 30, 1500, and 43500 seconds. The profiles are similar, but the film temperature profile for the [ ]^{a,c} clime case has better resolution of the subcooled region at the top of the dome at 1500 seconds and of the dryout elevation at 43500 seconds.

Figures 12-35 and 12-36 present the axial external dry surface temperature profile for the [ ]^{a,c} and [ ]^{a,c} clime cases at transient time t=0, 30, 1500, and 43500 seconds. The profiles are similar.

Figures 12-37 and 12-38 present the axial annulus air pressure profile for the [ ]^{a,c} and [ ]^{a,c} clime cases at transient time t=0, 30, 1500, and 43500 seconds. The pressure quickly decreases to the boundary condition value (14.7 psia) in both cases. The pressure at the bottom of the annulus is slightly higher than at the top due the density head.

Figures 12-39 and 12-40 present the axial annulus air temperature profile for the [ ]^{a,c} and [ ]^{a,c} clime cases at transient time t=0, 30, 1500, and 43500 seconds. The downcomer and riser air temperatures eventually establish similar profiles. The air temperature increases slightly as it flows downward, then increases rapidly (by about 30°F at 1500 and about 18°F at 43500 seconds) in the riser as it flows upward.

Figures 12-41 and 12-42 present the axial annulus air density profile for the [ ]^{a,c} and [ ]^{a,c} clime cases at transient time t=0, 30, 1500, and 43500 seconds. The profiles are similar.

Figures 12-43 and 12-44 present the axial annulus air velocity profile for the [ ]^{a,c} and [ ]^{a,c} clime cases at transient time t=0, 30, 1500, and 43500 seconds. The profiles are similar. The air velocity decreases at the tope of the riser as it enters the large open area above the dome.

Comparisons of the transient heat rate and heat releases integrated over height of the model are shown in Figures 12-45 and 12-46. Again, there is essentially no difference between the two cases.

By this comparison, it is concluded that the transient pressure and shell heat removal rates calculated by the AP600 containment model are not sensitive to the number of climes.

Stack Sensitivity Results

The number of stacks of climes in the base model were doubled (while maintaining the same total heat transfer area) and the case was run using WGOTHIC, Version 4.1. Figure 12-47 shows a comparison of the transient pressure for the double stack case with the base case. There is essentially no difference between the two cases. Comparisons of the transient heat rate and heat releases integrated over the height of the model are shown in Figures 12-48 and 12-49. Again, there is essentially no difference between the two cases.

These comparisons show the transient pressure and shell heat removal rate calculated by the AP600 containment model are not sensitive to the number of stacks.

Clime Conductor Numerical Mesh Point Sensitivity Results

The number of numerical solution mesh points through the thickness of each of the three conductors (shell, baffle, and concrete) that make up each clime in the base model was doubled and the case was run using WGOTHIC Version 4.1. Figure 12-50 shows a comparison of the transient pressure for the double mesh case with the base case. There is essentially no difference between the two cases. Comparisons of the transient

heat rate and heat releases integrated over the height of the model is shown in Figures 12-51 and 12-52. Again, there is essentially no difference between the two cases.

From these comparisons, it is concluded that the transient pressure and shell heat removal rates calculated by the AP600 containment model are not sensitive to the number of numerical mesh points within the conductors that comprise each clime.

12.4 SUMMARY

12.4.1 Simple Annulus Clime Model Noding Study

A two-channel annulus model was exercised over a range of film flow rates, and film temperatures with the code calculating air velocities associated with natural draft heating. For the cases considered, increasing the number of climes was observed to have no significant effect on the predicted heat removal rate. That is, the predicted heat removal rate was insensitive to the number of clime nodes used in the model. The predicted heat removal rate converges in all cases considered. Increasing the number of climes resulted in smoother axial heat flux and film temperature profiles for the wet tests. Adequate axial heat flux and temperature profiles were predicted without increasing the number of climes for the dry cases.

12.4.2 AP600 Containment Model Clime Noding Study

Using an AP600 containment model similar to, but not exactly the same as the Evaluation Model, the effect of doubling the number of clime nodes, doubling the number of stacks, and doubling the number of conductor mesh points was studied. In each case, code calculations were found to be unaffected by the variations in the model features.

These studies demonstrate that results obtained with the AP600 containment model are not sensitive to changes in the clime and annulus noding. Therefore, it is concluded that [ ]^{a,c} climes are adequate to predict the PCS performance for the Evaluation Model.

12.5 REFERENCES

12.1 Westinghouse Letter NTD-NRC-95-4563, B. A. McIntyre to T. R. Quay (NRC), "GOTHIC Version 4.0 Documentation," September 21, 1995.

12.2 Westinghouse Letter NTD-NRC-95-4462, N. J. Liparulo to T. R. Quay (NRC), EPRI Report RA-93-10, "GOTHIC Design Review, Final Report," May 15, 1995.

12.3 WCAP-14812, Revision 2, "Accident Specification and Phenomena Evaluation for AP600 Passive Containment Cooling System," April 1998.

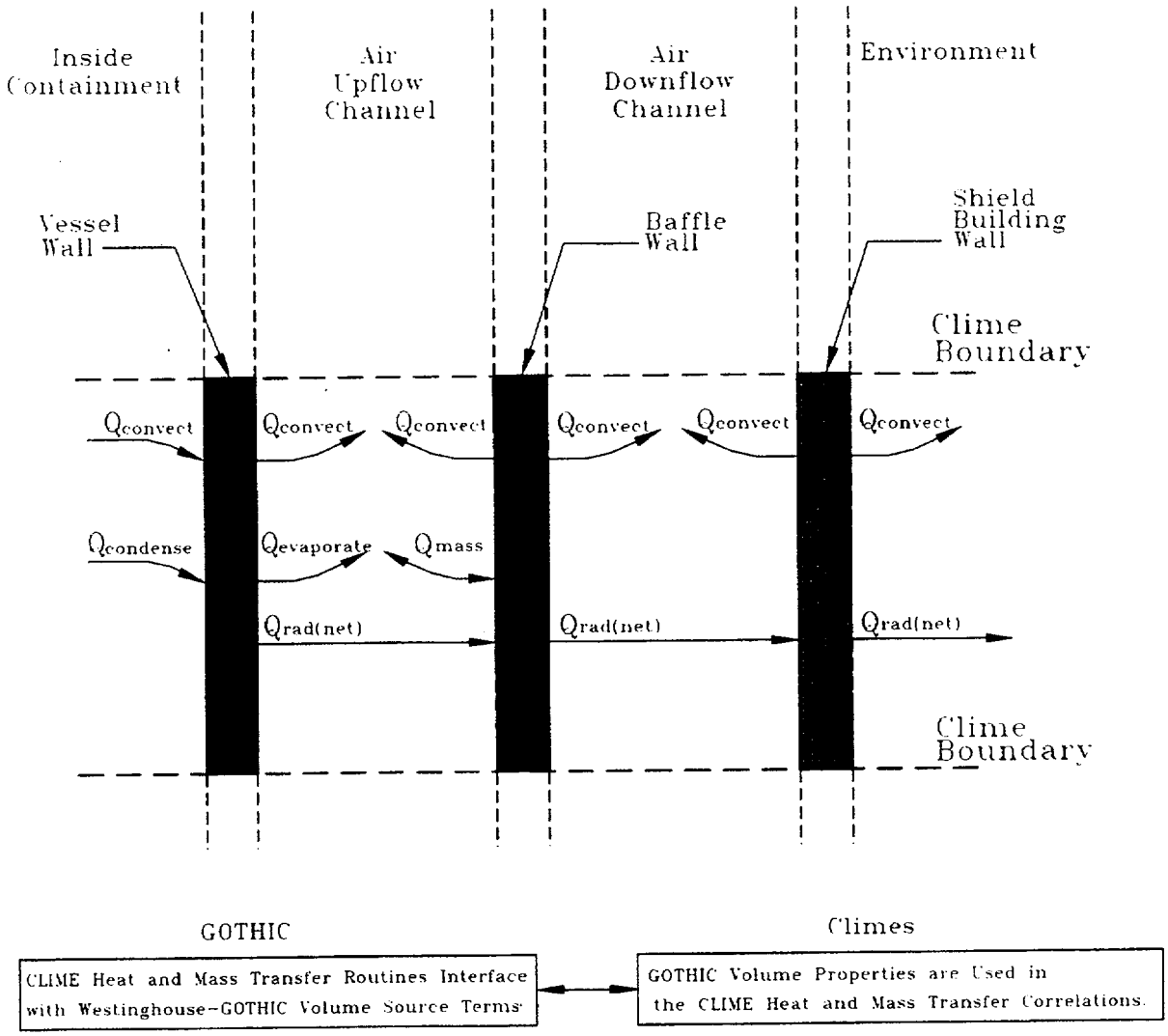

Figure 12-1 Westinghouse-GOTHIC Clime Wall Source Term Models

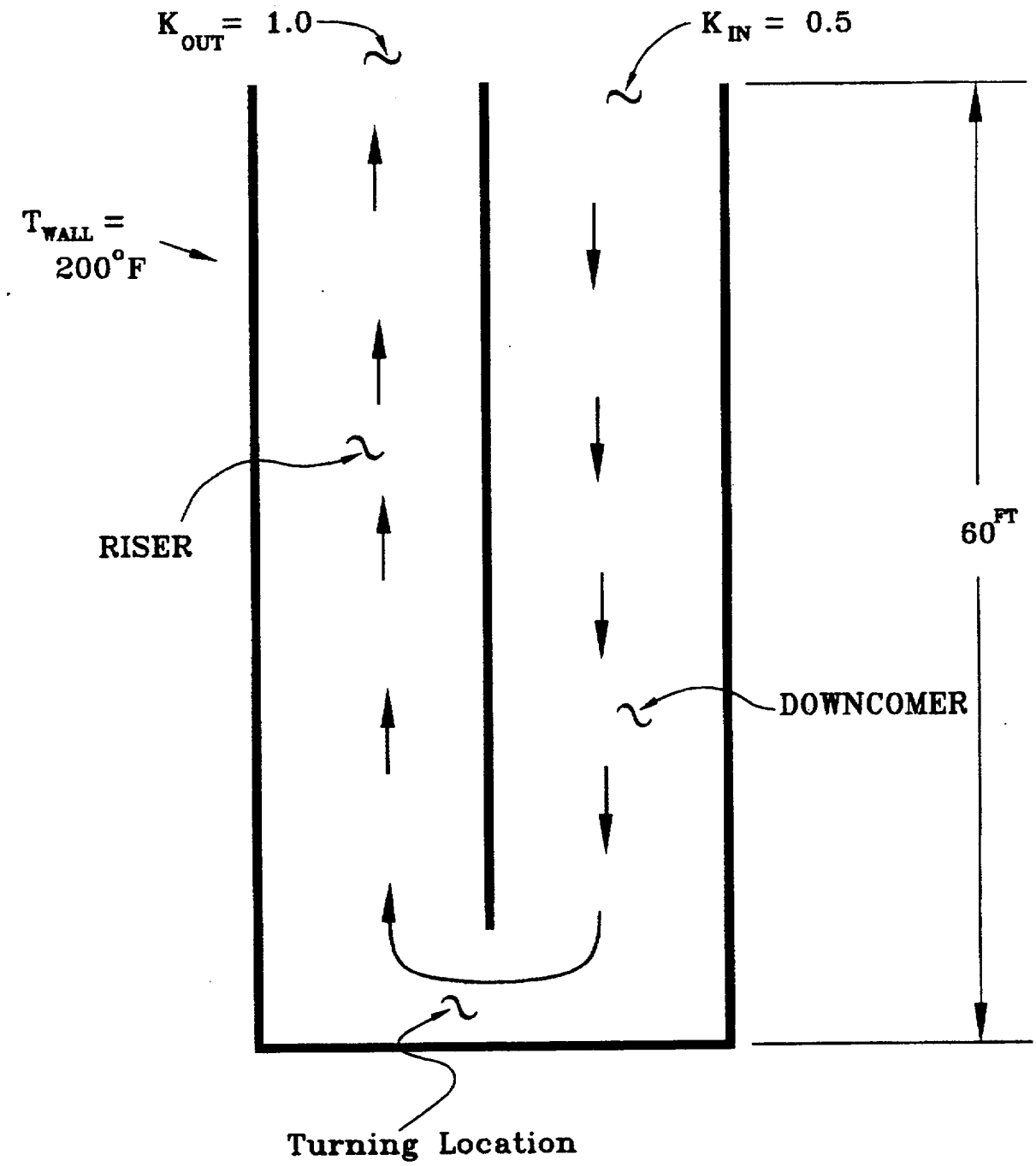

Figure 12-2 Simplified Line Diagram of Annulus Clime Model

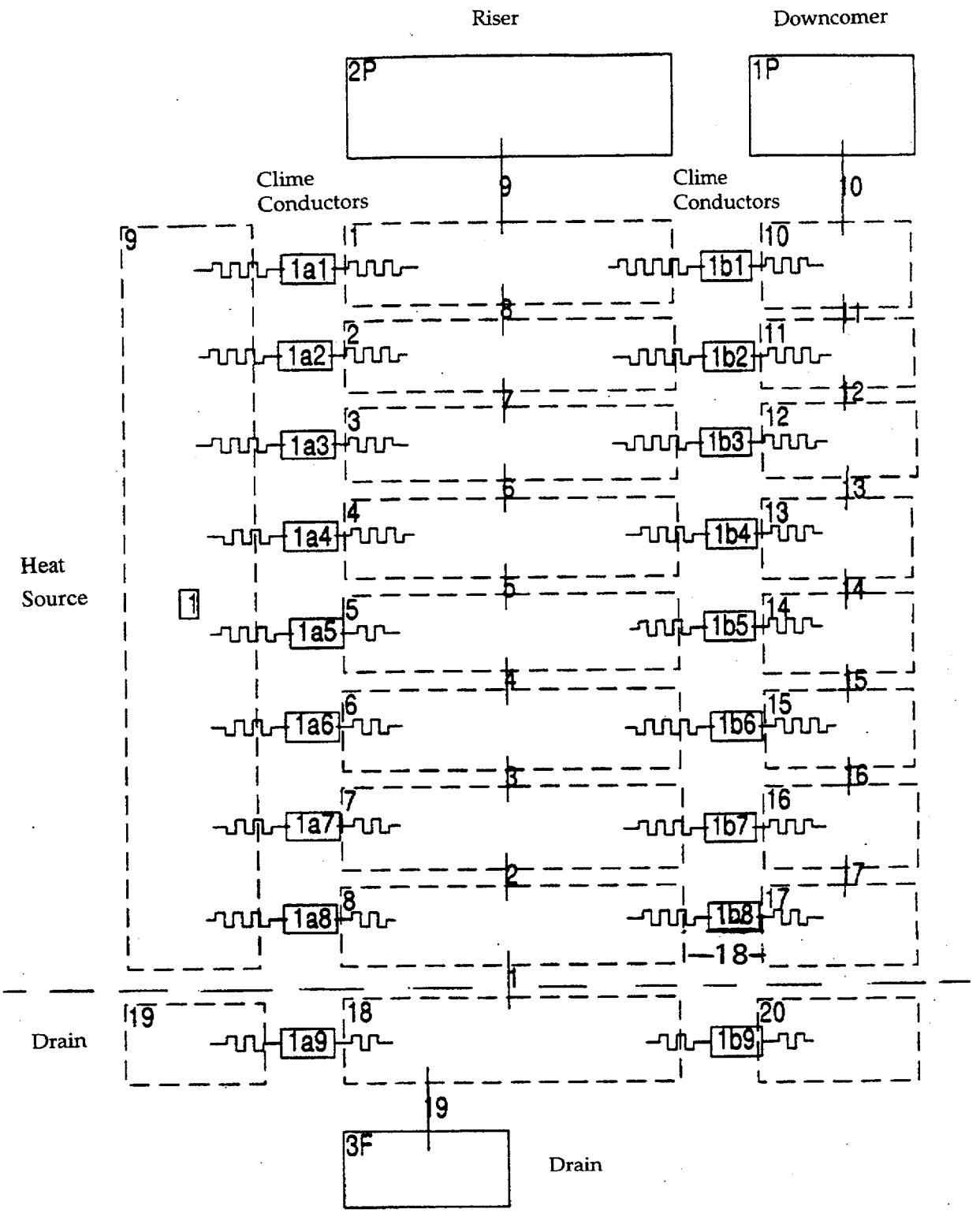

Figure 12-3 Noding Diagram, 8 Clime Node Model

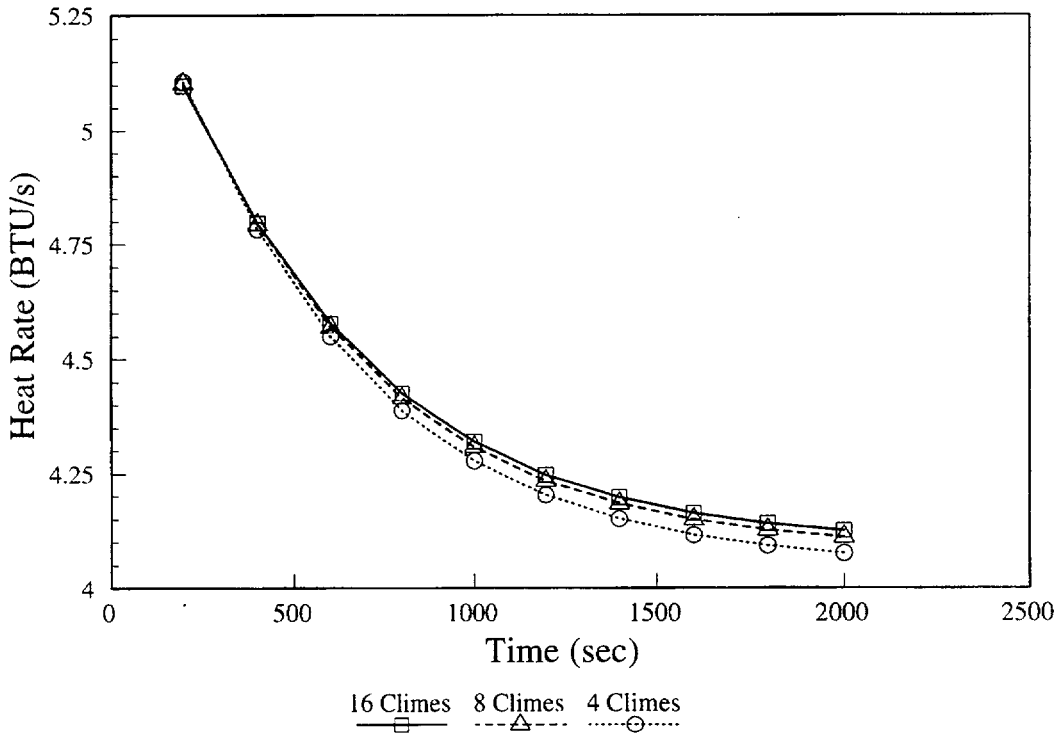

Figure 12-4 Comparison of Transient Heat Transfer Rates; Case 1

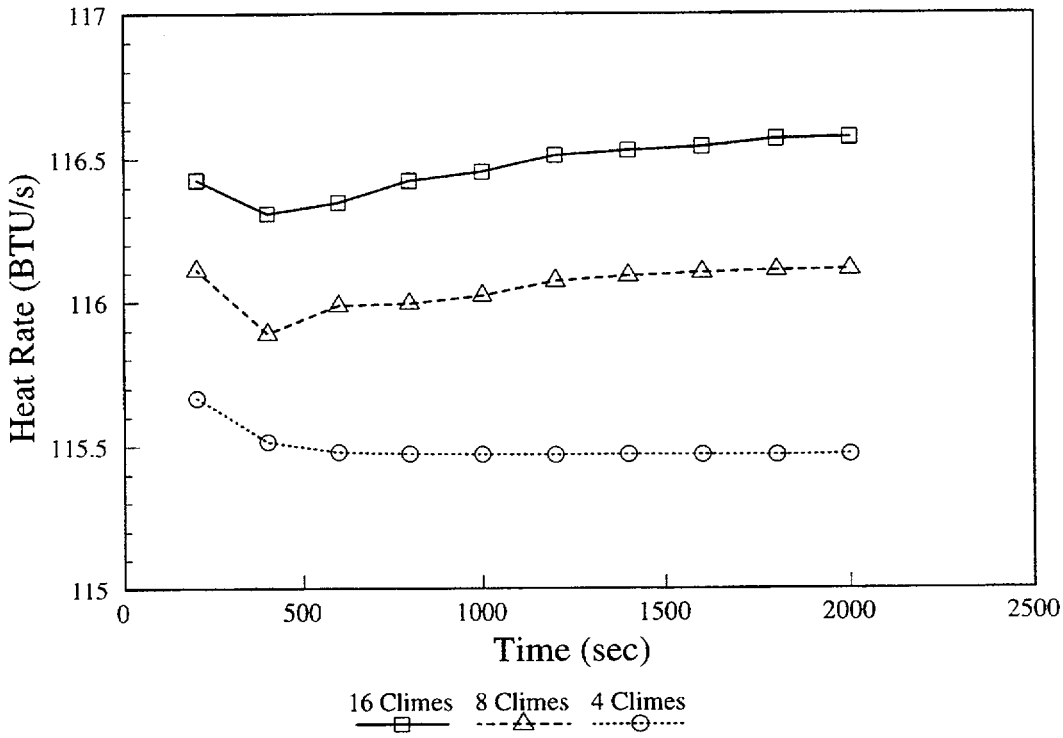

Figure 12-5 Comparison of Transient Heat Transfer Rates; Case 2

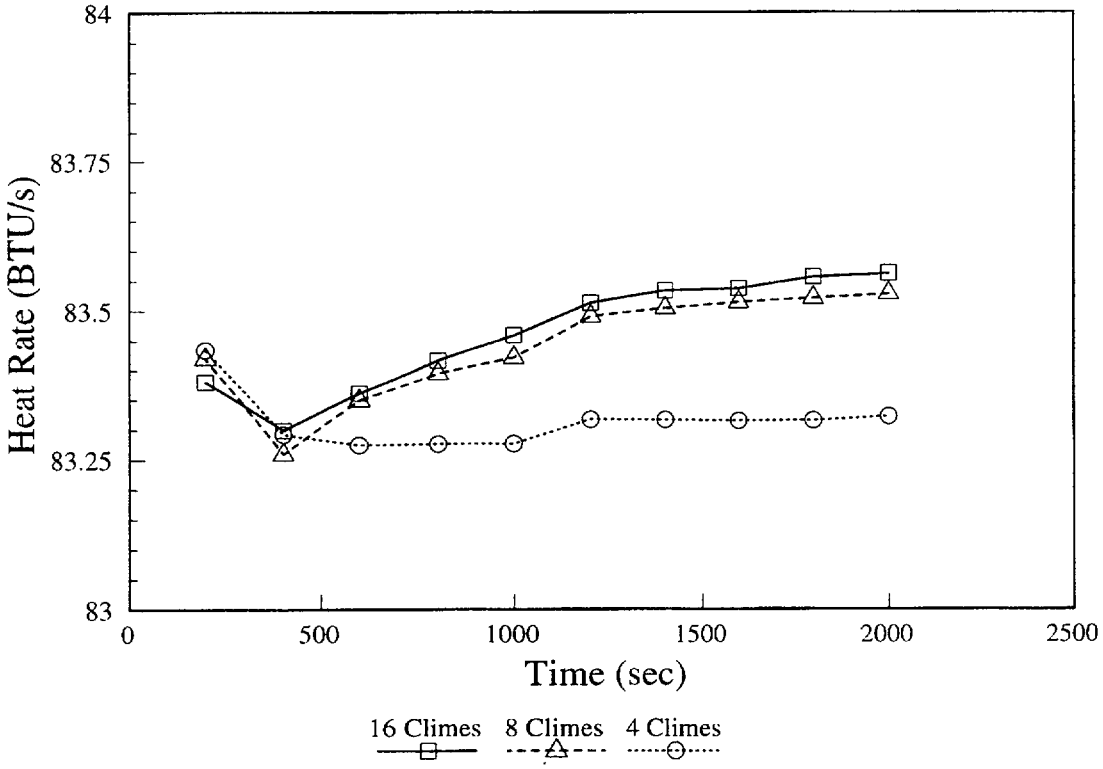

Figure 12-6 Comparison of Transient Heat Transfer Rates; Case 3

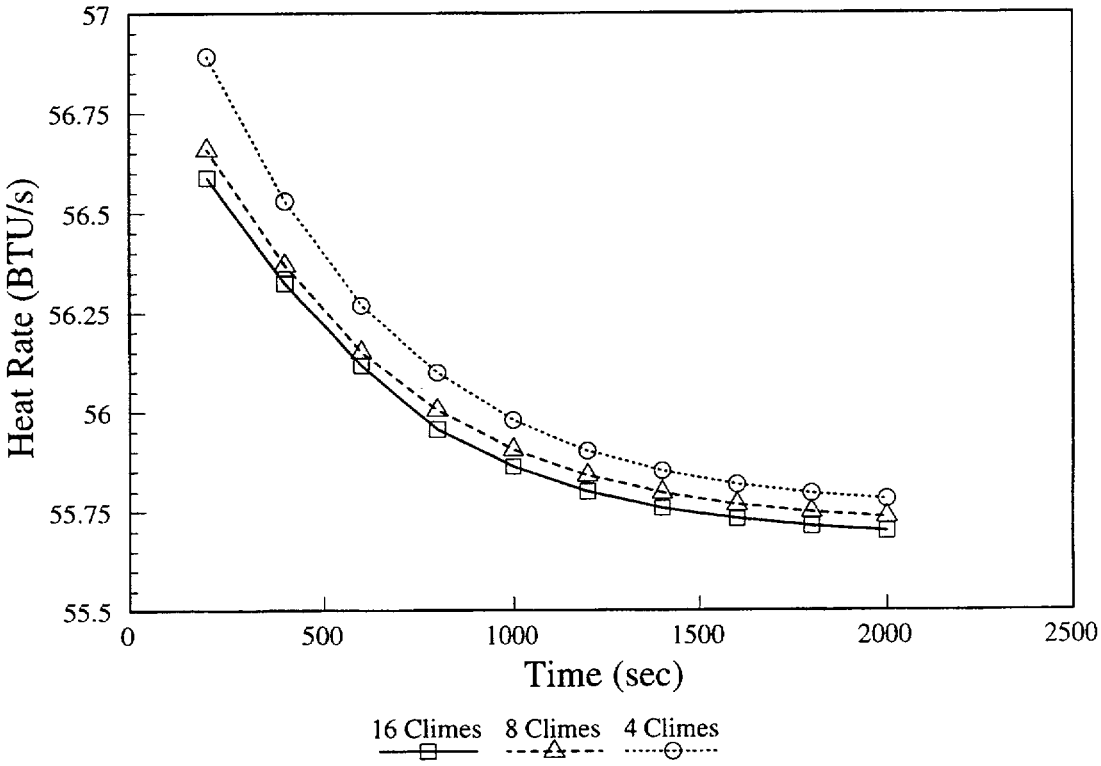

Figure 12-7 Comparison of Transient Heat Transfer Rates; Case 4

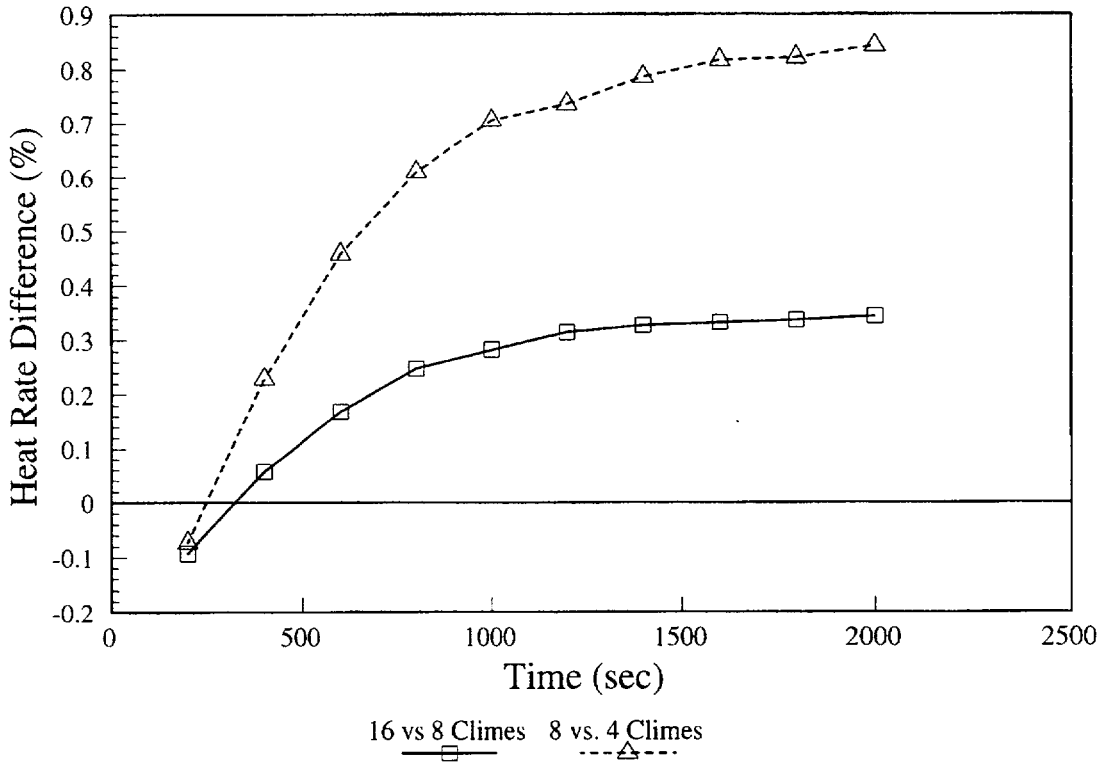

Figure 12-8 Comparison of Transient Heat Transfer Rate Differences; Case 1

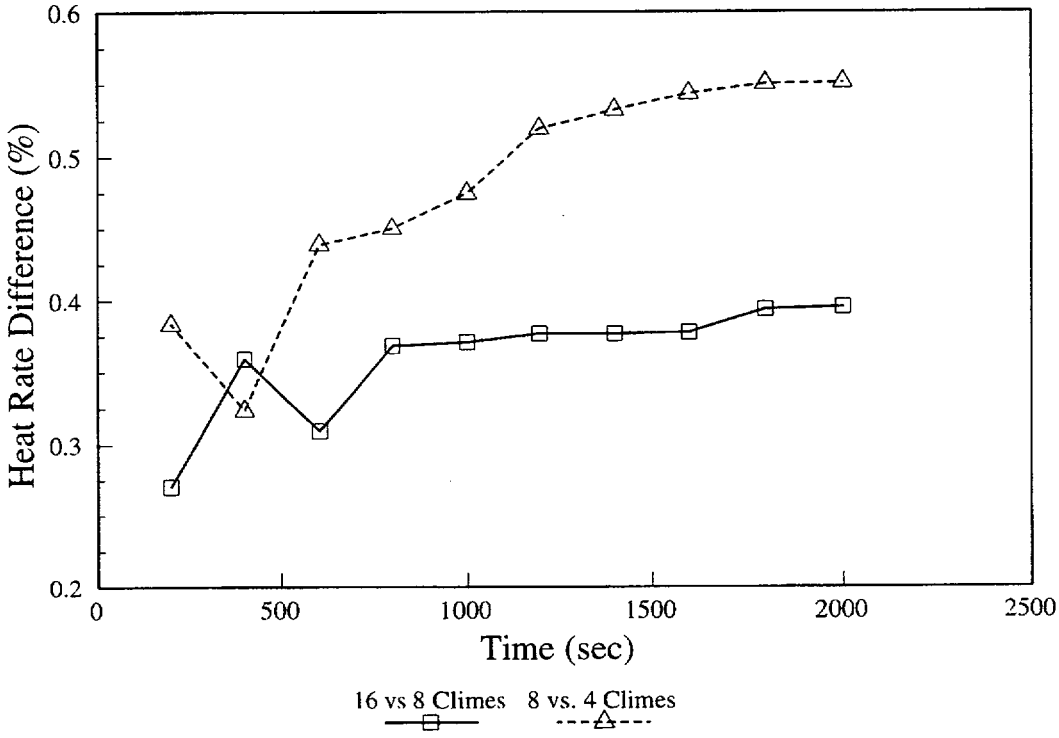

Figure 12-9 Comparison of Transient Heat Transfer Rate Differences; Case 2

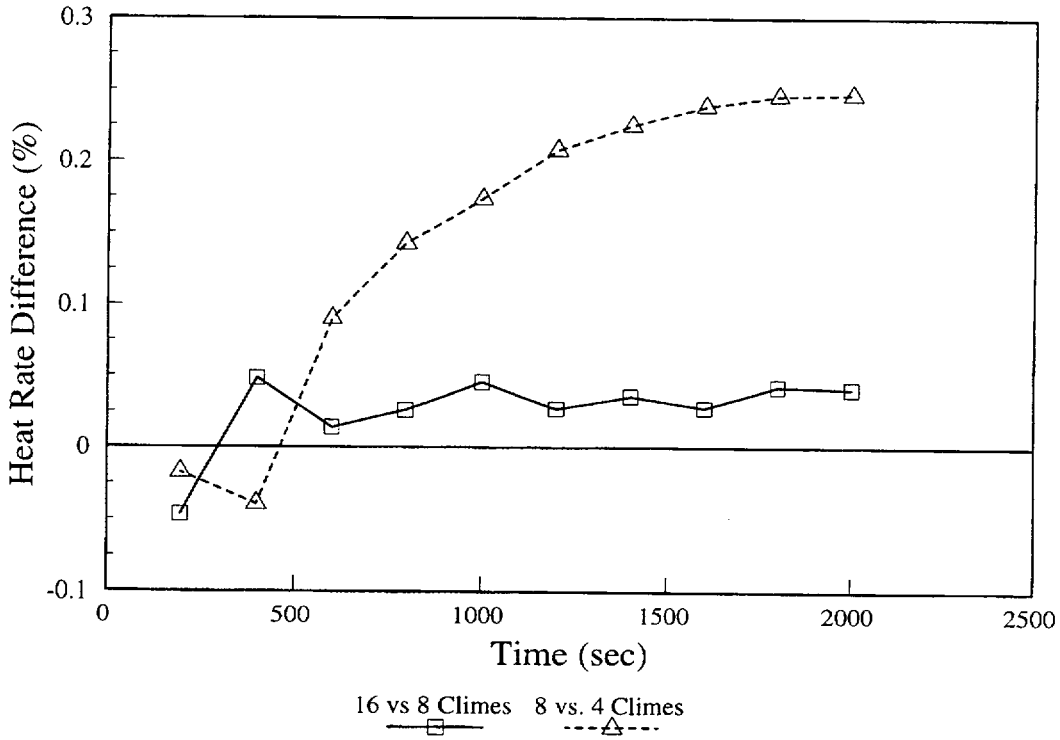

Figure 12-10 Comparison of Transient Heat Transfer Rate Differences; Case 3

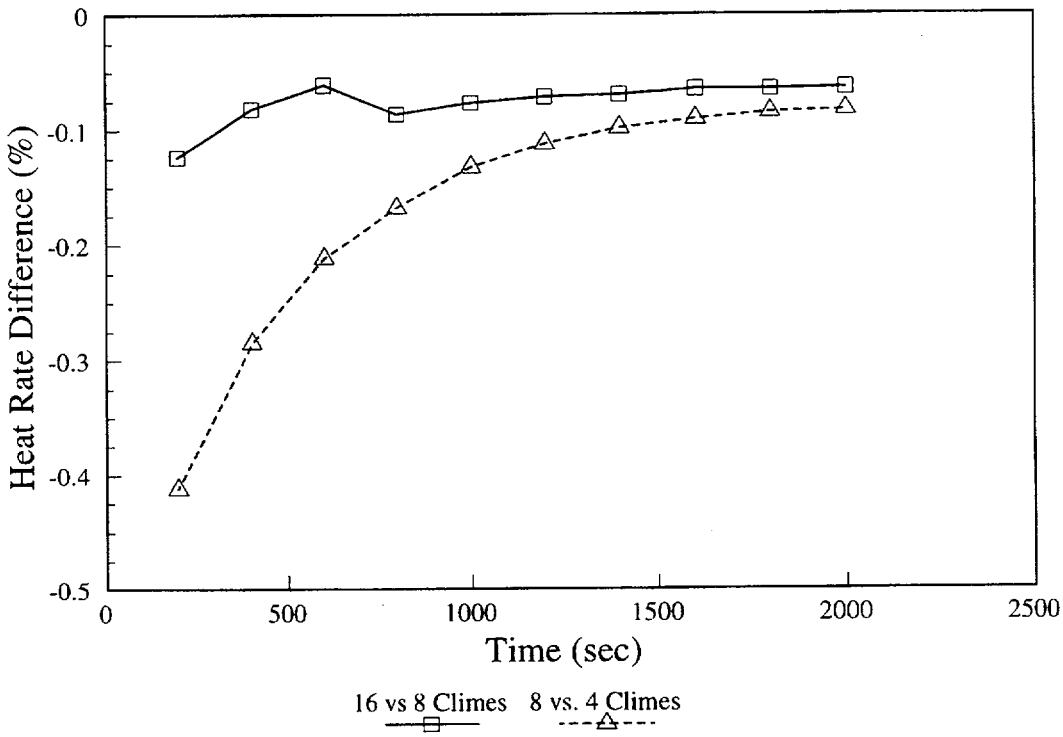

Figure 12-11 Comparison of Transient Heat Transfer Rate Differences; Case 4

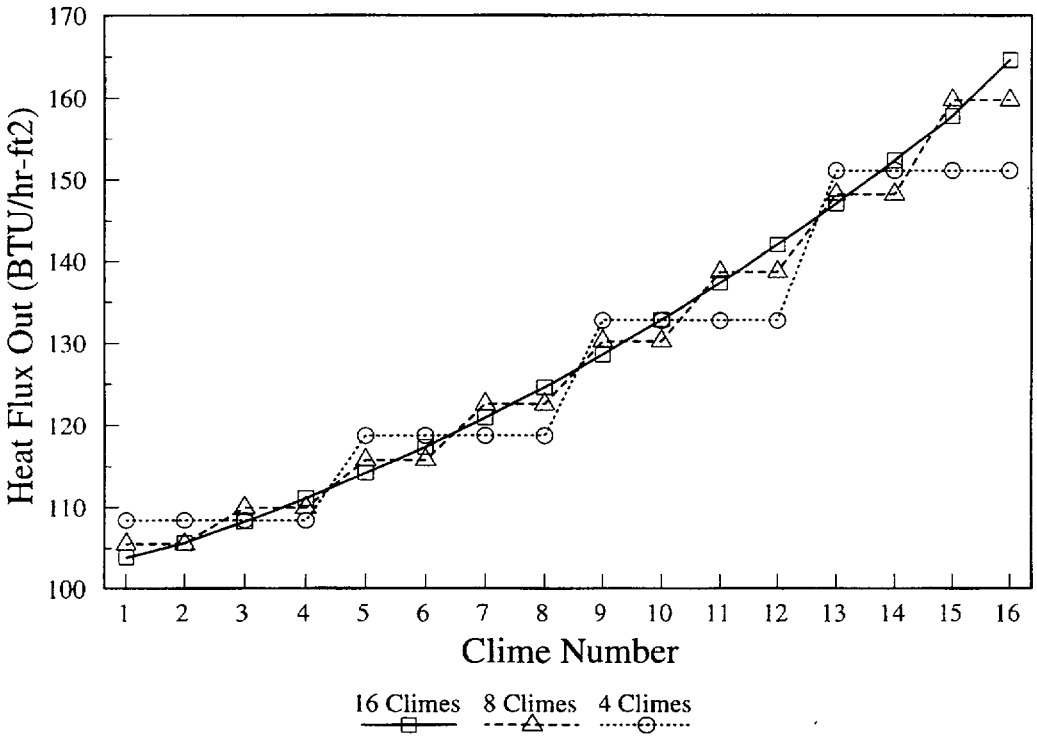

Figure 12-12 Comparison of Heat Flux Profiles; Time t = 2000 Seconds; Case 1

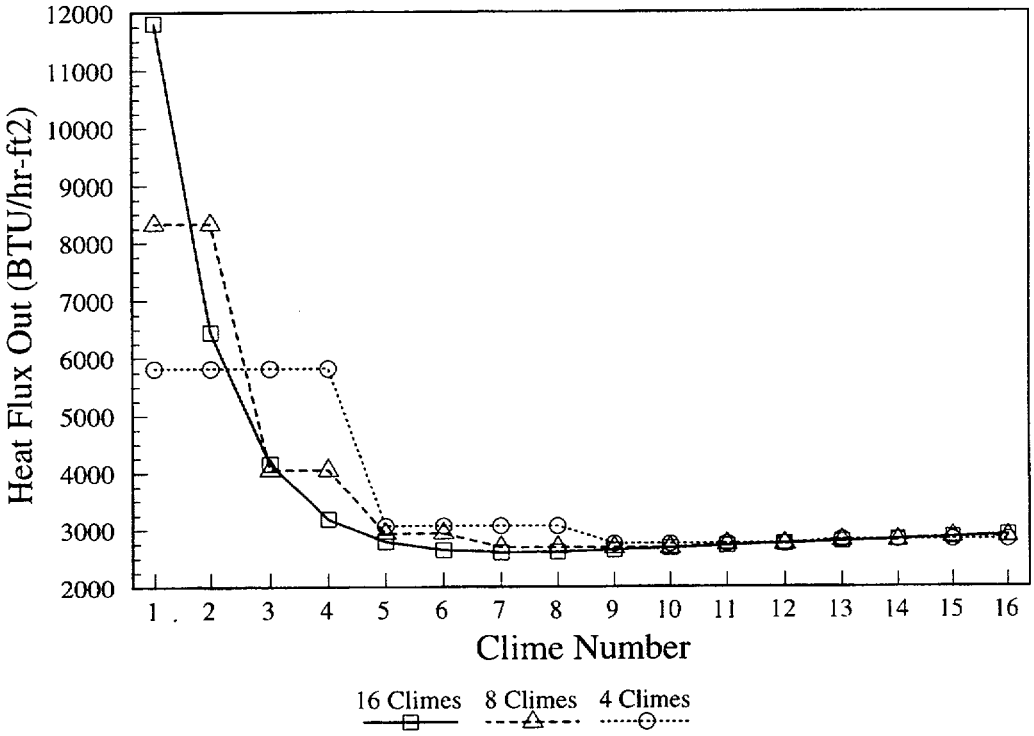

Figure 12-13 Comparison of Heat Flux Profiles; Time t = 2000 Seconds; Case 2

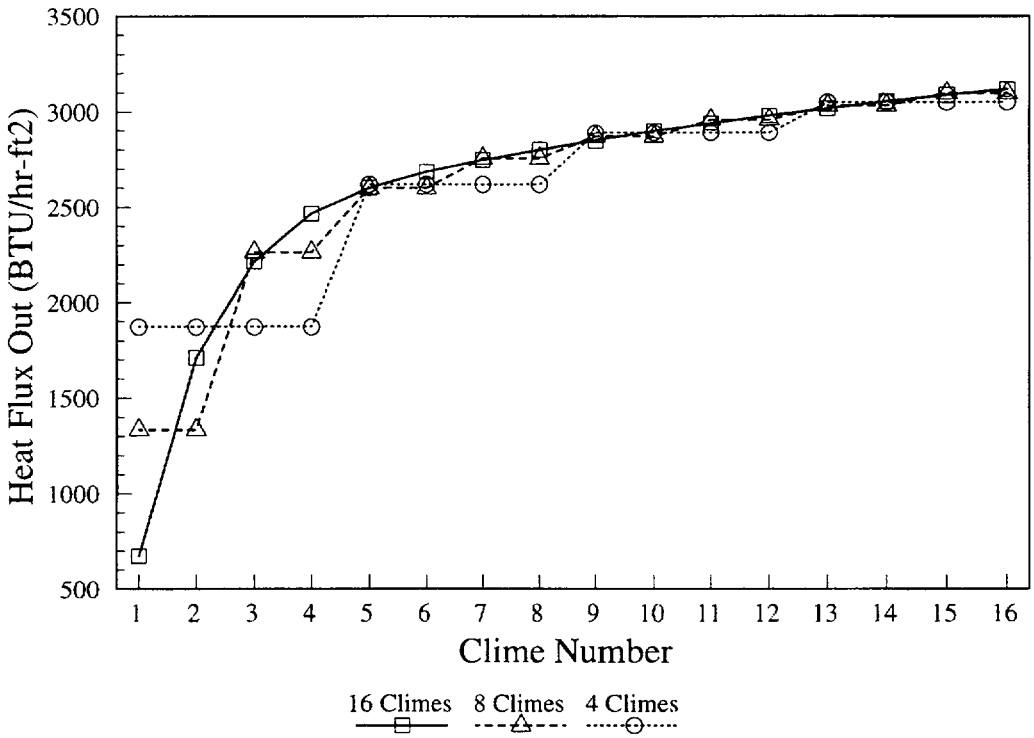

Figure 12-14 Comparison of Heat Flux Profiles; Time t = 2000 Seconds; Case 3

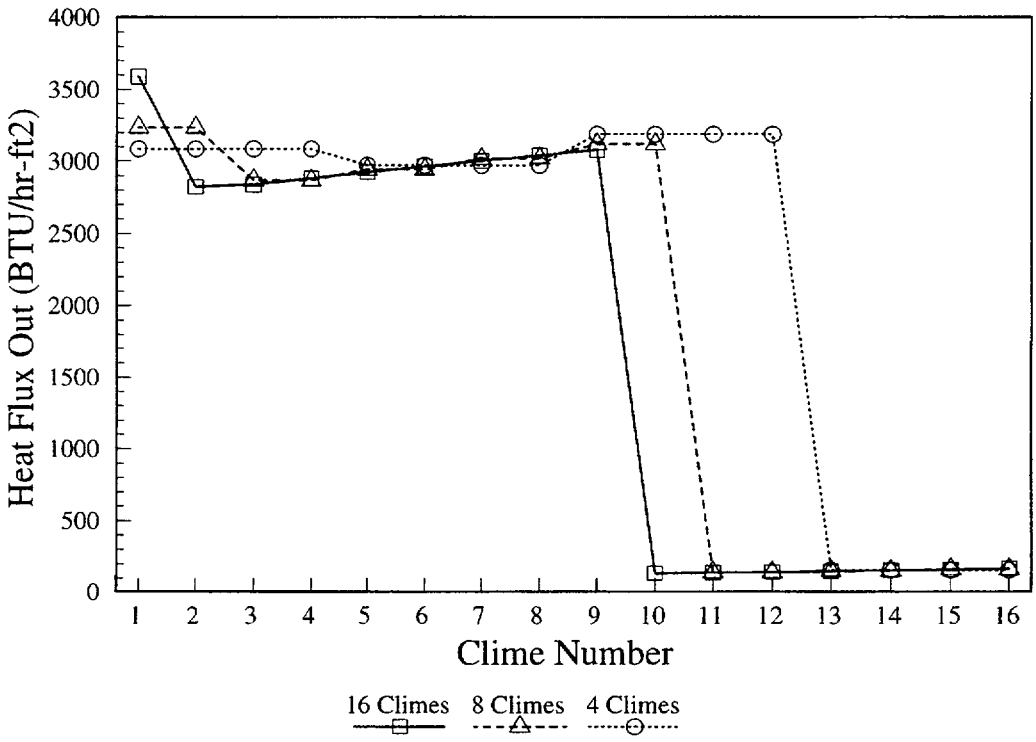

Figure 12-15 Comparison of Heat Flux Profiles; Time t = 2000 Seconds; Case 4

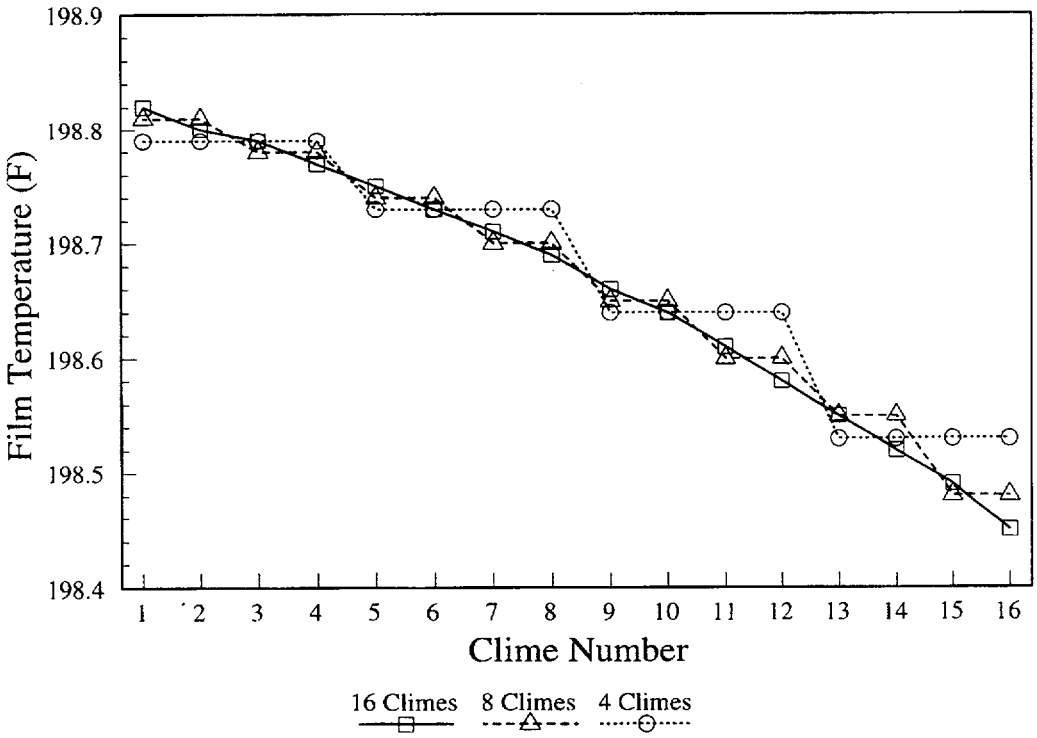

Figure 12-16 Comparison of Film Temperature Profiles; Time t = 2000 Seconds; Case 1

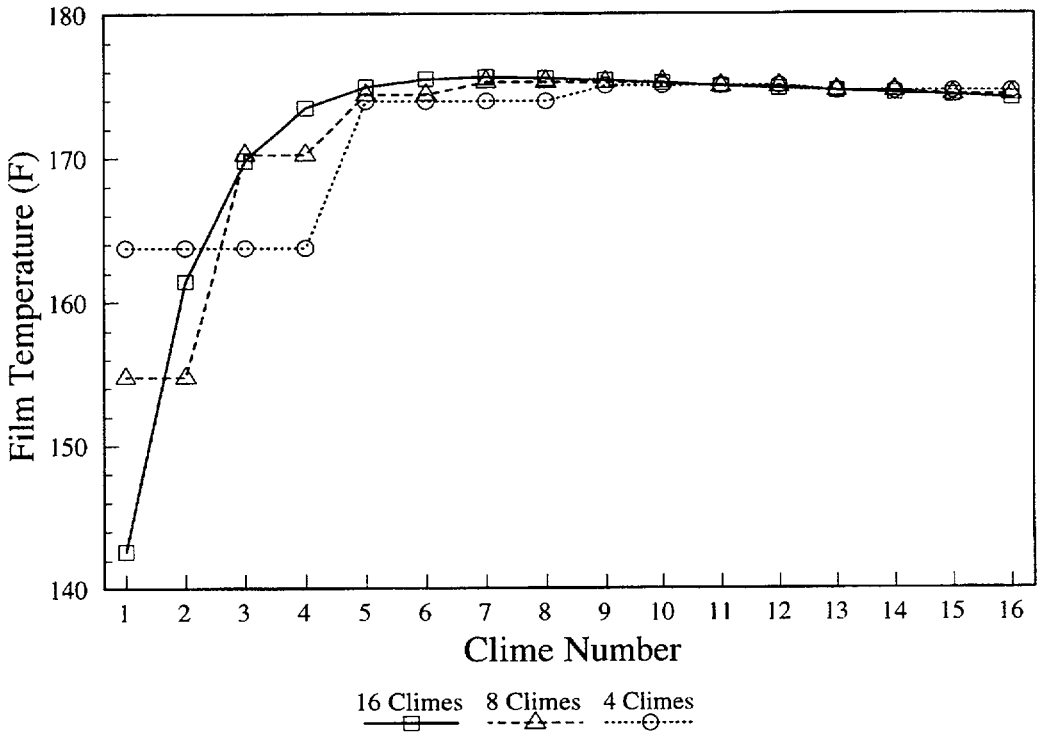

Figure 12-17 Comparison of Film Temperature Profiles; Time t = 2000 seconds; Case 2

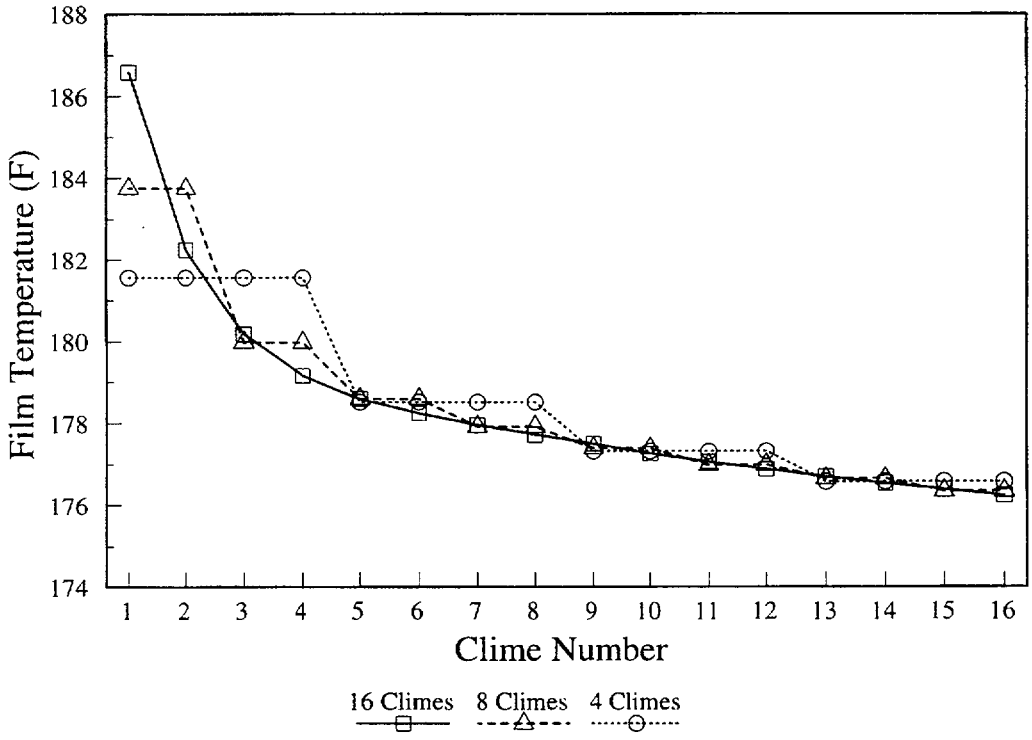

Figure 12-18 Comparison of Film Temperature Profiles; Time t = 2000 seconds; Case 3

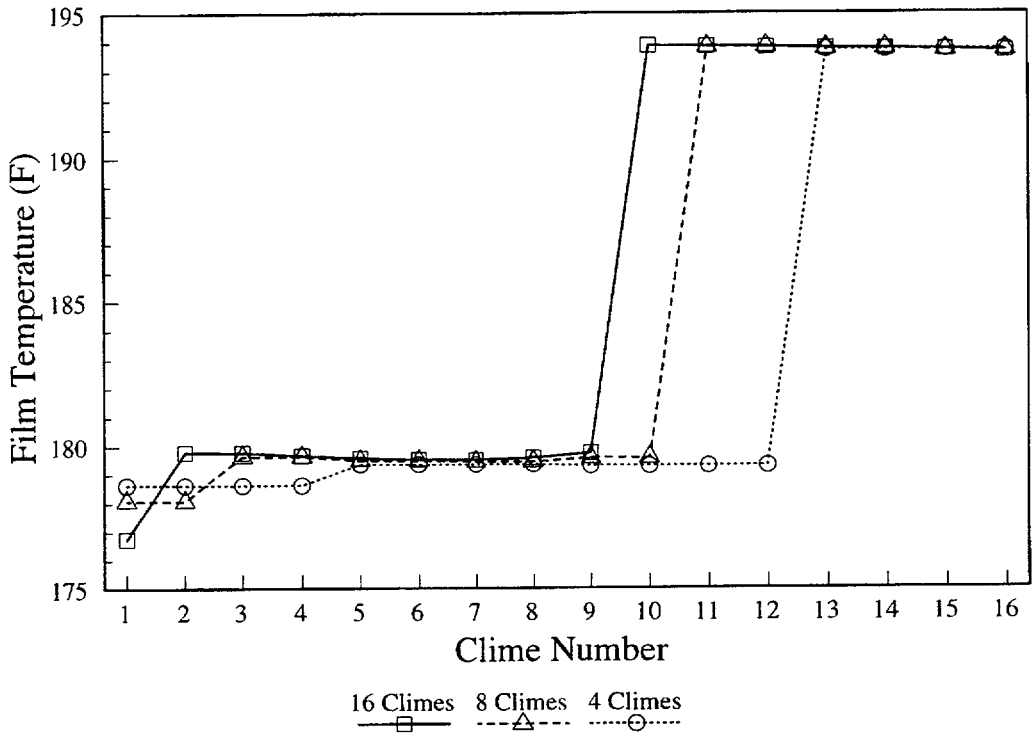

Figure 12-19 Comparison of Film Temperature Profiles; Time t = 2000 seconds; Case 4

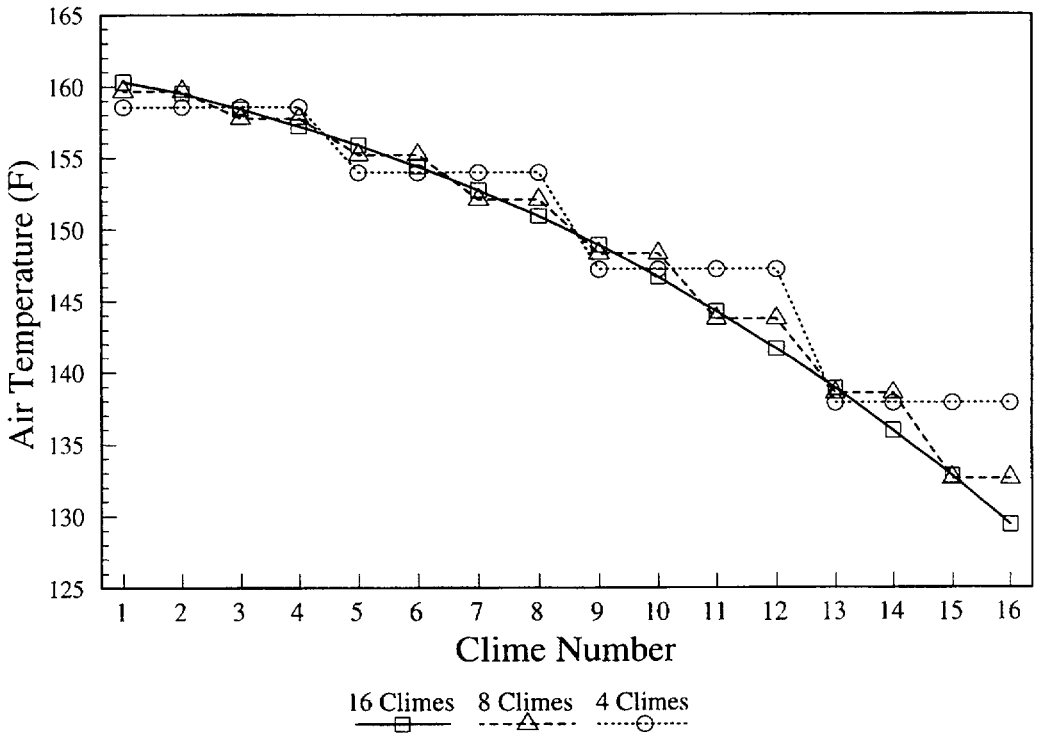

Figure 12-20 Comparison of Air Temperature Profiles; Time t = 2000 seconds; Case 1

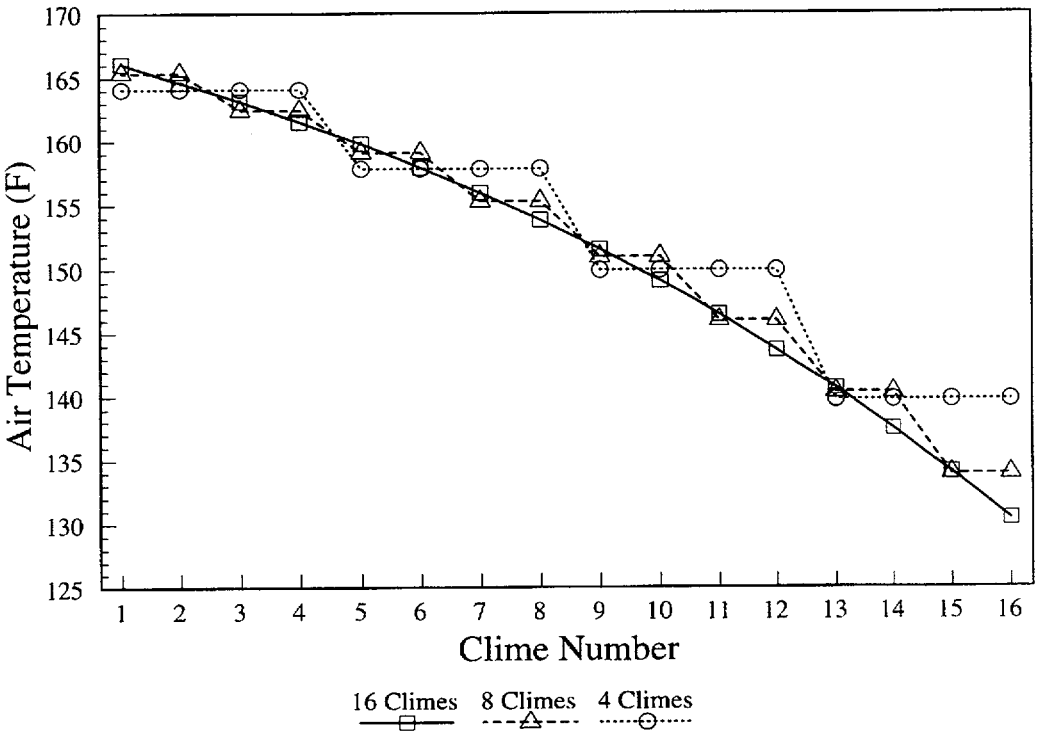

Figure 12-21 Comparison of Air Temperature Profiles; Time t = 2000 seconds; Case 2

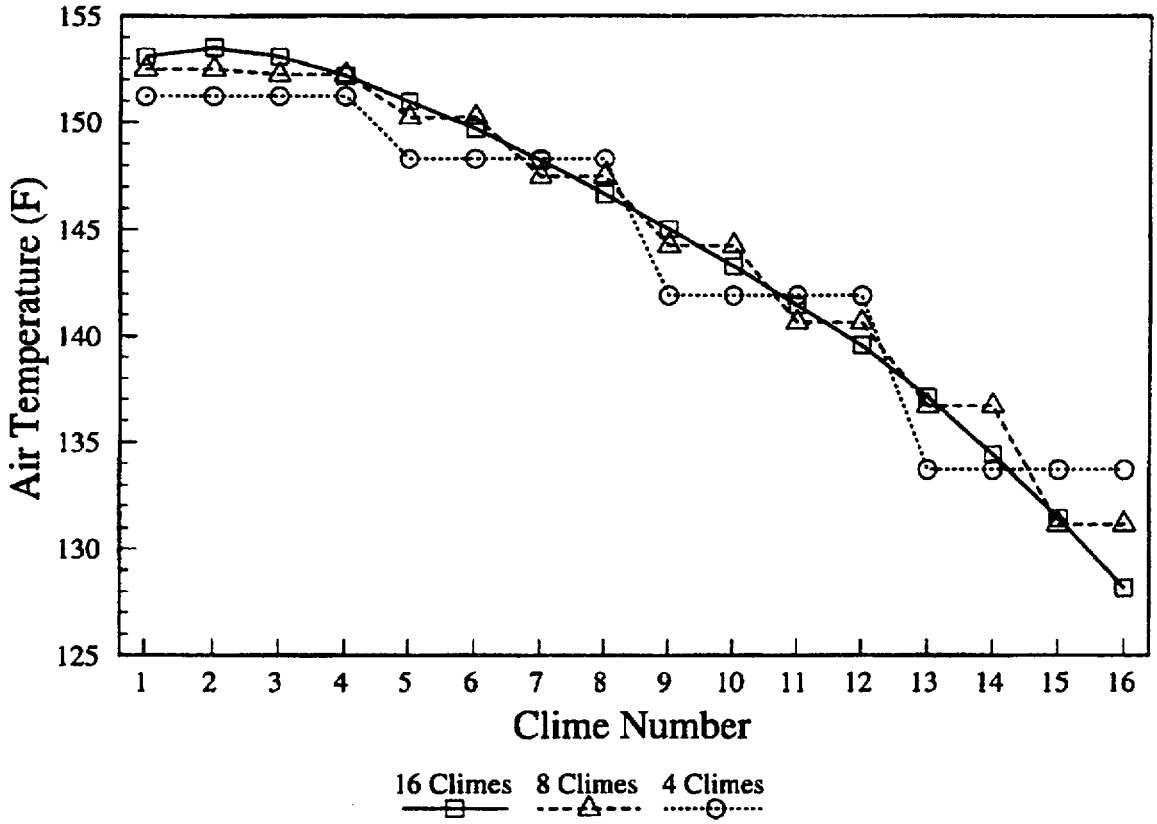

Figure 12-22 Comparison of Air Temperature Profiles; Time t = 2000 seconds; Case 3

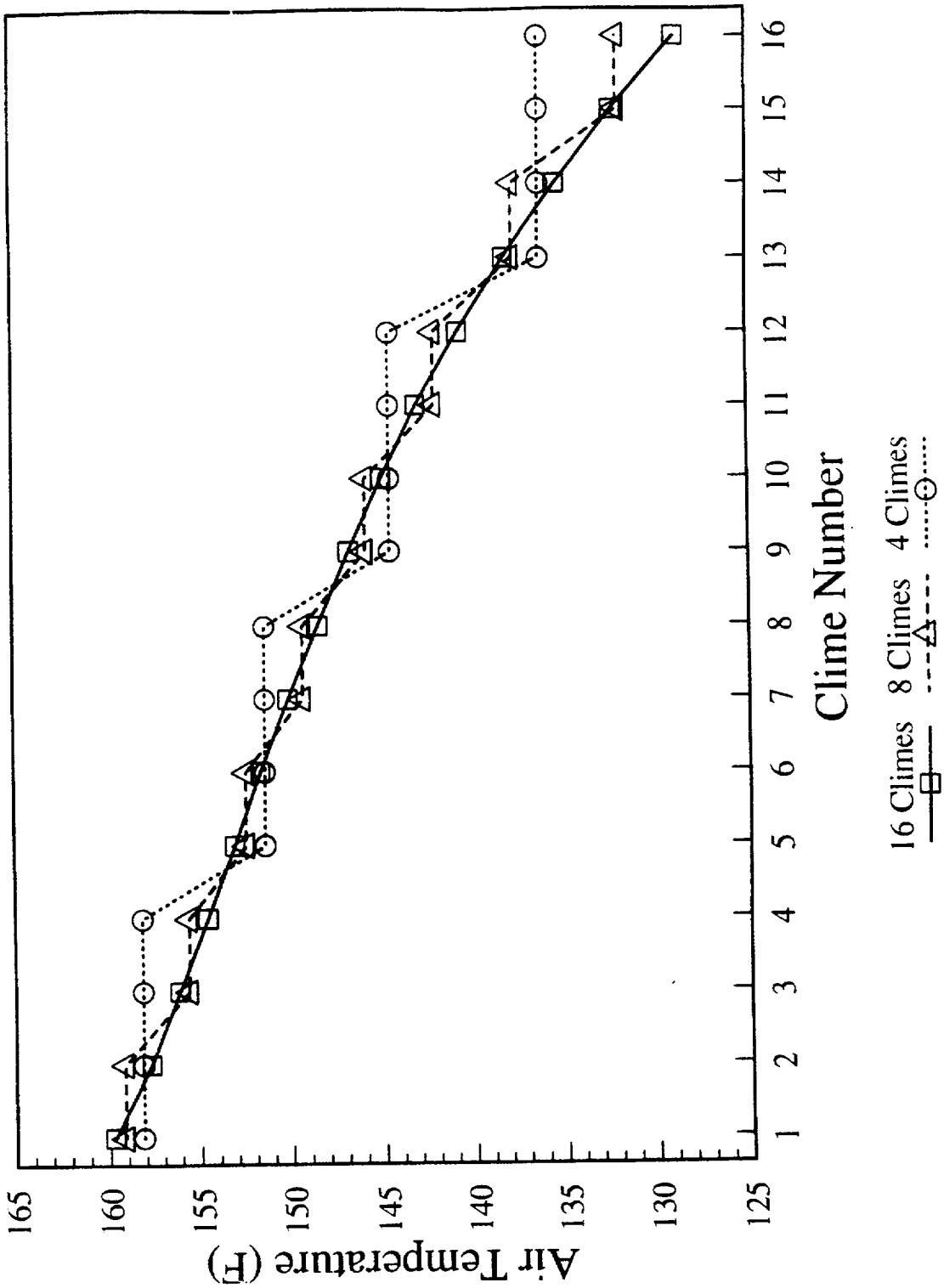

Figure 12-23 Comparison of Air Temperature Profiles; Time t = 2000 seconds; Case 4

(a,c)

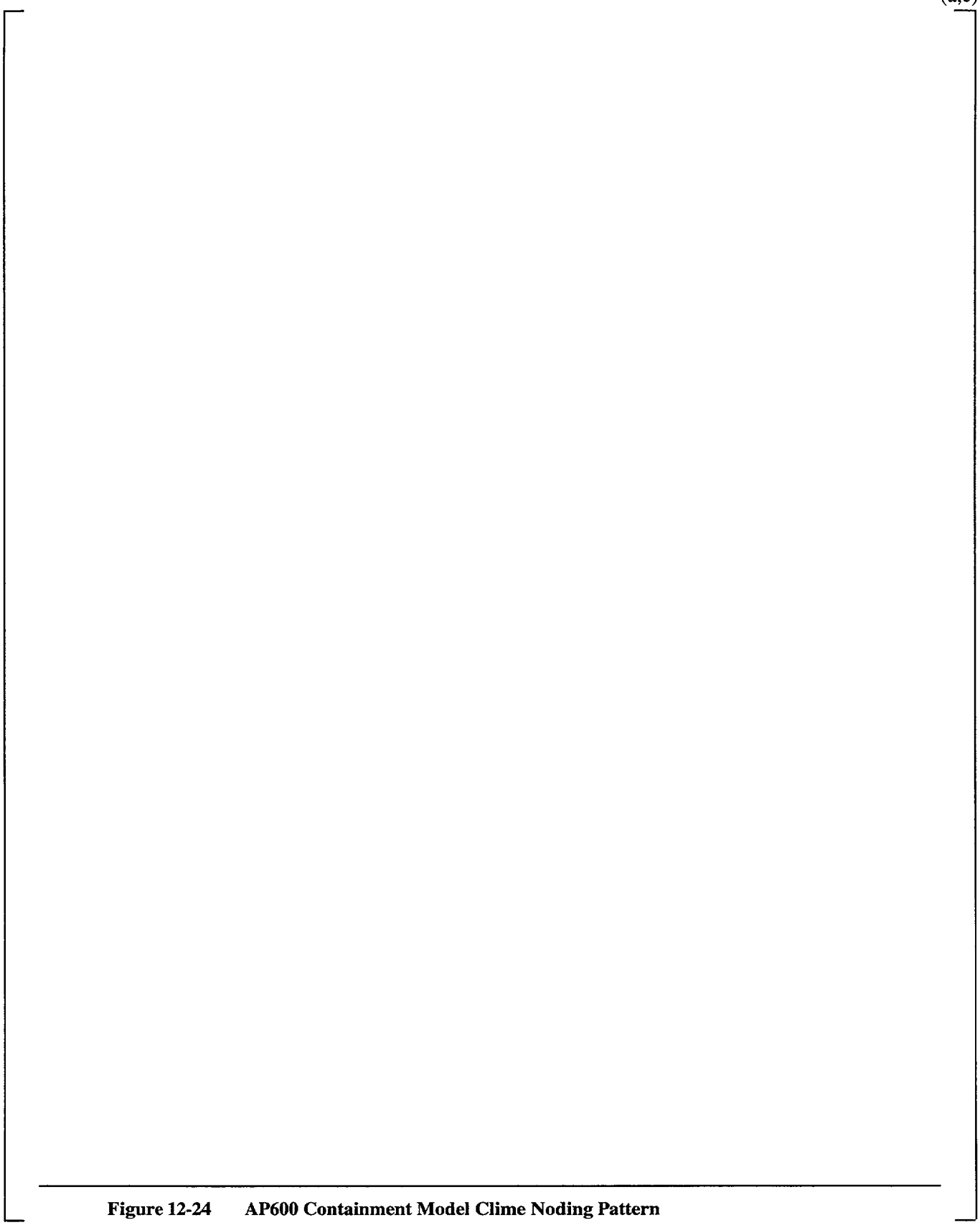

Figure 12-24 AP600 Containment Model Clime Noding Pattern

(a,c)

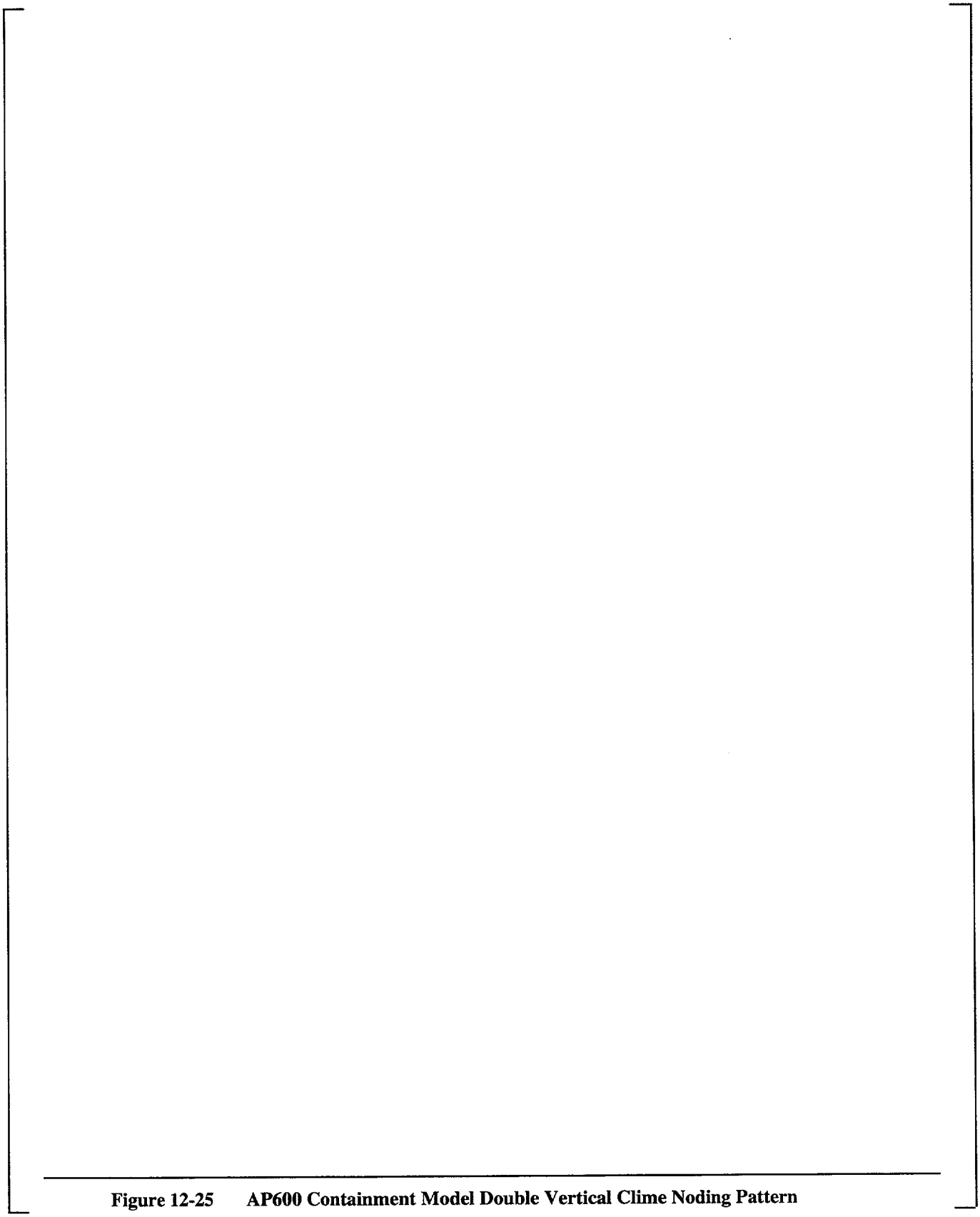

Figure 12-25 AP600 Containment Model Double Vertical Clime Noding Pattern

(a,c)

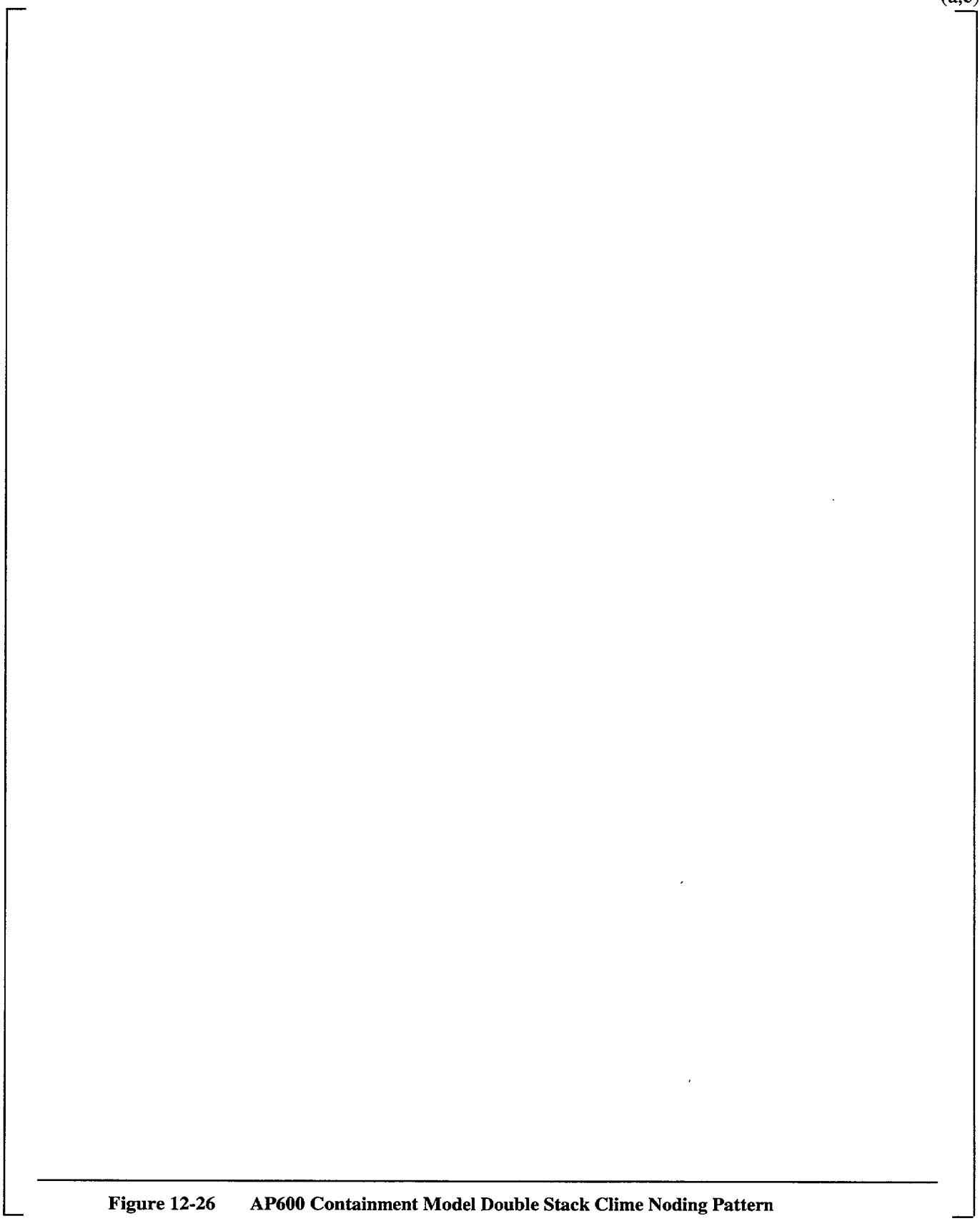

Figure 12-26 AP600 Containment Model Double Stack Clime Noding Pattern

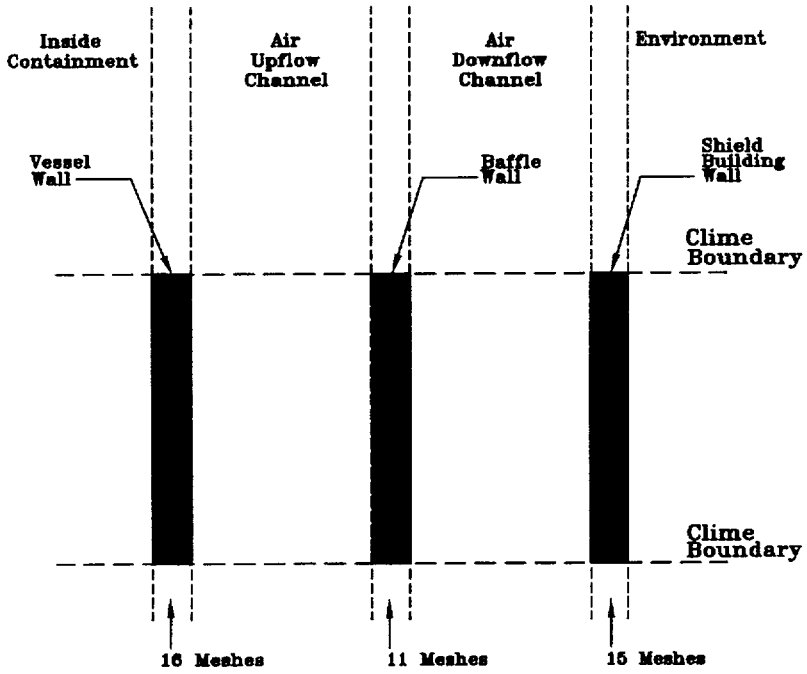

AP600 Containment Model

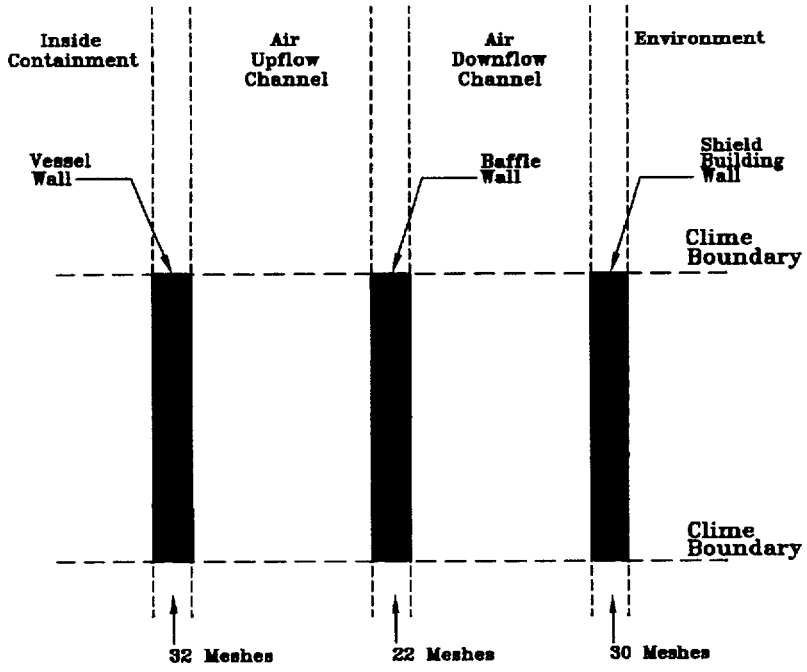

AP600 Mesh Sensitivity Model

Figure 12-27 AP600 Containment Model Double Mesh Point Clime Noding Pattern

(a,c)

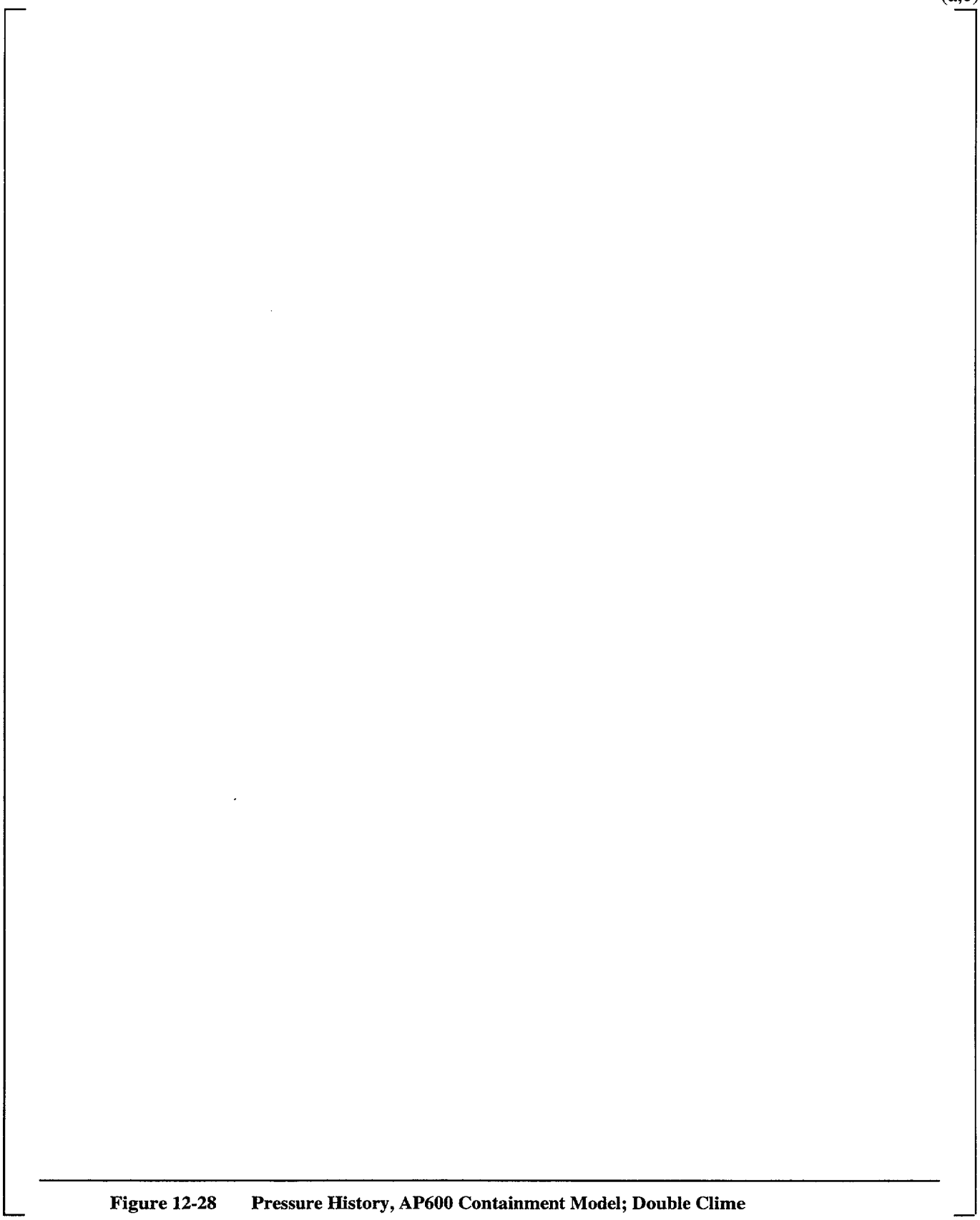

Figure 12-28 Pressure History, AP600 Containment Model; Double Clime

(a,c)

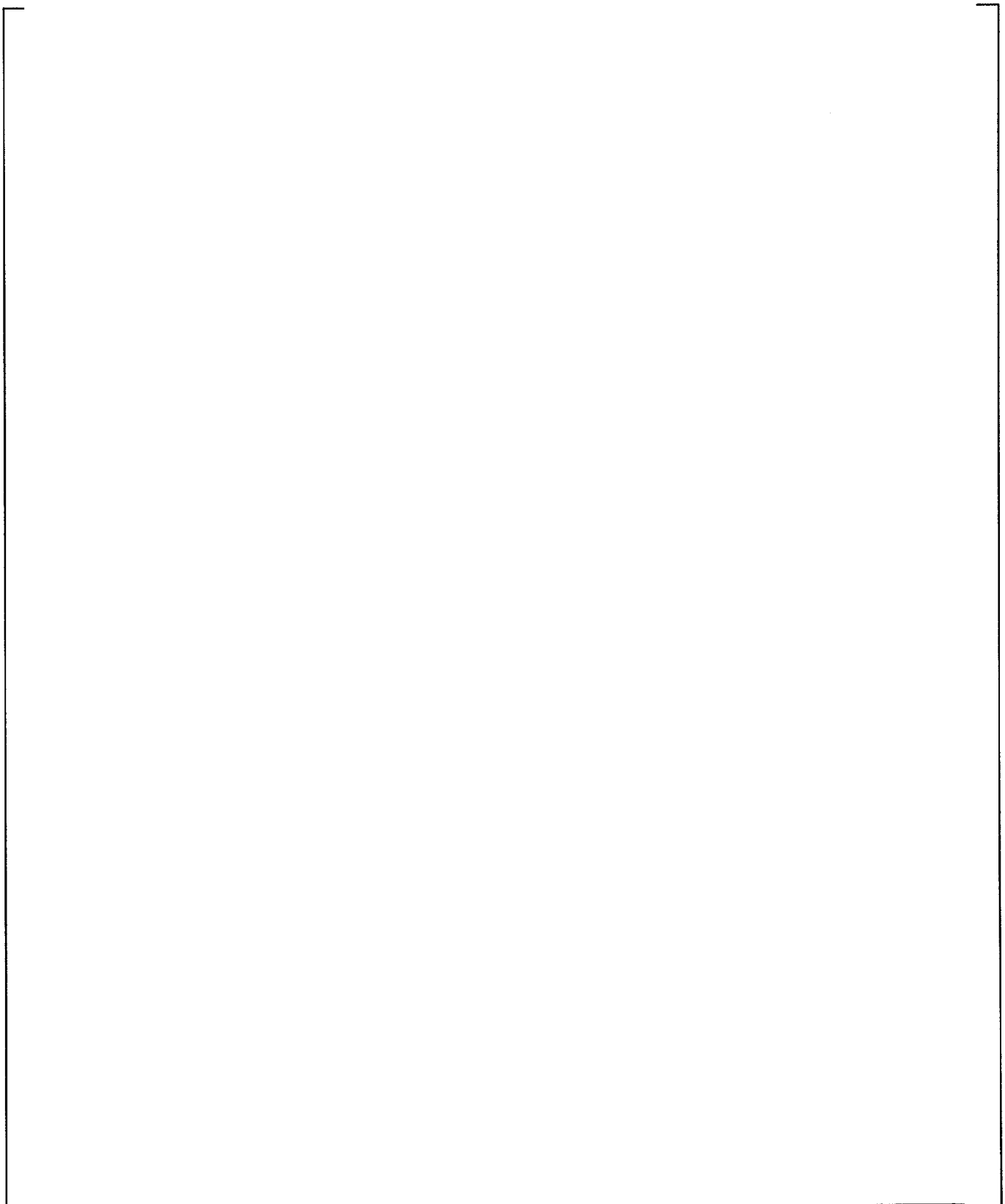

Figure 12-29 Wet Heat Flux vs. Clime; AP600 Containment Model, Base Case

(a,c)

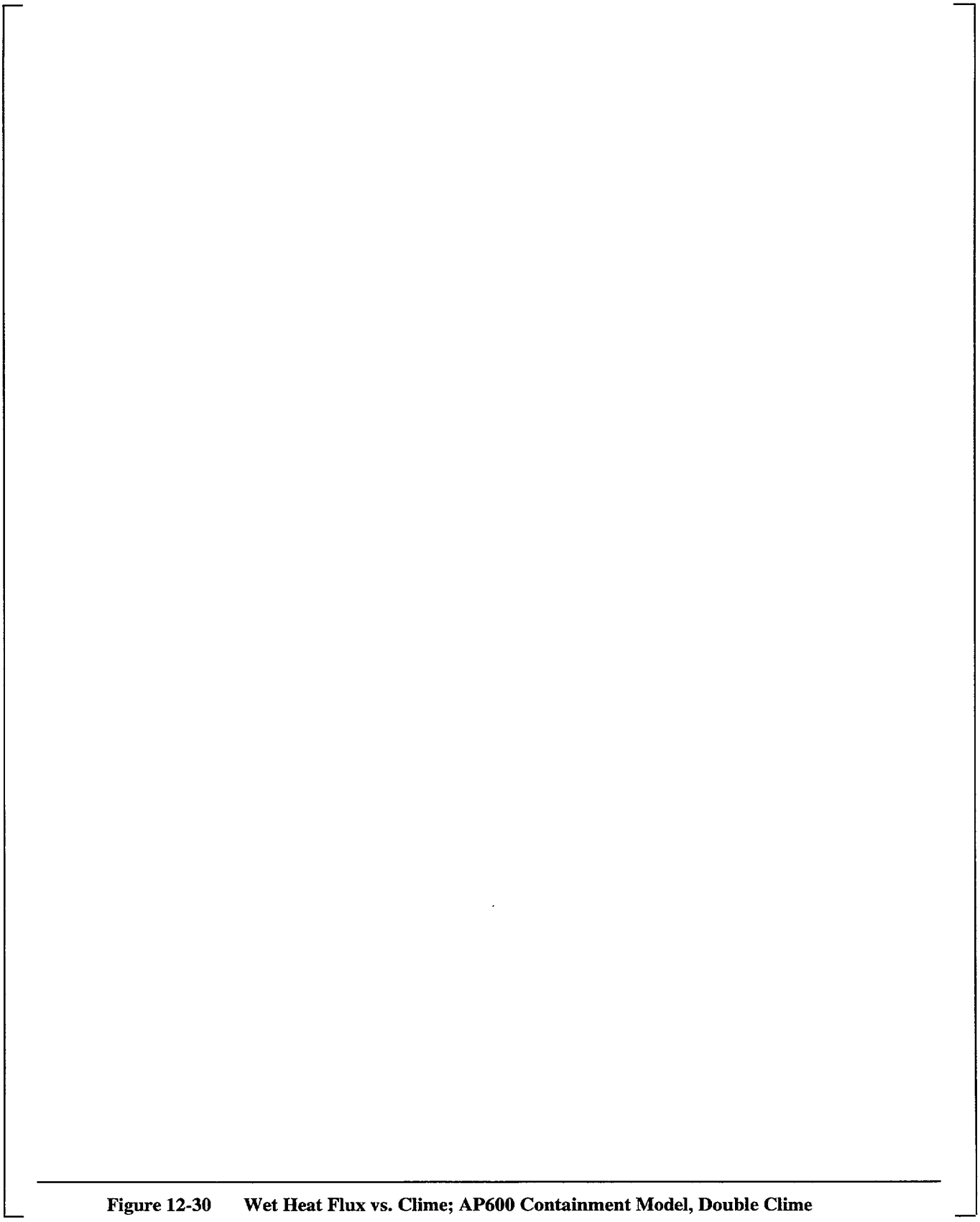

Figure 12-30 Wet Heat Flux vs. Clime; AP600 Containment Model, Double Clime

(a,c)

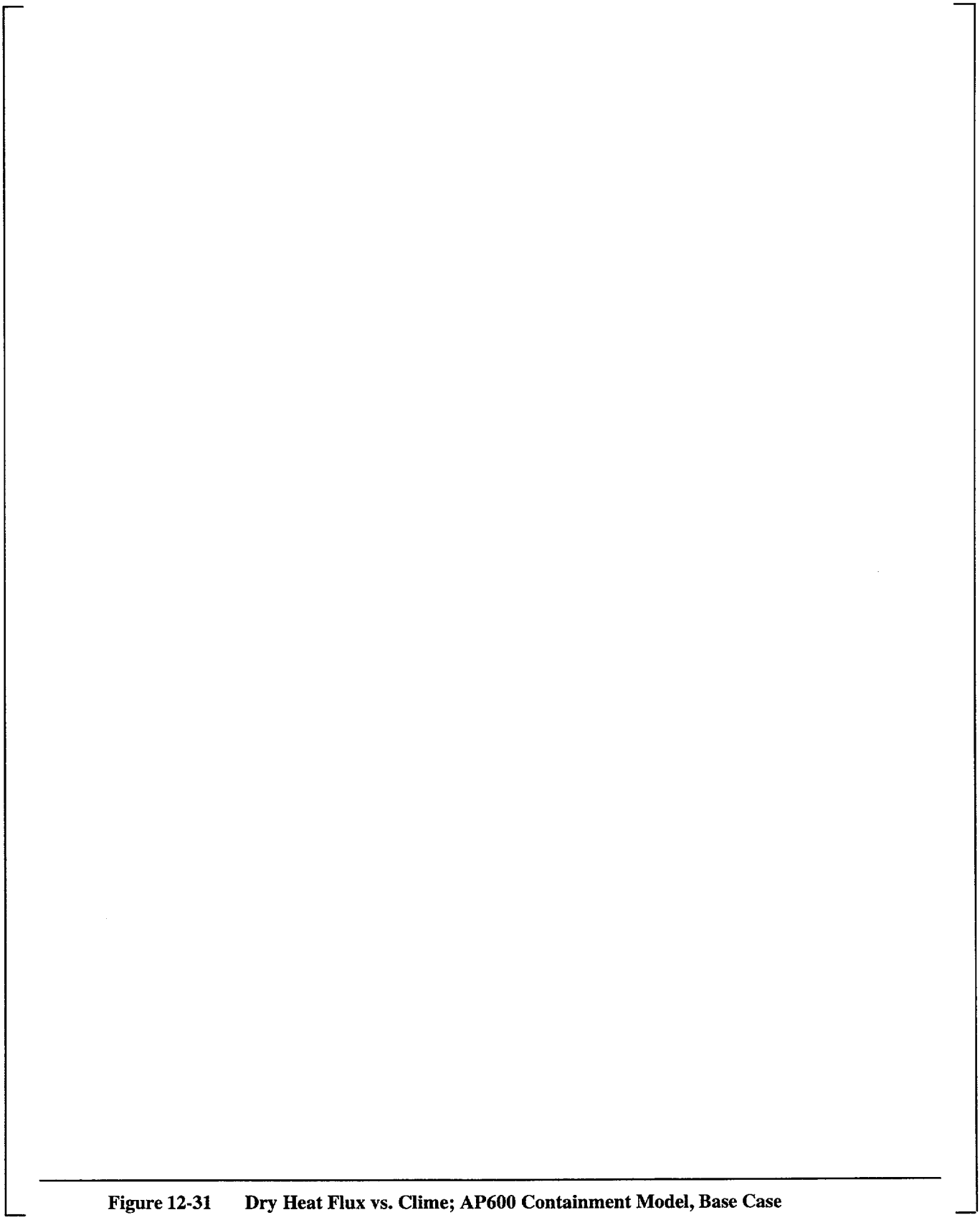

Figure 12-31 Dry Heat Flux vs. Clime; AP600 Containment Model, Base Case

(a,c)

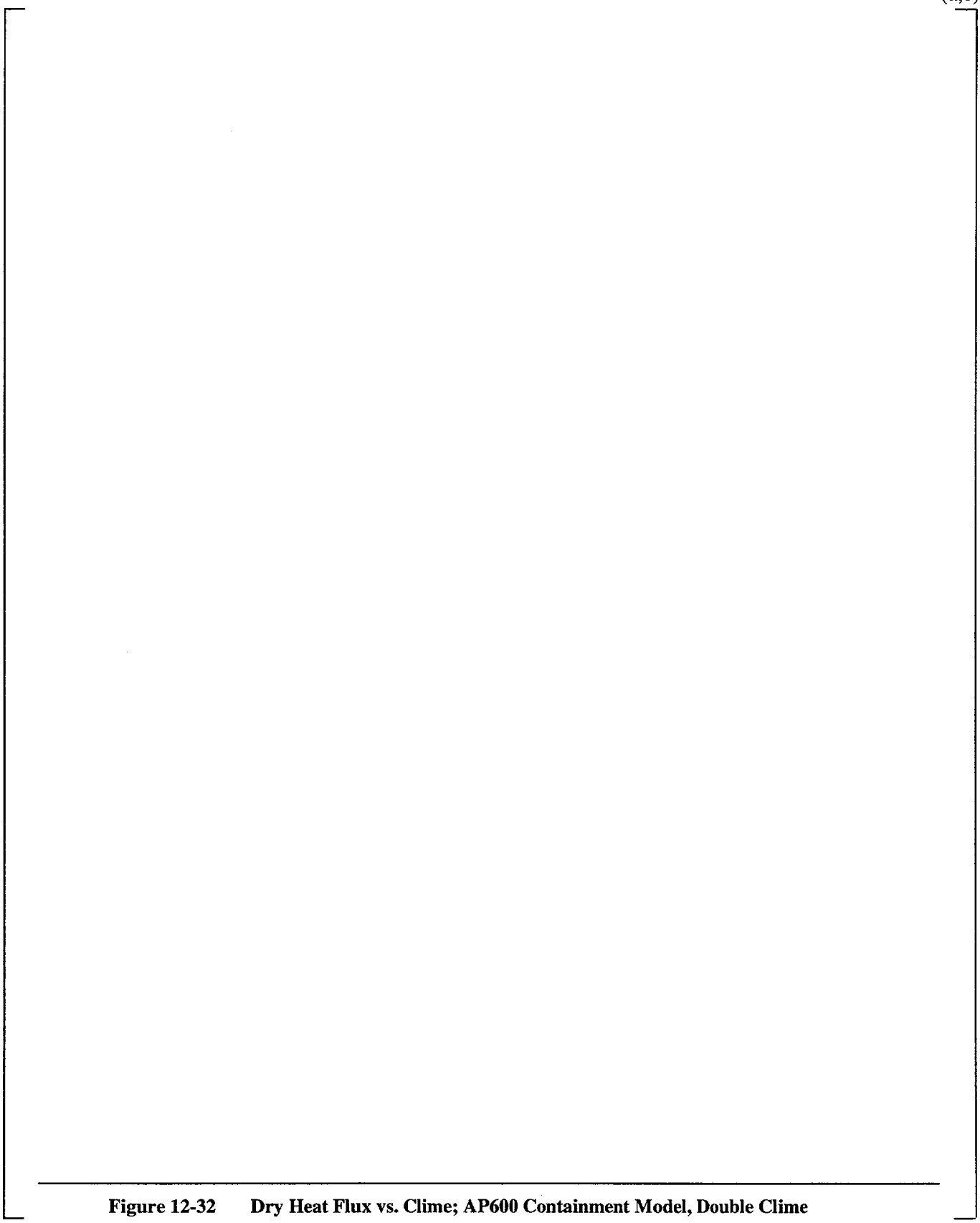

Figure 12-32 Dry Heat Flux vs. Clime; AP600 Containment Model, Double Clime

(a,c)

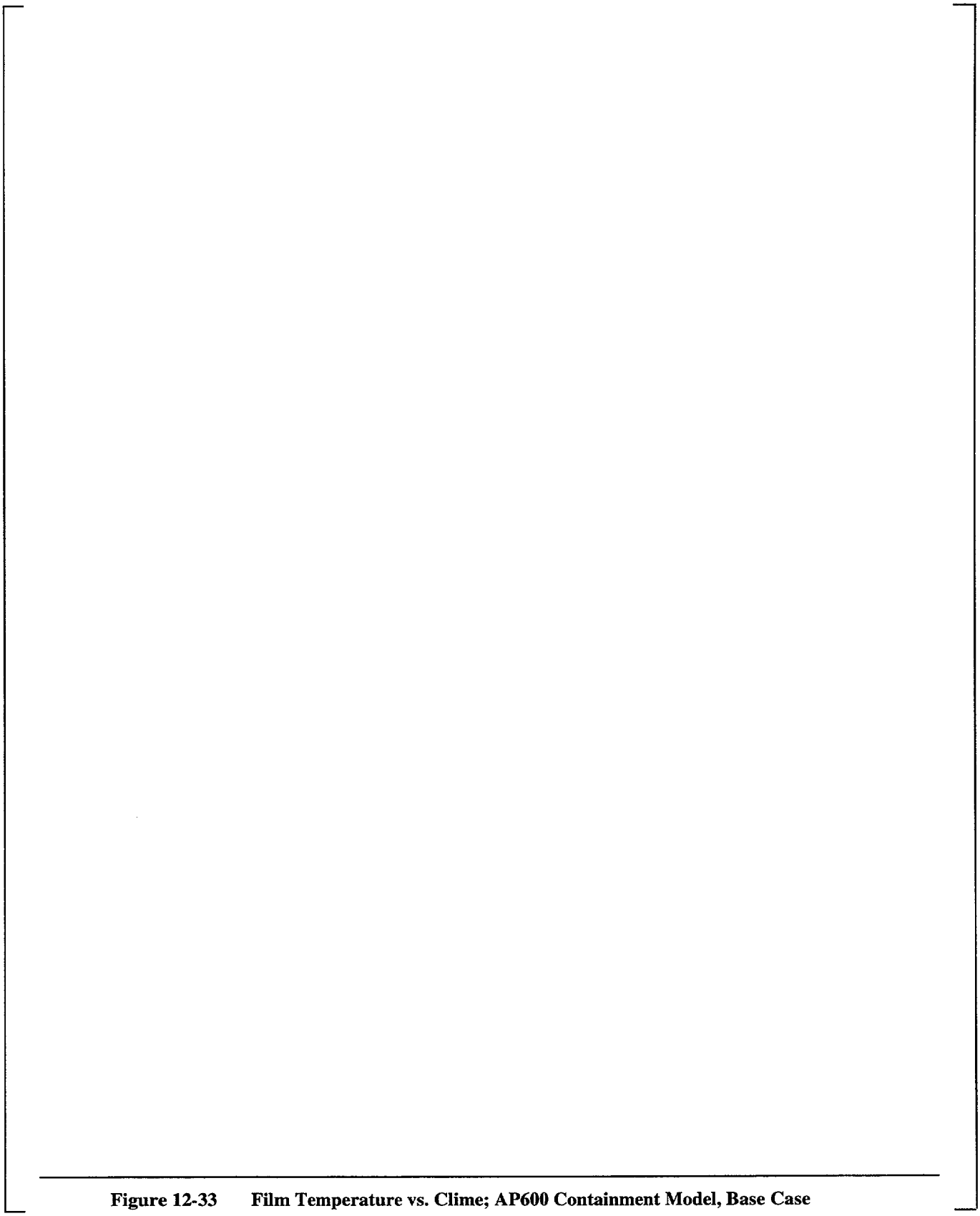

Figure 12-33 Film Temperature vs. Clime; AP600 Containment Model, Base Case

(a,c)

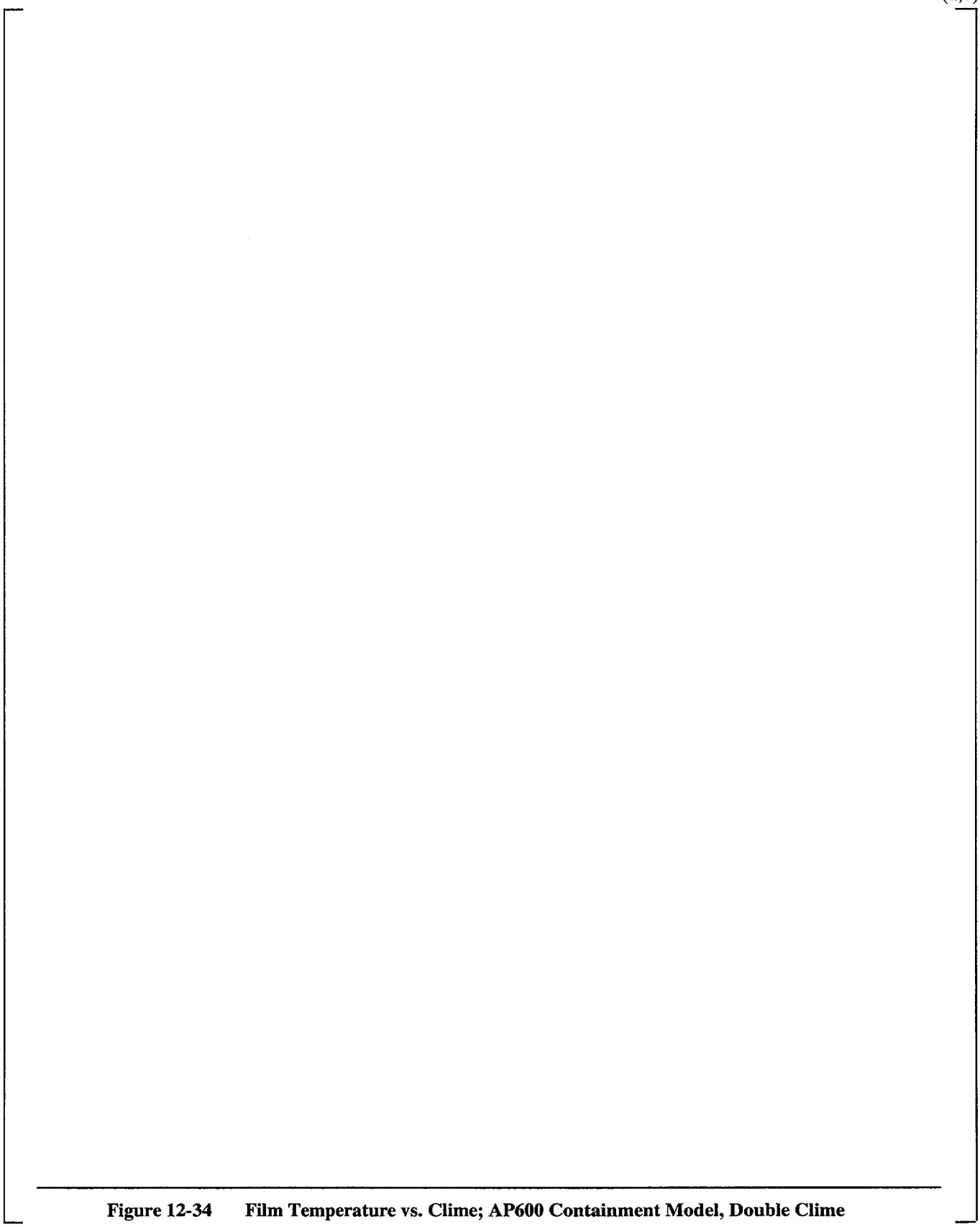

Figure 12-34 Film Temperature vs. Clime; AP600 Containment Model, Double Clime

(a,c)

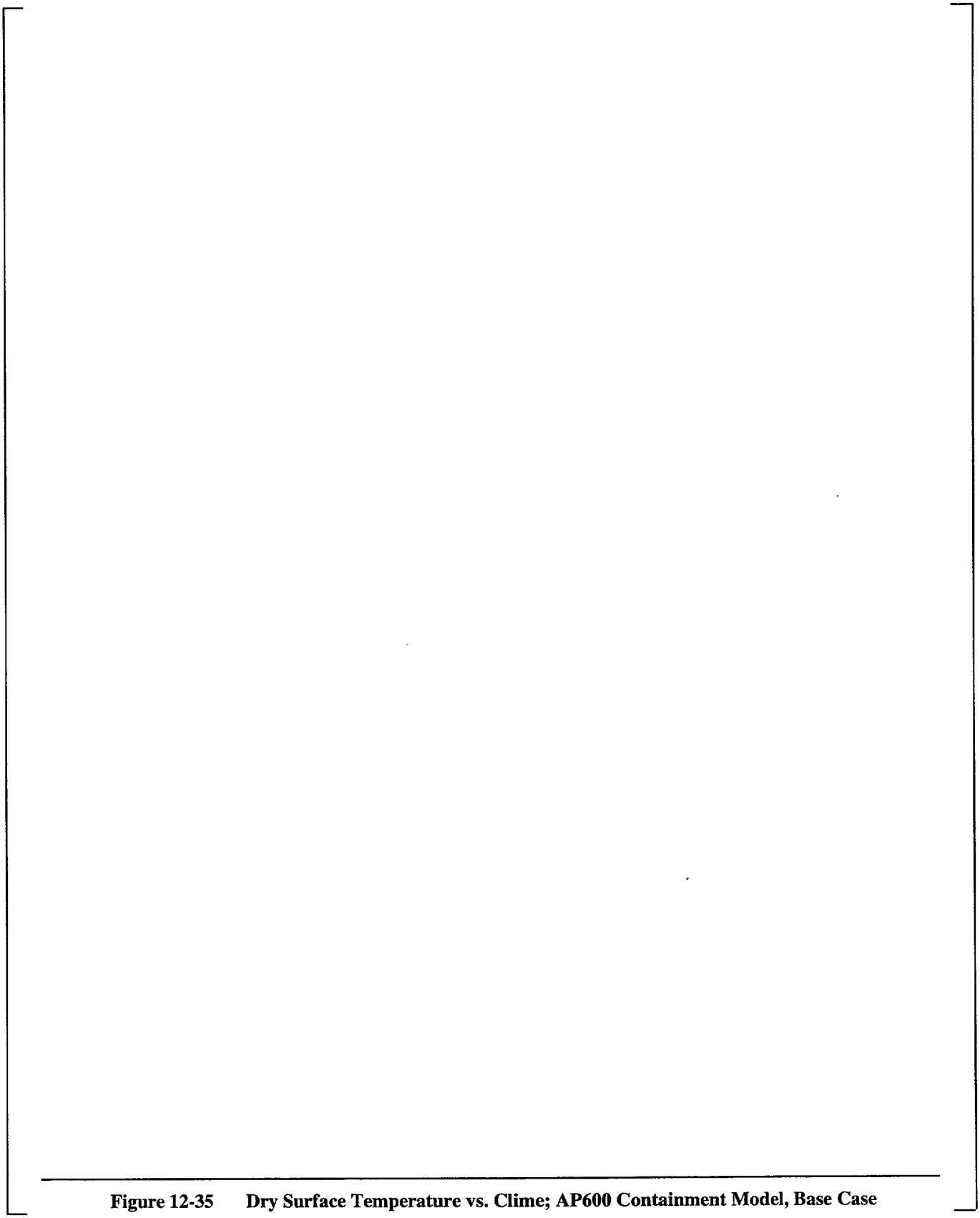

Figure 12-35 Dry Surface Temperature vs. Clime; AP600 Containment Model, Base Case

(a,c)

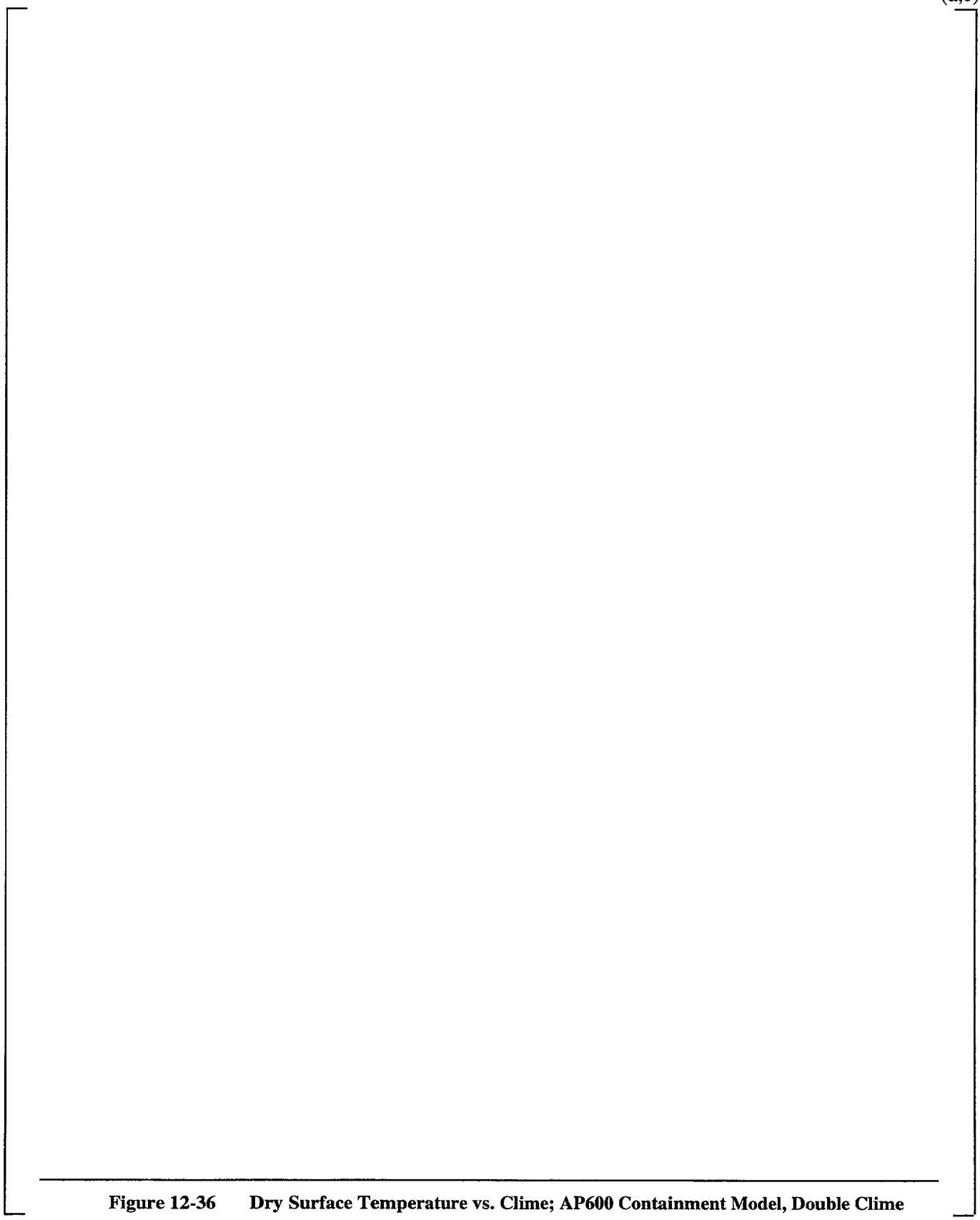

Figure 12-36 Dry Surface Temperature vs. Clime; AP600 Containment Model, Double Clime

(a,c)

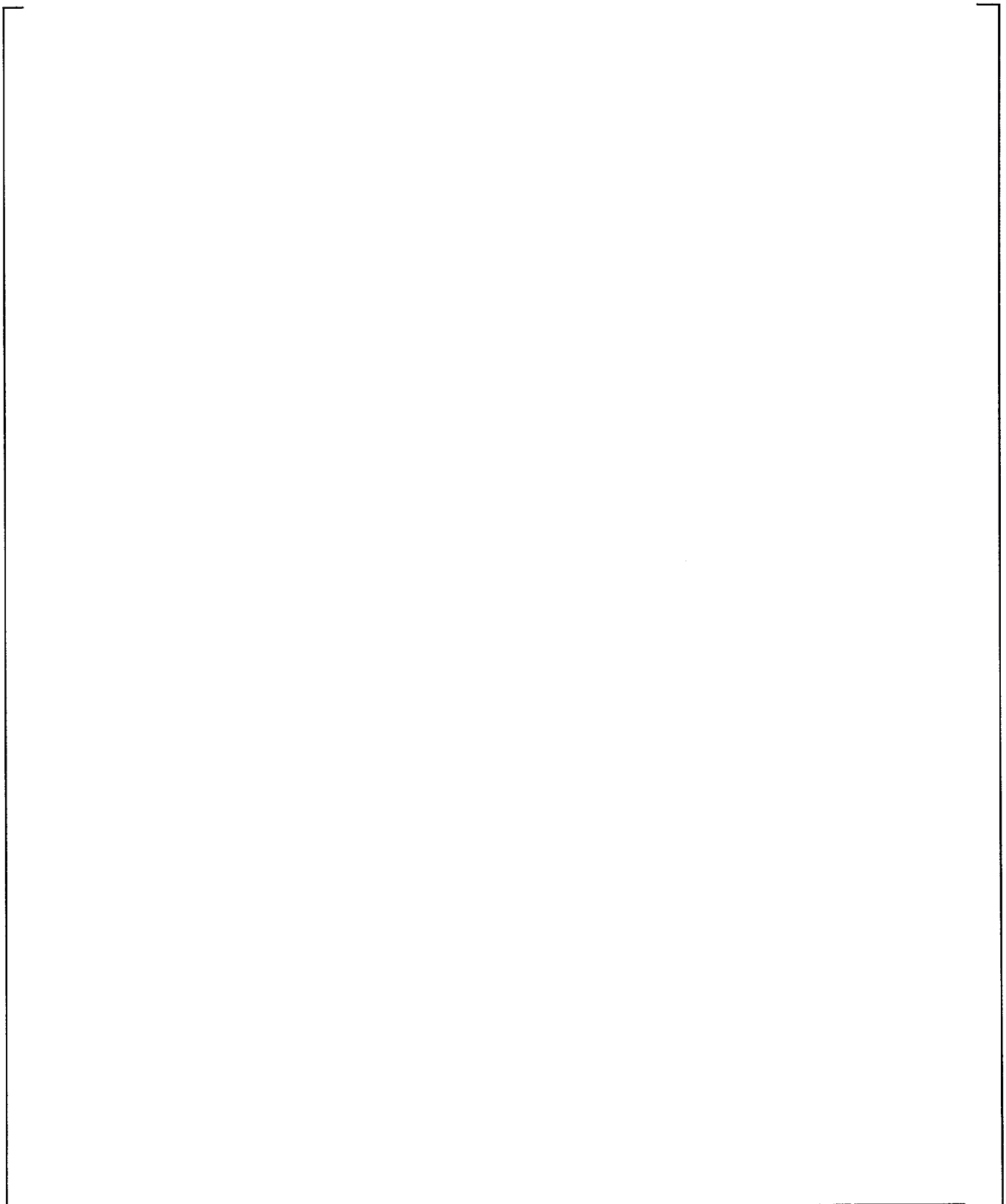

Figure 12-37 Annulus Pressure vs. Clime; AP600 Containment Model, Base Case

(a,c)

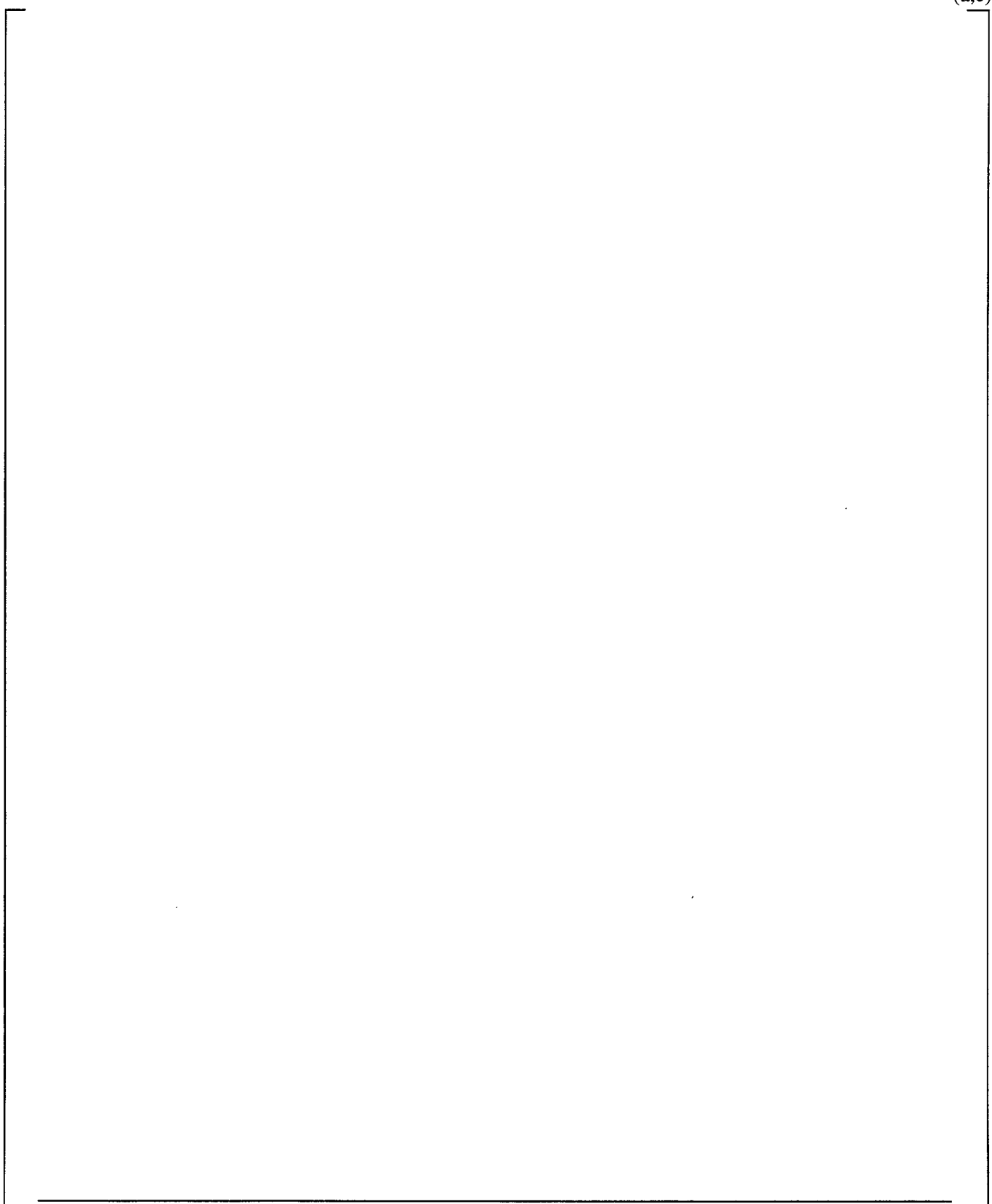

Figure 12-38 Annulus Pressure vs. Clime; AP600 Containment Model, Double Clime

(a,c)

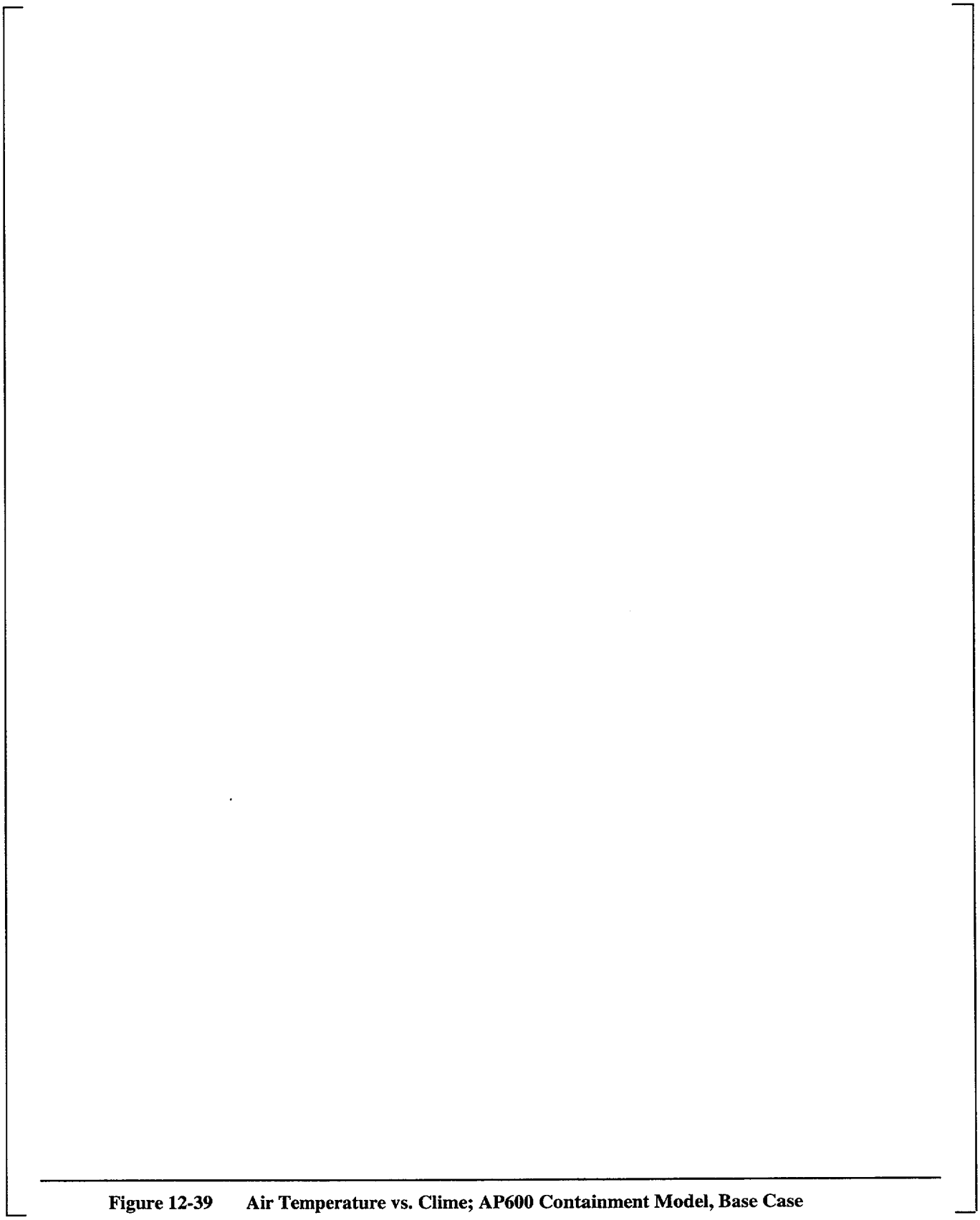

Figure 12-39 Air Temperature vs. Clime; AP600 Containment Model, Base Case

(a,c)

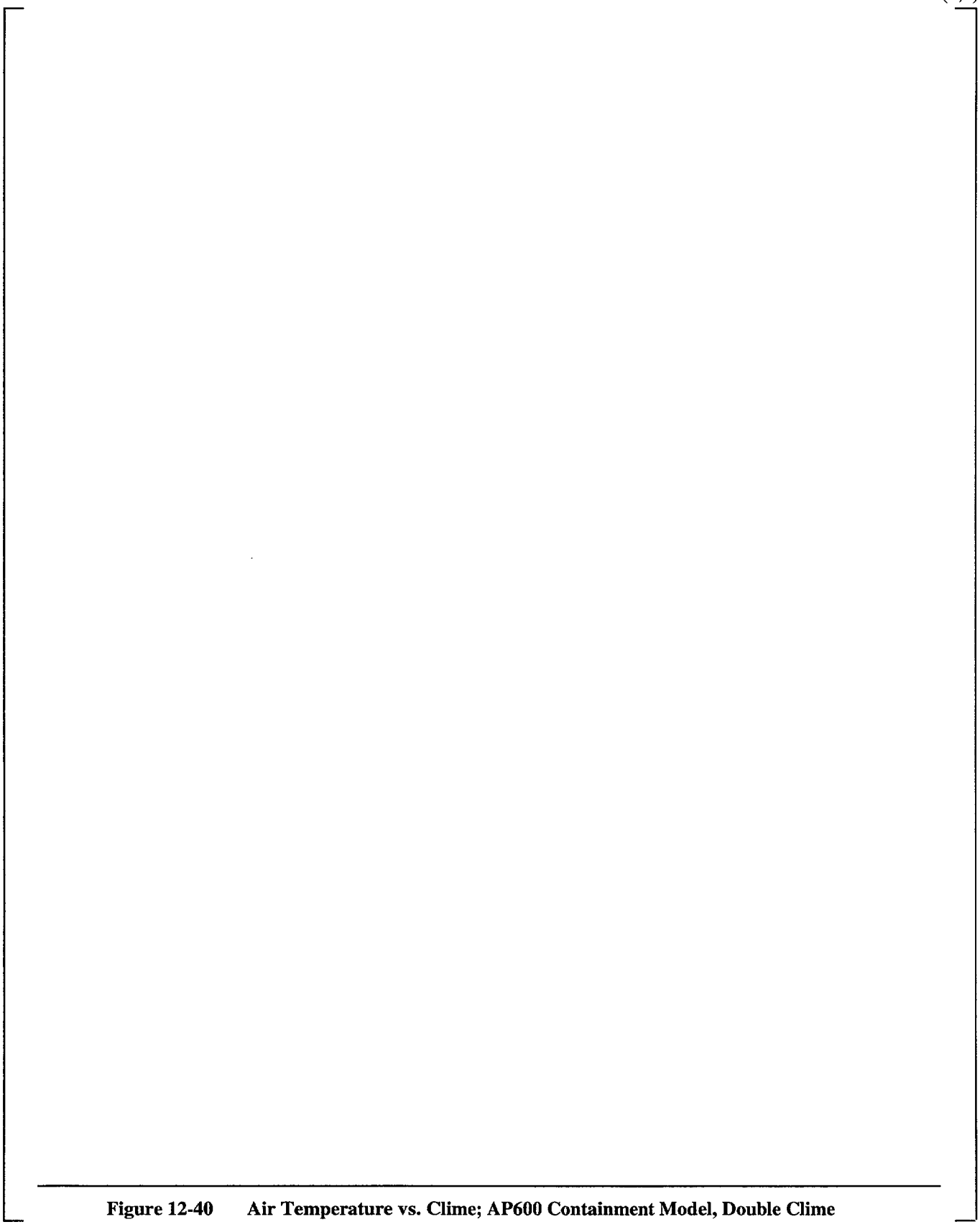

Figure 12-40 Air Temperature vs. Clime; AP600 Containment Model, Double Clime

(a,c)

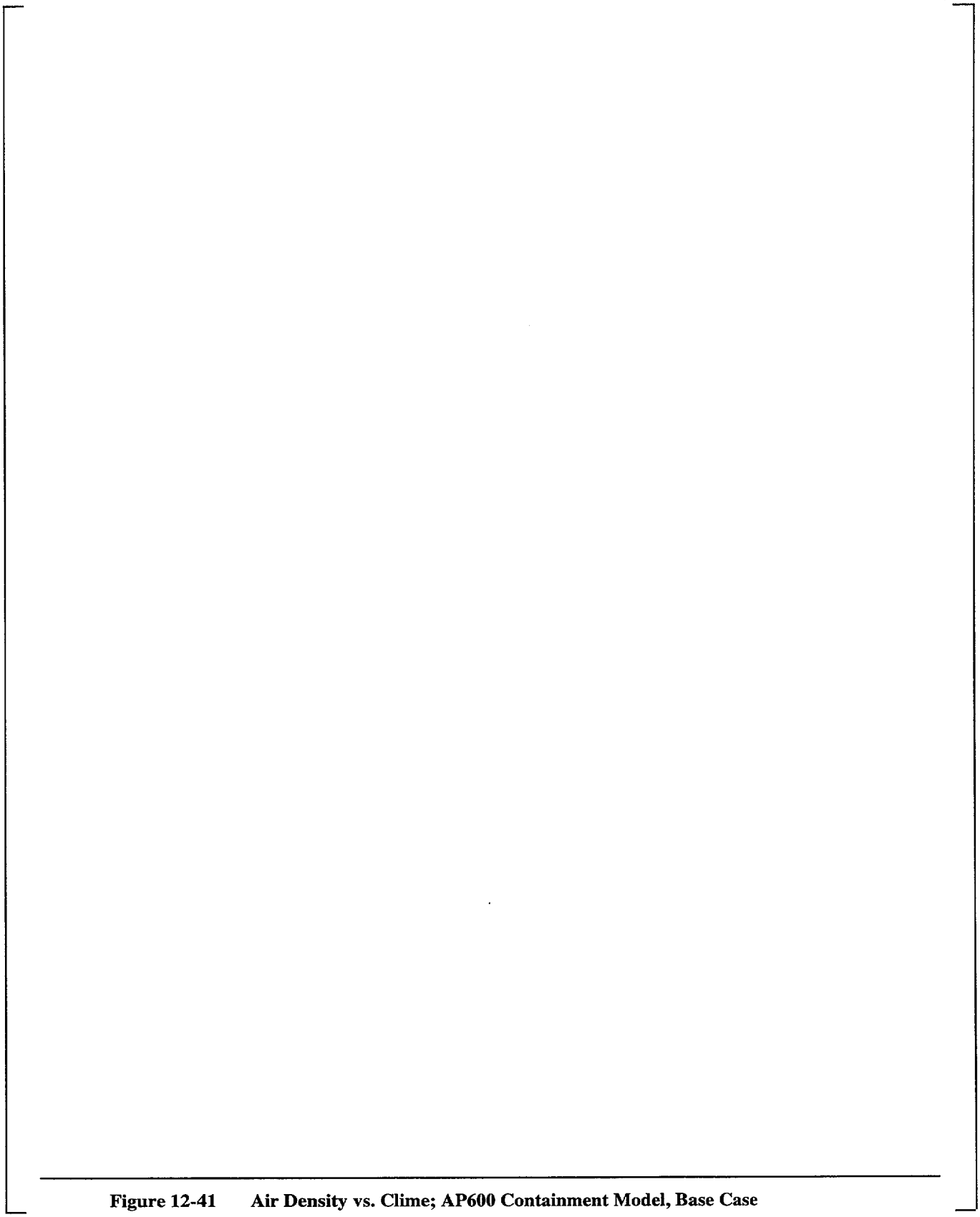

Figure 12-41 Air Density vs. Clime; AP600 Containment Model, Base Case

(a,c)

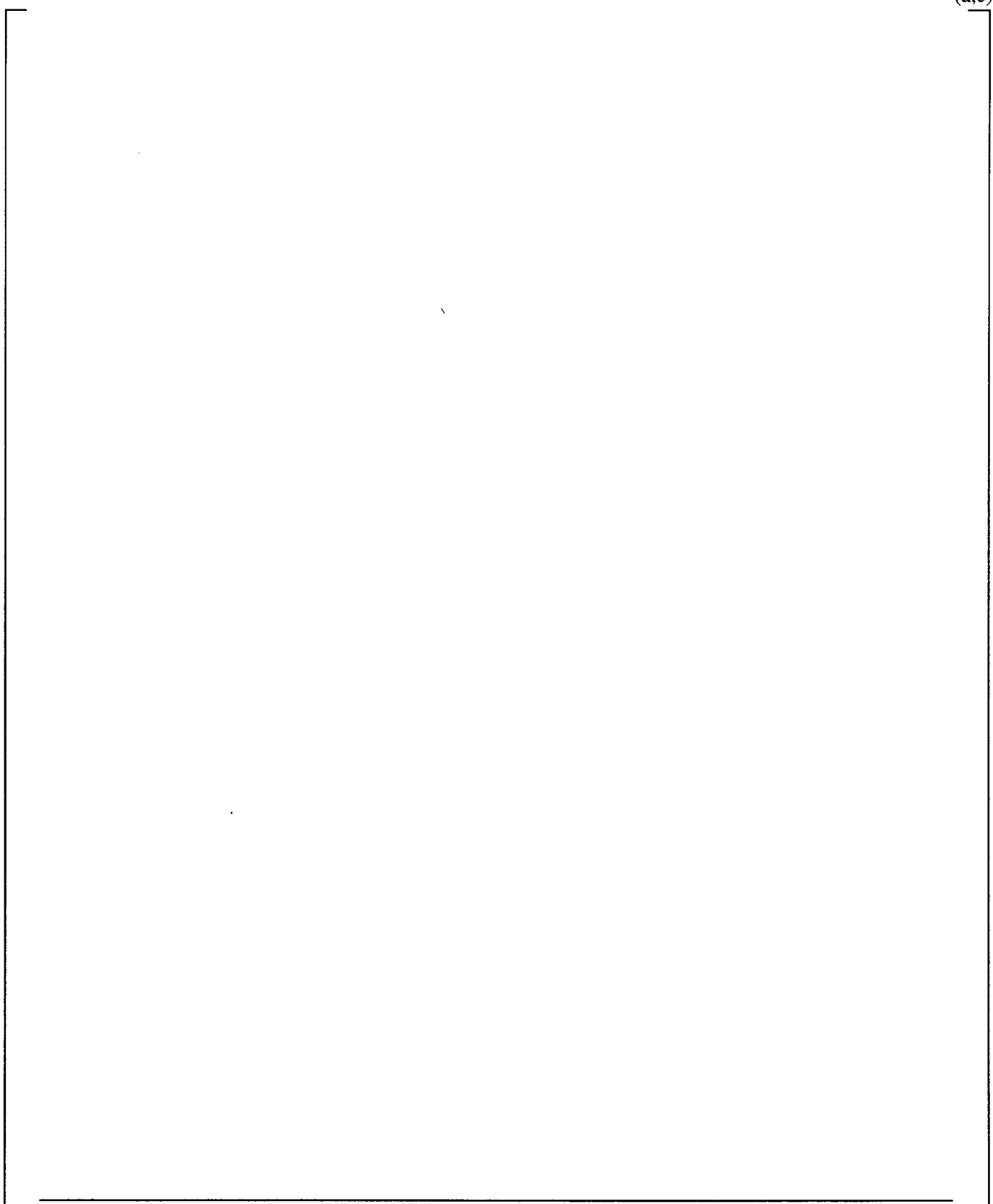

Figure 12-42 Air Density vs. Clime; AP600 Containment Model, Double Clime

(a,c)

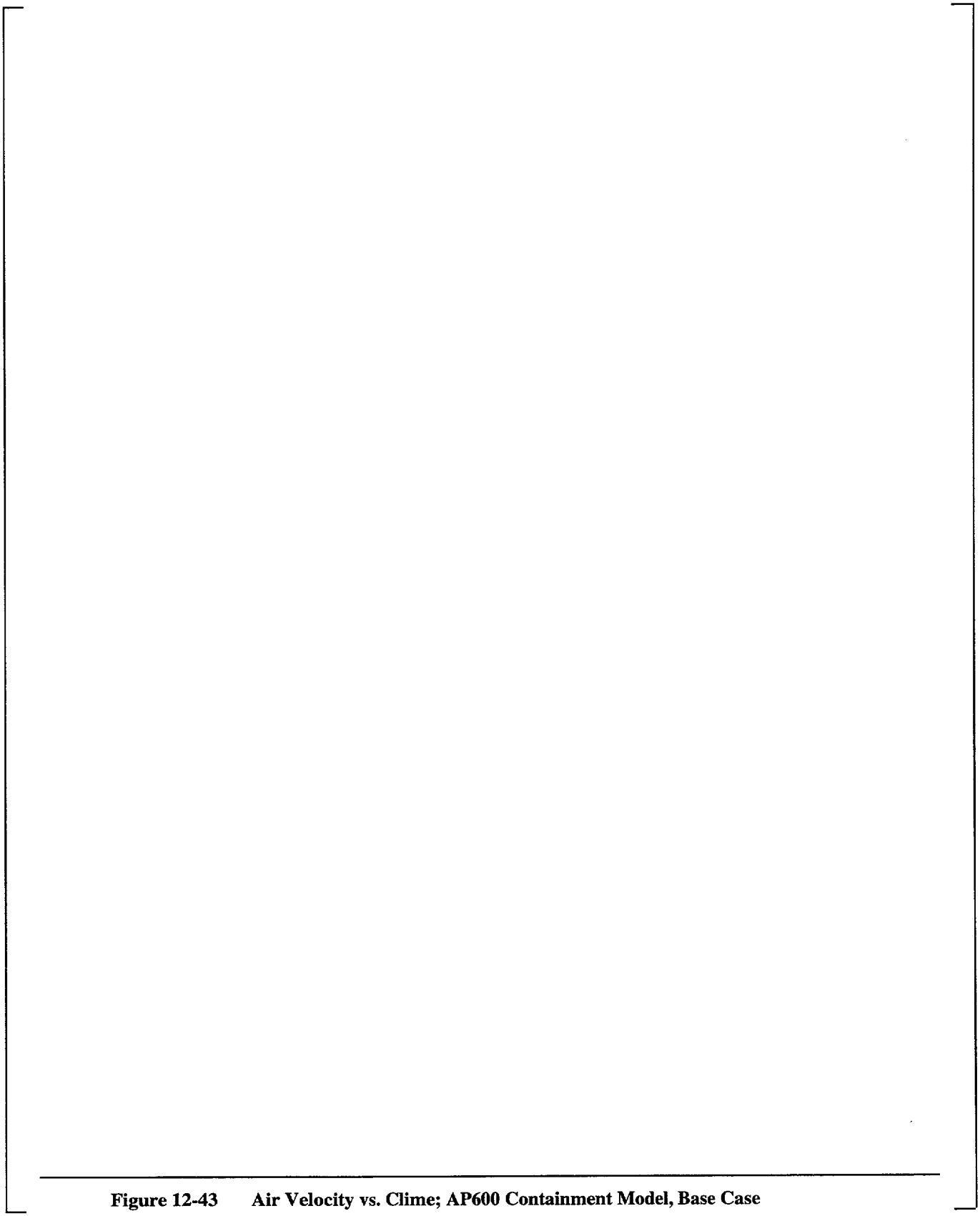

Figure 12-43 Air Velocity vs. Clime; AP600 Containment Model, Base Case

(a,c)

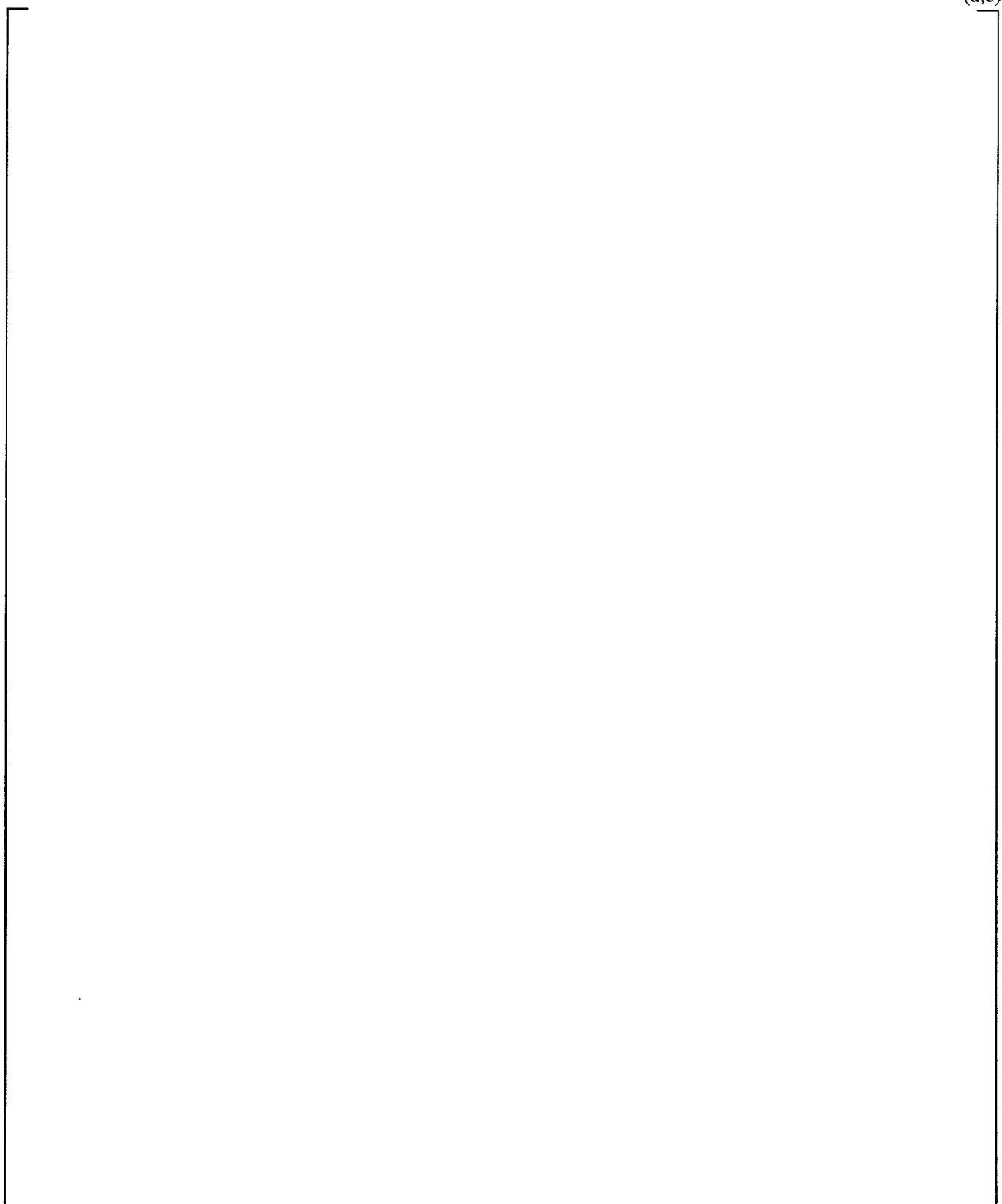

Figure 12-44 Air Velocity vs. Clime; AP600 Containment Model, Double Clime

(a,c)

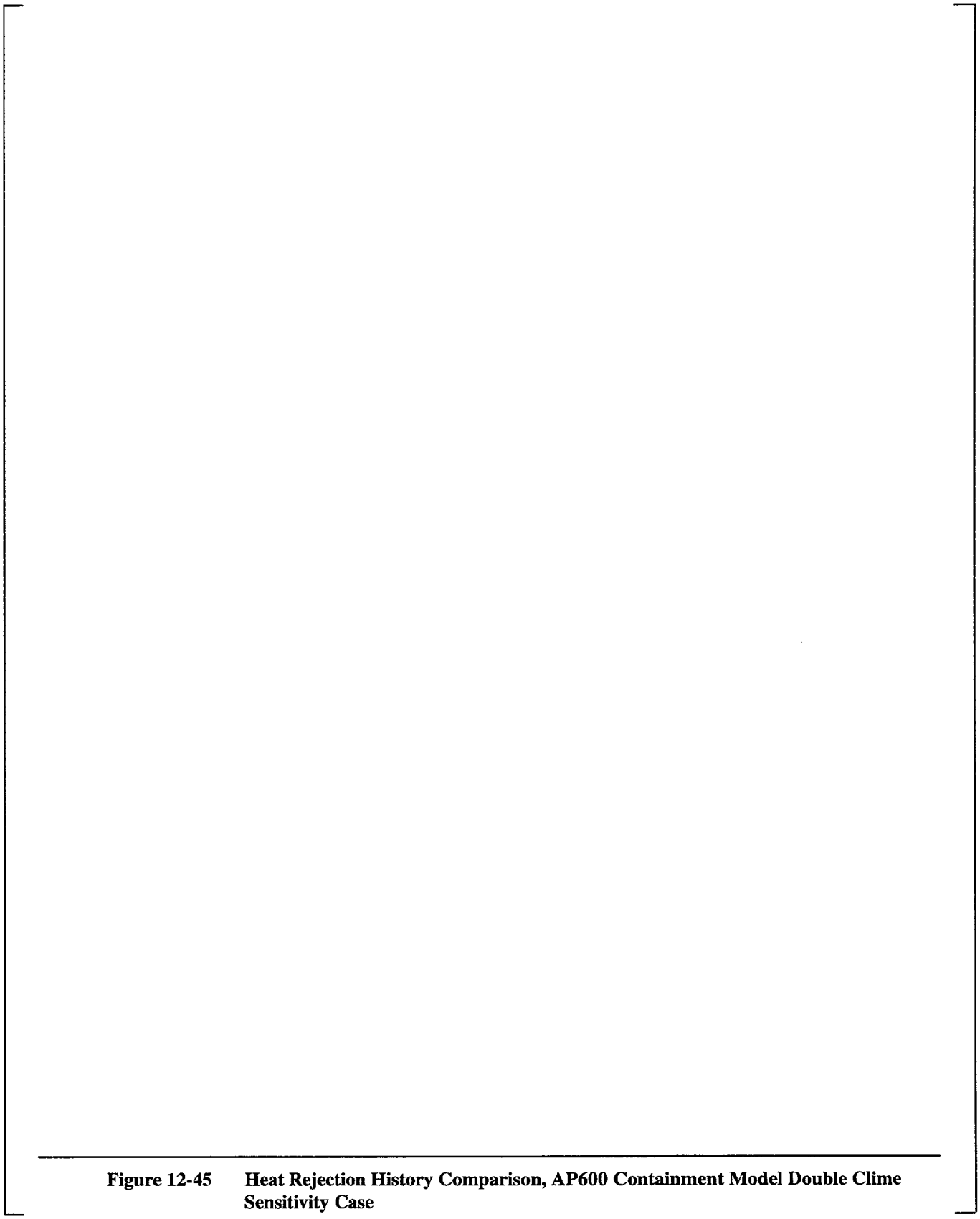

Figure 12-45 Heat Rejection History Comparison, AP600 Containment Model Double Clime Sensitivity Case

(a,c)

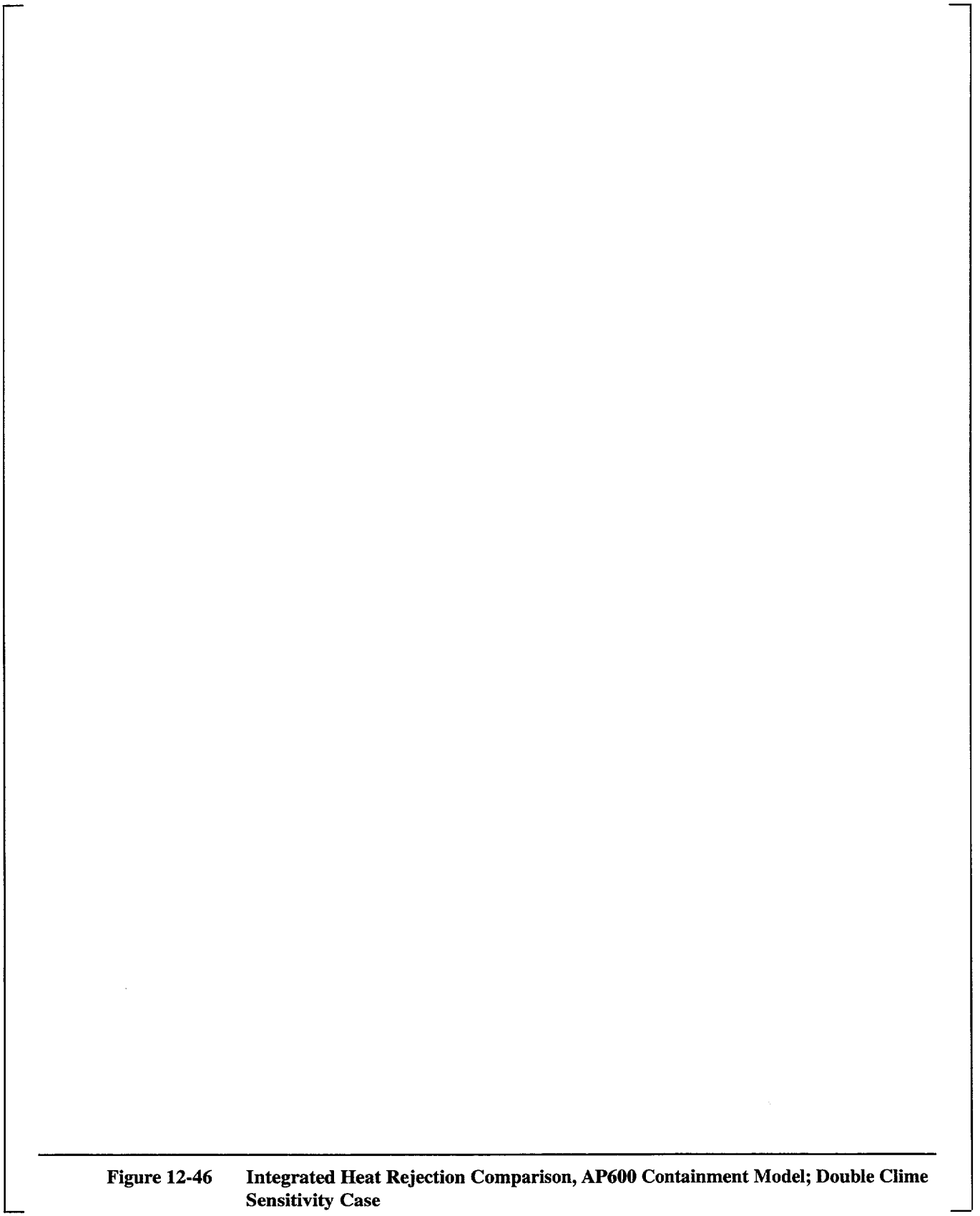

Figure 12-46 Integrated Heat Rejection Comparison, AP600 Containment Model; Double Clime Sensitivity Case

(a,c)

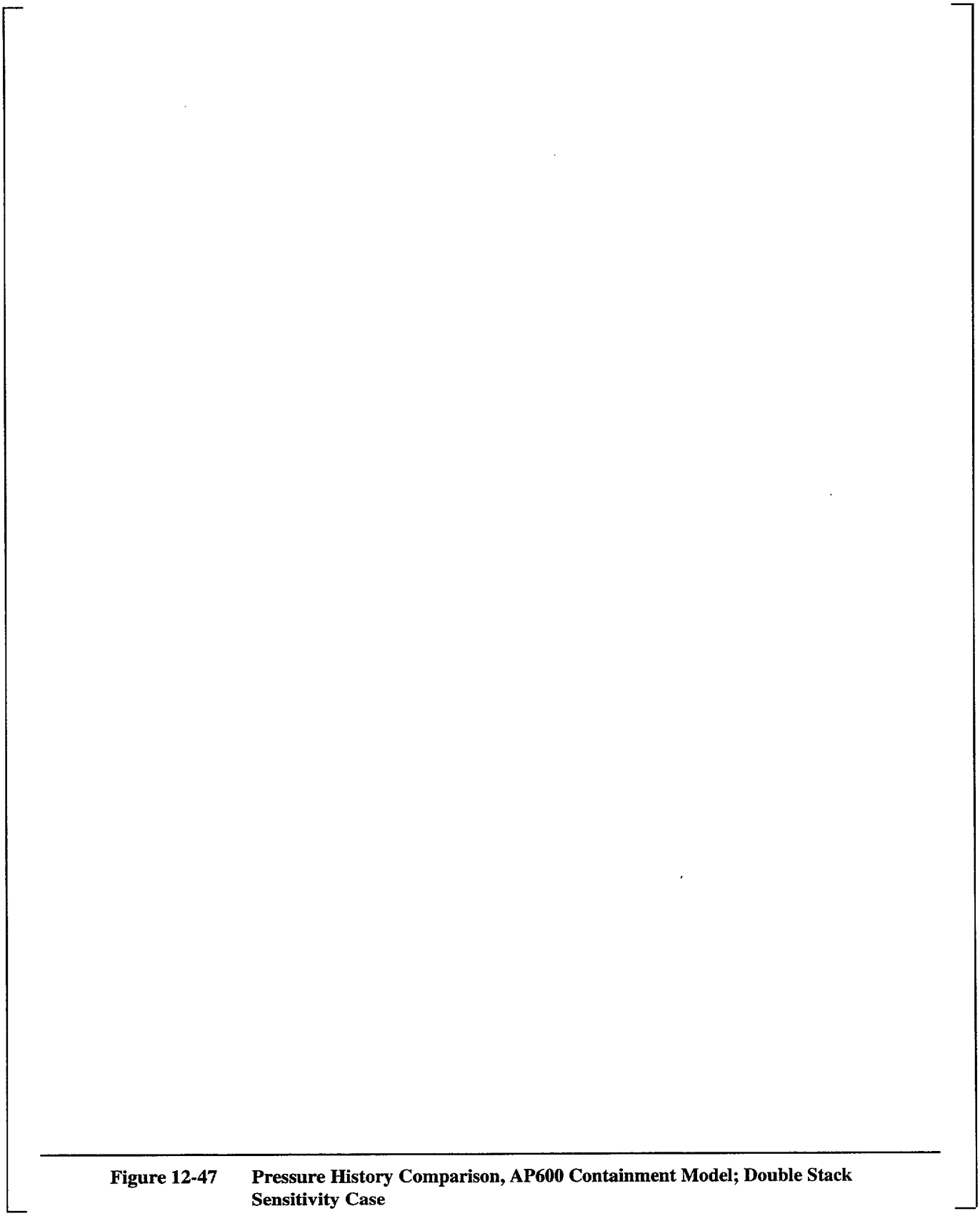

Figure 12-47 Pressure History Comparison, AP600 Containment Model; Double Stack Sensitivity Case

(a,c)

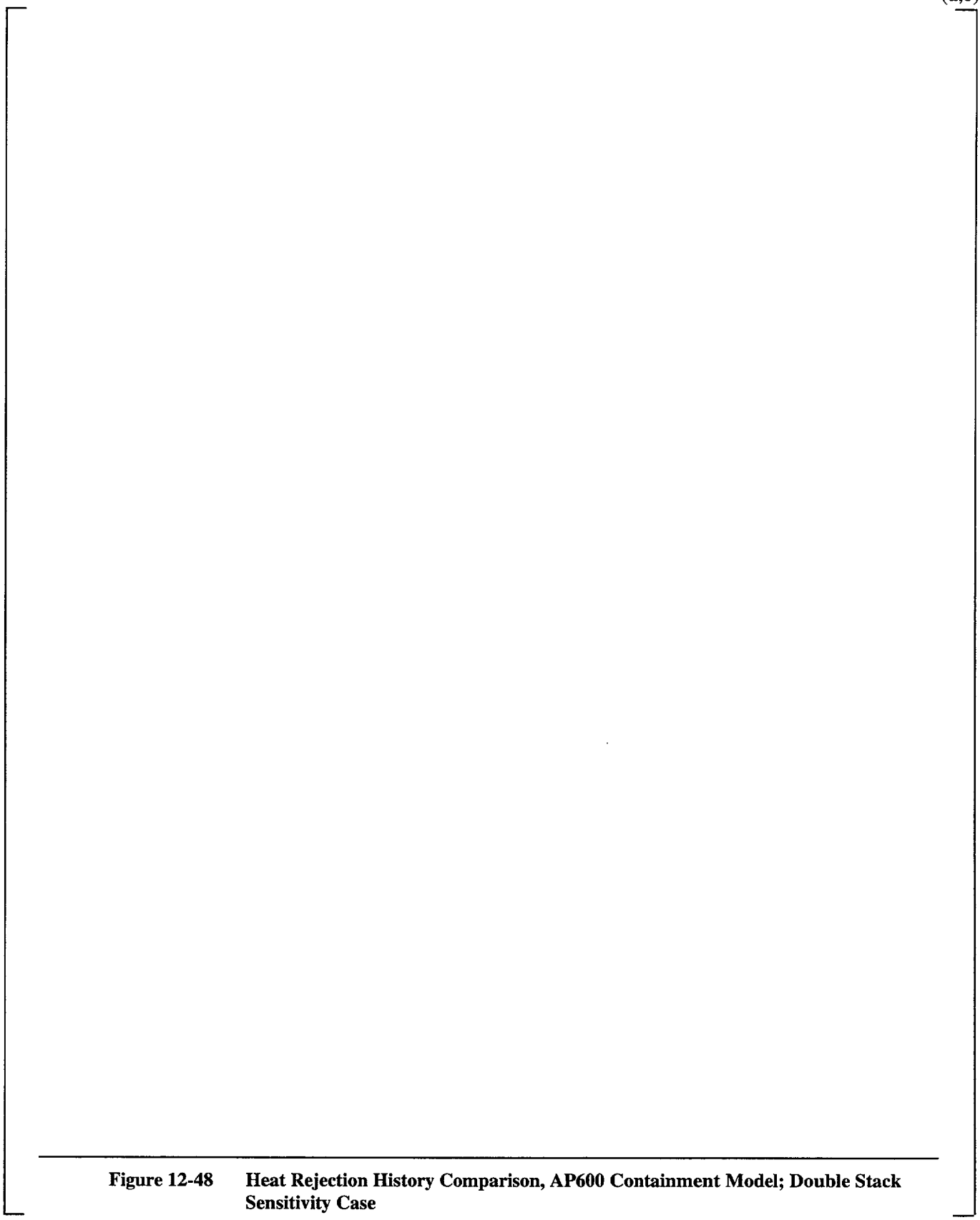

Figure 12-48 Heat Rejection History Comparison, AP600 Containment Model; Double Stack Sensitivity Case

(a,c)

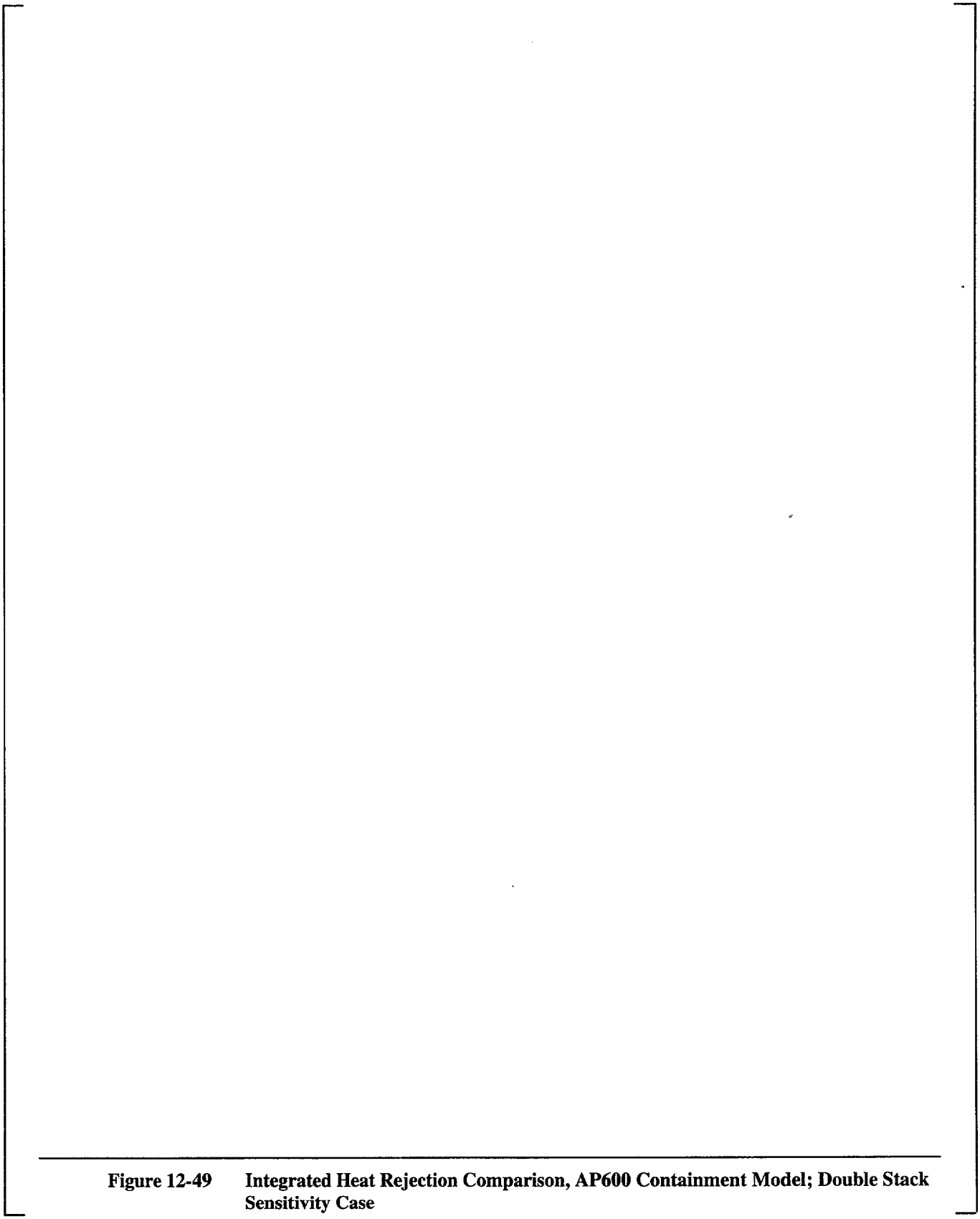

Figure 12-49 Integrated Heat Rejection Comparison, AP600 Containment Model; Double Stack Sensitivity Case

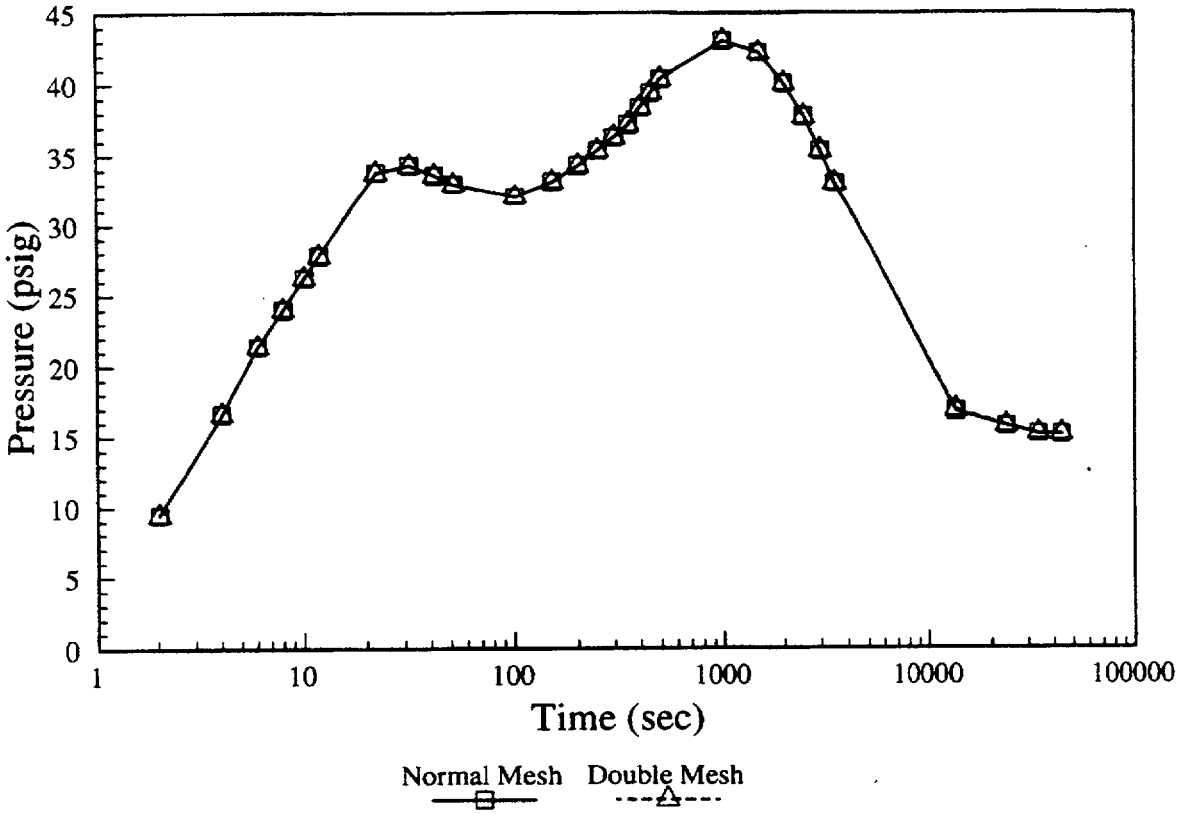

Figure 12-50 Pressure History Comparison, AP600 Containment Model; Double Mesh Sensitivity Case

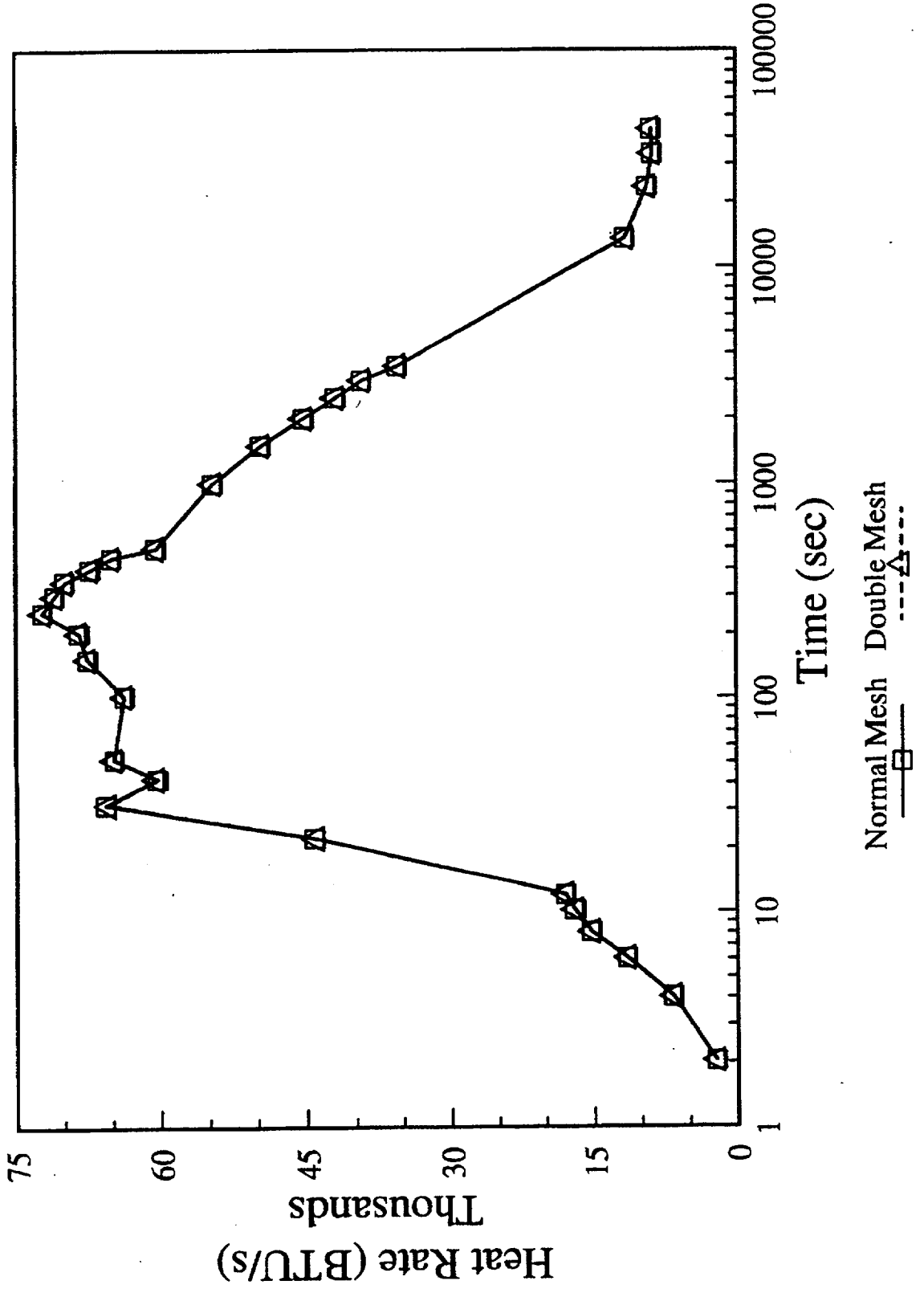

Figure 12-51 **Heat Rejection History Comparison, AP600 Containment Model; Double Mesh Sensitivity Case**

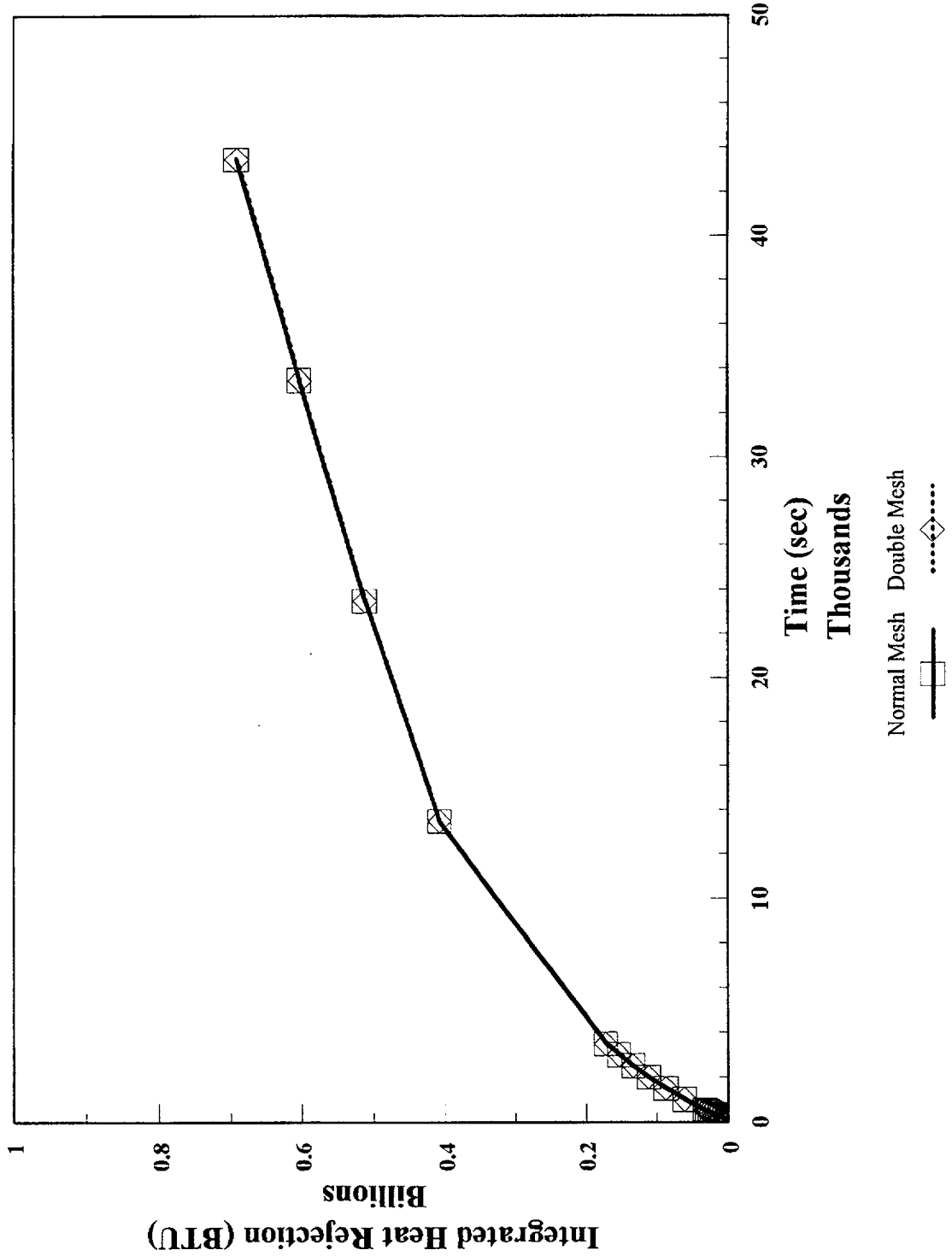

Figure 12-52 Integrated Heat Rejection Comparison, AP600 Containment Model; Double Mesh Sensitivity Case

Section 13

Description of AP1000 Plant Geometry in WGOTHIC Evaluation Model

This entire section (13) is proprietary to Westinghouse Electric Company.(a,c)

Section 14

LOCA Mass and Energy Release Calculation Methodology

TABLE OF CONTENTS

LIST OF TABLES

LIST OF FIGURES

14.1 INTRODUCTION

This section describes the method used to calculate the loss-of-coolant accident (LOCA) mass and energy releases that are used to calculate the containment pressure response for the Design Basis Analysis (DBA). The method maximizes both the magnitude and the rate of the mass and energy release to containment. This introduces substantial conservatism in the prediction of the peak containment pressure and temperature response following a LOCA event.

Section 10, Figure 10-1 presents a comparison of the WGOTHIC AP600 Containment Evaluation Model sensitivity to various input values and correlations. These are not single-effect sensitivities; the results are cumulative. Each additional sensitivity case modification is stacked upon those that immediately preceded it. These sensitivities provide insight into the effect of each parameter, individually, by comparison to the preceding case, as well as the total conservatism represented by these parameters. Case 7 (the heavy dashed line in Figure 10-1) represents the effect of removing some of the conservatism in the input mass and energy releases.

For Case 7, the mass and energy release calculation input was modified as follows:

- The nominal (without adding 5 F uncertainty) full power RCS temperatures were used
- The nominal (without adding 30 psi) full power RCS pressure was used
- The nominal (without adding uncertainty) RCS volume was used
- The nominal (without adding 2% uncertainty) full core power was used
- The nominal (without adding 15%) full power core stored energy was used
- The nominal CMT, accumulator, and IRWST fluid temperatures were used.

In addition to the input changes described above, the following calculational changes were made during the post-blowdown phase:

- The 1979 ANS decay heat standard for an 800-day average burnup (without adding the 2 sigma uncertainty) was used
- The post-blowdown refill period was modeled
- The broken loop steam generator energy was assumed to be released over a 1-hour period
- The intact loop steam generator energy was assumed to be released over a 2-hour period
- No zirc-water reaction energy was added.

A comparison of the mass and energy releases for Case 7 and the AP600 Containment Evaluation Model is shown in Figures 10-3 and 10-4.

As shown in Figure 10-1, by eliminating only a portion of the conservatism in the calculation of the mass and energy releases, there is a substantial decrease in the post-blowdown peak pressure (about 6 psi). The calculated peak containment pressure is reduced from the previous case by about 4.3 psi and is shifted to the end of blowdown. The largest effect of any other single change to one of the containment model input values is a reduction of about 3 psi. Therefore, the conservatism in the mass and energy calculation outweighs any other single modeling parameter.

14.2 BLOWDOWN MASS AND ENERGY RELEASE CALCULATION

The primary differences between the conventional plant design and the passive plant design are the engineered safety features. The safety features of conventional operating plants include both passive and active systems; the AP600 and AP1000 safety features are all passive. This difference only affects the long-term inventory makeup systems, not the system behavior during the blowdown phase.

The methodology for calculating the mass and energy release to containment during the blowdown phase is not affected by the passive safety systems. The only safety system that injects water during the blowdown phase is the accumulator system; the gravity-driven core makeup tanks (CMTs) cannot inject into the common direct vessel injection line against the pressure of the gas-charged accumulators. Accumulators are included in both the passive and active plant designs and are modeled with the NRC-approved DBA LOCA mass and energy release methodology. The AP600 uses spherical accumulators, whereas currently operating Westinghouse designed plants use cylindrical accumulators. The accumulator inventory is depleted well before the time of peak pressure so any difference in discharge rate associated with the different accumulator geometry would have an insignificant effect on the calculation for peak containment pressure.

The blowdown mass and energy releases are calculated using the SATAN-VI computer code. The SATAN-VI code, associated modeling assumptions, and noding structure for the mass and energy release calculations are documented in WCAP-10325-P-A (Reference 2). It has been reviewed and approved by the NRC for use in calculating the blowdown mass and energy releases for Westinghouse PWR containment integrity DBA. The blowdown phenomena modeled by the SATAN VI code are the same for all Westinghouse PWRs, including the AP600 design.

The variable noding structure of the SATAN model allows the user to simulate current and advanced reactor coolant system geometry with generalized control volumes. The standard Westinghouse PWR reactor coolant system noding structure is modified to specifically model the passive plant reactor coolant system geometry, which includes two cold legs in the coolant loops and a direct vessel injection (DVI) line to the downcomer.

14.3 POST-BLOWDOWN MASS AND ENERGY RELEASE CALCULATION

The post-blowdown phase consists of three periods: refill, reflood, and long-term cooling. The refill period occurs just after blowdown. During the refill period, the accumulators refill the downcomer and lower

plenum of the vessel with water. There are little or no releases during the refill period. The reflood period occurs just after refill. During the reflood period, the core is refilled with a 2-phase mixture of steam and water. Following reflood, the RCS fluid inventory and long-term cooling are maintained by the pumped safety injection system and recirculation system (conventional plants) or the core makeup tanks and gravity draining of the IRWST (passive plants).

The approved codes for conventional plant post-blowdown mass and energy release analyses would have had to have been significantly modified for them to have been used for passive plant analyses. Instead, a calculational method was developed to conservatively predict the AP600 and AP1000 post-blowdown mass and energy releases in a manner that is consistent with the current approved methods for DBA. A spreadsheet was used for the calculations to simplify accounting of the mass and energy sources and releases.

Mass Sources

Figure 14.3-1 illustrates the basic model for the AP600 and AP1000 post-blowdown mass and energy release calculation. All of the injection sources (accumulators, CMTs, and IRWST) are assumed to be delivered to the DVI line at a mass flow rate, m_{inject}. Flow from both accumulators refills the vessel following blowdown. The CMTs begin to inject just before the accumulators empty. The IRWST begins to gravity drain to the vessel (and spill from break) just before the CMTs empty.

The injected liquid mass flow rate delivered to the DVI line is calculated with a simplified resistance network. Two cases are considered: one with the line resistances maximized (to produce the minimum accumulator, CMT, and IRWST flow rates) and one with the line resistances minimized (to produce the maximum accumulator, CMT, and IRWST flow rates). The resistance network also calculates a flow rate around the loops and a flow rate out the broken cold leg stub, however, these are not used in the mass and energy release spreadsheet calculation. Instead, as shown in Figure 14.3-1, all of the injection flow that is delivered to the DVI line is assumed to pass through the core, hot legs, steam generators and out of the break. This maximizes the SG heat release rate, and is a source of conservatism in the analysis.

Energy Sources

The various sources of energy that are considered in the calculation, and their assumed release rates are summarized in Table 14-1. The release rates are biased to release energy (in the form of steam) to the containment early in the transient. The containment pressure response is dependent on the steam mass flow rate, so maximizing the steaming rate is conservative. The RCS metal energy release provides sensible heating of the injected liquid mass flow. The core decay heat and SG energy releases provide both sensible and latent heat to the injected liquid mass flow rate.

The SG equilibration time input value in the spreadsheet calculation is adjusted to maximize the steaming rate during the CMT injection phase. The SG equilibration times that are used for AP1000 are longer than AP600 because both the core decay heat and SG stored energy are higher in the AP1000.

Table 14-1 DECLG LOCA Energy Release Modeling

Time Frame	Source of Energy	Energy Release Rate
Accident initiation to end of blowdown (30 seconds)	Core, RCS and SGs	SATAN VI Calculation
End of blowdown + 180 seconds	The Zr-H_2O Reaction Energy for 1% of the Fuel Cladding	Constant
End of blowdown to end of reflood (400 seconds)	Core stored energy	Constant
End of blowdown + SGB equilibration	SG energy - broken loop	Exponential
End of blowdown + SGI equilibration	SG energy - intact loop	Exponential
End of blowdown + 60 minutes	RCS metal energy	Exponential
End of blowdown to 72 hours	Fission Product Decay	ANS 1979 + 2 sigma

Description of Calculational Method

Three basic steps in the calculational method determine the DBA mass and energy releases as a function of time after the blowdown phase. First, the individual contributions for each of the various sources of energy are calculated. Second, the vessel internal mass and break mass flow rate are calculated. Third, the break mass flow rate is partitioned into a steam and a 2-phase component. A check for conservation of mass and energy is performed at the end of each time step. This method for calculating the mass and energy releases after the blowdown phase is described in more detail below.

Calculation of Sources of Energy

1. The 1979 decay heat standard with 2 sigma uncertainty, all U-235 fission, and 3 years full power operation is used to calculate the core decay heat energy release rate at each time step.

2. [

   ]^{a,c} The core stored energy is released at a constant rate over the reflood period.

3. The Zr-H_2O reaction energy, corresponding to 1% clad oxidation, is released at a constant rate over the first 180 seconds of the reflood period.

4. The RCS metal energy is released exponentially. Using an exponential rate is conservative since this assumes the heat transfer rate is much larger than the rate of conduction through the metal. The equation for determining the stored metal energy as a function of time is:

$$Q(t) = Q_{final} + (Q_{initial} - Q_{final})*e^{-a(t-b)}$$

where: Q_{final} = stored metal heat at equilibration (BTU)
$Q_{initial}$ = stored metal heat at the end of blowdown (BTU)
a = inverse of the metal time constant (sec^{-1})
t = time (sec)
b = end of blowdown time (sec)

therefore, the release rate is:

$$\frac{dQ}{dt} = -a*(Q_{init} - Q_{final})*e^{-a(t-b)}$$

The stored metal heat and time at the end of blowdown are obtained from the SATAN output tables. The stored metal heat at equilibration, Q_{final}, is determined by the metal heat capacity and the equilibration temperature, $M*c_p*T_{eq}$. The metal heat capacity, $M*c_p$, is obtained from the SATAN input tables. The RCS temperature is assumed to reach an equilibrium value at the end of the reflood period. Using an equilibration temperature, T_{eq}, of [ ]^{a,c} was found to produce good agreement between the spreadsheet calculational method and the code calculated mass and energy releases for a conventional plant. This equilibration temperature value corresponds to [ ]^{a,c} the AP600 containment design pressure. A higher equilibration temperature value of [ ]^{a,c} is used for AP1000 since the containment design pressure is higher than AP600. The equilibration temperature is held constant for the post-blowdown calculation.

The metal time constant is the metal heat capacity divided by the heat transfer rate. Because the heat transfer rate is variable, the time constant is arbitrarily increased to release 99% of the RCS metal energy (in excess of the equilibration temperature) over 60 minutes.

5. The steam generator stored energy at the end of blowdown is released using the same equation shown above for the RCS metal energy release rate. The stored energy and time at the end of blowdown are obtained from the SATAN output tables. The stored energy at equilibration is determined by the metal and fluid heat capacity and the equilibration temperature, $\{(M*c_p)_{fluid} + (M*c_p)_{metal}\}* T_{eq}$. The steam generator fluid and metal heat capacity input values are obtained from the SATAN input tables.

The stored energy in the broken loop and intact loop steam generators is released at different rates. The time constants for AP600 are set to values similar to standard plant analyses. Because the AP1000 CMT injection flow rate limits the steaming rate, the AP1000 time constants are adjusted to provide a more mechanistic representation of the steam generator energy release relative to the available core makeup flow, and to maximize the steaming rate during the CMT injection period.

Calculation of the Vessel Liquid Mass

6. During the reflood period, the mass of liquid in the vessel is assumed to increase exponentially according to the following equation:

$$M(t) = M_{final} + (M_{initial} - M_{final}) * e^{-c(t-b)}$$

where: M_{final} = RCS mass at the end of reflood (lbm)
$M_{initial}$ = RCS mass at end of blowdown (lbm)
c = inverse reflood time constant (sec^{-1})
t = time (sec)
b = end of blowdown time (sec)

At the end of the reflood period, the RCS is assumed to be at a saturation temperature of [ ]^{a,c} with a vessel void fraction of [ ]^{a,c}. These assumptions were found to produce good agreement between the spreadsheet calculational method and the code calculated mass and energy releases for a conventional plant.

The RCS liquid mass at the end of the reflood period, M_{final}, is calculated using the following equation:

$$M_{final} = V*(1-alpha)*rho$$

where: V = Vessel volume (ft^3)
alpha = Vessel void fraction at end of reflood
rho = Saturated liquid density at [ ]^{a,c} (lbm/ft^3)

The temperature and amount of mass in the vessel at the end of reflood are held constant throughout the long-term cooling phase. These assumptions maximize the steam release rate because there is no additional filling of the vessel and, because the temperature does not decrease, the latent heat of vaporization does not increase.

An initial value for the RCS fluid mass is given in the SATAN summary table. The RCS initial mass input for the spreadsheet calculation, $M_{initial}$, is artificially instantaneously increased to eliminate the time delay associated with refilling the downcomer and lower plenum of the vessel. Eliminating the refill period shifts the mass and energy releases earlier in time and results in an increase in the predicted peak containment pressure.

The reflood time constant is related to the vessel volume, the injected mass flow rate and the steaming rate. The time constant is set to allow the vessel mass to reach 99% of the M_{final} value in approximately 400 seconds. This time frame is consistent with reflooding times for conventional Westinghouse PWR designs with similar vessel volume and injection rates.

Calculation of the Break Vapor and 2-Phase Mass Flow Rates

Steps 7 through 10 describe the method that is used to calculate the break mass flow rate and to partition it into the vapor and 2-phase flow components for input to the WGOTHIC Containment Evaluation Model.

7. The break mass flow rate is defined as the difference between the injected mass flow rate and the time derivative of the vessel liquid mass, as shown in the equation below:

$$m_{break} = m_{inject} - c*(M_{final} - M_{initial}) * e^{-c(t-b)}$$

Following the end of the reflood period (400 seconds), the total flow released from the break is equal to the injected flow; no additional inventory is stored in the RCS.

8. The core inlet enthalpy is calculated by dividing the RCS metal energy release rate by the injected liquid mass flow rate, and summing this with the enthalpy of the injected flow, $h_{core} = h_{inject} + Q_{metal}/m_{inject}$. After injection stops, the core inlet enthalpy is set to a constant value. This value is based on the upper bound fluid temperature in the containment sump.

9. The total break flow rate is partitioned into a steam and a 2-phase component. Because the containment pressure is dependent on the steam release, the steam mass flow rate is maximized by assuming 95% of the core energy and all of the steam generator energy is used to produce steam. The steam and 2-phase fluid break mass flow rates are calculated using the following equations:

$$m_{steam} = \min \{ m_{break}, (0.95 * Q_{core} + Q_{SG})/(h_g - h_{core}) \}$$
$$m_{2\text{-}phase} = m_{break} - m_{steam}$$

where: Q_{core} = Sum of the core decay heat, stored energy and Zr-H_2O reaction release rates (BTU/s)
Q_{SG} = Sum of the broken and intact SG energy release rates (BTU/s)
h_g = Steam enthalpy at the equilibration temperature (BTU/lbm)
h_{core} = Core inlet enthalpy (BTU/s)
m_{break} = Total break mass flow rate (lbm/s)

Note, because the steam enthalpy is assumed to remain constant at the equilibration temperature, the steam generator energy is used to produce additional steam release, rather than superheat the steam. This maximizes the steam release rate.

10. The enthalpy of the 2-phase break fluid is calculated using the following equation:

$$h_{2\text{-}phase} = \min \{ h_g, h_{core} + 0.05 * Q_{core} / m_{2\text{-}phase} \}$$

where all terms have been defined previously. The limit is applied to prevent the 2-phase enthalpy from exceeding h_g when the 2-phase mass flow rate is very small.

Check for Energy Conservation

11. Conservation of energy is checked at the end of each time step. [

]^{a,c}

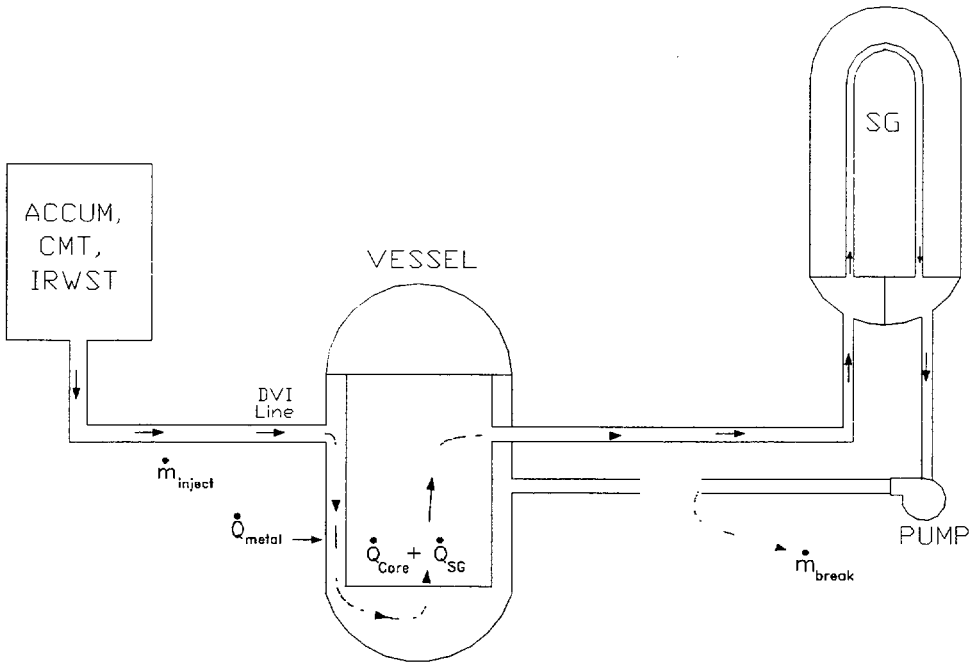

Figure 14.3-1 Spreadsheet Mass and Energy Release Schematic

14.4 Comparison of SATAN/Spreadsheet Releases with WCOBRA-TRAC Calculated Releases

The AP1000 DECL LOCA mass and energy releases calculated using the SATAN/spreadsheet method were compared to the WCOBRA-TRAC (WCT) code calculated results to demonstrate the amount of conservatism in the calculation. The comparison was run out 2000 seconds; this is beyond the calculated time of peak containment pressure. Although this version of the WCT code was not designed to produce LOCA mass and

energy releases that would be conservative for use in calculating containment peak pressure, it should nevertheless mechanistically calculate a reasonable estimate of the releases.

The blowdown mass and energy comparison is shown in Figures 14.4-1 and 14.4-2. SATAN predicts a higher blowdown mass and energy release rate than WCT. The post-blowdown mass and energy comparison is shown in Figures 14.4-3 and 14.4-4. The spreadsheet method calculates a higher release rate than WCT because the spreadsheet releases the SG energy at a much higher rate than WCT.

The integrated mass and energy releases are compared in Figures 14.4-5 and 14.4-6. The SATAN/spreadsheet method predicts approximately a 50-percent higher integrated mass and energy release than WCT, by the time peak pressure occurs. This difference results in a 20 psi higher calculated peak pressure as shown in Figure 14.4-7.

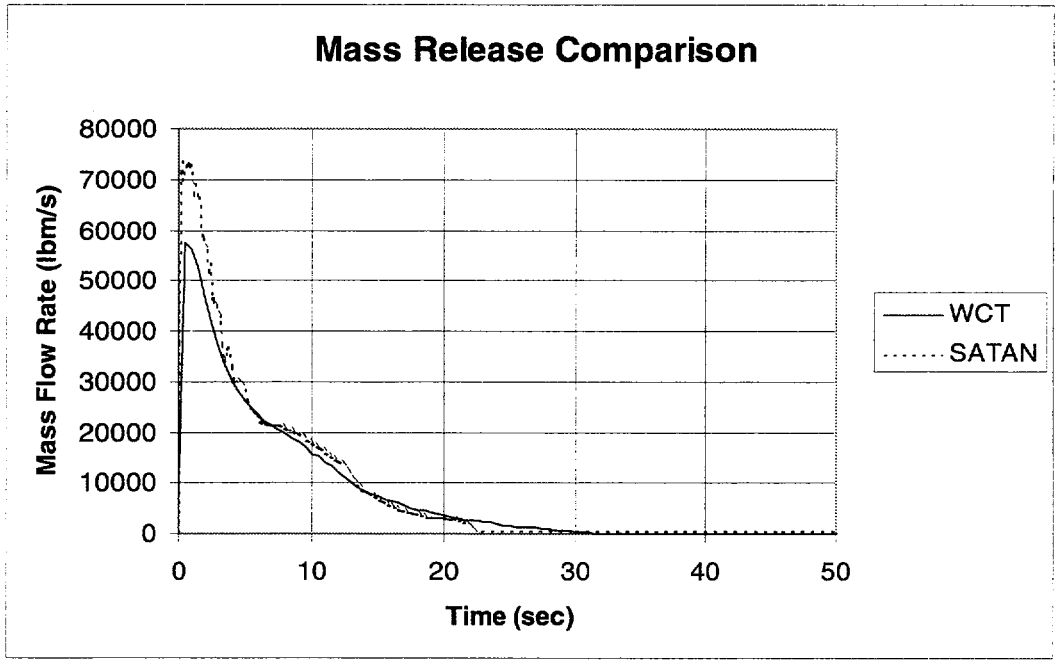

Figure 14.4-1

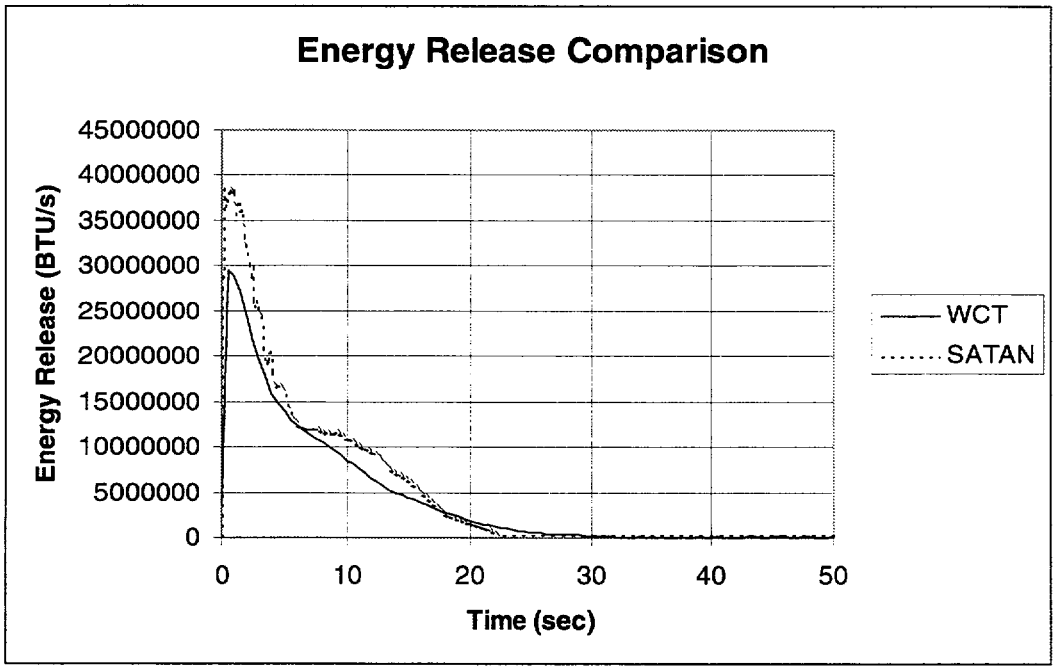

Figure 14.4-2

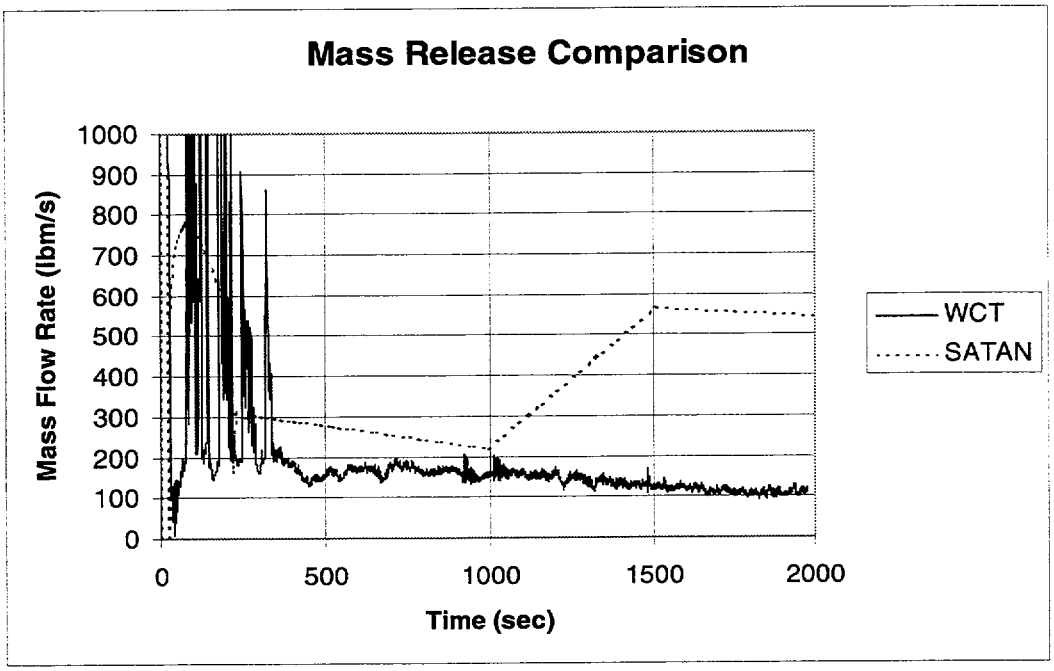

Figure 14.4-3

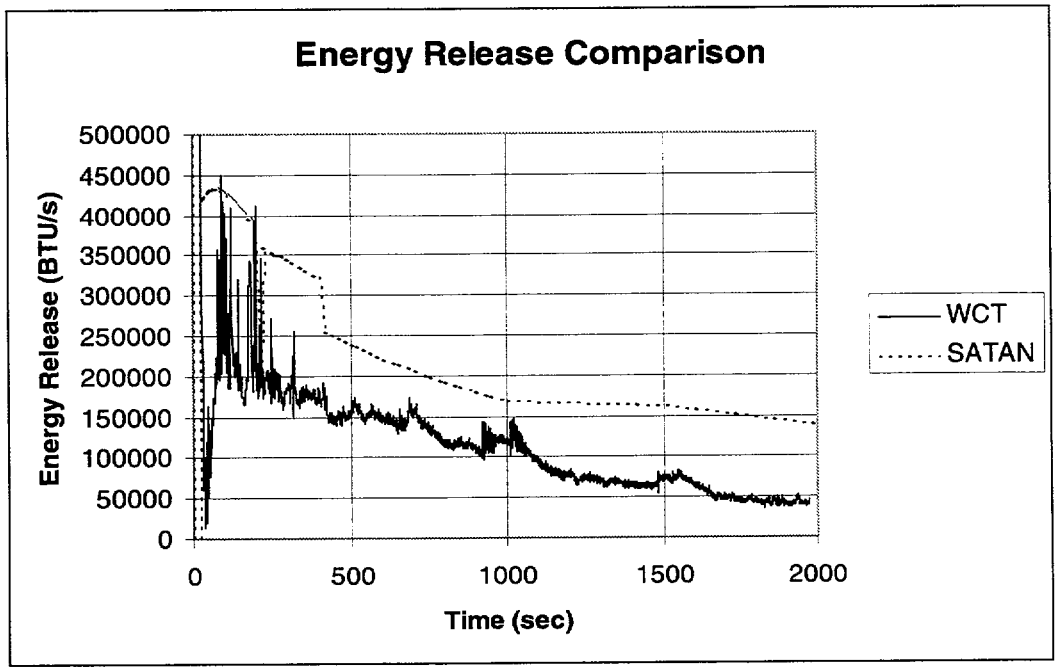

Figure 14.4-4

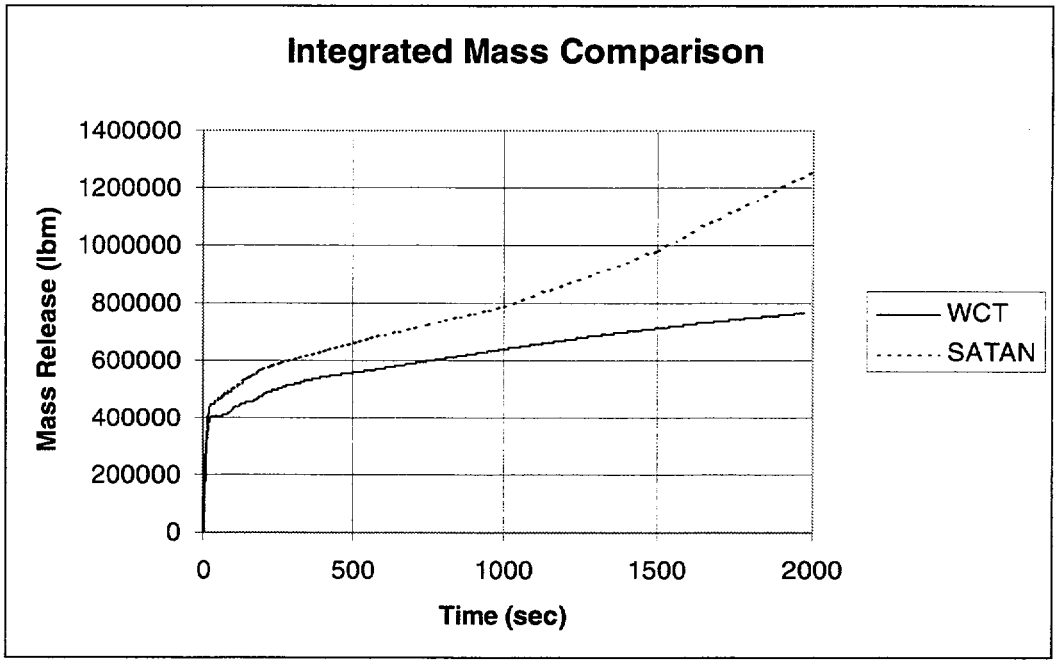

Figure 14.4-5

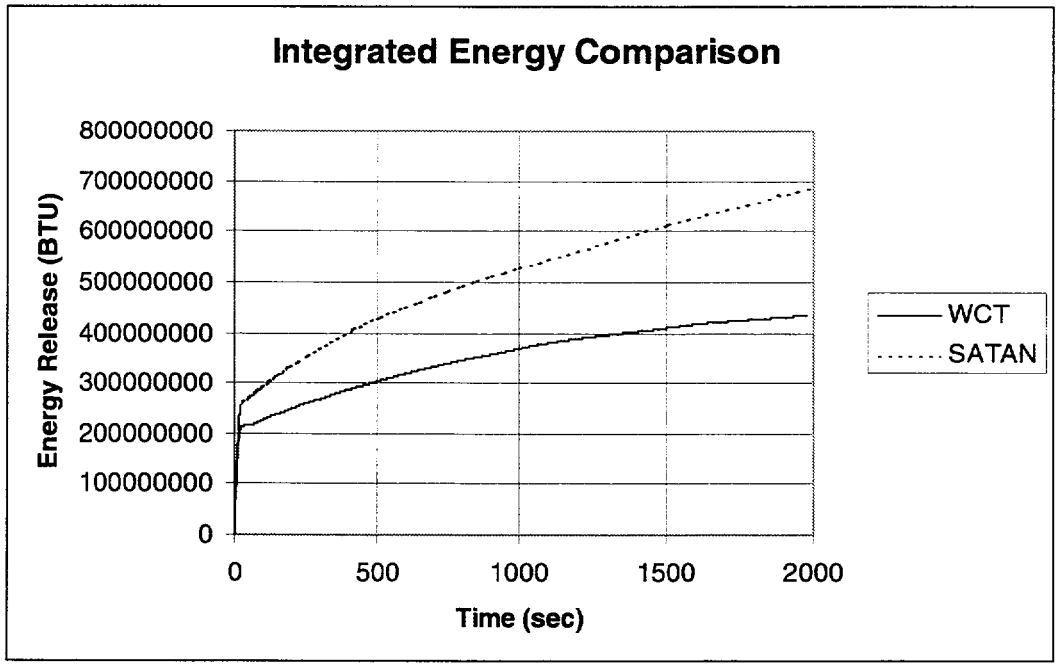

Figure 14.4-6

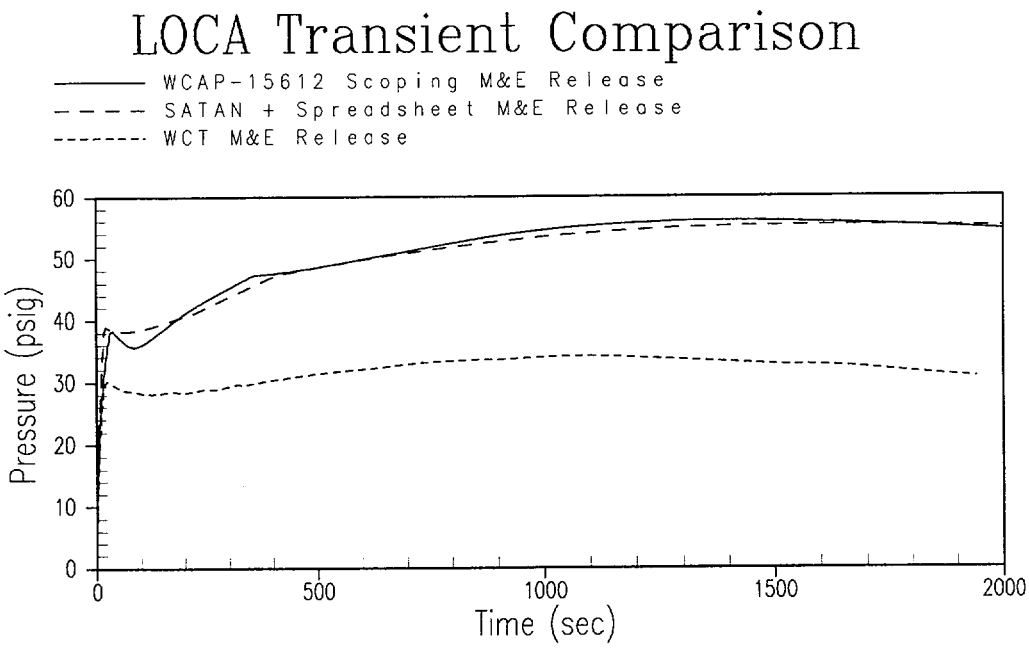
LOCA Transient Comparison
WCAP-15612 Scoping M&E Release
SATAN + Spreadsheet M&E Release
WCT M&E Release
Pressure (psig)
Time (sec)
0
10
20
30
40
50
60
0
500
1000
1500
2000

Figure 14.4-7

14.5 Summary and Conclusions

The methodology, used to predict mass and energy releases to the containment during the blowdown phase of the Large LOCA accident for the AP600 and AP1000 containment DBA, is consistent with the methodology approved by the NRC for current operating plants. The approved methodology yields conservatively high total energy and energy release rates to the containment atmosphere, consistent with regulatory guidance for Design Basis Analyses.

A spreadsheet calculation method is applied to calculate the post-blowdown mass and energy releases for the AP600 and AP1000. Because the containment pressure is dependent on the steam release, the break steam mass flow rate is maximized in the calculation. The transient flow rates for the accumulators, CMTs and IRWST, are calculated using a resistance network. These flow rates, along with the conditions at the end of the SATAN blowdown mass and energy release analysis, are input to the spreadsheet. The spreadsheet accounts for the same sources of energy and uses similar energy release rates as the conventional plant analysis. A comparison of the releases predicted by the spreadsheet and the approved mass and energy release analysis codes/models show that the spreadsheet provides a conservatively high prediction of the release to containment. Therefore, the spreadsheet method for calculating the post-blowdown mass and energy releases used in the AP600 and AP1000 containment analysis is consistent with the methodology approved by the NRC for current operating plants.

14.6 References

1. WCAP-10325-PA, "Westinghouse LOCA Mass and Energy Release Model for Containment Design March 1979 Version," May 1983